Development of Technical Bases for Using Infrared Thermography for Nondestructive Evaluation of Fiber Reinforced Polymer Composites Bonded to Concrete

by
Mónica Anastasia Starnes

Bachelor of Science in Civil Engineering
University of New Mexico, Albuquerque, New Mexico, 1997

Master of Science in Civil Engineering
University of New Mexico, Albuquerque, New Mexico, 1998

Submitted to the Department of Civil and Environmental Engineering
in partial fulfillment of the requirements for the
Degree of Doctor of Philosophy in Structures and Materials
at the
MASSACHUSETTS INSTITUTE OF TECHNOLOGY

September 2002

Author .....
Department of Civil and Environmental Engineering
August 16, 2002

Certified by .....
Eduardo Kausel, Professor of Civil and Environmental Engineering
Department of Civil and Environmental Engineering

Accepted by .....
Oral Buyukozturk, Chairman
Departmental Committee on Graduate Studies

Development of Technical Bases for Using Infrared Thermography for Nondestructive Evaluation of Fiber Reinforced Polymer Composites Bonded to Concrete

by
Mónica Anastasia Starnes

Submitted to the Department of Civil and Environmental Engineering
on August 16, 2002 in partial fulfillment of the requirements for the
Degree of Doctor of Philosophy in Structures and Materials

Abstract

Fiber-reinforced polymer (FRP) composites, in the form of pultruded laminates or built-up woven fabrics, are being used widely to strengthen existing concrete and masonry structures. The success of these materials in performing their intended functions depends, to a large extent, on how well they are bonded to themselves and to the substrate. There is a need for an efficient and reliable method to detect and characterize defects at the substrate interface and within multi-ply systems. Infrared thermography is well suited for this purpose because it is inherently sensitive to the presence of near-surface defects and can interrogate large areas efficiently. Before infrared thermography can be developed into a standard methodology, however, an understanding is needed of the effects of testing parameters and different types of defects. This dissertation focuses on establishing the potential for quantitative infrared thermography, that is, not only detecting but also characterizing subsurface flaws. Numerical and experimental methods are used to investigate the effectiveness of infrared thermography to estimate the width of subsurface flaws in fiber-reinforced polymer laminates bonded to concrete.

First, a dimensional analysis of a simplified case of one-dimensional heat diffusion in an infinite half space is performed to establish the parameters that affect the thermal response of the test object. The results from the dimensional analysis identified the factors that had to be investigated in the parametric study.

Next, the finite-element method is used to carry out parametric analyses of the thermal response of simulated defects in fiber-reinforced polymer laminates applied to a concrete substrate. In this study, a "defect" is an air gap between laminates, at the laminate/substrate interface, or in the substrate. The aim is to assess the potential for quantitative infrared thermography in not only detecting a flaw but also being able to describe its physical characteristics. Six parametric studies are presented, namely: 1) relationships between the thermal input, the maximum signal, and the maximum surface temperature; 2) effect of thermal material properties of FRP composites and concrete; 3) effects of flaw depth and the number of FRP layers; 4) effect of flaw thickness; 5) effect of flaw width and estimation of flaw width; and 6) a multi-parameter screening study to determine relevant factors. From these simulations, procedures are established for selecting the thermal input and estimating the flaw depth and width.

The third component of the investigation focuses on laboratory studies. Controlled-flaw experiments are performed to evaluate the potential of infrared thermography testing to quantitatively assess subsurface flaw in FRP bonded to concrete. First, a qualitative test is successfully performed to evaluate the potential for detection of each simulated flaw embedded in the test object. The next two experiments involve quantitative thermography testing of an air void embedded at the interface between a pultruded FRP laminate and the concrete substrate. A comparison between the quantitative infrared thermography test and finite-element simulations of the same test is also performed. Good agreement between experimental thermal response parameters and those calculated from finite-element models provides assurance of the validity of parametric studies based on numerical simulations. Controlled-flaw experiments are also performed to verify the procedure for estimating the width of subsurface flaws. Good agreement is found between the estimated and actual flaw dimensions. Data smoothing is shown to be effective in removing "noise" from measured temperature profiles. An experimental screening experiment is carried out to determine the relevant factors affecting the thermal response of the controlled-flaw specimens. The results indicate that the depth of the flaw is the only relevant factor affecting the time to maximum signal. Finally, an experiment is performed to determine the degree of repeatability of infrared thermography testing and the assessment of adequate sampling rate. It is concluded that sampling rates of 1 Hz are adequate for quantitative evaluation of FRP bonded to concrete.

The results of investigation provide demonstrable evidence of the potential of infrared thermography to characterize the depth and width of flaws (air voids) embedded in FRP composites bonded to concrete.

Thesis supervisor: Eduardo Kausel
Title: Professor of Civil and Environmental Engineering

Acknowledgements

I would like to express my most sincere admiration and gratefulness to my doctoral advisor, Professor Eduardo Kausel. I will always be deeply thankful for his continuing guidance, mentorship, and encouragement.

I also want to express my deep admiration to Dr. Nicholas Carino, my advisor at the National Institute of Standards and Technology (NIST). His encouragement for seeking scientific and engineering discovery will always be with me.

I would also like to express my gratitude to the remaining members of my committee: Dr. Jerome Connor, Dr. Oral Buyukozturk, and Dr. Shi-Chang Wooh. Their support and guidance is greatly appreciated.

I am deeply thankful to the National Science Foundation. Its support through the Graduate Research Fellowship has allowed me to pursue my goals for advanced learning.

I would also want to thank NIST and, specially, the Building and Fire Research Laboratory for funding my investigation during the last two years. While at NIST, I have had the great pleasure of collaborating with the some of the most distinguished and innovative engineers and researchers in the country. I am greatly thankful to my colleagues at NIST's Structures Division, especially Dr. John Gross and Dr. H.S Lew, for their enduring technical help and friendship. I also want to express thanks to Mr. Andre Witcher, of the Structures Division, for his help with the fabrication of the experimental apparatus, and to Dr. Daniel Flynn and Dr. William Healy, of the Building Environment Division, for their help and lessons in the field of heat transfer.

Finally, I would like to profoundly thank my family and friends for their support through the years. Their support, encouragement, and patience have always allowed me to fulfill my goals.

Table of Contents

Chapter 1

Introduction

1.1 Background

The trend in civil engineering is toward the development of high-performance structures that incorporate advanced materials. Moreover, the up front application of advanced materials in civil engineering structures incorporates the use of fiber composites. Fiber-reinforced polymer (FRP) composites are two-phase engineered materials that combine high performance fibers within a polymer matrix. Typically, FRP composites are reinforced by long unidirectional continuous fibers. These advanced materials are characterized by their high strength, high stiffness, low density, and durability. Consequently, wide application of advanced composites may allow engineers to design innovative structures.
Most FRP materials are generally used as thin elements or structural subsystems. In civil engineering applications, FRP composites are undertaking a major role in the rehabilitation of existing civil infrastructure. Rehabilitation involves the repair and strengthening of functional or structural deficiencies of structural components. For this purpose, composite layers or laminates are primarily bonded to existing reinforced concrete and masonry structures using adhesives such as epoxy resins. The primary purpose of bonded FRP composites is to enhance the structural capacity of the rehabilitated structure.

However, the major factor that contributes to the optimum performance of the composite system is the quality of bond between the FRP and the concrete or masonry substrate. For example, in beam and wall applications, fabricators must be able to guarantee bond and sufficient development length and anchorage of the FRP laminates. Yet, standard quality control procedures to assess the integrity of FRP composite systems still need to be developed for civil engineering applications. Ultimately, quality control of the final product is a requirement for the successful implementation of any new material in structural engineering systems.

Furthermore, the final mechanical properties of FRP composites are affected by environmental aspects such as temperature, moisture, and contaminants. As such, the quality of a FRP composite is influenced by the manufacturing process and where (factory vs. *in situ*) the composite is fabricated. For civil structures, installation and curing of FRP composites occur typically in the field rather than in a controlled environment. Generally, installation involves manual application of fabric and resins. Thus, there is potential for high variability of the final product unless appropriate quality control procedures are used. Composite thickness,

interlaminar adhesion, and substrate bonding must be carefully monitored. Additional defects intrinsic to this process are air voids and contaminants, which may accelerate the formation of in-service delaminations and debonds in the FRP composite.

A variety of techniques exist for installation of external FRP composite systems. The most common techniques in civil engineering applications are wet lay-up, prepreg, precured shells, resins infusion, and pultruded sheet. Figure 1.1 illustrates some of the applications of FRP composites for rehabilitation of civil engineering structures.

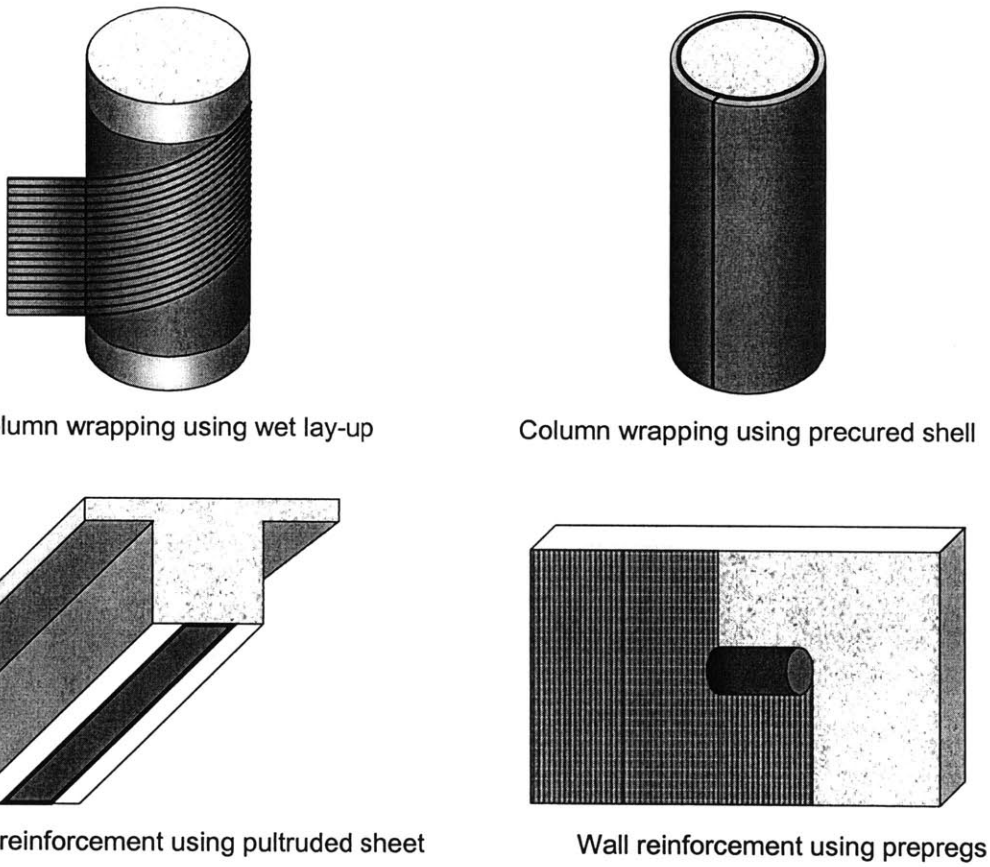

Fig. 1.1 Examples of applications of FRP composites for rehabilitation purposes

Lay-up using fabric, tape, or tow is probably the most used technique (Karbhari et al., 1998). The installation process is simple: fiber fabric or tow is wrapped or wound around the structural member; resin is then impregnated using a wet bath. The primary advantages of this technique are that it provides the maximum flexibility for installation and is economical. Because installation involves manual application of fabric and resins, variability of the final product is to be expected. Air voids and contaminants are defects intrinsic to this process.

Prepreg laminates are sheets of resin-preimpregnated fibers. Prepreg lay-up is similar in installation procedure to wet lay-up. These laminates are also manually placed on the structural

element. Although, generally more expensive than wet lay-up systems, prepreg systems are more consistent and have fewer defects. Additionally, prepregs need high curing temperatures, which produce higher glass transition temperature of their matrices. Despite the benefits of using prepregs, researchers claim that the application of these composites to masonry walls may be difficult due to the inherent stiffness of the plies (Christensen et al., 1996).
Precured shells are manufactured in a factory and then bonded in the field. The primary application of these jackets is for retrofitting of columns. The controlled fabrication process assures the quality of the FRP shell. However, adequate bonding of the shell to itself and to the concrete structure is critical.

The resin infusion process is a recently developed installation method. Dry fibers are first applied to the structure (primarily columns) and then followed by infusion of resin using a vacuum. Resin infusion systems are cured at ambient temperatures. Low glass transition temperature is a disadvantage. This technique achieves higher uniformity in the composite than wet lay-up.

Finally, the pultrusion manufacturing method allows fabrication of continuous cross sectional components (rods, laminates, channels, etc.). They are manufactured at the factory and externally bonded to the concrete structure in the field. Pultruded composites are mostly used in beam applications where thin strips are bonded to the tensile faces. Due to the high quality control at the factory, these FRP systems posses high uniformity and a minimum amount of defects within the composite but they must still be bonded to the structure in situ.

1.2 Motivation

FRP composites bonded to concrete are, by their nature and installation method, prone to high variability of thickness and other internal anomalies. Effective quality control methods for these composite systems must provide quantitative information regarding the thickness and fiber content of the applied composite and amount, location, and size of defects at any given time through the life of the structure. In addition, FRP composites are starting to be widely used without a complete understanding of the structural mechanics and durability properties of these materials. The inherent danger of erroneous expectations about the capabilities of FRP composites is an incentive for the development of reliable nondestructive evaluation techniques. Nondestructive testing (NDT) methods together with mechanics and durability studies should be able to predict structural reliability and material integrity and thus, allowing for the prioritization of the repair cycle of civil infrastructure.

Nondestructive testing techniques for FRP composites are already widely researched and used in the aerospace industry for both manufacturing quality control and routine maintenance inspection. Yet, the quality of the manufacturing process, sizes of the structures, boundary and environmental conditions, and available budget for inspection of aerospace structures are quite different from those of civil structures. Thus quality control of composite materials used in civil engineering applications requires the development of reliable NDT techniques and standard test methods for this particular application.

Nondestructive testing techniques can be categorized into two major groups: electromagnetic methods and mechanical vibration methods. Likewise, electromagnetic methods are subdivided

into nuclear, radar, thermography, magnetic, and electric. Mechanical vibration methods include ultrasonics, acoustic emissions, acousto-ultrasonics, vibration methods, and coin tap testing.
Nuclear NDT methods such as radiography (X-rays) are of very limited use in the inspection of fiber reinforced polymers. The method has been tried for the determination of structure composition, density, permeability, thickness, fiber volume ratio, and moisture content, among others. The method does not detect interlaminar defects such as voids, debonds, and delaminations. The primary reason why interlaminar defects are not detected is that most flaws are perpendicular to the X-ray beam making detection nearly impossible. Debonds can not be detected because the absorption of the adherent is generally very high. The only solution for optimum inspection is the introduction of radio-opaque penetrants. However, penetrants require surface breaking and are highly toxic.

The bases for radar testing are very simple. A beam of electromagnetic energy is sent to the tested structure. Portions of the energy are transmitted through the structure but the remaining energy is reflected back from each boundary (surface, layer, or flaw) encountered. An example of radar methodology is short-pulse radar, which uses microwave energy. This method is used for the evaluation of delaminations and water content in concrete. Additionally, thickness, density, fiber orientation, volume ratio, material degradation, and flaws of FRP composites can be inspected using short-pulse radar. However, radar technology needs further improvements in antenna resolution for its application to FRP composites bonded to concrete structures.
Thermographic techniques (infrared thermography, liquid crystal thermography, etc.) consist in applying heat to the structure and observing the temperature gradients on the surface of the specimen. Infrared thermography is best suited for detection of anomalies near the surface of the specimen. Thus, detection of internal anomalies in thin FRP composites bonded to concrete is possible. In civil applications, current infrared thermography testing of FRP composites is focused on qualitative estimates of the state of the structure. The reason for the qualitative nature of the results is the complex relationship between the variables affecting the thermal response of the bonded assemblies.

Three examples of magnetic testing are magnetic induction, flux-leakage method, and nuclear magnetic resonance or magnetic resonance imaging (MRI). Both magnetic induction and flux-leakage testing are only effective for ferrous materials. Thus, testing of FRP composites is unfeasible. Nuclear magnetic resonance is widely used in other fields such as medicine. Only small specimens can be tested in a lab environment, hence making this method irrelevant to civil engineering applications.

Eddy-current is the most popular electric technique for testing FRP composites. Two basic methods are used on the determination of stacking sequence: resistive eddy-current path and resistive capacitive eddy-current path. On the resistive eddy-current path technique, the electric current passes from one fiber to another at the points of contact. On the other hand, the resistive capacitive eddy-current path method allows for an interfiber capacitive path in addition to the resistive path. Since the method requires a conductive material, glass fiber reinforced polymers cannot be tested. This method can determine the stacking sequence in carbon fiber reinforced polymers (CFRP). Eddy-current is also limited to composites with high fiber-volume ratio. An additional disadvantage is that eddy-current methods are insensitive to porosity, delaminations, and other nonconductive inclusions in the material.

Ultrasound techniques such as pulse echo, impulse echo, impulse response, surface waves, and plate wave method are widely used in civil engineering inspections. In this technique, a stress pulse is introduced to the surface using a transmitter. After the introduction of the pulse, a series of compression waves develop through the depth of the specimen. Waves are reflected to the surface by cracks or ply interfaces giving quantifiable data about the state of the material. Currently pulse echo is the most successful ultrasonics methods for testing composite materials in aerospace applications. Pulse echo techniques can determine the depth of FRP composites and their elastic modulus. However, due to the high attenuation of FRP composites, only low frequencies can be used to test these materials. This is a problem because most available T/R transducers are designed for higher frequencies.

Acoustic emission testing records elastic stress waves generated by localized cracking in the structure. Analysis of the wave propagation gives the extent of damage of the structural member. Although the method is widely used in lab and factory settings, field use is limited. The primary reason for this limitation is the high occurrence of noise contamination in civil engineering applications. Acousto-ultrasonic methods are very similar to ultrasonic techniques. They provide, however, information that is more detailed.

Dynamic or vibration methods include techniques such as resonant frequency, pulse velocity, and lamb-wave methods. The resonant frequency method evaluates the dynamic modulus of the structure using its fundamental frequency. This technique requires a transducer to be acoustically coupled to the test object using a liquid couplant. The structure or test object directly affects the resonance frequency and signal amplitude of the transducer. The transducer, which usually operates in the 25 Hz to 500 Hz band, produces a specific standing wave in the test object. The presence of an internal flaw changes the pattern in the standing wave of the material. Although very successful in aerospace structures, this method is limited to laboratory size specimens. The primary reason for the small specimen size is that small defects have little effect on the natural frequency of the structure (i.e. large civil structure). Therefore, resonance testing is usually conducted on individual structural components to detect localized damage.

Coin tap test is the method most widely used for the detection of flaws such as delaminations and debonds. This method is simple, inexpensive, and requires minimum instrumentation. However, the test is extremely localized and qualitative in nature. Quantitative techniques are currently being investigated and developed at the Center for NDE. An example of a potential quantitative technique is the Computer-Aided Tap Tester (CATT).

Two optical techniques show potential for testing FRP composites: laser doppler vibrometer and shearography. The laser doppler vibrometer technique is based on the local-membrane vibration of the composite laminates at the location of the internal flaw. The vibration is produced by exciting the FRP composite using piezoelectric actuators such as PZT. The surface of the test object is then scanned with a laser. The method is able to image debonds between concrete substrates and the bonded FRP composites. However, the surface of the test object needs to be covered with reflecting tape in order to produce the required doppler effect.

Shearography is based on the principles of laser interferometry. As such, it requires the superposition, or in this case the subtraction, of two speckle patterns of the test object under different strain conditions. This technique employs a single laser beam, which is expanded and

projected onto the surface of the test object. An image of the surface of the test object is taken with the shearography camera before the loading is applied. This camera incorporates a bifringent lens that shifts the recorded image. The specimen is then loaded to produce the needed strain. The strain condition may be produced using various techniques such as vacuum stressing, thermal stressing, and vibrational excitation. A second image of the loaded specimen is recorded and subtracted from the before-loading image. The image processing produces a series of fringes that quantify the amount of strain in the test object. Research has shown that internal flaws are detectable using shearography (der Hovanesian et al., 1995). The technique also allows for the estimation of the depth of the anomaly. The primary inconvenient of this technique is the high cost of the equipment.

The final nondestructive testing technique is infrared thermography. This method is based on the measurement of the radiation emitted by the sample. This radiation is proportional to the surface temperature of the test object. Internal flaws produce significant changes in the thermal diffusion pattern of the sample. These changes may be seen on the surface of the sample at which the temperature above the flaw is different from the temperature above the sound material.

All of these NDT methods have advantages and disadvantages. The best technique to detect and characterize a defect depends on the extent of the critical flaw size, the size of the structure being tested, and the environment in which the inspection is carried out. Successful implementation of any NDT method requires the technique to be accurate, cost efficient, and easy to use. The technique should be able to detect the size, type, and location of typical flaws. In addition, for civil engineering applications, the ideal inspection technique must allow for *in situ* and preferably global testing for most civil engineering applications. Global testing refers to the ability to measure the characteristic of the complete structural element from a single element.

Nondestructive testing of FRP composites presents a variety of difficulties due to material characteristics such as anisotropy, high electrical resistance, variable ultrasonic attenuation, and non-magnetism. Thus, uncommonly used methods like infrared thermography may be more suitable for testing FRP composites than most traditional testing methods based on sonic and electromagnetic wave propagation techniques.

The versatility and global testing nature of infrared thermography makes this technique an ideal method for civil engineering inspections. Infrared thermography has already been used to assess the severity of structural systems. Present inspection of composites using infrared thermography is focused on qualitative rather than quantitative estimates of the state of the structure. Current inspection data is not being exploited fully because of the lack of scientific research about the relationship between variables affecting the thermal response of the bonded laminates, lack of standard data collection, and insufficient understanding of radiometric theory by thermography inspectors (Connolly, 1991).

In order to allow widespread use of thermography for quantitative assessment of FRP applied to concrete and masonry structures, a standard test method is needed. However, to develop such a standard, it is necessary to develop a greater understanding of the factors affecting the thermal response of FRP composites.

1.3 Research Objectives

Infrared thermography (IR) is an inspection method currently used successfully to locate subsurface flaws in FRP laminates bonded to concrete (Hawkins et al., 1999). Trial case studies performed by the FHWA and New York DOT (Alampalli et al., 2001), among others, confirmed that infrared thermography is a promising NDE method considering testing speed and ability to detect flaws. Inspections using infrared thermography, however, are primarily focused on qualitative assessment of the state of the structure. The qualitative nature of the results is due to the complex relationships between the variables affecting the thermal response of the bonded laminates. Nevertheless, the need for defect characterization, not just defect detection, has promoted research in quantitative infrared thermography. Knowledge of the fundamental parameters affecting heat transfer and infrared testing are needed to develop the foundation for quantitative thermographic inspection of civil structures. Therefore, experimental and analytical studies are needed to determine the capabilities and limitations of IR thermography for quantitative assessment of FRP bonded to concrete and masonry.

This doctoral dissertation focuses on experimental and analytical studies to establish the scientific bases for the development of a standard methodology for using infrared thermography in nondestructive evaluation of concrete and masonry structures strengthened with FRP composites. This research aimed to facilitate the development of standard methodology for quantitative infrared thermography testing of FRP composites bonded to concrete.

1.4 Research Approach

The research project has a multiple component approach. The investigation starts with a literature search, which includes an overview of the civil engineering applications of FRP composites, various nondestructive evaluation methods, and a literature review of infrared thermography (its theoretical principles and recent research).

The second phase of the investigation focuses on analytical studies including non-dimensional analysis and a series of extensive parametric studies involving numerical modeling. Finite element modeling is used of the parametric studies.

The final phase of the research project involves controlled-flaw laboratory studies. This phase of the research involves the fabrication and testing of specimens with simulated anomalies in bonded FRP laminates.

1.5 Outline of Thesis

This thesis is composed of six chapters, including this introductory chapter.

Chapter 2 summarizes the theoretical principles of infrared thermography and relevant research in the field. Relevant studies in thermography are reviewed and outlined from an extensive literature survey. The literature review focuses on numerical modeling, finite-element and finite-difference, of infrared thermography testing.

Chapters 3 and 4 present analytical studies of thermal evolutions typical of infrared thermography testing. Chapter 3 develops the dimensional analysis of the simplified heat transfer problem of a multi-layer semi-infinite space heated with a heat flux pulse. The results from the dimensional analysis helps identify some of the variables needed to be investigated in the parametric study of Chapter 4.

Chapter 4 present analytical studies of the main parameters affecting thermal evolution in infrared thermography testing by using finite-element modeling. Both single-parameter and multi-parameter investigations are carried out. The primary objective of the single-parameter study is to investigate the effect of several factors on the thermal response during thermography testing. The following investigations are performed for the single-parameter studies:

- Effect of thermal input
- Effect of thermal material properties
- Effect of flaw depth
- Effect of flaw thickness
- Effect of flaw width and width estimation

The multi-parameter study investigates which parameters that characterize subsurface flaws (depth, thickness, and width) affect the thermal responses. The importance of the parameters and their interactions are ranked and quantified.

Chapter 5 describes a series of laboratory studies. This chapter focuses on experimental research and validation of theoretical models. This chapter summarizes testing procedures involving construction of controlled-flaw test specimens, design and construction of experimental configuration, determination of input heat flux, determination of material emissivity, and active infrared thermography testing. Qualitative and quantitative thermography tests are described. Results from testing of a subsurface air void are compared with finite-element simulations to verify the validity of the numerical modeling from Chapter 3. Also, simple procedure for flaw width estimation is demonstrated. Next, a screening experiment is carried out to verify the results from the multi-parameter investigation described in Chapter 3. The final experiment describes the investigation involving test repeatability and effect of sampling rate.

Chapter 6 summarizes the results of the analytical and experimental studies of the thesis. Conclusions, leading to assessments for future research, are extracted.

Chapter 2

Literature Review

2.1 Introduction

Infrared thermography is being used successfully for defect detection in fiber-reinforced polymer (FRP) laminates bonded to concrete. Inspections using infrared thermography are mostly focused on qualitative assessment of the presence of flaws. The qualitative nature of the results is due to the complex relationships between the variables affecting the thermal response of the bonded laminates. This qualitative nature of the inspections stems from the complex relationships between the variables affecting the thermal response of the bonded laminates. The need for defect characterization, not just defect detection, has promoted a series of research projects in quantitative infrared thermography.

This chapter summarizes the theoretical principles behind infrared thermography nondestructive testing. Additionally, the state-of-the-art in quantitative infrared thermography is examined through a literature survey of research done by other researchers. The literature review focuses on numerical simulations of IR thermography. This survey concentrates in applications from the aerospace and manufacturing industries because of the lack of research in the quantitative inspection of civil structures using IR thermography.

2.2 Theoretical Principles

Infrared thermography, as a tool for flaw detection, is based on the principle that heat transfer in any material varies with the presence of flaws or any other change in material thermal properties. Figure 2.1 is a schematic of a concrete substrate with several FRP laminates applied to the surface. There is a flaw within the FRP layer and this flaw affects the flow of heat into and out of the FRP-concrete composite. The difference in heat flow through the flawed and unflawed regions causes localized energy differences on the surface of the test object, which can be measured using an infrared detector or radiometer. Through data processing, the measured infrared radiation is transformed into a surface temperature distribution and recorded in the form of thermograms (isotherm plots). The relation between surface temperature and emitted radiation is based on the Stefan-Boltzmann (Eq.2.1) and Wien displacement (Eq.2.2) principles, as follows

$$W = \varepsilon \sigma T^4 \tag{2.1}$$

$$\lambda_{max} = \frac{b}{T} \tag{2.2}$$

where,

W = radiant intensity (W/m^2),
ε = emissivity of the test object (dimensionless quantity),
σ = Stefan-Boltzmann constant (5.67x10^{-8} W/(m^2·K^4)),
T = absolute temperature (K),
λ_{max} = wavelength of the maximum radiation intensity (μm), and
b = Wien displacement constant (2897 μm/K).

Thermal anomalies in the thermogram indicate the presence of subsurface flaws in the test object. Equation 2.1 indicates that the emitted radiation is a nonlinear function of temperature, and Eq. 2.2 indicates that the wavelength of the peak intensity decreases with increasing temperature. At near room temperatures, the wavelength is in the infrared region of the electromagnetic spectrum. The emissivity is a property of the surface and has a value between zero and one. An emissivity value of one is found in perfect emitters such as a black body.

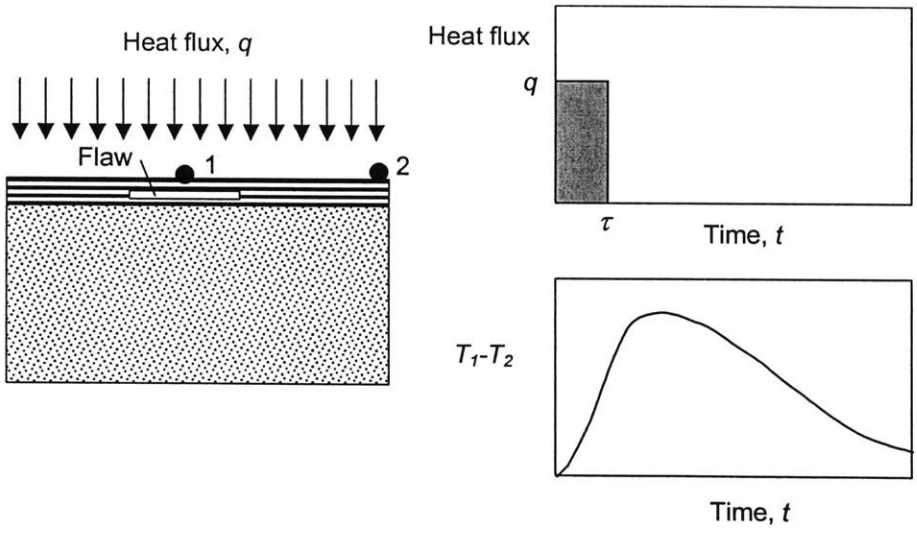

Fig. 2.1 Schematic of the infrared thermography method to detect presence of a flaw based on surface temperature differences

Infrared thermography is subdivided into two major testing approaches: *passive* IR thermography and *active* IR thermography. For both methods, the temperature of the test object must be different from ambient. The difference between the two methods is that an external thermal stimulus is required for active thermography, while in passive thermography the specimen itself is the source of the temperature difference. Passive thermography usually involves steady state thermal conditions and active thermography generally involves transient

heat transfer phenomena. Flaw detection and characterization in civil engineering structures require active thermography. In addition, defect characterization requires the use of time-resolved IR thermography. Using this technique, the surface temperature of the test object is monitored and analyzed as a function of time, instead of being monitored statically at only one particular point in time.

Infrared thermography is currently used for defect detection in FRP laminates bonded to concrete (Hawkins et al., 1999). However, inspections using infrared thermography are mostly focused on qualitative assessment of the state of the structure. The qualitative nature of the results is due to the complex relationships between the variables affecting the thermal response of the bonded laminates. Defect characterization, however, requires quantitative inspection techniques.
Quantitative characterization of internal anomalies requires the study of the transient heat transfer phenomenon. Starting with the general case, the thermal evolution in a material is governed by the theory of diffusion (Lienhard, 1981) as follows

$$\vec{\nabla} \cdot K \vec{\nabla} T + Q = \rho c \frac{\partial T}{\partial t} \tag{2.3}$$

where,

$\vec{\nabla}\cdot$ = divergence operator,
K = heat conductivity tensor,
$\vec{\nabla}$ = gradient operator,
T = temperature,
Q = internal heat generation,
ρ = density,
c = specific heat, and
t = time.

The term "thermal evolution" refers to the spatial and temporal distribution of temperature within the test object.-If the change in the conductivity tensor is relatively small with respect to the temperature of the material, equation 2.3 simplifies to

$$K\left(\nabla^2 T\right) + Q = \rho c \frac{\partial T}{\partial t} \tag{2.4}$$

where ∇^2 is the Laplacian operator. For example, in the Cartesian coordinate system, the Laplacian is defined as

$$\nabla^2 T = \frac{\partial^2 T}{\partial x^2} + \frac{\partial^2 T}{\partial y^2} + \frac{\partial^2 T}{\partial z^2} \tag{2.5}$$

When heat is applied suddenly to the surface of an object, transient heat flow occurs until thermal equilibrium is reached. During transient heat flow, the temperature at any point in the object changes with time. If the object has large dimensions perpendicular to the direction of uniform heat input and area of uniform heat input large enough compared to measurement depth,

heat flows parallel to the input, and the problem is reduced to one-dimensional heat flow. One-dimensional transient heat flow theory states that the temperature within the object changes in a nonlinear manner upon a step change in surface temperature, as follows (Lienhard, 1981):

$$T_d = T_\infty + (T_i - T_\infty)\ erf\left(\frac{y}{2\sqrt{\alpha t}}\right) \tag{2.6}$$

where,

T_d = temperature at any depth y in the object,
T_∞ = applied constant temperature at the surface of the specimen,
T_i = initial temperature of the solid,
erf = the Gaussian error function for ( ),
t = time, and
α = thermal diffusivity of the material.

Thermal diffusivity is defined as

$$\alpha = \frac{k}{\rho c} \tag{2.7}$$

where,

k = thermal conductivity,
ρ = density, and
c = specific heat.

Thermal diffusivity affects how fast a material changes temperature under transient conditions.

The nonlinear behavior described in Eq. 2.6 is illustrated in Fig. 2.2. Figure 2.2 shows the temperature history at various depths of a concrete slab after a constant temperature of 10 °C is applied at the surface.

In summary, during transient heat transfer through an object, surface temperature changes caused by internal anomalies in the material are time dependent. Surface temperatures depend on the elapsed time and the type, size, and depth of the defect. The surface temperature distribution is established by measuring the emitted radiation using an infrared camera. Accurate measurement of the surface temperature distribution depends on knowing the value of the emissivity of the surface and on environmental "noise" such as atmospheric attenuation and air movement.

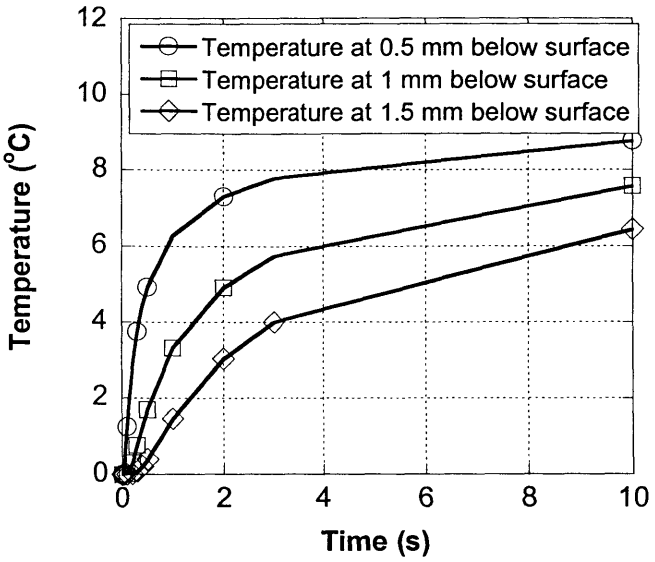

Fig. 2.2 Example of nonlinear behavior of thermal evolutions

2.3 Literature Review

This section presents a summary of a literature review of research involving infrared thermography testing. The literature survey indicates that, from an analytical point of view, most researchers choose to investigate infrared thermography using numerical simulations. Since infrared thermography is a very versatile testing technique, this section summarizes only a few investigations of interest, primarily those involving FRP composites or multi-layer systems.

2.3.1 Close-Form Versus Numerical Analytical Studies

Looking back at the diffusion principle, Eq. 2.3, the solution for heat transfer phenomena is simple, and of close form, for linear one-dimensional evolutions. Most engineering systems, however, involve complex geometries and boundary conditions that must be considered in their analysis. Additionally, when the thermal flow encounters a buried flaw, heat begins to flow in other directions in addition to the original direction of the flow, which was normal to the surface of the material under testing. Elementary analytical solutions are unattainable once the thermal phenomenon involves two-dimensional and three-dimensional transient events. Numerical modeling is the only analytical method capable of simulating realistic heat transfer problems. Furthermore, numerical analysis provides approximate solutions to the complex model within a small percentage of the exact solution. Thus, high accuracy could be easily achieved if the analytical model is properly outlined. In the past, the main disadvantage of numerical simulation, particularly for complex geometries, has been the large computation time and data storage space required to obtain the solution. However, these problems have become trivial due to the speedy development of both computer processing power and data storage.

In the field of nondestructive testing, numerical modeling is used to predict experimental data, validate test results, evaluate potential testing procedures, and aid further developments in the field. Numerical methods are effective resources for the validation and understanding of test results and the improvement of successful testing methods. Past research has focused on the evaluation of the various parameters that influence thermal evolution.

2.3.2 Summary of Investigations

Recent analytical investigations of heat transfer phenomena applied to infrared thermography have provided some general conclusions regarding diagnostic capabilities of this NDT method. The parameters investigated include material properties, attributes of anomalies, thermal stimulation, observation time, and testing mode. Brief descriptions of conclusions from parametric studies using numerical methods are discussed in this section.

2.3.2a Material Properties

Since active thermography is based on transient thermal evolution, the thermal response depends on the elapsed time and on the material properties of the materials tested. Both thermal conductivity and diffusivity are the primary material properties that affect thermal response of the structure.

Based on the thermal properties and the time dependency of thermal phenomena, deeper anomalies in a material are detected later (Cielo et al., 1987) and with decreased contrast (Allport et al., 1988)

$$t \approx \frac{z^2}{\alpha} \tag{2.7}$$

$$c \approx \frac{1}{z^3} \tag{2.8}$$

where, t is the detection time, z is the depth of the anomaly, and c is the detection contrast. Detection contrast is defined by Allport et al. (1988) as

$$c = \frac{T_d - T_b}{T_b} \tag{2.9}$$

where, T_d is the surface temperature above the defect and T_b is the surface temperature in the background. Based on this nonlinear dependency of defect depth and time of observation, time-resolved infrared thermography is required for quantitative measurement of anomalies in the structure.

Thermal conductivity and diffusivity are the primary material properties linked to thermal diffusion and thus, to the thermal behavior of a particular material. These two material properties are particularly important for the detection of internal flaws using infrared

thermography. For example, Vavilov et al. (1993) reported that an increase on thermal conductivity of the sound material by 10% tends to enhance the temperature contrast, and thus, detectability, by 10%. However, increases of thermal diffusivity by 10% may amplify the contrast only 5%. Hence, thermal conductivity is the main property affecting temperature contrast between sound and flawed areas. Furthermore, considering the material properties of the flaw itself, thermal conductivity again proves to be far more relevant than diffusivity for defect detection.

Thermal diffusivity is the primary material property affecting optimum detection time. For instance, materials with high thermal diffusivity are difficult to inspect using infrared thermography due to the fast thermal response of the material. Looking at a particular engineering application, Connolly (1991) reported that low thermal diffusivity coatings bonded to high thermal conductivity substrate produce high defect detectability. On the other hand, defect detectability on specimens with high thermal diffusivity coatings and low diffusivity substrate was significantly lower. The primary reason for the low detectability was that the fast thermal event experienced at the surface of the specimen was difficult to capture.

Considering the temporal effects on thermography, Vavilov et al (1993) stated that observation time is significant for materials with high diffusivity because of their fast thermal response. High diffusivity materials are difficult to inspect using infrared thermography. CFRP composites are transitory materials with a medium value of diffusivity. Thus, capturing thermal evolutions of CFRP with infrared equipment may be a complex task. The authors reminded that for the one-sided or reflection thermography case, maximum thermal contrast occurs after the temperature maximum.

Three-dimensional heat diffusion effects through the material tend to produce rounding effects on the thermograms of the anomaly. The amount of roundness may vary depending on the material composition of the test object. Rounding effects observed on the temperature field of delaminated composites were investigated by Varis (1995). The rounding of the edges of the defect was primarily caused by the difference in thermal conductivities of the anisotropic material. In this particular case, the composite material tested included both glass and graphite fibers. The highest temperature differences were observed at the glass fiber location. The numerical simulation indicated that the temperature signal in the carbon fiber area was too small to be detected experimentally with the chosen infrared equipment. This indicates the need for specific test procedures for particular applications and materials.

Varis et al. (1995) also concluded that the effect of anisotropy was minimal when the defect was located in the interface of deeper layers.

2.3.2b Defect Characteristics

Defect characterization involves several parameters: type, size, depth, and thickness of the defect.

Type of Defect

In IR thermography testing of FRP composites, the most typical anomalies investigated are delaminations, debonds, and inclusions parallel to the surface of the specimen. This type of flaw is easily detected using infrared thermography provided the optimum testing conditions (i.e. thermal input, observation time, etc.). However, partially conductive anomalies such as resin rich/poor areas block only a portion of the heat flux through the material. This behavior produces a reduction in thermal contrast making it difficult to detect the anomaly. Cracks perpendicular to the surface of the sample are also anomalies that difficult to detect.

Cracks perpendicular to the surface of the sample require the use of nontraditional methods in order to be detected. Some of these techniques include the use of innovative heating techniques such as electric current and moving line heating.

Post-processing of temperature data such as the calculation of the Laplacian of the temperature distribution also allows for the detection of cracks. Results show that it is possible to detect surface cracks and short and shallow cracks provided their depth is at least half the thickness of the sheet. However, cracks should have large thermal contrast resistance in order to be detected.

Size of Defect

Vavilov et al. (1993) points out the importance of size on detection. This dependence involves both diameter and thickness of the flaw.

The flaw has to be larger in diameter than its depth under the surface in order to be detectable (Rantala et al., 1991). Additionally, a decrease of flaw size produces a rounder image as well as a decrease in thermal contrast. Rantala also concluded that the estimated size of the delamination was smaller than its actual size.

For defect characterization, it is necessary to determine the relationship between the actual defect size and the estimated defect size observed in the thermograms. Numerical simulations such as finite element analysis tend to overestimate the experimental results. One of the reasons for the overestimation is the ideal testing assumptions applied to the numerical model. An additional source of size inaccuracies may arise from the selected signal measuring technique. Simple signal measuring techniques such as the selection of a temperature signal threshold above noise levels, lack precision. This technique is also highly dependent on noise and time (Vavilov, 2000). Another simple method is the full-width at half-maximum (FWHM) technique. This technique consists on determining the location at which the value of the signal is half the maximum signal. The FWHM method provides size predictions with estimation errors on the order of 15%. The FWHM tends to underestimate the true size of the defect. However, the method is simple enough to be used successfully in practice. Introducing methods that are more complex may solve the lack of accuracy. For example, a successful method is the computation of the Laplacian or second derivatives of the temperature profile. The technique involves the determination of the location at which the inflation point ($d^2T/dx^2 = 0$) of the temperature profile occurs. This technique is computationally intense. However, it provides the most accurate results.

Connolly et al. (1990) presented analytical and experimental techniques to examine carbon-carbon composite materials. Connolly et al. concluded that most infrared inspections tend to overestimate the actual flaw size to an order of 1.5 to 3 times. Thus, as further research, the authors stated that it is necessary to determine the relationship between the actual and the estimated defect size.

Depth of Defect

Infrared thermography testing is more successful on detecting superficial defects on thick specimens. The research demonstrated that testing of CFRP should be restricted to specimens containing flaws between 1.5 mm and 2 mm deep.

Detection of delaminations decreases as the depth of the defect increases (Fig. 2.3). Increasing the depth of the flaw also increases the time for maximum thermal signal and maximum thermal contrast. Additionally, partially conductive anomalies located deep in the material may be difficult to detect and quantify (Allport et al., 1988).

The depth of the flaw affects the rounding behavior of the surface temperature above the defect due to diffusivity. Deeper flaws develop more rounded edges than flaws located near the surface. For optimum detection, testing of CFRP should be restricted to specimens containing flaws between 1.5 mm and 2 mm deep (Vavilov, 1993).

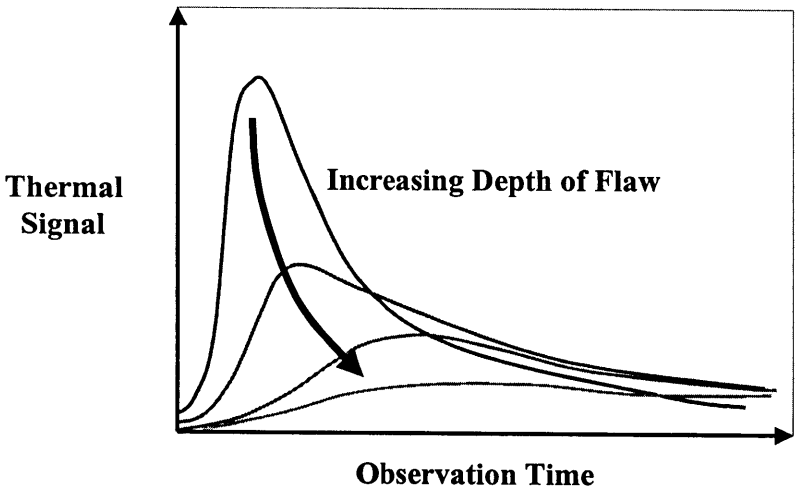

Fig.2.3 Effect of depth of flaw in the thermal signal
and the observation time

Vavilov (2000) also investigated the effect due of multiple and overlapped defects on temperature data. For the case of multiple flaws, he observed that average temperature were higher that for cases with a single flaw. As expected, the primary reason for the increase in temperature was the influence of nearby anomalies. The problem of overlapped defect was more complex, since near-the-surface flaws may eclipse deeper anomalies. This situation tended to produce an increase in the temperature signal, which could easily be misinterpreted as a single flaw having higher thermal resistance.

Thickness of Defect

The final factor for characterization of internal defects involves the thickness of the flaw or, its analogous, the thermal resistance of the flaw. The thermal resistance is directly proportional to the thickness of the flaw (Özişik, 1985)

$$R = \frac{\Delta z}{k} \tag{2.10}$$

where R is the thermal resistance, Δz is the thickness, and k is the thermal conductivity of the flaw.

Increasing the thermal resistance of the defect improves the thermal contrast at the surface of the specimen (Fig. 2.4).

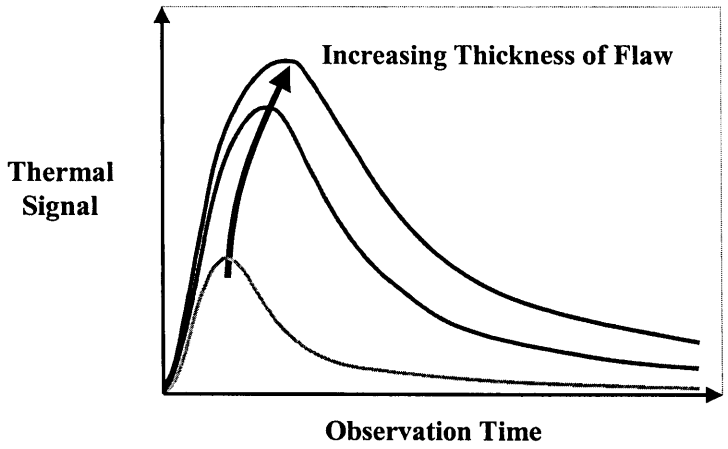

Fig. 2.4 Effect of thickness of flaw in the thermal signal and the observation time

2.3.2c Thermal Input

Active infrared thermography involves the application of an external thermal impulse to the structure under testing. As such, the type, amplitude, and duration of the thermal stimulus are relevant to the optimum detection of subsurface flaws.

Several types of thermal stimulus are available for thermographers. Uniform heating, moving line heating, and spot heating are among the traditional methods. Uniform heating usually involves heating the surface of the specimen with high power lamps. However, obtaining substantially uniform heating is difficult. Line heating typically involves moving a thermal line along the surface of the specimen. Both, moving gas flame and laser sources are commonly used for this procedure. Spot heating is the less productive mode of heating; thus, it is seldom used.

From the simulation perspective, moving line heating is the most complex method since it involves transverse diffusion effects on the material. Nonetheless, the effect of transverse

diffusion on the line heating method allows for the detection of cracks perpendicular to the surface, which are undetectable with traditional static heat sources.

The Joule-effect-heating technique is among the nontraditional heating methods that may be used to detect perpendicular-to-the-surface defects. The procedure consists on clamping the specimen with electrodes and applying an electric current. Moreover, the electric current flows in the direction parallel to the tested surface. Within the flawed specimen, the electrical flow creates a distinctive distribution of electric current density. By the Joule effect, this current density is converted into heat, thus, producing transient thermal effects. Currents of 2000 A to 3000 A are sufficient to detect open-to-the-surface cracks. Nevertheless, this technique is only applicable to materials able to conduct electricity.

Most researchers agree that thermal pulses with high intensity and short duration produce the highest temperature gradients and thus, better flaw detection (Lulay et al., 1994). Generally, pulse duration must be as short as possible in order to attain the highest thermal contrast. For example, Vavilov et al. (1993) concluded that carbon composites benefited of heat intervals of less than 0.5 seconds. Also, defects close to the heated surface required shorter heating pulses. However, a potential practical problem is that short pulses may not be capable to deliver enough heat to raise the temperature of the surface sufficiently (Connolly, 1991). The greater the quantity of heat supplied, the greater the temperature signal. Thus, an optimum balance between the magnitude of the pulse and its duration must be found for each specific engineering application (Starnes et al., 2002).

Vavilov (2000) studied the effect of uneven heating on thermography results. Uneven heating introduced low frequency variations in the recorded temperature signal. Vavilov suggested normalizing the temperature data in order to eliminate the effects of uneven heating.

2.3.2d Observation Time

The optimum observation time is defined as the moment of maximum thermal signal or contrast. At this instant, the image of the buried flaw emerges well defined and sharp-edged. As the time increases the image becomes increasingly round due to the diffusion effect. Additionally, increasing the depth of the flaw lengthens the time to maximum contrast.

The optimum observation time depends highly on the material properties of the test object. As previously stated, thermal diffusivity has a major effect on observation time. Hence, due to their fast thermal response, high diffusivity materials are difficult to inspect using infrared thermography. Most FRP composites used in civil infrastructure have low to medium diffusivity values; thus, they are good candidates for this testing technique.

2.3.2e Testing Mode

There are two methods of observation for infrared thermography: reflection (one-sided) and transmission (two-sided). Figure 2.5 illustrates the configurations for one-sided and two-sided testing. Each method has its advantages and disadvantages. For example, observation by reflection provides greater resolution but the thickness of the tested layer must be small. Using

this technique, testing of CFRP must be restricted to thin layers containing defects at a maximum depth of 2 mm (Vavilov, 1993). Thick test objects should rely on observation by transmission. On the other hand, observation through transmission does not provide depth information and has weak resolution. Two-sided IR thermography is inadequate for quantitative nondestructive evaluation.

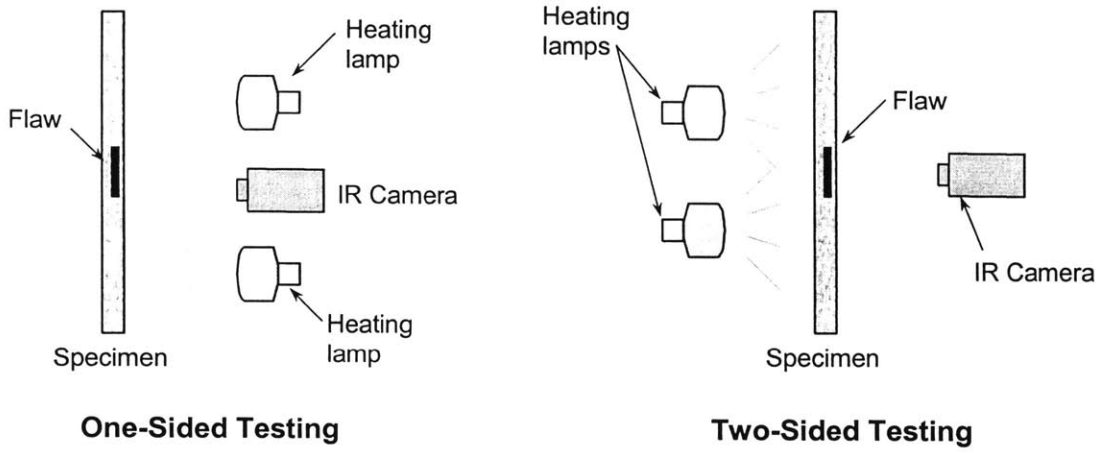

Fig. 2.5 Schematic of one-sided and two-sided testing modes

The thermographic configuration is also relevant to the observation time. In general, reflection thermography is more time dependent than transmission thermography (Vavilov et al., 1993). Thus, in order to get time-stable responses, reflection or two-sided configurations should be used whenever possible.

2.3.2f Additional Considerations

Additional considerations involve ambient conditions during *in situ* inspection. The accuracy of thermography measurements depends highly of environmental conditions such as solar radiation, cloud cover, ambient temperature, wind speed, and surface moisture. For example, over long distances (meters) absorption of IR signal by the atmosphere must be taken into account.

Most of the errors in the simulation solutions arise from the simplification of the testing conditions. To better simulate *in situ* testing conditions, most numerical algorithms allow for the incorporation of convection heat losses and, with some software packages, ambient noise into the model. The incorporation of ambient conditions in the numerical model notably increases the amount of calculation time and computer memory required. Hence, researchers must assess and balance the benefits of accurate modeling with the amount of computation time and data storage available.

2.3.3 Simulation Outputs Versus Experimental Data

In their collaborative research, Cowell and Burleigh (1990) assessed the potential detection of defects on carbon composites. The researchers used computer simulations and experimental trials to determine the types, sizes, and depth of detectable defects. Two-sided active infrared thermography using uniform heating over the surface of the specimen was selected. Comparison of numerical and experimental data showed consistent disagreement among the results.

Cowell clarified that the disagreement between experimental and theoretical result were due to assumptions made on the modeling process. For example, uniform heating was assumed over the entire top surface of the laminate. Uniform heating is hardly achieved in real testing. As an additional source of error, the material properties of the composite were not measured for comparison with those of the numerical simulation. Hard to predict convective losses could have caused supplementary inaccuracies.

Other researchers such as Hamzah et al. (1996) have successfully compared results from experimental and theoretical studies. Hamzah et al., for example, investigated the potential size estimation of back-drilled holes in bakelite plates. The agreement between experimental and numerical results confirmed the potential of infrared thermography as a quantitative NDT method.

2.4 Summary

Infrared thermography is still an immature nondestructive inspection method. Both, technology and techniques are rapidly evolving without complete understanding of the parameters affecting inspection procedures and results.

Investigations of all the parameters affecting thermal transfer through the structure and infrared testing techniques are needed to develop the bases for quantitative infrared thermography. Such investigations require both, experimental and theoretical approaches.

This literature review provided a general summary of recent investigations in the field of quantitative infrared thermography. Most investigations focused on the evaluation of the various parameters involved in heat transfer phenomena. The parametric studies were performed on different engineering applications, which illustrate the versatility of infrared thermography. All the reviewed investigations, however, have focused in the aerospace and manufacturing industries. The lack of studies involving civil engineering applications and materials indicates that further research is required to establish the effect of relevant parameters on the thermal response and standards for successful quantitative testing of FRP composites bonded to concrete structures using infrared thermography.

Chapter 3

Dimensional Analysis

3.1 Introduction

The third chapter focuses on preliminary analytical studies of the heat diffusion problem involved in thermography testing. The objective of the analytical study carried out in this chapter was the determination of relevant parameters that describe the transient heat transfer phenomenon. This was done through dimension analysis of a simplified model.

3.2 Dimensional Analysis

Dimensional analysis is used to isolate the relevant parameters that need to be examined for a specific physical phenomenon. The results from the dimensional analysis will help identify the variables that need to be investigated in subsequent parametric studies.

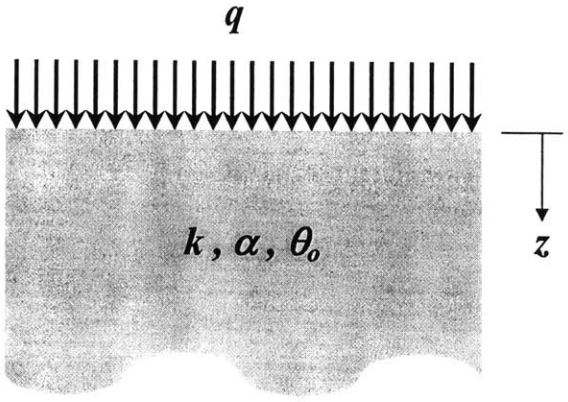

Fig. 3.1 Semi-infinite half-space studied on dimensional analysis

For the purpose of simplicity a homogeneous semi-infinite half-space was investigated (Fig. 3.1). The top surface of the model was heated with a uniform heat flux q. The semi-infinite half-space had a thermal conductivity k, thermal diffusivity α, and initial temperature θ_o. One-dimensional transient heat transfer in the z-direction was assumed.

The governing equation that defines the heat transfer problem is the following partial differential equation, which represents a one-dimensional, linear, and purely diffusive phenomenon:

$$\frac{\partial^2 \theta}{\partial z^2} = \frac{1}{\alpha}\frac{\partial \theta}{\partial t} \tag{3.1}$$

where θ is the temperature, z is the depth, t is the time, and α is the thermal diffusivity of the material. Initially, the test object is at a temperature θ_o, thus the initial condition of the problem is

$$at\ t = 0; \quad \theta = \theta_o;\ \theta - \theta_o = 0 \tag{3.2}$$

The top surface is heated with a uniform heat flux, thus the boundary conditions are the following:

$$at\ z = 0; \quad -k\frac{\partial \theta}{\partial z} = q \tag{3.3}$$

$$at\ z = \infty; \quad \theta = \theta_o; \quad \theta - \theta_o = 0 \tag{3.4}$$

Observation of the governing equation and its initial and boundary conditions indicates that the dependent variable is the change in temperature $\theta(z,t)$-θ_o. As previously mentioned, one of the fundamental principles of infrared thermography inspection is the change in surface temperature. The change in temperature is a function of the spatial and temporal parameters, the thermal diffusivity, the thermal conductivity, and the prescribed heat flux:

$$\theta - \theta_o = f(z,t,\alpha,k,q) \tag{3.5}$$

thus, there are 5 parameters that influence the temperature behavior (N=5). The five parameters on the right hand side of Eq. 3.5 are the independents arguments. The change in surface temperature θ-θ_o is the dependent variable. Thus, equation 3.5 describes the relationship between N+1 physical parameters that characterizes the heat transfer problem.

Next, the system of units is selected. The Length-Mass-Time-Temperature (L-M-T-Θ) system is used for this particular analysis. Each independent parameter could be expressed as a product of the units involved in its definition, for example

$$[A] = L^a M^b T^c \Theta^d \tag{3.6}$$

where the exponents are dimensionless numbers that follow from the quantity definition. Following the L-M-T-Θ system, the five independent quantities expressed in Eq. 3.5 could be expressed as follows:

$$[z] = L^1 M^0 T^0 \Theta^0 \tag{3.7}$$

$$[t] = L^0 M^0 T^1 \Theta^0 \tag{3.8}$$

$$[\alpha] = L^2 M^0 T^{-1} \Theta^0 \tag{3.9}$$

$$[k] = L^1 M^1 T^{-3} \Theta^{-1} \tag{3.10}$$

$$[q] = L^0 M^1 T^{-3} \Theta^0 \tag{3.11}$$

Observation of the dimensions of the independent variables indicate that four of the variables, z, t, q, and k, have independent dimensions, while α have dependent dimensions. The thermal diffusivity α has dependent dimensions because it could be expressed as a function of z and t

$$[\alpha] = [z]^2 [t]^{-1} \tag{3.12}$$

Thus, there is a subset of k=4 dimensionally independent dimensions physical quantities. The following step involves defining N-k+1 invariants. Observation of the independent and dependent physical quantities indicate that there should be N-k+1=2 dimensionless numbers.

For the purpose of constructing the two required dimensionless variables, the following linear transformations of the 6 physical quantities were performed:

$$z = Z z^* \tag{3.13}$$

$$t = T t^* \tag{3.14}$$

$$\alpha = A \alpha^* \tag{3.15}$$

$$k = K k^* \tag{3.16}$$

$$q = Q q^* \tag{3.17}$$

$$\theta - \theta_o = \Theta \theta^* \tag{3.18}$$

where z^*, t^*, α^*, k^*, q^*, and θ^* are dimensionless counterparts of the physical quantities z, t, α, k, q, and θ-θ_o of dimensions Z, T, A, K, and Θ. Substituting the linear transformations into the diffusion equation, Eq. 3.1 transforms into:

$$\left(\frac{Z^2}{AT}\right)\frac{\partial\theta^*}{\partial t^*} = \alpha^* \frac{\partial^2\theta^*}{\partial z^{*2}} \tag{3.19}$$

Additionally, the initial and boundary conditions, Eqns. 3.2, 3.3, and 3.4, transform into the following:

$$at\ t = 0; \quad \theta - \theta_o = \Theta\theta^* = 0 \tag{3.20}$$

$$at\ z = 0; \quad -\left(\frac{K\Theta}{ZQ}\right)k^* \frac{\partial\theta^*}{\partial z^*} = q^* \tag{3.21}$$

$$at\ z = \infty; \quad \theta - \theta_o = \Theta\theta^* = 0 \tag{3.22}$$

In order for the transformed set to satisfy the same equation as those in the original diffusion problem, the following should be true:

$$\left(\frac{Z^2}{AT}\right) = 1 \tag{3.23}$$

and

$$\left(\frac{K\Theta}{ZQ}\right) = 1 \tag{3.24}$$

Equivalently, using the linear transformation, two dimensionless parameters, π and π_1 are obtained.

$$\pi = \frac{k(\theta - \theta_o)}{zq} = \frac{k^*\theta^*}{z^*q^*} \tag{3.25}$$

$$\pi_1 = \frac{z}{\sqrt{\alpha t}} = \frac{z^*}{\sqrt{\alpha^* t^*}} \tag{3.26}$$

The dimensionless parameters π indicate that the temperature θ can be solved in terms of the distance, the input thermal flux, and the thermal conductivity of the solid. The dimensionless parameter π_1 relates the distance and the diffusion length $\sqrt{\alpha t}$. The diffusion length is the distance over which the effects of a sudden, localized change in temperature can be felt after a time t. For cases in which $z >> \sqrt{\alpha t}$ the thermal effect is imperceptible.

3.3 Summary

The dimensional analysis demonstrates that in the case of a semi-infinite half-space solid the physical quantities that influence the thermal evolution are z, t, k, α, and q. In the case of a solid containing a subsurface flaw or inclusion, additional physical quantities, such as the thermal resistance of the flaw, should be taken into consideration. The results from the dimensional analysis will help identify the variables needed to investigate in the parametric study of Chapter 4.

Chapter 4

Parametric Studies

4.1 Introduction

The complexity of transient heat transfer phenomena remains a key obstacle to the effective use of quantitative infrared thermography for flaw detection. The greatest contributor to the complexity is the dependency of thermal evolutions on space as well as time. Furthermore, the time dependency is nonlinear. From a theoretical perspective, solutions to heat transfer problems could be attained by direct computation of the thermal diffusion equation or by using numerical algorithms. Most heat transfer problems, however, can only be solved using numerical analysis. In addition to being the only analytical method to provide results, numerical modeling provides the most effective method for analysis of heat transfer phenomena.

The flexibility of numerical analysis allows the engineer to simulate different testing scenarios such as, passive vs. active thermography, steady state vs. transient heat transfer, or linear vs. nonlinear modeling (due to material properties). Because of its diverse simulation capability and high performance, computer modeling is a cost efficient alternative to experimental testing. Furthermore, in some engineering fields, the impressive performance of properly verified numerical modeling has caused the replacement of otherwise expensive and time consuming experimental testing with computer simulation. Computer simulation tends to reduce the overall cost of engineering research and design projects. In the field of nondestructive testing, numerical modeling is used to predict experimental data, conduct parametric studies, evaluate potential testing procedures, and aid further developments in the field.

The second component of the research program involved numerical modeling of infrared thermography testing of FRP layers bonded to concrete substrates. The study focused on the evaluation of the various parameters that influence thermal evolution (the spatial and temporal variations of surface temperature). Understanding how these diverse parameters affect heat transfer is the key to successful implementation of testing procedures, inversion algorithms, and ultimately, inspection standards. Observation and evaluation of surface temperature variations as a function of time were expected to indicate the size, shape, orientation, and depth of internal anomalies.

4.2 Single-Factor Parametric Study

The finite element method (FEM) was the chosen analytical tool for this phase of the project. The first parametric study involved evaluation of single parameters that affect the thermal response.

The objectives for the single-factor parametric study were the following:

- optimize heating time and intensity for maximum image contrast,
- determine the effects of material properties on the measurement of thermal signals,
- investigate the effect of flaw depth,
- examine the effect of type of flaw (delamination versus debond),
- study the effect of defect thickness on flaw detection and characterization; and
- determine minimum detectable flaw size.

All the analytical simulations were performed using ANSYS 5.6.

4.3 Parametric Study No. 1: Effect of Thermal Input

The first parametric study involved the evaluation of the effect of the amplitude (heat flux) and duration of the input thermal pulse. Heat pulse was modeled as a rectangle or "hat" function of amplitude q and duration τ, as illustrated on Fig. 4.1.

The parametric study was designed to answer several questions:

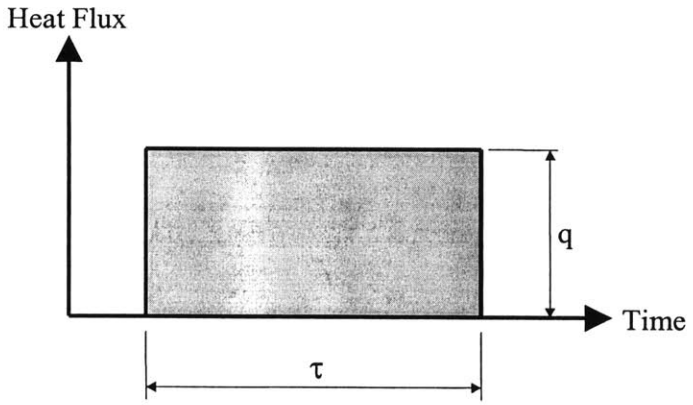

Fig. 4.1 Square thermal impulse

- understand diffusion behavior due to different pulse durations and heat flux inputs,
- determine an appropriate heating period or pulse duration for typical FRP composites,
- determine the optimal combination of input heat flux and pulse duration for FRP composites applied to concrete substrates.

The investigation was focused on the estimation of optimal thermal energy for experimental

configurations relevant to civil engineering applications. The study involved eighteen different simulations with trial pulse durations ranging from 0.05 s to 3 s, and applied heat flux ranging from 5,000 W/m^2 to 100,000 W/m^2.

For the purpose of comparison, two-dimensional (2-D) and three-dimensional (3-D) models were used. Models that included free convection cooling were also compared with models that did not include cooling of the surface of the test object. These comparisons provided insight on the best options to proceed with the parametric studies.

4.3.1 2-D Models

The first set of simulations involved two-dimensional models. The simulation object consisted of a 100 mm long by 20 mm thick concrete slab covered with two layers of carbon FRP. Each layer of CFRP was 0.5 mm thick. The bonded FRP contained a flaw delamination at the interface with the concrete substrate. The delamination had a length of 25 mm and a thickness of 0.2 mm, which correspond to a thermal contact resistance of 8.33×10^{-3} m^2/W.

The thermal contact resistance can be estimated using equation 4.1 (Özişik, 1985)

$$R = \frac{\Delta y}{k_y} \tag{4.1}$$

where, R is the contact resistance, Δy is the thickness of the flaw, and k_y is the thermal conductivity of air in the y-direction. As a note, in this model the x-direction corresponds to the length of the specimen and the y-coordinate corresponds to the thickness. Since plane two-dimensional modeling was used, the slab is of infinite size in the z-direction.

The interface flaw was located at the center of the model. The model to be analyzed was simplified by using plane symmetry. Thus, only a half section was modeled (Fig. 4.2). The model was constructed using rectangular blocks with the following dimensions in meters (Fig. 4.3).

The material properties of the model were those of concrete for the substrate, air for the defect, and CFRP for the bonded composite. The CFRP layer in direct contact with the concrete had the fibers running in the x-direction, while the outer CFRP layer had the fibers running in the z-direction. The material properties are presented in Table 4.1. The material properties were gathered from Maldague (1993) and MatWeb (a material information resource in the World Wide Web).

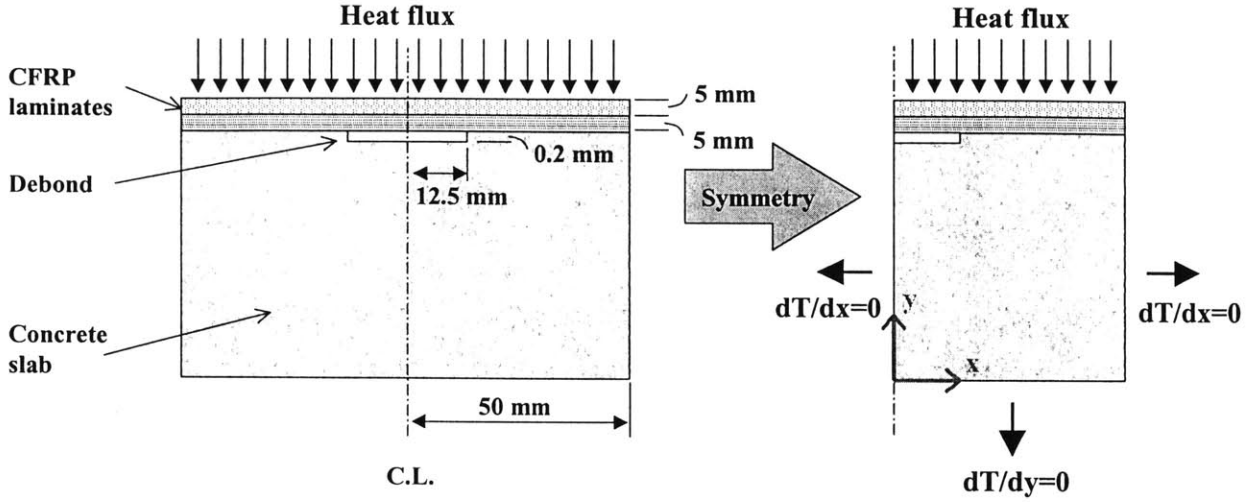

Fig. 4.2 Two-dimensional simulation test object

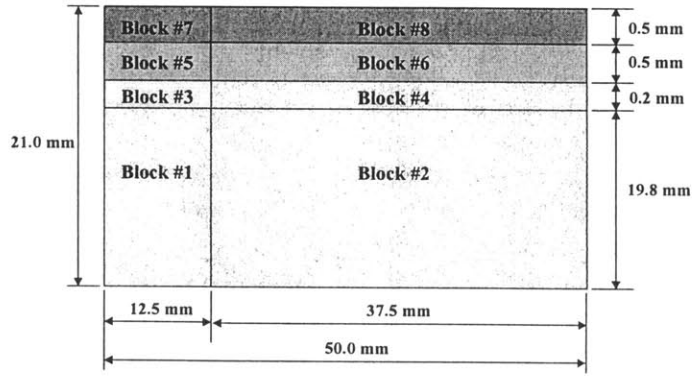

Block #1	x_1 =	0.0000	x_2 =	0.0125
	y_1 =	0.0000	y_2 =	0.0198
Block #2	x_1 =	0.0125	x_2 =	0.0500
	y_1 =	0.0000	y_2 =	0.0198
Block #3	x_1 =	0.0000	x_2 =	0.0125
	y_1 =	0.0198	y_2 =	0.0200
Block #4	x_1 =	0.0125	x_2 =	0.0500
	y_1 =	0.0198	y_2 =	0.0200
Block #5	x_1 =	0.0000	x_2 =	0.0125
	y_1 =	0.0200	y_2 =	0.0205
Block #6	x_1 =	0.0125	x_2 =	0.0500
	y_1 =	0.0200	y_2 =	0.0205
Block #7	x_1 =	0.0000	x_2 =	0.0125
	y_1 =	0.0205	y_2 =	0.0210
Block #8	x_1 =	0.0125	x_2 =	0.0500
	y_1 =	0.0205	y_2 =	0.0210

Fig. 4.3 Two-dimensional geometry of blocks used to generate finite-element mesh

Table 4.1 Material properties

	Material 1 Concrete	Material 2 CFRP (outer layer)	Material 3 CFRP (inner layer)	Material 4
ρ (kg/m^3) =	2400	1600	1600	1.2
c (J/kg·K) =	800	1200	1200	700
k_x (W/m·K) =	1.5	7	0.8	0.024
k_y (W/m·K) =	1.5	0.8	0.8	0.024
k_z (W/m·K) =	1.5	0.8	7	0.024

The model was meshed using 2-D thermal solid elements. Four-noded quadrilateral elements were used. In particular, PLANE55 elements were selected from ANSYS library. The test object was meshed using "mapped meshing" instead of "free meshing". Free meshing is simpler and faster, but, the mesh may contain some triangular elements in addition to quadrilaterals. In addition, element size is not as consistent as in mapped meshing. Mapped meshing allows the user to directly control the element size and type in the model. For this particular parametric study, the global element length in the x-direction was set to 1 mm. Mesh refinement, however, was applied to the thin composite layers and at the flaw location. The thickness of each composite ply was subdivided into four elements, while the thickness of the flaw and adjacent concrete was subdivided into two elements (Fig. 4.4). The rest of the concrete specimen was meshed using a graded mesh with finer mesh (in the y-direction) at the top and coarser mesh at the bottom of the specimen. Specifically, the average element size for the concrete was 0.00275 m with a "spacing ratio" of 10. The spacing ratio is the ratio of the dimension of the largest element to the dimension of the smallest element.

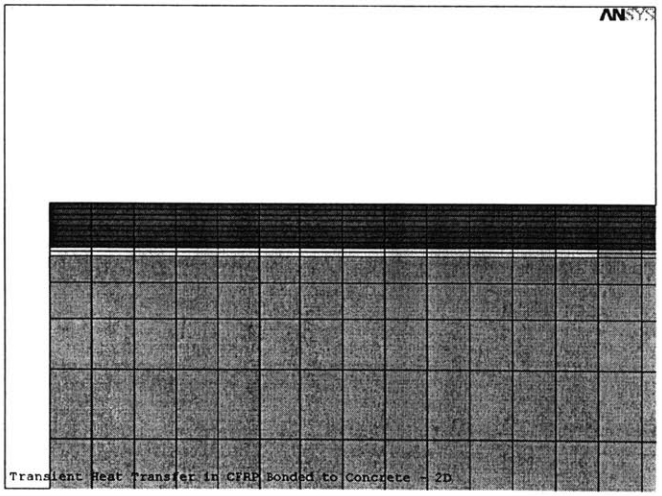

Fig. 4.4 Close up of two-dimensional meshing at the location of the flaw

4.3.2 3-D Model

The second set of simulations involved three-dimensional models. The simulation object consisted of a 100 mm long by 100 mm wide by 20 mm high concrete slab. The slab was covered with two layers of carbon FRP. Each layer of CFRP was 0.5 mm thick. The specimen contained a flaw (debond) at the interface of the CFRP and the concrete substrate. The delamination had an area of 25 mm $\times$ 25 mm and a thickness of 0.2 mm, which corresponds to a thermal contact resistance of 8.33×10^{-3} m^2/W.

The delamination was located at the center of the test model. The modeling of the test object was simplified by using planes of symmetry; so that only one quarter of the model was simulated. The test object was created using 16 individual blocks. The individual blocks were "glued" together using boolean operations. Although this procedure may seem time-consuming and redundant, it actually facilitated the mapped meshing procedure.

Similarly to the 2-D model, the material properties of the 3-D model were those of concrete for the substrate, air for the defect, and CFRP for the bonded composite. The CFRP layer in contact with the concrete had the fibers running in the x-direction, while the external CFRP had the fibers running in the z-direction.

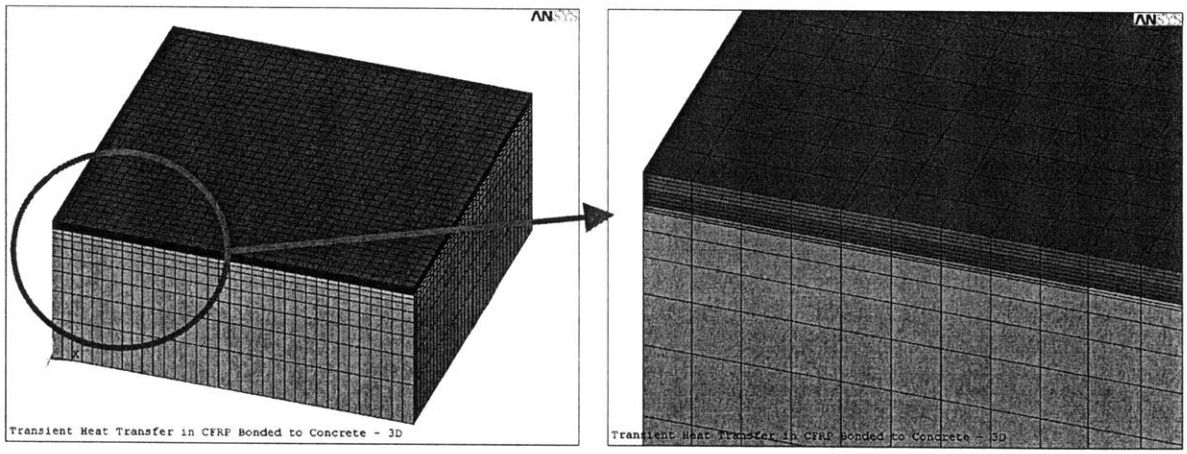

Fig. 4.5 Three-dimensional meshing of simulation object

The model was meshed using 3-D thermal solid elements. In particular, eight-noded quadrilateral SOLID70 elements were used. The general element size was set to 1.5 mm; however, mesh refinement was used for the thin composite layers and for the flaw. The thickness of each composite ply was subdivided into four elements, and the thickness of the flaw and adjacent concrete was subdivided into two elements (Fig. 4.5). The bulk of the concrete slab was meshed using a graded mesh with finer grid at the top and a coarser grid at the bottom of the specimen. Specifically, the average element size for the concrete was 0.00275 m with a spacing ratio of 10 in the y-direction.

4.3.3 Thermal Loading and Boundary Conditions

The analysis was defined as a transient heat transfer problem. A square pulse of intensity q and duration τ (Fig. 4.6) was applied to the top surface of the test object (Fig. 4.7). Adiabatic conditions ($dT/dx = 0$, $dT/dy = 0$, and $dT/dz = 0$) were assumed for the additional surfaces. Adiabatic conditions on these surfaces implied that no heat flux was transferred on those planes. This assumption was realistic with actual physical conditions of such an experiment. The initial temperature for all the cases was set to 23 °C as the standard ambient temperature. Eighteen different analyses were performed with pulse durations varying from 0.05 s to 3 s, and heat flux varying from 5,000 W/m^2 to 100,000 W/m^2.

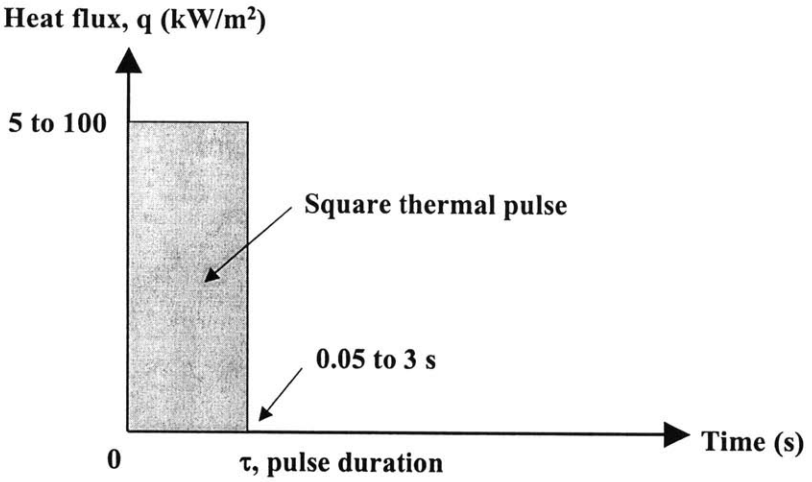

Fig. 4.6 Square thermal pulse

For simplification, uniform heating and no cooling losses were assumed for all of the eighteen analyses. One trial simulation, however, was performed to determine the effect of free convection cooling on the test object. Free convection cooling occurs naturally on any surface, which is in contact with a fluid and is subject to a change in temperature. The trial simulation used the two-dimensional model with a thermal input of 100,000 W/m^2 for 0.5 seconds. To provide for the free convection effect, surface elements (SURF151) with a heat transfer coefficient of 2.0 W/m^2·°C and temperature of 23 °C were added to the two-dimensional model. In ANSYS, SURF151 elements are thermal surface effect elements, which are used to apply multiple surface loads to the surfaces of solid elements. For this particular model, the surface elements chosen (SURF151) consisted of a 2-noded (no thickness) elements. The heat transfer coefficient was applied to the surface elements and the ambient temperature was applied to an added extra node.

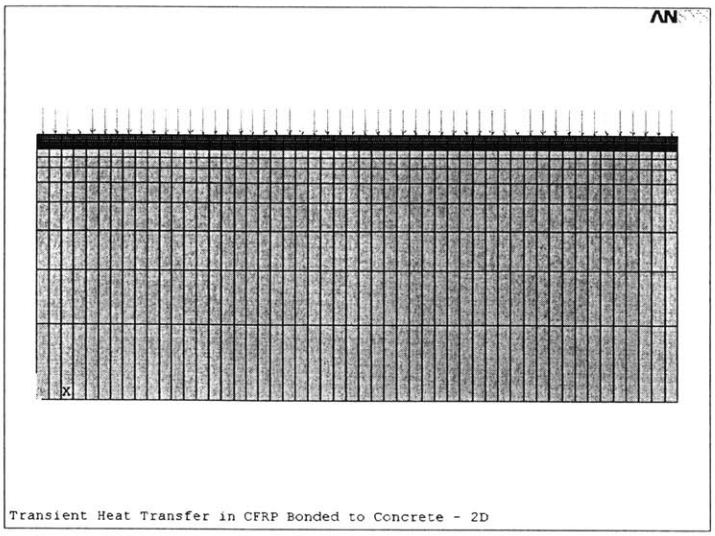

Fig. 4.7 Application of thermal load

The heat transfer coefficient is defined as the following

$$h = \frac{k\,Nu}{L} \tag{4.2}$$

where, Nu is the Nusselt number, k is the thermal conductivity of the fluid and L is the length of the solid surface. The Nusselt number is estimated using the expression for a horizontal wall with uniform heat flux applied to the top surface (Özişik, 1985)

$$Nu = 0.13(Gr\,Pr)^{1/3} \quad \text{for} \quad Gr\,Pr \leq 2x10^{8} \tag{4.3}$$

where, Nu was the Nusselt number, Gr was the Grashof number, and Pr was the Prandtl number. The Nusselt number is a dimensionless value that represents the ratio of heat transfer by convection to that by conduction across a characteristic length

$$Nu = \frac{hL}{k} \tag{4.4}$$

where, h is the heat transfer coefficient, L is the length of the solid surface, and k is the thermal conductivity of the fluid. Similarly, the Grashof number represents the ratio of the buoyancy force to the viscous force acting on a fluid. Its value is defined as

$$Gr = \frac{g\beta\left(T_w - T_\infty\right)}{\nu^2} \tag{4.5}$$

where, g is the acceleration due of gravity, $\beta = 1/T_f$, $T_f = (T_\infty+T_w)/2$, T_∞ is the ambient temperature, T_w is the temperature reached by the wall, and ν is the kinematic viscosity of air. The Prandtl number is also a dimensionless parameter that represents the ratio of molecular

diffusivity of momentum to molecular diffusivity due to heat. Values for Pr are usually tabulated for materials at specific temperatures (Özişik, 1985).

For this trial problem, T_∞ and T_w were specified as 296 K and 298 K, respectively. The Grashof number was computed as 9.67×10^5. The Prandtl number was 0.712. The average heat transfer coefficient was computed by combining equations 4.2 and 4.3, as expressed in equation 4.6

$$h = 0.13 \frac{k}{L} (Gr\ Pr)^{1/3} \tag{4.6}$$

The results of the analysis were examined in terms of thermal signal and thermal contrast. Thermal signal is defined as

$$\Delta T = T_{defect} - T_{background} \tag{4.7}$$

where, T_{defect} is the surface temperature above the internal flaw and $T_{background}$ is the surface temperature in the background where no internal flaw is present. The thermal contrast C is defined as

$$C = \frac{\Delta T}{T_{background} - T_o} \tag{4.8}$$

where, ΔT is the thermal signal, $T_{background}$ is the surface temperature in the background where no internal flaw is present, and T_o is the initial or ambient temperature (23 °C). Both the thermal signal and the thermal contrast are widely used by researchers for flaw detection. The use of thermal signal versus contrast depends on the investigator's preference. Signal is the most widely used measuring technique to detect buried flaws. Some authors, however, prefer using the thermal contrast because this normalized value is independent of the amount of heat applied to the specimen.

The results indicated that free convection cooling provided a temperature difference of only 0.12 °C in the thermal signal, and 0.03 °C in the thermal contrast, with respect to the results of the same model without cooling. The small difference in results did not justify the high increment in computation time for the more complex model. Therefore, free convection cooling was not considered in these parametric studies.

The input thermal loading for the different analyses is indicated in Table 4.2. The information regarding the simulations is tabulated in groups to better compare the results. Problem 1 through 4 had the same input heat flux with varying pulse duration. On the other hand, problems 4 through 18 were grouped by a specific pulse duration with varying input heat flux. Problems 1 through 4 included 2-D and 3-D analyses, while the rest of the models involved only 2-D analyses.

Table 4.2 Description of thermal input for different analyses

Problem no.	Pulse duration, τ (s)	Heat flux, q (W/m^2)
1	1	100,000
2	0.5	100,000
3	0.1	100,000
4	0.05	100,000
4	0.1	100,000
5	0.1	50,000
6	0.1	10,000
1	1	100,000
9	1	50,000
8	1	25,000
7	1	10,000
10	1	5,000
11	2	25,000
12	2	20,000
13	2	10,000
14	2	5,000
18	3	20,000
15	3	15,000
16	3	10,000
17	3	5,000

The simulations involved transient analyses. ANSYS uses a time integration procedure to estimate the solution at discrete points in time (integration time steps, ITS). Selection of the appropriate time step is important to provide both accurate and stable results. For example, if the time step is too small, unstable oscillations may occur and result in thermal behavior that is physically incorrect. Large time steps, however, may miss to capture the temperature gradients adequately. To avoid problems with the integration time stepping, ANSYS suggests to input a conservative initial time step and allow automatic time stepping to take place. In its automatic time stepping routine, ANSYS increases the time step as needed while checking for stability and convergence of the results at each time step.

For comparisons, all simulations used the same time step pattern (automatic stepping with same initial, maximum, and minimum time steps). The initial time step was estimated using the initial time step criterion (ANSYS Heat Transfer Manual, 2000), which is a function of the element size in the direction of the flow and the thermal diffusivity of the material

$$ITS = \frac{\Delta y^2}{4\alpha} \tag{4.9}$$

where, *ITS* is the recommended initial time step, Δy is the element size in the y-direction, and α is the diffusivity of the material.

The Biot and Fourier numbers provide a rough estimate of the initial time step. The Biot number, *Bi*, expresses the ratio of convective and conductive thermal resistance (ANSYS Heat Transfer Manual, 2000)

$$Bi = \frac{h\Delta y}{k} \tag{4.10}$$

where, h is the heat transfer coefficient for convection losses, Δy is the mean element length in the direction of heat flow, and k is the thermal conductivity. Likewise, the Fourier number, *Fo*, or dimensionless time, quantifies the relative rates of heat conduction and heat storage in the material (ANSYS Heat Transfer Manual, 2000)

$$Fo = \frac{k\Delta t}{\rho\, c\,(\Delta y)^2} \tag{4.11}$$

where, k is the thermal conductivity, Δt is the time step, ρ is the density of the material, c is the specific heat of the material, and Δy is the mean element length in the direction of the heat flow.

As previously mentioned, convection cooling was not considered. Thus, the Biot number was zero. For the case $Bi<1$, a reasonable time step ,Δt, was estimated using the expression (ANSYS Heat Transfer Manual, 2000)

$$\Delta t = \beta \frac{\rho\, c(\Delta y)^2}{k} \tag{4.12}$$

where, β is a scaling factor with values ranging from $0.1 < \beta < 0.5$. Time steps are more or less conservative depending on the value of β that is chosen.

Based on the properties of the composite layers and $\beta = 0.25$, the estimated initial time step was 0.009 seconds. ANSYS requires that the minimum time step must be smaller than the initial time step. The selected minimum time step was 0.008 seconds. The maximum time step selected for the simulations was greater that the time step suggested by equation 4.12. The selected maximum time step for the simulations was 0.5 seconds. Automatic time stepping was carried out during the analysis. The simulation data were recorded at every time step.

4.3.4 Results

The simulations illustrated the dynamic thermal behavior of the test object due to the thermal impulse. Additionally, the 3-D model revealed the two-dimensional thermogram of the surface temperature. Surface temperature data was gathered at each node over the entire period of simulation.

Figure 4.8 shows the temperature distribution of the three-dimensional model for problem number 1. The temperature values are in °C.

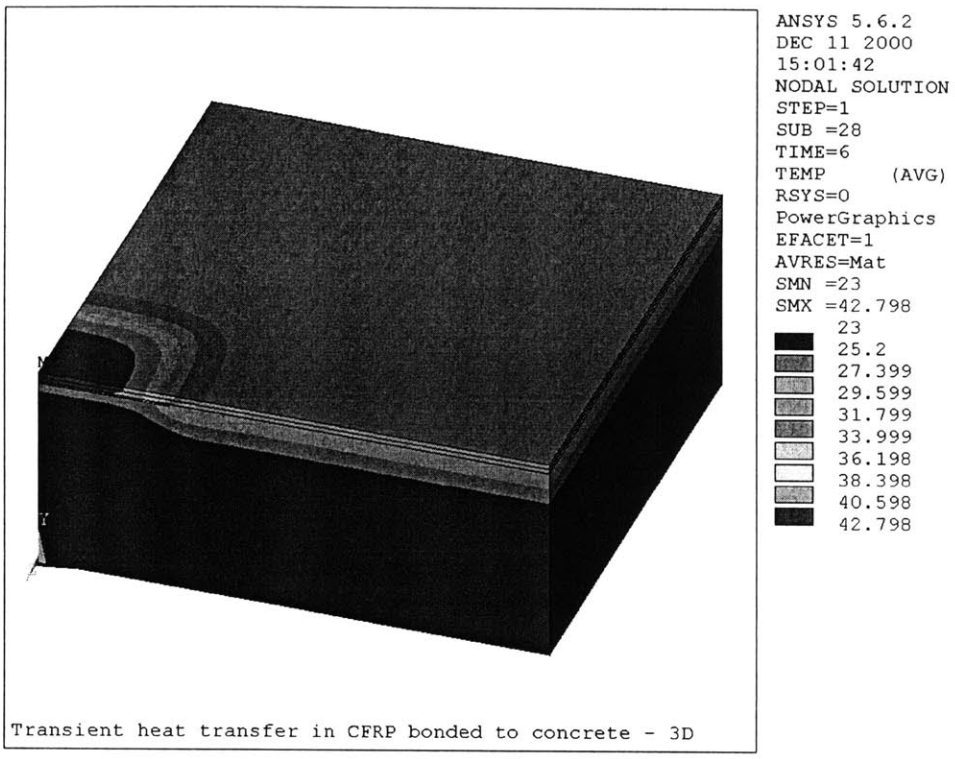

Fig. 4.8 Temperature distribution at 6 seconds (q = 100,000 W/m^2, τ = 0.5 s)

As mentioned, there are two basic measurements used to detect flawed and sound areas: thermal signal and thermal contrast. Most researchers in the field of quantitative thermography used either of these two parameters. Both the thermal signal and the thermal contrast were calculated for the entire duration of the test.

Problems 1 through 4 were analyzed using both two-dimensional and three-dimensional models. The results demonstrated that the value of the maximum signal differed slightly for the two models. Thermal contrast, however, differed to a greater degree. For example, focusing on problem number 1, the maximum thermal signal for the 2-D model was 24.4 °C and was reached at 5.24 s after the beginning of the simulation. Maximum thermal contrast occurred later than the maximum thermal signal. The maximum thermal contrast was observed 11 s after the start of the simulation, and had a value of 1.79. The three-dimensional model provided similar temperature values. For instance, the maximum thermal signal of 23.8 °C was reached at 4.64 s after the beginning of the simulation. The maximum contrast occurred at 11.59 s and had a value of 1.67. Plots illustrating the thermal signal and thermal contrast behaviors are presented in Fig. 4.9 and 4.10.

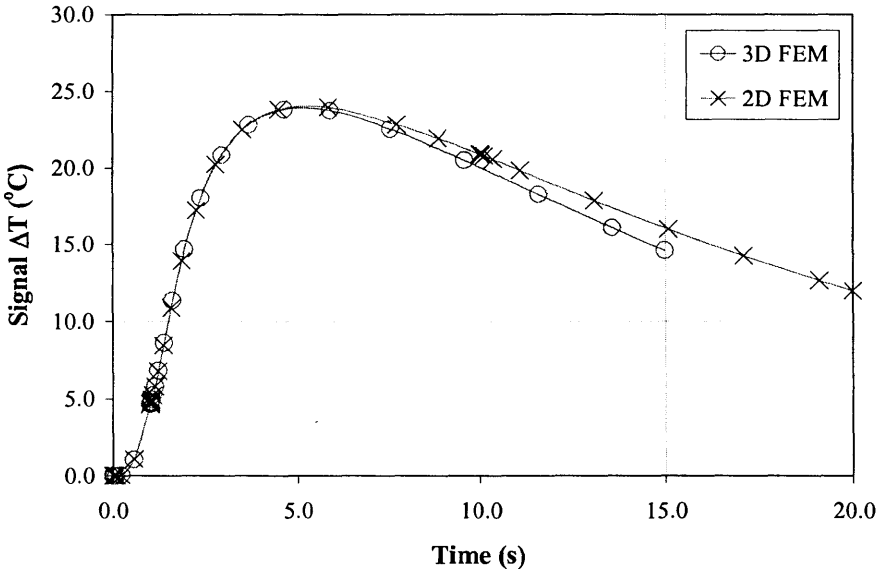

Fig. 4.9 Thermal signal for problem 1 (q = 100,000 W/m^2, τ = 1 s)

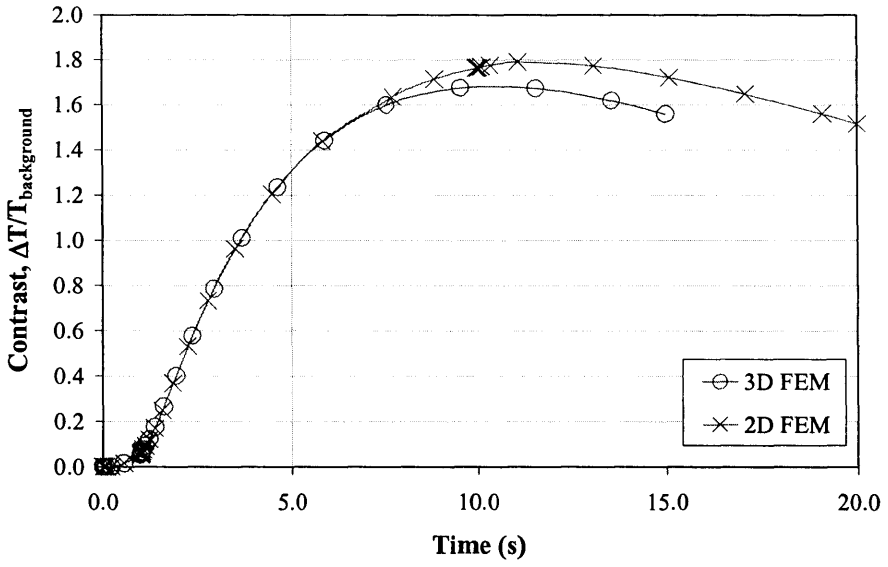

Fig. 4.10 Thermal contrast for problem 1 (q = 100,000 W/m^2, τ = 1 s)

The results indicated that the thermal signal for the three-dimensional case decayed slightly faster than for the two-dimensional case. This difference, however, occurred mostly after the maximum signal had been reached. Because three-dimensional models are more computationally intensive than two-dimensional models, the small difference in signal results justified the use of the simpler 2-D model for subsequent simulations.

The results for problems 1 through 18 are presented in Table 4.3. Table 4.3 provides data regarding the pulse duration (τ), the input heat flux (q), input energy per unit area (product of q and τ), maximum surface temperature (T_{max}), time and value of the maximum thermal signal, and time and value of maximum thermal contrast. The results are for two-dimensional simulations. A first look at the results indicated that for a given input thermal flux the magnitude and time for maximum thermal signal increase with pulse duration (Fig. 4.11).

Table 4.3 Results of simulations 1 through 18

Problem	τ (s)	q (W/m^2)	Energy ($q\cdot\tau$) (J/m^2)	T_{max} (°C)	Maximum Signal		Maximum Contrast	
					t_s (s)	ΔT_{max} (°C)	t_c (s)	$\Delta T_{max}/\Delta T_{backgr}$
1	1	100,000	100,000	114.25	5.24	24.41	11.24	1.83
2	0.5	100,000	50,000	84.85	5.17	12.24	10.67	1.83
4	0.1	100,000	10,000	50.18	5.23	2.46	10.73	1.83
3	0.05	100,000	5,000	41.39	4.75	1.22	10.75	1.83
4	0.1	100,000	10,000	50.18	5.23	2.46	10.73	1.83
5	0.1	50,000	5,000	36.59	5.23	1.23	10.73	1.83
6	0.1	10,000	1,000	25.72	5.00	0.25	10.70	1.83
1	1	100,000	100,000	114.25	5.24	24.41	11.24	1.83
9	1	50,000	50,000	68.63	5.24	12.20	11.24	1.83
8	1	25,000	25,000	45.81	5.24	6.10	11.24	1.83
7	1	10,000	10,000	32.13	5.24	2.44	11.24	1.83
10	1	5,000	5,000	27.56	5.24	1.22	11.24	1.83
11	2	25,000	50,000	58.54	5.7	12.14	11.70	1.83
12	2	20,000	40,000	51.43	5.7	9.71	11.70	1.83
13	2	10,000	20,000	37.21	5.7	4.86	11.70	1.83
14	2	5,000	10,000	30.11	5.7	2.43	11.70	1.83
18	3	20,000	60,000	60.83	6.41	14.49	11.91	1.83
15	3	15,000	45,000	51.37	6.41	10.86	11.91	1.83
16	3	10,000	30,000	41.91	6.41	7.24	11.91	1.83
17	3	5,000	15,000	32.46	6.41	3.62	11.91	1.83

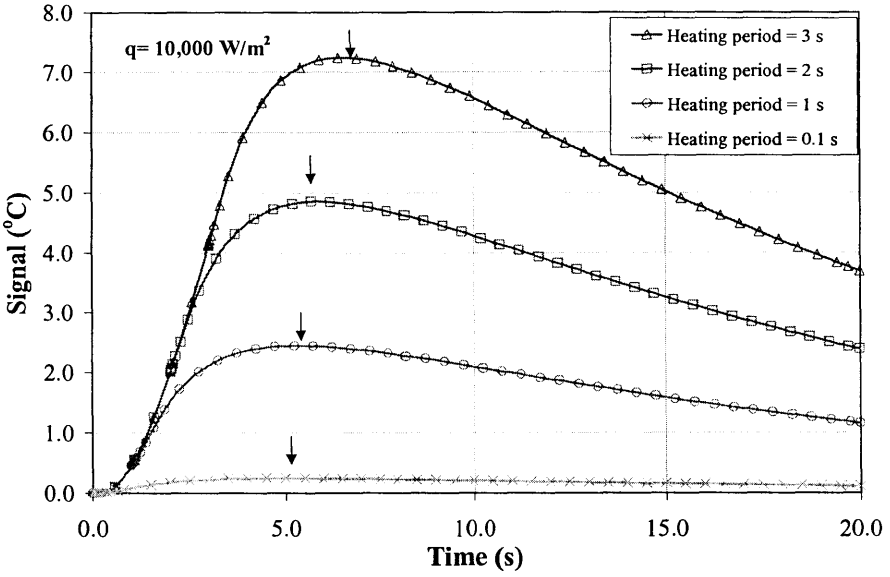

Fig. 4.11 Thermal signal for simulations with increasing pulse duration for q = 10,000 W/m^2

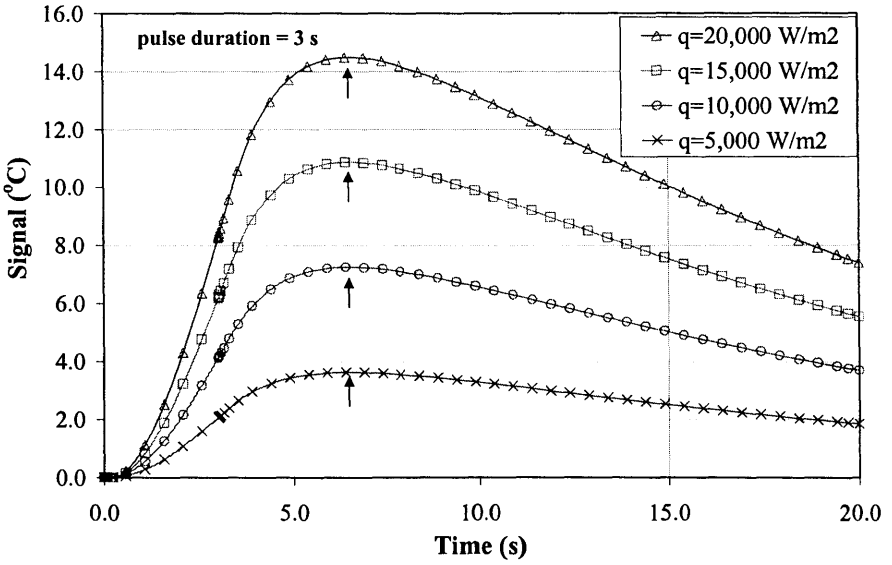

Fig. 4.12 Thermal signal for simulations with different heat flux input and same pulse duration τ = 3 s

Comparison of the results for equal pulse duration shows that the time for maximum signal does not depend on the heat flux but depends on the heating period. As long as the pulse duration remained constant, the time for maximum signal did not change with added energy (Fig. 4.12).

As expected, for a given pulse duration the maximum signal increases with increasing input heat flux (Fig. 4.12).

The time for maximum signal increases in a nonlinear manner with increasing pulse duration, τ, as illustrated in Fig.4.13. The variation in time for maximum signal is only 1.4 seconds for heat pulse durations varying from 0.1 s to 3 s.

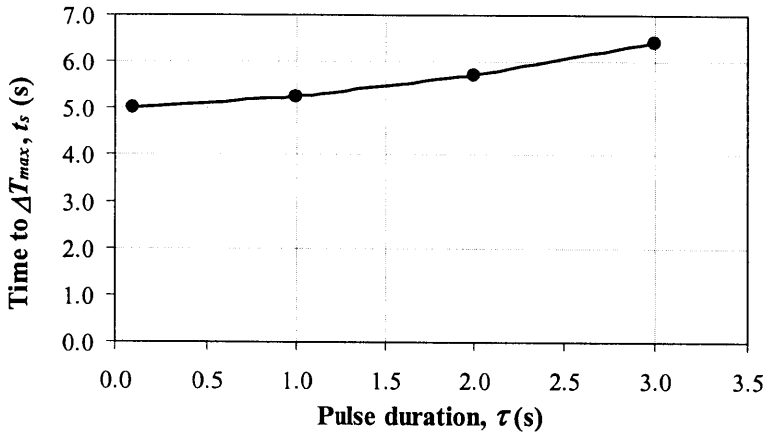

Fig. 4.13 Time for maximum signal as a function of pulse duration

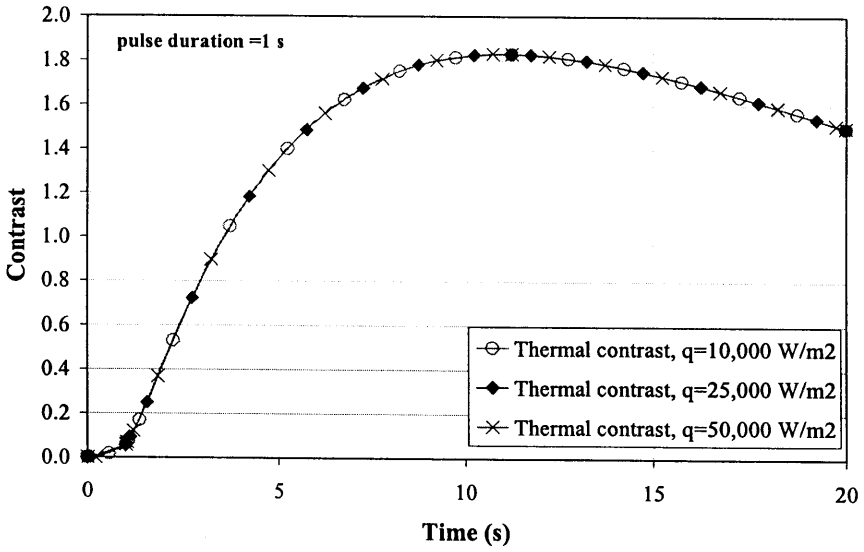

Fig. 4.14 Thermal contrast for problems 7, 8, and 9

An additional observation is that the magnitude of the contrast is independent of the heat flux (Fig. 4.14). This behavior arises because of the normalized nature of the contrast variable. Thus, contrast is a function of the test object (e.g., material properties, flaw depth, thickness, etc.). This behavior may play an important role in the "inverse" problem.

The time for maximum contrast increases with the pulse duration. The rate of increase, however, decreases with longer heating periods as shown in Fig. 4.15. For a variation in pulse duration of 0.1 s to 3 s the time for maximum contrast varied from 10.7 s to 11.9 s.

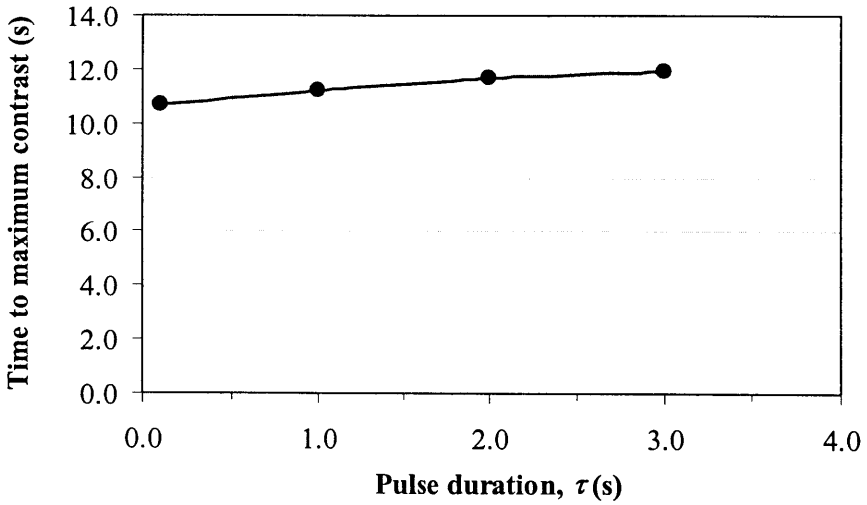

Fig. 4.15 Time for maximum contrast

Further comparisons indicated that for a given pulse duration the maximum thermal signal increases linearly with heat flux, that is, $\Delta T_{max} = \beta \cdot q$ (Fig. 4.16). As an example, for a heating period of 2 seconds, the maximum thermal signal increases at a rate of 0.0005 °C/(W/m^2). The rate at which ΔT increases with q, increases with the heating period as indicated in Table 4.4.

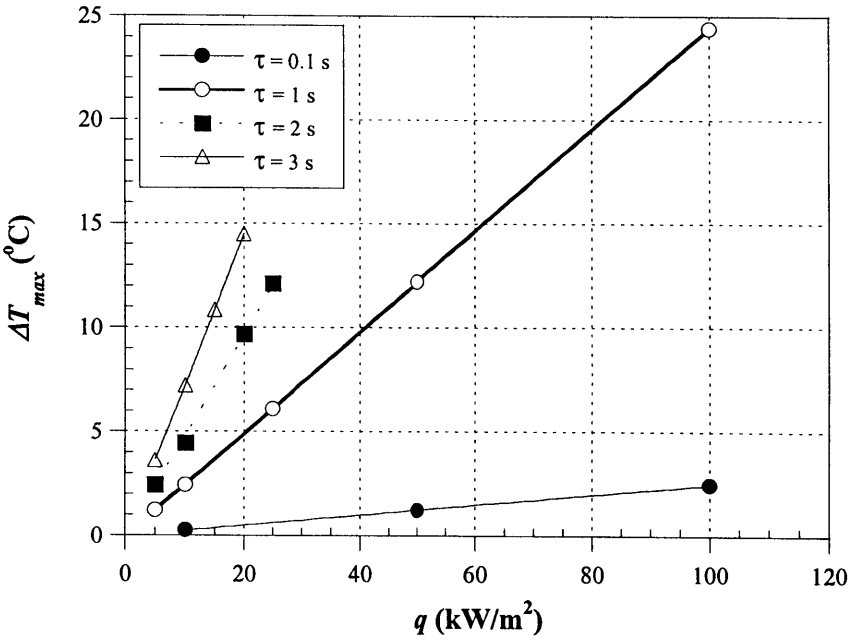

Fig. 4.16 Maximum signal as a function of thermal flux

Table 4.4 Increase in maximum thermal signal as a function of heat flux for different heating periods

Heating period, τ (s)	Rate of increase, β (°C/(W/m^2))	Equation
0.1	0.000025	$\Delta T_{max} = 0.00002\ q$
1.0	0.000244	$\Delta T_{max} = 0.0002\ q$
2.0	0.000482	$\Delta T_{max} = 0.0005\ q$
3.0	0.000724	$\Delta T_{max} = 0.0007\ q$

Figure 4.17 shows the variation of the slopes in Fig.4.16 as a function of pulse duration. It is seen that the slopes are a linear function of pulse duration.

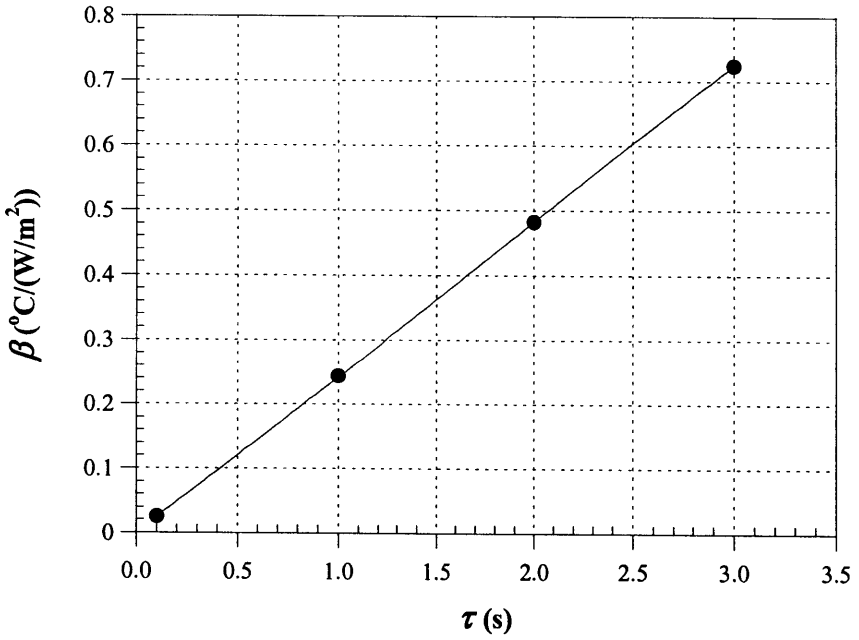

Fig. 4.17 Variation of the slope, β, as a function of pulse duration

The straight-line relationship is $\beta = 0.00024 \cdot \tau$. Thus, the value of the maximum thermal signal is

$$\Delta T_{max} = 0.00024\ \tau\ q \tag{4.13}$$

This equation can be rewritten to express the input heat flux required to produce a desired maximum thermal signal as a function of the pulse duration

$$q = \frac{\Delta T_{max}}{0.00024\,\tau} \tag{4.14}$$

Equation 4.14 represents a family of curves corresponding to combinations of q and τ to produce

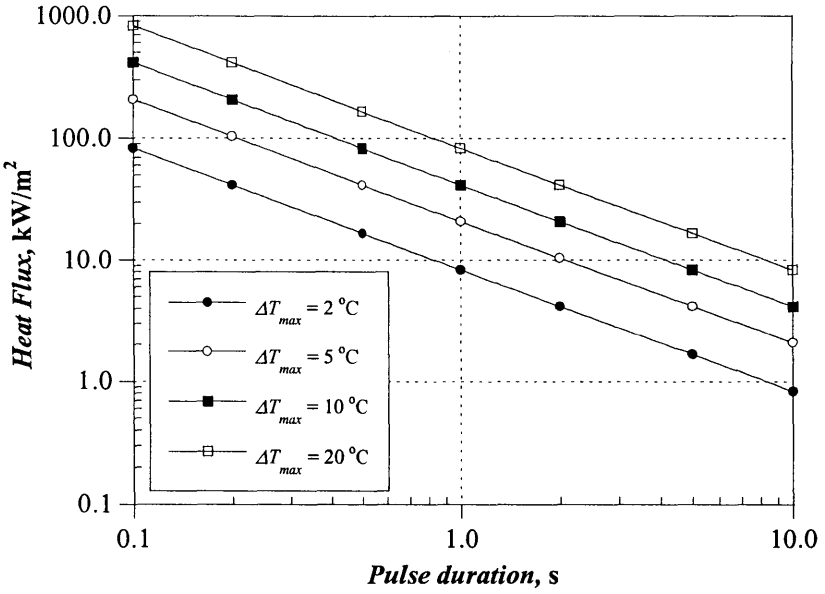

Fig. 4.18 Heat flux versus pulse duration for different maximum thermal signal

a given ΔT_{max}. Figure 4.18 shows these curves when plotted using log scales.

Examination of Eq. 4.13 shows that there is an elegantly simple relationship between the maximum thermal signal and the thermal input. The product τq is the area beneath the heating pulse and represents the input energy per unit area, that is,

$$E(J/m^2) = q(W/m^2)\cdot\tau(s) \tag{4.15}$$

Thus, the maximum signal is a linear function of the input energy

$$\Delta T_{max} = 0.00024E \tag{4.16}$$

Figure 4.19 is a plot of the maximum signal versus energy values given in Table 4.3. The linear relationship is confirmed. This provides a powerful tool for selecting the thermal input to achieve a desired signal. Infinite combinations of input flux and pulse duration will result in the same maximum signal (Fig. 4.18). The only differences will be the time when the maximum signal is obtained and the maximum surface temperature that is attained.

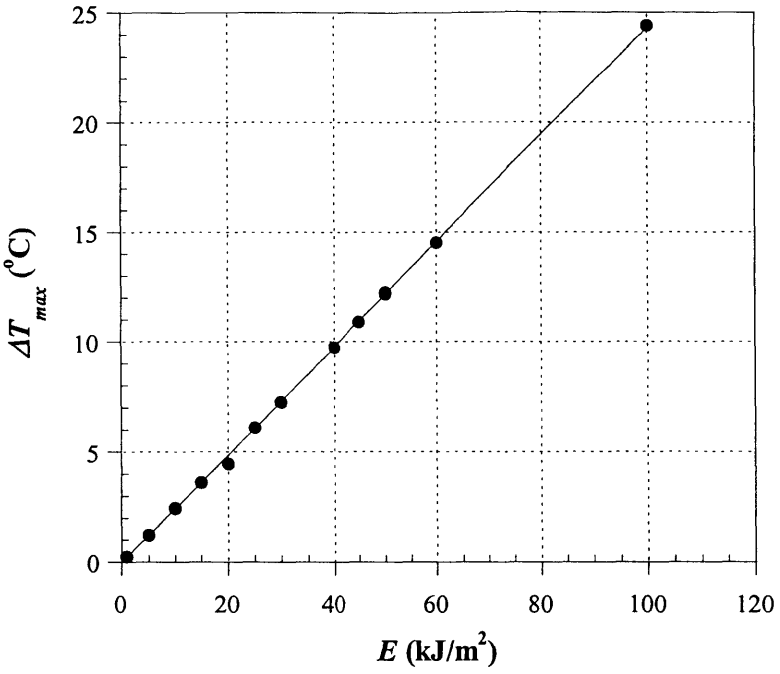

Fig. 4.19 Maximum signal versus energy

The maximum surface temperature reached during thermographic testing is an important consideration for the successful application of this technique to FRP composites. The reason for the need to estimate the maximum temperature is the low glass transition temperature of these materials. When the temperature of the resin of the composite increases above the glass transition temperature, T_g, the mechanical properties of the matrix are degraded. Glass transition temperatures for CFRP used in civil engineering applications are on the order of 53 °C (Christensen et al., 1996).

Further analysis of the results in Table 4.3 indicated that, for a given pulse duration, the maximum surface temperature increases linearly with the heat flux. Thus, the maximum surface temperature is described by

$$T_{max} = 23 + \gamma(\tau)\, q \tag{4.17}$$

where, $\gamma(\tau)$ is the slope of the line for a given pulse length. The linear behavior is illustrated in Fig. 4.20.

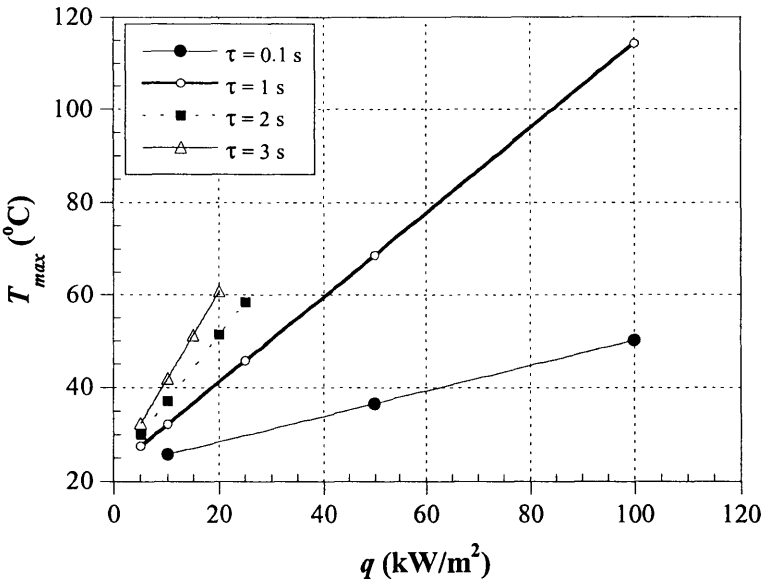

Fig. 4.20 Maximum surface temperature as a function of heat flux for different pulse durations

Table 4.5 lists the slopes (γ) of the lines in Fig. 4.20, and it is seen that the slopes increase with pulse duration. Figure 4.21 shows the values of γ as a function of pulse duration. It is clear that the relationship between γ and τ is not linear. A quadratic function provided a good fit to the points in Fig. 4.21.

Table 4.5 Maximum surface temperature as a function of input heat flux for different pulse duration

Heating period, τ (s)	**Rate of increase, γ (°C/(W/m^2))**	**Equation $T_{max} = \gamma q + 23$**
0.1	0.0003	$T_{max} = 0.00027\ q + 23$
1.0	0.0009	$T_{max} = 0.00091\ q + 23$
2.0	0.0014	$T_{max} = 0.00142\ q + 23$
3.0	0.0019	$T_{max} = 0.00189\ q + 23$

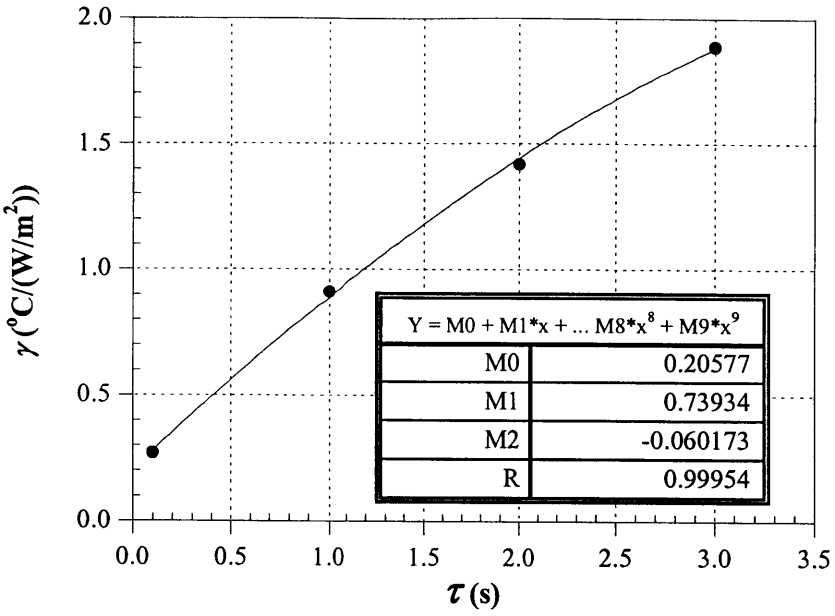

Fig. 4.21 γ as a function of pulse duration

The maximum surface temperature attained for a given pulse duration was found to be a linear function of input energy. This is illustrated in Fig. 4.22.

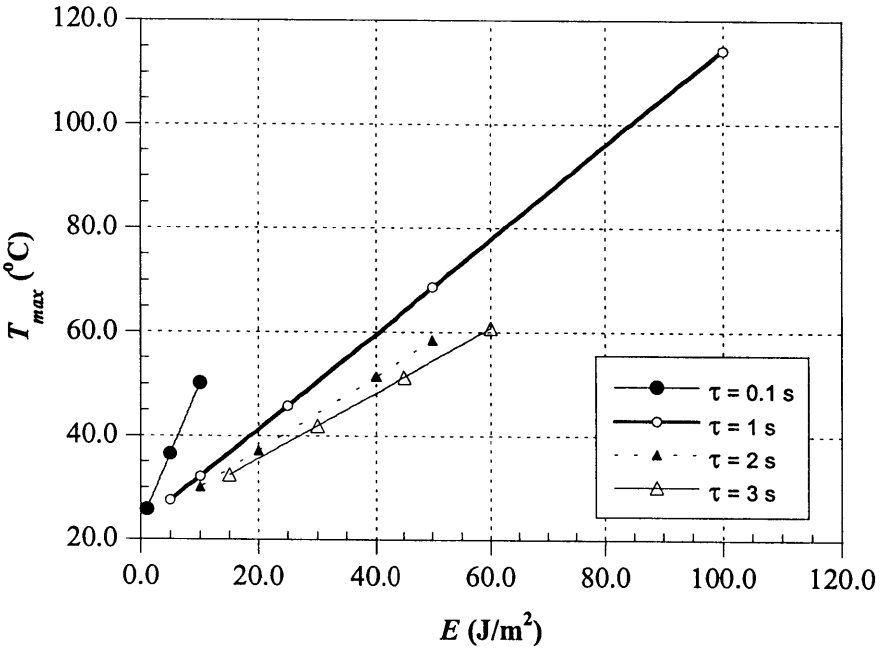

Fig. 4.22 Maximum surface temperature versus input energy

Thus, the relationship between T_{max} and E is

$$T_{max} = \delta(\tau)E + 23 \tag{4.18}$$

where, $\delta(\tau)$ is the slope of the line for a given pulse duration. Table 4.6 shows the value of δ for different pulse durations and these are plotted in Fig. 4.23. These results show that the value of δ is a highly nonlinear function of pulse duration. For short duration pulses, δ is large and surface temperature is more sensitive to the input energy than for longer duration pulses.

Table 4.6 Maximum surface temperature as a function of input energy for different pulse duration

Heating period, τ (s)	**Rate of increase, δ ($°C/(J/m^2)$)**	**Equation $T_{max} = \delta E + 23$**
0.1	0.0003	$T_{max} = 0.0027\ E + 23$
1.0	0.0009	$T_{max} = 0.00091\ E + 23$
2.0	0.0014	$T_{max} = 0.00071\ E + 23$
3.0	0.0019	$T_{max} = 0.00063\ E + 23$

An approximate functional relationship for $\delta(\tau)$ was established as follows:

1. Assume that the relationship for $\gamma(\tau)$ is a quadratic function (see Fig. 4.21)

$$\gamma(\tau) = a + b\tau + c\tau^2 \tag{4.19}$$

2. Substitute into Eq. 4.17

$$T_{max} = \left(a + b\tau + c\tau^2\right)q + 23 \tag{4.20}$$

3. Use the definition E= τ·q

$$T_{max} = E\left(\frac{a}{\tau} + b + c\tau\right)q + 23 \tag{4.21}$$

4. Therefore,

$$\delta(\tau) = \frac{a}{\tau} + b + c\tau \tag{4.22}$$

A least-squares fit of Eq. 4.22 to the points in Fig. 4.23 resulted in the following values for the constants a, b, and c:

$$a = 0.793 \quad (0.040)$$

$$b = 0.192 \quad (0.005)$$

$$c = -0.076 \quad (0.017)$$

where the numbers in parentheses are the standard errors of the coefficients.

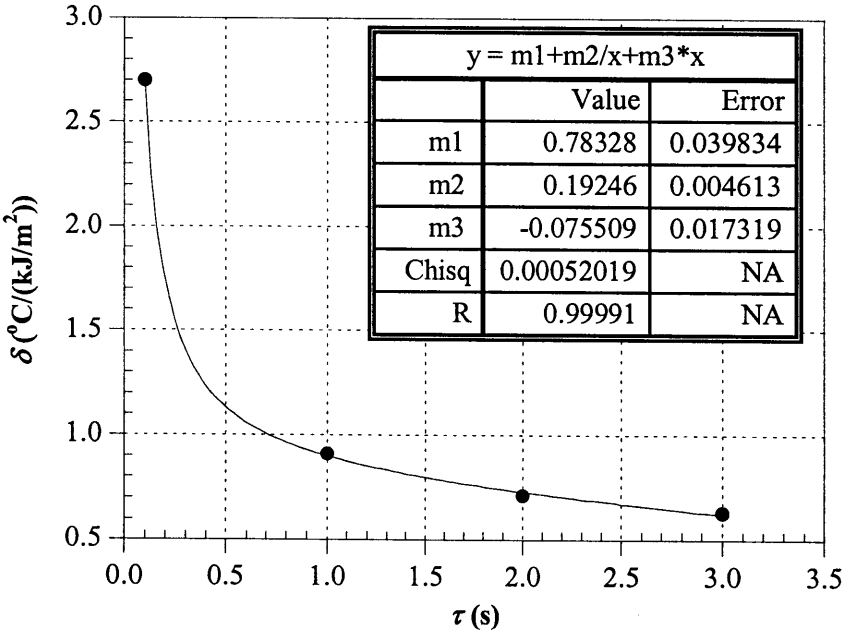

Fig. 4.23 Values of δ as a function of pulse duration

Figure 4.23 shows that the function given by Eq. 4.22 provides a good fit to the results. It is now possible to estimate the relationships between T_{max} and E for any value of τ from 0.1 s to 3 s. Examples are show in Fig. 4.24.

Figures 4.22 or 4.24 show that for a given input energy the maximum surface temperature increases with decreasing pulse duration. This behavior is explained as follows. For equal input energy, a short pulse duration requires a larger input heat flux, q. Since it takes time for the input energy to diffuse into the object, the higher the input flux the higher will be the surface temperature rise. This effect is illustrated in Figs. 4.25 and 4.26, which show the temperature distributions at the time of maximum surface temperature for E values of 10,000 J/m^2 and pulse durations of 0.1 s and 2 s, respectively.

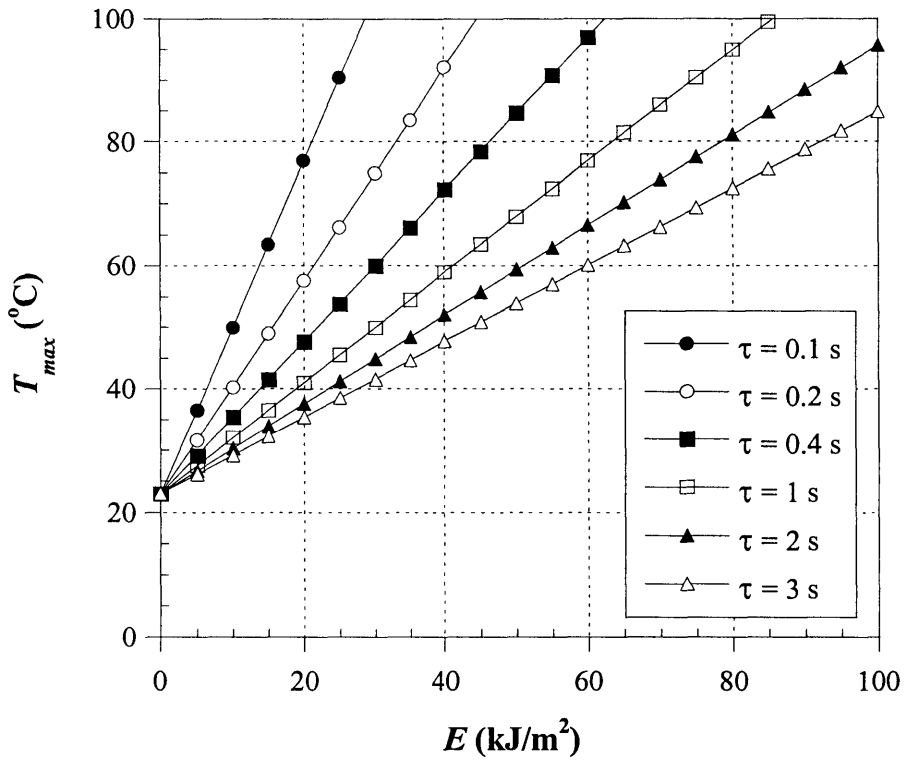

Fig. 4.24 Estimation of the maximum surface temperature as a function of the input energy for different pulse durations

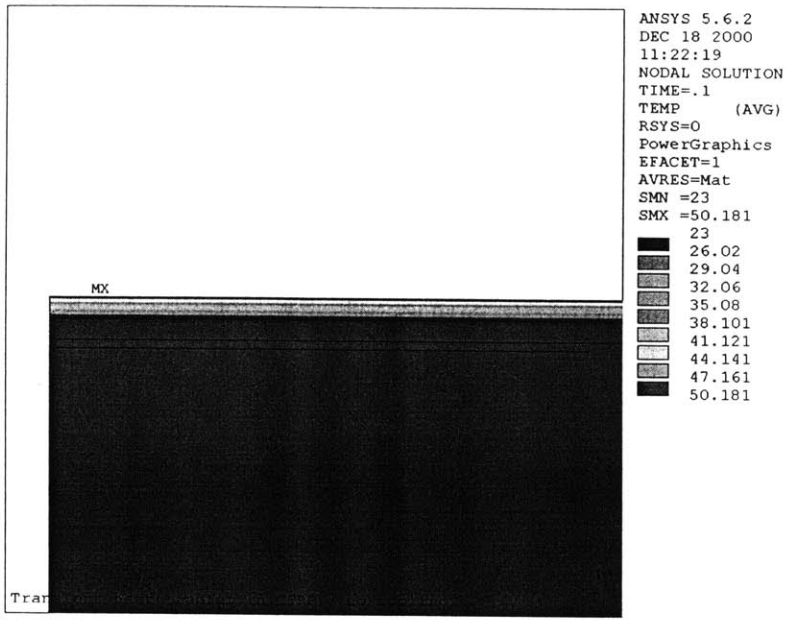

Fig. 4.25 Illustration of thermal diffusion at time of maximum temperature for problem 4 ($\tau = 0.1$ s, $q = 100{,}000$ W/m^2)

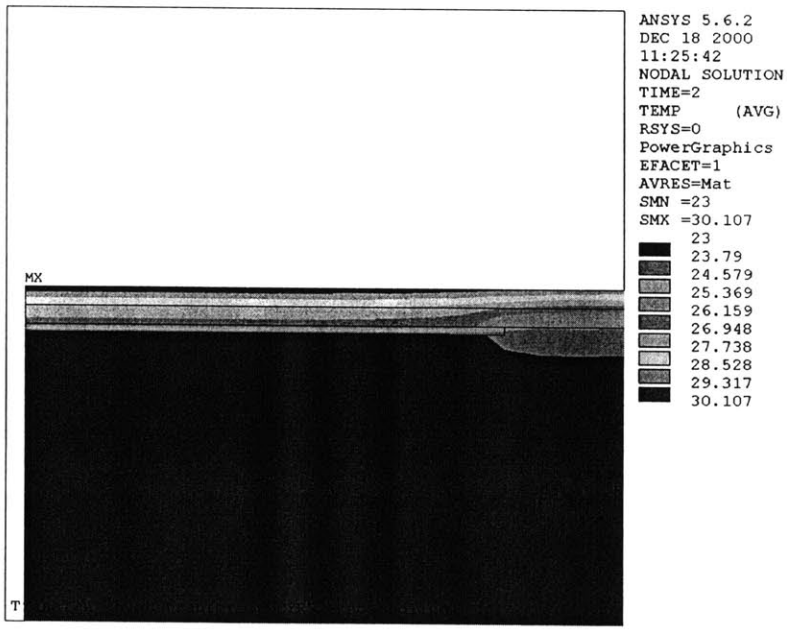

Fig. 4.26 Illustration of thermal diffusion at time of maximum temperature for problem 14 ($\tau = 2$, $q = 5{,}000$ W/m^2)

The results of this parametric study have provided valuable insight into the interaction between thermal input and a given defect. The key to successful flaw detection using infrared thermography is to have a sufficiently large surface temperature gradient. For a given flaw geometry, Fig. 4.19 shows that the maximum surface temperature difference is a linear function of the input energy (expressed in J/m^2). Thus, a maximum value of input energy can be established for a given minimum signal. The selection of the pulse duration to produce the minimum input energy is governed by the maximum surface temperature that can be tolerated. For example, suppose we desire a thermal signal of $\Delta T_{max} = 10$ °C. According to Fig. 4.19, the required input energy is about 40 kJ/m^2. Suppose it is desired to limit the surface temperature to 50 °C. Assuming that the initial temperature is 23 °C, Fig. 4.24 shows that the pulse duration should not be less than 2 s. The required input heat flux will be lower for a longer pulse duration. For a pulse duration of 2 s the required input flux is 20 kW/m^2, and for a 3 s duration it is 13.3 kW/m^2. Of course, these relationships are applicable to the specific object that was used in these simulations. One of the objectives of subsequent simulations is to examine how these relationships are affected by changes in the test object.

4.3.5 Summary

The first parametric study was designed to answer several questions regarding the effect of thermal input. The focus of the initial investigation was to

- understand diffusion behavior due to different heating and heat flux inputs,
- find appropriate thermal inputs for typical FRP composites bonded to concrete.

The test object presented a delamination at the FRP/concrete interface and 2-D analysis were used to reduce computational efforts. Several conclusions were reached after analyzing several models with varying thermal stimuli:

- For a given heating time (pulse duration), time for maximum signal is independent of the applied heat flux.
- Time for maximum signal depends on pulse duration. It increases nonlinearly with increasing pulse duration. The rate at which the time for maximum signal increases, rises with pulse duration.
- The time for maximum contrast increases with increasing pulse duration; however, the rate of increase decreases with τ.
- The magnitude of the thermal signal increases linearly with input energy (product of input heat flux and pulse length).
- The magnitude of the thermal contrast is independent of both heat flux and heating period.
- For a given pulse duration, maximum surface temperature increases linearly with heat flux. The rate of increase rises with pulse duration, since more energy is applied to the specimen.

- For a given pulse duration, maximum surface temperature increases linearly with input energy. The rate of increase, however, decreases non-linearly with longer heating periods.

These results have led to a simple approach for selecting the thermal input so as to obtain a desired thermal signal while limiting the surface temperature due to heating. The next series of studies will examine the effects of thermal properties and geometry on the thermal response.

4.4 Parametric Study No. 2: Effect of Thermal Material Properties

Because it is expected that the thermal properties of installed FRP laminates may differ from nominal values, it is important to understand how thermal response is affected by thermal properties. Hence, the second parametric study involved the evaluation of the effect of thermal material properties of FRP and concrete on the thermal response. The study had two objectives:

- gain an understanding of thermal diffusion behavior due to different values of thermal conductivity and specific heat,

- establish if accurate determination of material thermal properties is required for quantitative IR thermography of FRP laminates applied to concrete.

The parametric study focused on the analysis of the transient heat transfer behavior of CFRP bonded to concrete. Five different sets of analyses were performed involving a total of 28 finite element simulations. The first two sets of analyses involved changing thermal properties in the CFRP laminates. The next two sets of analyses corresponded to simulations in which the material properties of the concrete substrate varied. The final set of simulations involved different combinations of thermal conductivity and specific heat of FRP and concrete.

4.4.1 Geometry of Model

The geometry of the models was the same as in parametric study #1. The model consisted of a 10 cm long by 2 cm high concrete substrate covered with two layers of carbon FRP (Fig.3.2). Each layer of CFRP was 0.5 mm thick. The bonded FRP contained a flaw (debond) at the interface with the concrete substrate. The debond had a length of 2.5 cm and a thickness of 0.1 mm, which corresponded to a thermal contact resistance of 4.17×10^{-3} m^2/W. As before, the interface flaw was located at the center of the analytical model. Plane two-dimensional modeling was assumed; the z-coordinate represented an infinitely large width of the specimen. Modeling was simplified using plane symmetry.

The model was meshed using 2-D thermal solid elements, specifically, four-noded quadrilateral PLANE55 elements. The test object was meshed using mapped meshing. The global element length was set to 1 mm. Mesh refinement, however, was applied to the thin composite layers and at the flaw. The thickness of each composite ply was subdivided into four elements. Similarly, the thickness of the flaw and adjacent concrete was subdivided into two elements. The rest of the concrete specimen was meshed using a graded mesh with finer mesh at the top and coarser mesh at the bottom of the specimen. The average element thickness for the concrete was

0.00275 m and the spacing ratio was 10.

4.4.2 Material Properties

The variables in this parametric study were the thermal properties of the different constituents of the test object. The CFRP layer in direct contact with the concrete had the fibers running in the x-direction, while the external CFRP had the fibers running in the z-direction. Two material properties were varied: thermal conductivity and specific heat.

In general, the density and mechanical properties of most materials are well documented and provided by most manufacturers. The thermal properties of novel materials such as FRP composites, however, are usually not reported by the manufacturers. Thus, it is vital to determine how changes in thermal properties would affect the thermal diffusion behavior. The material properties are presented in Tables 4.7, 4.8, and 4.9. Problem 19 incorporated the material properties of a "control" test object used for comparison purposes. The material properties of the test object for problem 19 were changed in the various analyses. Table 4.8 summarizes the material properties for the simulation in which the thermal conductivity (problems 19 through 26) and the specific heat (problems 19, 27, 28, and 29) of FRP were varied. It is important to note that thermal conductivity was varied in the direction parallel to the fiber as well as perpendicular to the fiber. Likewise, Table 4.9 summarizes the material data for the models in which the thermal conductivity (problems 19, 30, 31, and 32) and the specific heat (problems 19, 33, 34, 35) of the concrete substrate were varied. The range of values for the thermal properties of CFRP and concrete were selected from available literature (ASHRAE Handbook; Maldague, 1993) and electronic databases (MatWeb Materials Property Database).

Table 4.7 Material properties of concrete and CFRP for "control" case.

Problem #	Material	ρ (kg/m^3)	c (J/kg·°C)	$k_{parallel\ to\ fiber}$ (W/m·°C)	$k_{perpendicular\ to\ fiber}$ (W/m·°C)
19	Concrete	2400	800	1.5	1.5
	CFRP	1600	1200	7.0	0.8

Table 4.8 Material properties: changing the thermal conductivity and specific heat of CFRP.

Problem #	Material	ρ (kg/m^3)	c (J/kg·°C)	$k_{parallel}$ (W/m·°C)	$k_{perpendicular}$ (W/m·°C)	% change
20	CFRP	1600	1200	8.8	1.0	25
21	CFRP	1600	1200	10.5	1.2	50
22	CFRP	1600	1200	12.25	1.4	75
23	CFRP	1600	1200	14.0	1.6	100
24	CFRP	1600	1200	15.75	1.8	125
25	CFRP	1600	1200	17.5	2.0	150
26	CFRP	1600	1200	21	2.4	200
27	CFRP	1600	1020	7	0.8	-15
28	CFRP	1600	1080	7	0.8	-10
29	CFRP	1600	1140	7	0.8	-5

Table 4.9 Material properties: changing the thermal conductivity and specific heat of concrete.

Problem #	Material	ρ (kg/m^3)	c (J/kg·°C)	k (W/m·°C)	% change
30	Concrete	2400	800	1.4	-5
31	Concrete	2400	800	1.6	10
32	Concrete	2400	800	1.8	20
33	Concrete	2400	880	1.5	10
34	Concrete	2400	960	1.5	20
35	Concrete	2400	1040	1.5	30

Eight additional analyses were performed to explore the interaction of the material properties of the FRP and the concrete. The simulations involved the following combinations of material properties:

- low k_{FRP} and low $k_{concrete}$
- low k_{FRP} and high $k_{concrete}$

- high k_{FRP} and low $k_{concrete}$
- high k_{FRP} and high $k_{concrete}$
- low c_{FRP} and low $c_{concrete}$
- low c_{FRP} and high $c_{concrete}$
- high c_{FRP} and low $c_{concrete}$
- high c_{FRP} and high $c_{concrete}$

For the development of these eight models the material properties of previous simulations were used. The material properties for the eight combinations are presented in Table 4.10.

Table 4.10 Material properties for simulations 36 through 43

Combination	Problem	k_{FRP} (W/m·°C)		$k_{concrete}$ (W/m·°C)	c_{FRP} (J/kg·°C)	$c_{concrete}$ (J/kg·°C)
		parallel	perpendicular			
low k_{FRP}-low k_{conc}	36	7	0.8	1.425	1200	800
low k_{FRP}-high k_{conc}	37	7	0.8	1.8	1200	800
high k_{FRP}-low k_{conc}	38	15.75	1.8	1.425	1200	800
high k_{FRP}-high k_{conc}	39	15.75	1.8	1.8	1200	800
low c_{FRP}-low c_{conc}	40	7	0.8	1.5	1020	800
low c_{FRP}-high c_{conc}	41	7	0.8	1.5	1020	1040
high c_{FRP}-low c_{conc}	42	7	0.8	1.5	1200	800
high c_{FRP}-high c_{conc}	43	7	0.8	1.5	1200	1040

4.4.3 Thermal Loading and Boundary Conditions

The analysis was defined as a transient heat transfer problem. A square pulse of intensity 20,000 W/m^2 was applied at the top surface of the model. The duration of the thermal flux was 2 s. Adiabatic conditions ($dT/dx = 0$ and $dT/dy = 0$) were assumed for the additional surfaces. The initial temperature of the model and the ambient temperature was set to 23 °C, as the standard ambient temperature.

For comparison purposes, the same time stepping was used for all the problems. The initial time step was 0.009 seconds. The automatic time stepping capability of ANSYS was used with minimum and maximum time steps of 0.008 s and 0.1 s, respectively. A sensitivity analysis was performed to determine an appropriate maximum time step for this particular study. The first set of analyses (those involving changing thermal conductivity of the CFRP) were performed using three different maximum time steps, 0.009 s, 0.1 s, and 0.5 s. The maximum time step of 0.5 s was found to be too large to fully capture the thermal evolutions of these particular sets of simulations. Maximum time steps of 0.009 s and 0.1 s successfully captured the thermal

behavior of the models. The maximum time of step of 0.1 s was selected as a balance between computational economy and accuracy.

The simulation output (nodal temperatures) was recorded at every time step.

4.4.4 Results

4.4.4a Effect of Thermal Conductivity of FRP

The finite element simulations illustrated the thermal behavior of the test object due different material properties of both the FRP composite laminates and the concrete substrate.

As previously mentioned, the first set of analyses examined the effect of changing the thermal conductivity of the CFRP. The thermal conductivity was increased up to three times the thermal conductivity of the "control" test object. The results indicated that changes in the thermal conductivity of the composite layers produce nonlinear changes in the thermal response of the test object. The parameters used to characterize the thermal response are:

- the maximum surface temperature, T_{max},
- the maximum difference in surface temperature, or the signal, ΔT_{max},
- the time when the maximum signal occurs, t_s,
- the maximum contrast, $\Delta T_{max}/\Delta T_{back}$, and
- the time for maximum contrast, t_c.

A summary of the results for the first set of analyses is presented in Table 4.11.

Table 4.11 Results for simulations involving changes in the thermal conductivity of CFRP.

Problem	$k_{perpendicular\ to\ fiber}$ (W/m·K)	T_{max} (°C)	Maximum Signal		Maximum Contrast	
			t_s (s)	ΔT_{max} (°C)	t_c (s)	$\Delta T_{max}/\Delta T_{backg}$
19	0.8	51.6	5.75	9.92	11.25	1.86
20	1.0	49.9	5.24	10.09	10.14	1.84
21	1.2	48.7	4.94	10.18	9.34	1.82
22	1.4	47.8	4.64	10.24	8.74	1.79
23	1.6	47.2	4.36	10.27	8.24	1.76
24	1.8	46.7	4.23	10.28	7.83	1.73
25	2.0	46.3	4.13	10.27	7.43	1.70
26	2.4	45.6	3.83	10.24	6.83	1.65

The results in Table 4.11 illustrate some interesting points regarding the effect of thermal conductivity of the FRP composite on the thermal evolutions. For example, as shown in Fig. 4.27, the maximum surface temperature decreases nonlinearly with increasing thermal conductivity of the FRP layers. Thermal conductivity is defined as the time rate of heat flow

through a unit area of material induced by a unit temperature gradient (ASTM C 168-97). As would be expected, the input thermal energy is transferred to the interior of the test object at a faster rate as the thermal conductivity increases. Thus for a given thermal input, the maximum surface temperature decreases with increasing thermal conductivity due to the diffusion effect, that is, the thermal energy diffuses more quickly into the interior rather than concentrate at the surface.

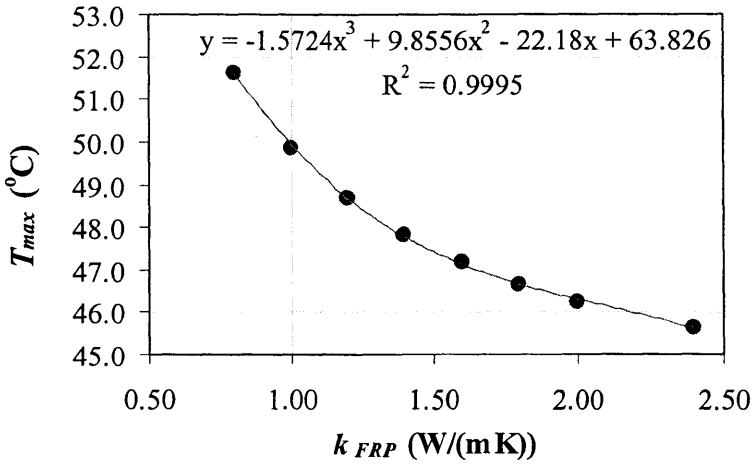

Fig. 4.27 Effect of thermal conductivity of CFRP on maximum surface temperature.

In these analyses, the thermal conductivity of the FRP was increased by 200% but the maximum temperature decreased only 6 °C. Thus the maximum surface temperature does appear to be very sensitive to the conductivity of the FRP laminate for the case of a debond below two layers of FRP.

Figures 4.28 and 4.29 show the surface temperatures as a function of time for a point over the center of the flow and point at the boundary of the test object, respectively. The difference in the way the surface temperature rises and decays is due in part to the change in thermal properties; but, is also related to the geometry of the test object (e.g., depth of flaw, number and thickness of CFRP layers, etc.).

It is seen that the maximum thermal signal varies nonlinearly with increasing thermal conductivity. The maximum thermal signal increases with increasing thermal conductivity until the thermal conductivity reaches 125% of the initial value. Further increases in thermal conductivity resulted in a slight decrease in the maximum thermal signal. Figure 4.30 shows the thermal signal as a function of time for problems 19 through 26 and Fig. 4.31 shows the maximum signal as a function of the thermal conductivity of the FRP.

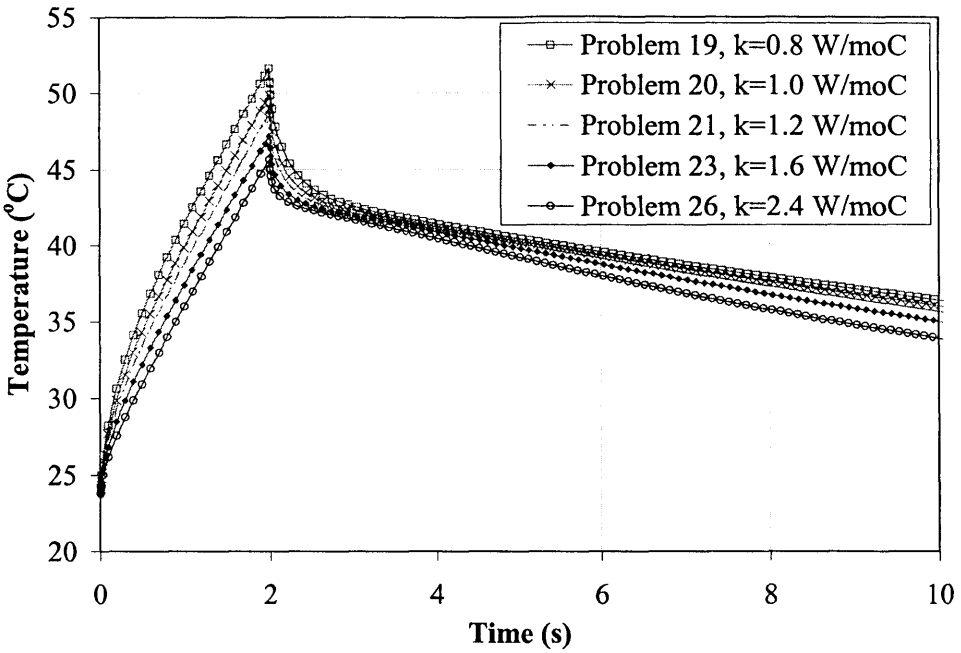

Fig. 4.28 Effect of thermal conductivity of CFRP on surface temperature above the flaw.

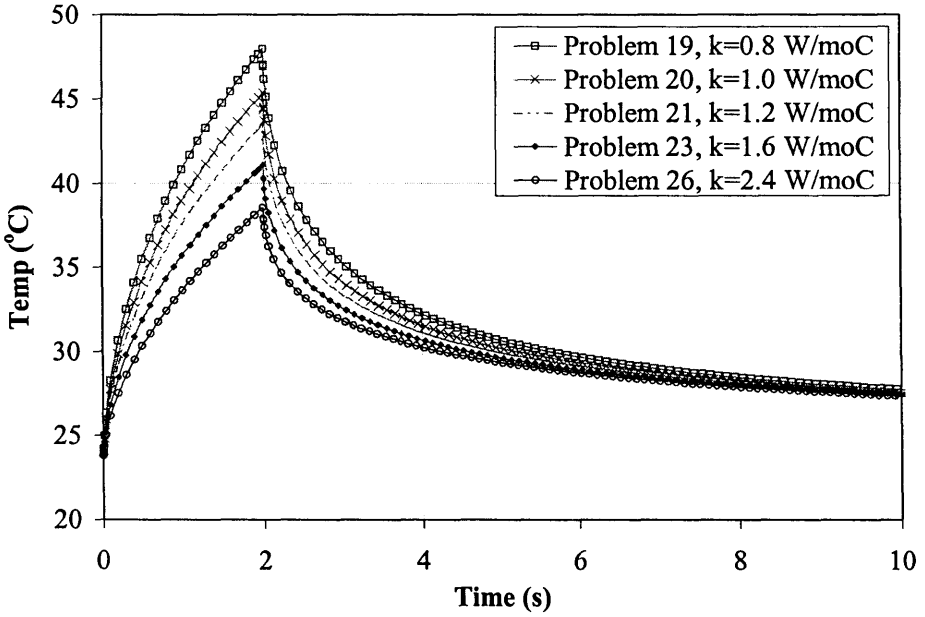

Fig. 4.29 Effect of the thermal conductivity of CFRP on the surface temperature of the background.

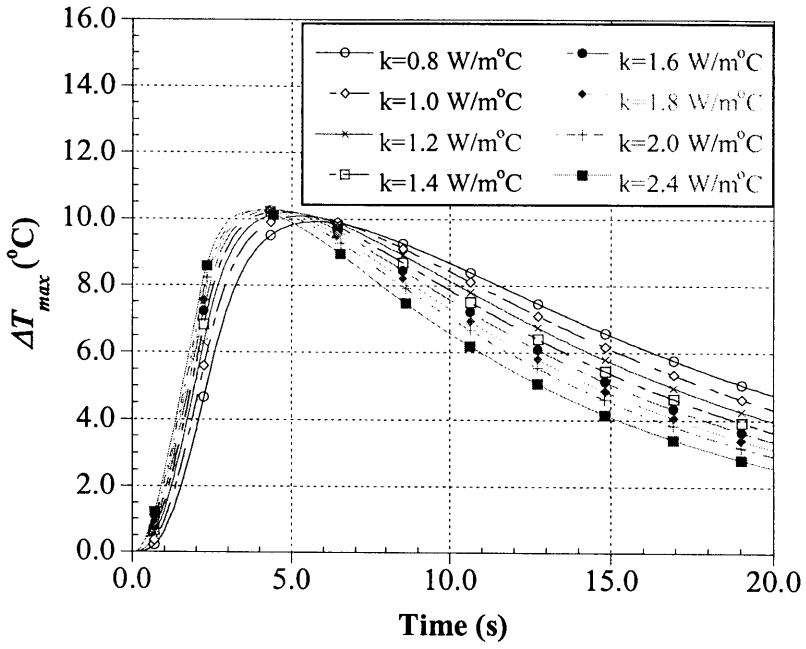

Fig. 4.30 Thermal signal for problems 19 through 26 (k_{FRP} = 0.8 W/m·°C to 2.4 Wm·°C)

A polynomial of fourth order was fitted to the results in Fig. 4.31. The resulting relationship between maximum signal and thermal conductivity was

$$\Delta T_{max} = -0.114\,k^4 + 0.912\,k^3 - 2.849\,k^2 + 4.054\,k + 8.084 \tag{4.23}$$

where, ΔT_{max} was the maximum signal and k was the thermal conductivity of the CFRP. The maximum increase in thermal signal, ΔT_{max}, coincided with a 125% increase of the thermal conductivity of the FRP ($k_{perpendicular}$ = 1.8 W/m·K). The maximum change in ΔT_{max} was 0.35 °C, which represents an increase in signal of only 3.6 %. Thus, for the test object used in these analyses, the thermal signal is not very sensitive to the thermal conductivity of the FRP laminates.

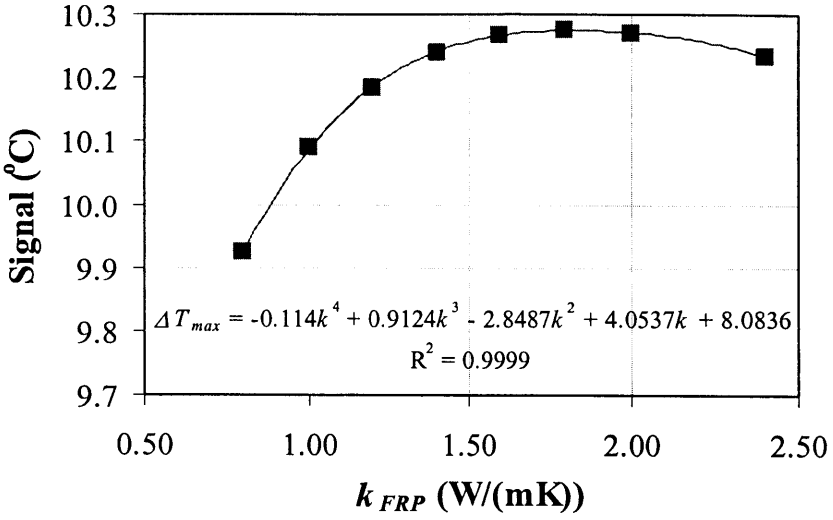

Fig. 4.31 Maximum thermal signal as a function of thermal conductivity of FRP

Figure 4.32 shows the time for maximum signal versus the thermal conductivity of the FRP. Overall, the time for maximum thermal signal decreases with increasing thermal conductivity due to the increasing diffusivity of the FRP. The thermal front travels faster through the material, thus increasing the speed of cooling of the surface. The decrease in detection time has a nonlinear behavior as illustrated in Fig. 4.32.

This behavior indicates that as the thermal conductivity of the FRP increases there will be less time from when the heat source is removed and when the maximum signal occurs. For a two-fold increase in thermal conductivity the time for maximum signal decreases from about 4 s to about 6 s. Thus it appears that increasing the conductivity of the FRP would not have a detrimental effect on the ability to detect the debond.

Figure 4.33 shows the evolution of thermal contrast as a function of thermal conductivity of the FRP, and Fig. 4.34 show the variation of the maximum thermal contrast. The maximum thermal contrast decreased with increasing thermal conductivity of the FRP. Unlike the thermal signal, however, the thermal contrast varied linearly with increasing thermal conductivity. The decrease in thermal contrast was on the order of 0.028 per 0.2 W/m·K increase in thermal conductivity. Based on the "control", this decrease represented a 1.5% decrease in contrast per 25% increase in thermal conductivity.

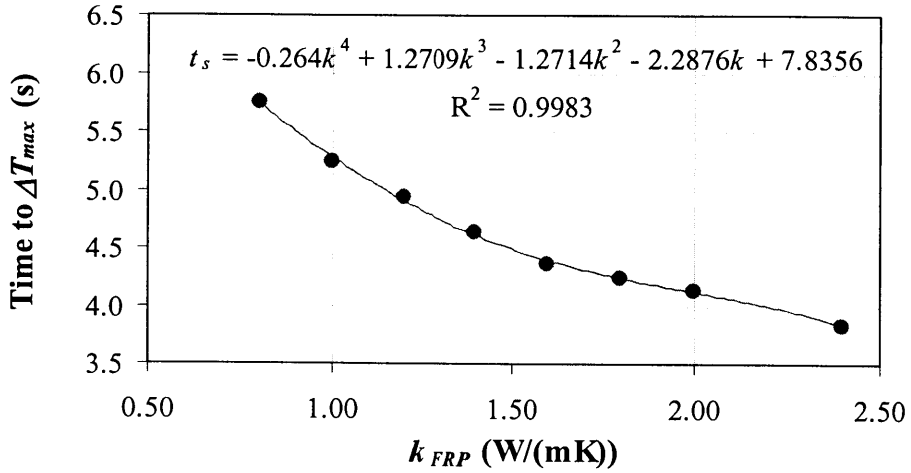

Fig. 4.32 Time for maximum signal as a function of the thermal conductivity of FRP

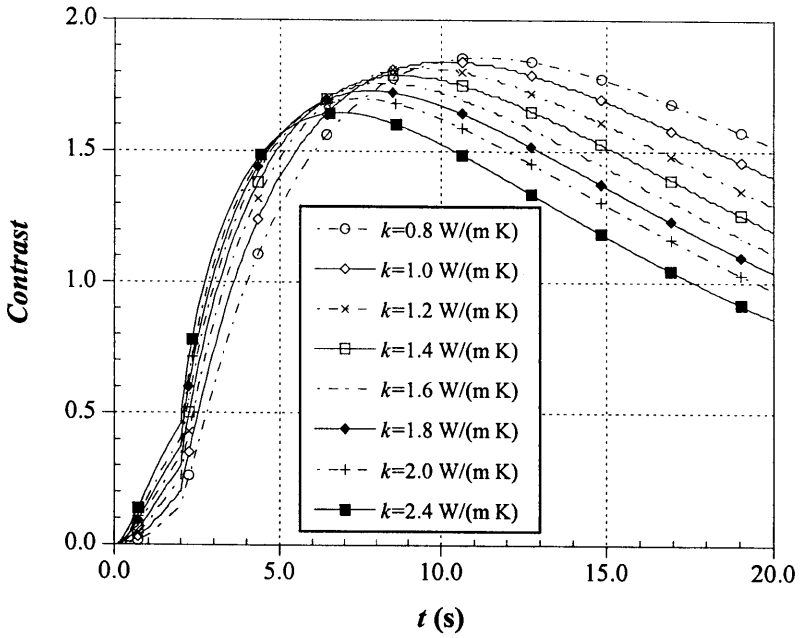

Fig. 4.33 Thermal contrast for problems 19 through 26 (k_{FRP} = 0.8 W/m·K to 2.4 W/m·K)

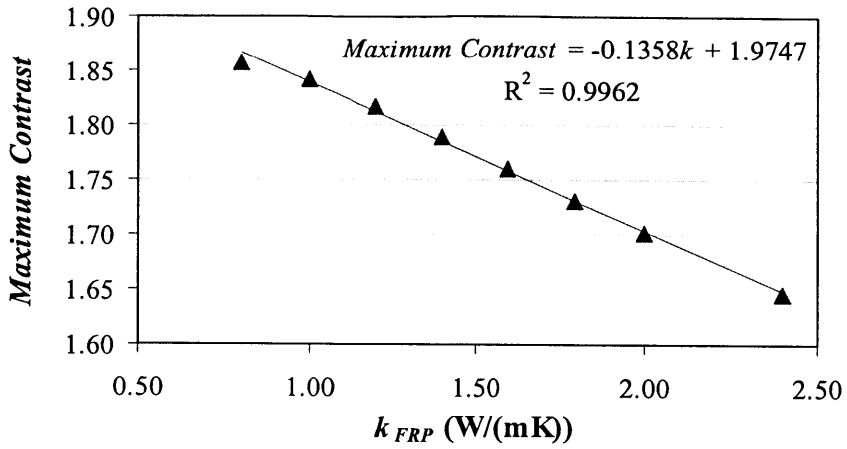

Fig. 4.34 Maximum thermal contrast as a function of thermal conductivity of FRP

Similarly to the time for maximum signal, the time for maximum contrast also decreased nonlinearly with increasing conductivity of the FRP. The decrease, however, followed a power function as shown Fig. 4.35. For this particular test object the power function was

$$t_c = 10.16\, k_{FRP}^{-0.45} \tag{4.24}$$

where, t_c was the time for maximum contrast, and k_{FRP} was the thermal conductivity of the CFRP. The time for maximum contrast decreased by 3 s with two-fold increase in the thermal conductivity of FRP. Thus it appears that thermal contrast is affected by thermal conductivity more than the thermal signal.

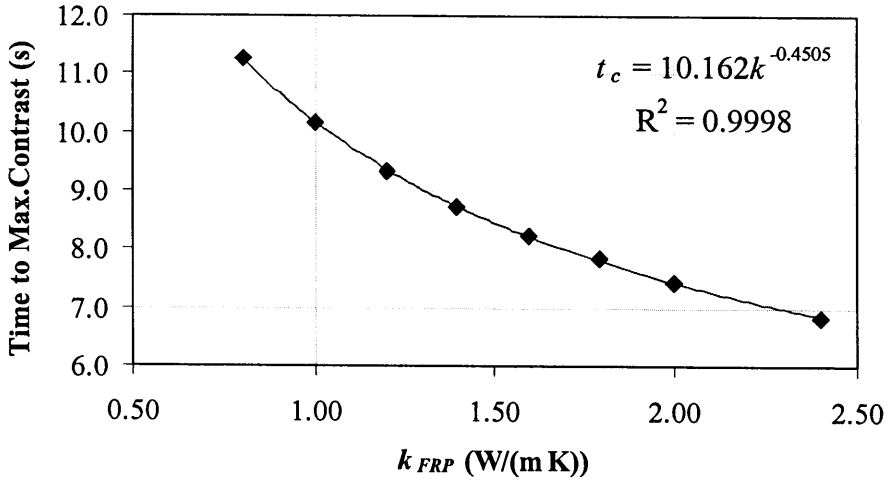

Fig. 4.35 Time to maximum contrast as a function of the thermal conductivity of FRP.

4.4.4b Effect of Specific Heat of FRP

The next set of analyses (problems 19 and 27 through 29) involved the investigation of the effect of the specific heat of FRP on the heat transfer phenomenon. As a reminder, the specific heat of a material is a measure of the amount of energy required to raise the temperature of a unit mass of the material by 1K. The units are J/kg·K.

The first results investigated were the effect of the specific heat on the maximum surface temperature. Table 4.12 summarizes the results as the specific heat was decreased from 1,200 J/kg·K to 1,020 J/kg·K. The results indicated that changes in the specific heat of the FRP affected the responses in a linear manner.

Table 4.12 Results for simulations involving changes in the specific heat of FRP.

Problem	c_{FRP} (J/kg·K)	T_{max} (°C)	Maximum Signal		Maximum Contrast	
			t_s (s)	ΔT_{max} (°C)	t_c (s)	$\Delta T_{max}/\Delta T_{backg}$
27	1,020	55.1	5.05	12.03	9.75	2.04
28	1,080	53.8	5.25	11.25	10.25	1.95
29	1,140	52.6	5.55	10.55	10.75	1.91
19	1,200	51.6	5.75	9.92	11.25	1.86

Figure 4.36 show the variation in the maximum surface temperature with increasing specific heat. The maximum surface temperature decreased with increasing specific heat. For this particular test object, the maximum surface temperature decreased at a rate of 0.019 K/(J/kg·K).

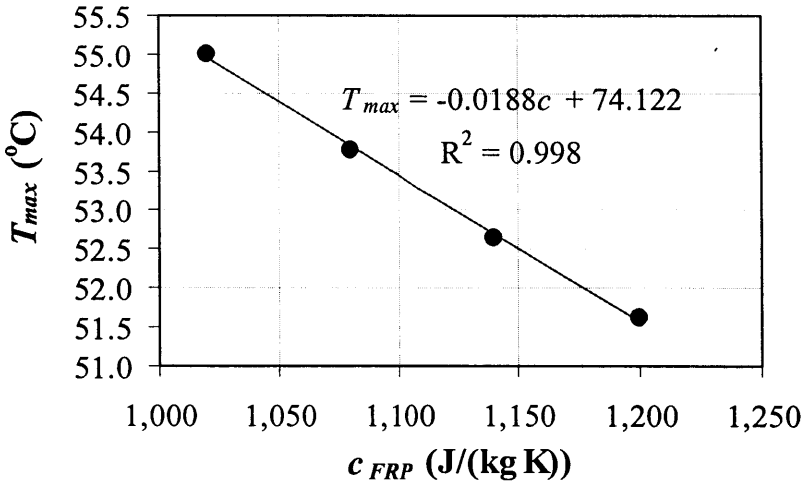

Fig. 4.36 Maximum surface temperature as a function of the specific heat of FRP

The behavior shown in Fig. 4.36 is not surprising. A material with higher specific heat requires a higher energy input to raise its temperature. Since the energy input was the same for all analyses, higher specific heat values of the FRP layers produced lower surface temperatures.

Figure 4.37 shows the evolution of the thermal signal for the different values of specific heat. Both the maximum signal and the time for maximum signal were affected linearly. Figure 4.38 shows that the maximum signal decreased linearly with increasing specific heat at a rate of 0.012 K/(J/kg·K).

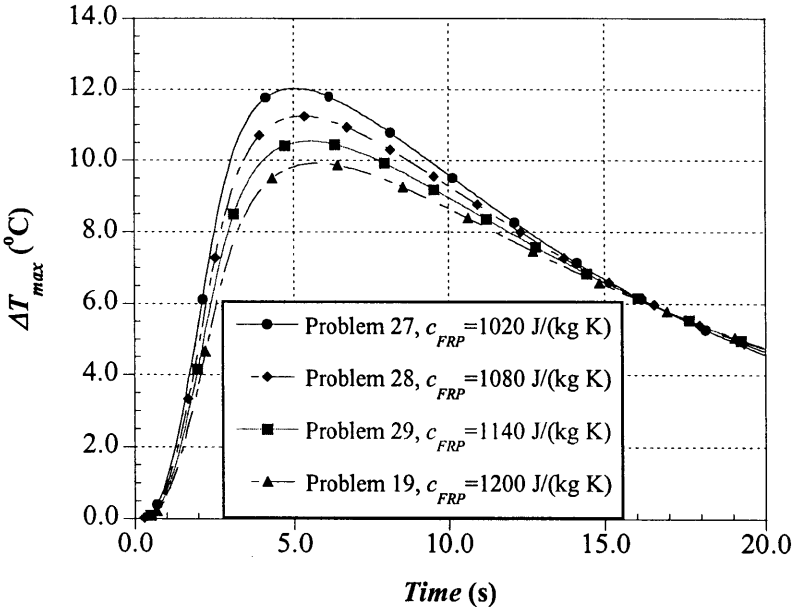

Fig. 4.37 Thermal signal for problems 19 and 27 through 29 (c_{FRP}=1020 J/kg·K through 1200 J/kg·K)

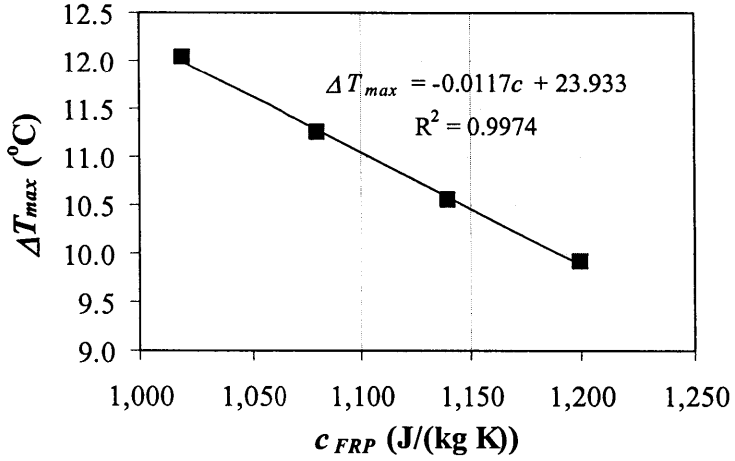

Fig. 4.38 Maximum thermal signal as a function of the specific heat of FRP.

A comparison of Figs. 4.31 and 4.38 shows that, on a relative basis, changes in the specific heat of the FRP affected the maximum thermal signal more than the changes in the thermal conductivity. For example, while a change of 125% in k_{FRP} produced only about a 4% change in the maximum signal, a change of 15% in the specific heat produced a change of 21%.

Figure 4.39 shows that the time for maximum signal increased linearly with increasing specific heat. The increase, however, was small; with a change in specific heat from 1,020 J/kg·K to 1,200 J/kg·K, the time of maximum signal increased only 0.7 s.

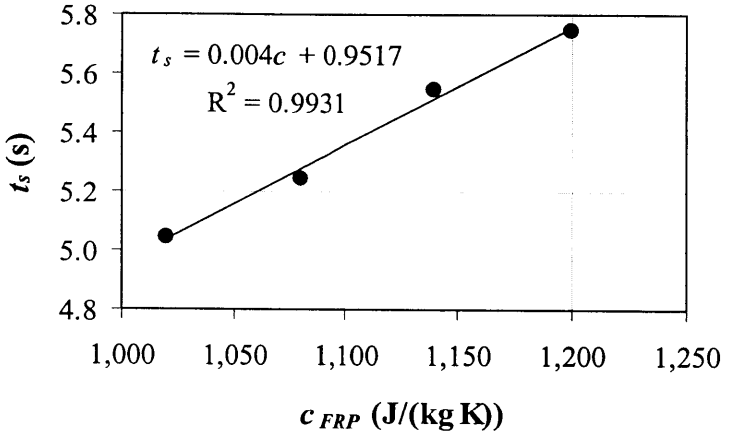

Fig. 4.39 Time for maximum signal as a function of the specific heat of CFRP.

An interesting observation was that the changes in the thermal signal were driven primarily by changes in the surface temperature above the flaw. Surface temperatures above the defect were affected by changes in the specific heat of the composite layers (Fig. 4.41), whereas in the background temperature was not affected by the specific heat of the FRP (Fig. 4.41).

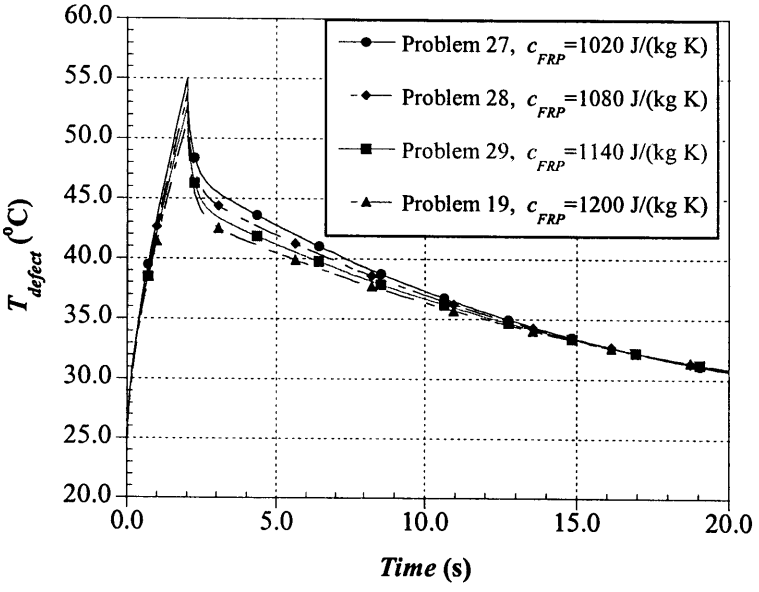

Fig. 4.40 Surface temperature above the defect

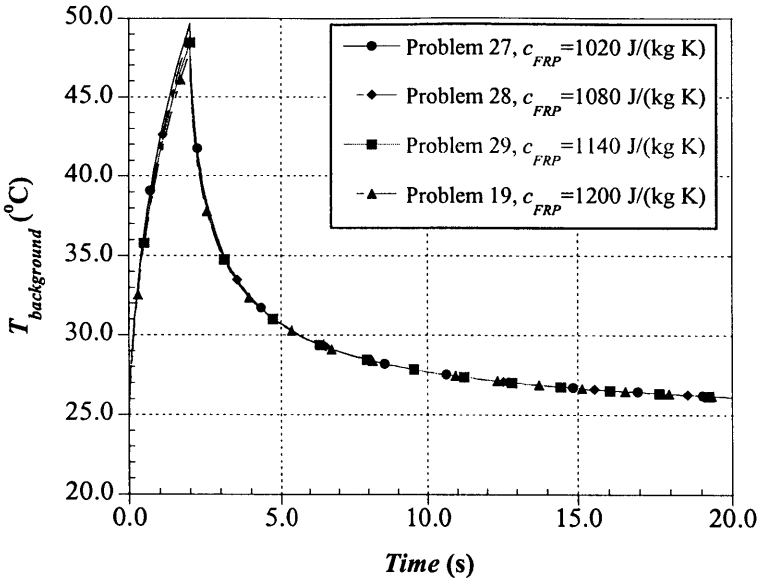

Fig. 4.41 Surface temperature in the background

Figure 4.42 shows the evolution of the thermal contrast for the different specific heats of the FRP. The thermal contrast was affected in a way similar to the thermal signal. Figure 4.43 shows that the maximum thermal contrast decreased linearly with increasing specific heat, and Fig. 4.44 shows that the time of the maximum thermal contrast increased linearly with specific heat. For the increase of specific heat from 1,020 J/kg·K to 1,200 J/kg·K, the time for maximum contrast increased by about 1.5 s.

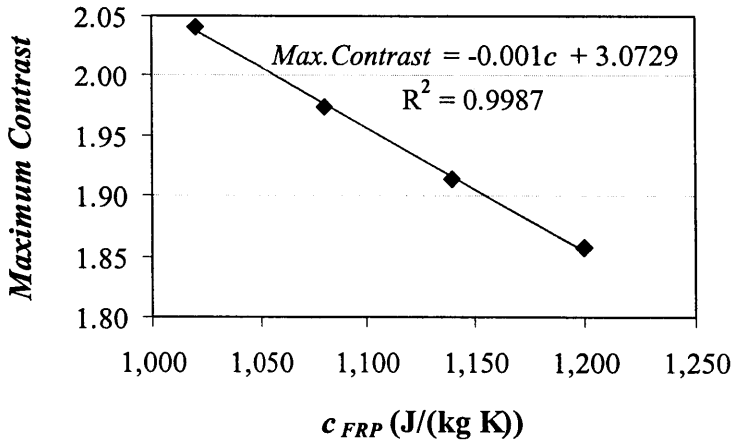

Fig. 4.43 Maximum thermal contrast as a function of the specific heat of FRP.

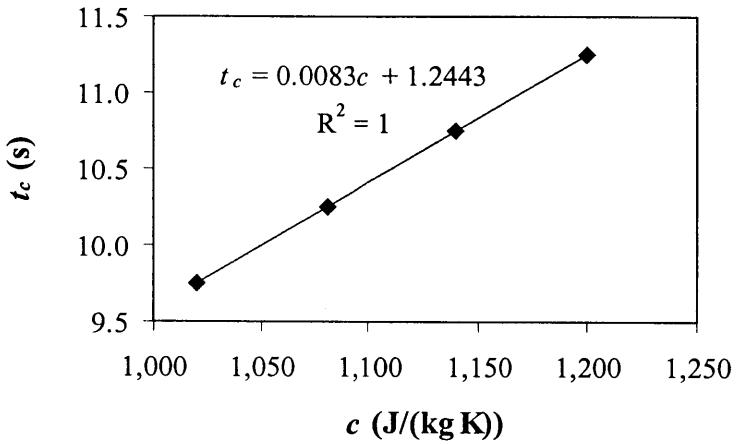

Fig. 4.44 Time for maximum thermal contrast as a function of the specific heat of CFRP

The increase in time required for maximum signal and maximum contrast is the effect of the decreased diffusivity with increasing specific heat. As a reminder, thermal diffusivity is inversely proportional to the specific heat. Thus, the higher the value of the specific heat of the material, the lower the diffusivity and the slower the thermal evolutions.

In summary, changing the specific heat of the FRP layers from 1,020 J/kg·K to 1,200 J/kg·K resulted in significant reductions in the maximum thermal signal and maximum contrast. The reduction, however, are not likely to have a significant impact on the ability to detect the presence of the debond.

4.4.4c Effects of the Thermal Conductivity of the Concrete

The next set of analyses (problems 19 and 30 through 32) involved changing the thermal conductivity of the concrete substrate. As shown in Table 4.9, the thermal conductivity was decreased by 5% and increased up to 20% from the value for the concrete in the "control" test object. Table 4.13 summarizes the results obtained in this set of simulations.

Table 4.13 Results for simulations involving changes in the thermal conductivity of concrete.

Problem	k_{conc} (W/m·K)	T_{max} (°C)	Maximum Signal		Maximum Contrast	
			t_s (s)	ΔT_{max} (°C)	t_c (s)	$\Delta T_{max}/\Delta T_{backg}$
30	1.4	51.6	5.75	9.82	11.25	1.80
19	1.5	51.6	5.75	9.92	11.25	1.86
31	1.6	51.6	5.75	10.12	11.25	1.96
32	1.8	51.6	5.75	10.29	11.25	2.07

The maximum surface temperature above the defect was not affected by the change in thermal conductivity of the substrate. This is because the flaw acts as an insulator, and only changes in

the material above the flaw and/or in the flaw itself would affect the surface temperature above the flaw.

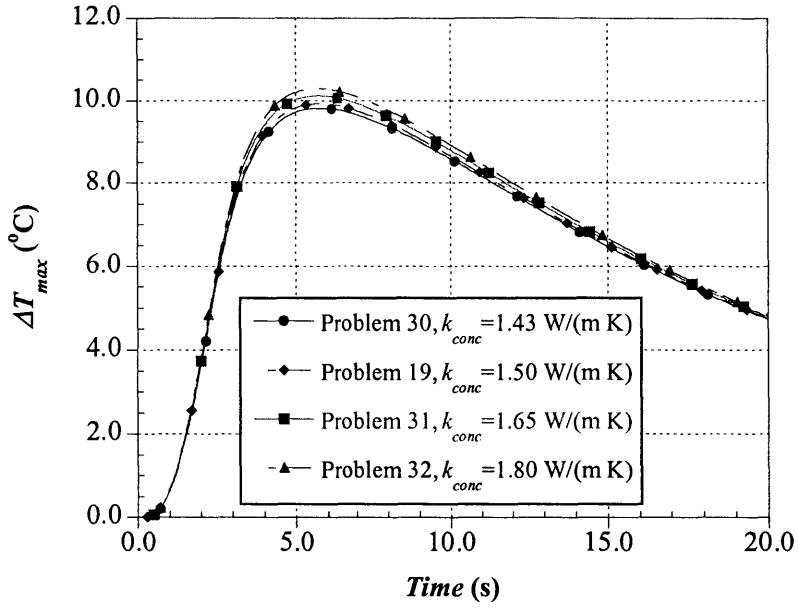

Fig. 4.45 Thermal signal for problems 19 and 30 through 32 (k=1.43 W/m·K through 1.8 W/m·K)

An increase in the thermal conductivity of the concrete, however, produced a decrease in the background surface temperature. Again, higher thermal conductivity means that there is less resistance to heat flow through the material. Thus, the thermal front travels faster and energy is transmitted to the interior of the object. As shown in Fig. 4.45 and Table 4.13, the decrease in the background surface temperature increases the maximum thermal signal.

The maximum thermal signal increased linearly with the thermal conductivity of the concrete according to the following equation

$$\Delta T_{max} = 1.27 k_{conc} + 8.02 \tag{4.25}$$

where, ΔT_{max} is the maximum thermal signal and k_{conc} is the thermal conductivity of the concrete substrate. Increases in the maximum thermal signal were on the order of 0.2 °C for a 10% increase in the thermal conductivity of the substrate. The time for maximum thermal signal, however, remained constant at 5.75 s.

As shown in Fig. 4.46 and Table 4.13, the thermal contrast also experienced an increase with increasing thermal conductivity of the substrate. The increase in maximum thermal contrast was also a linear function of the thermal conductivity as expressed by the equation

$$Max.contrast = 0.705 k_{conc} + 0.799 \tag{4.26}$$

The changes in the thermal contrast were minor. The maximum thermal contrast increased about 0.1 per 10% increase in thermal conductivity. The time for maximum contrast remained constant at $t = 11.2$ s.

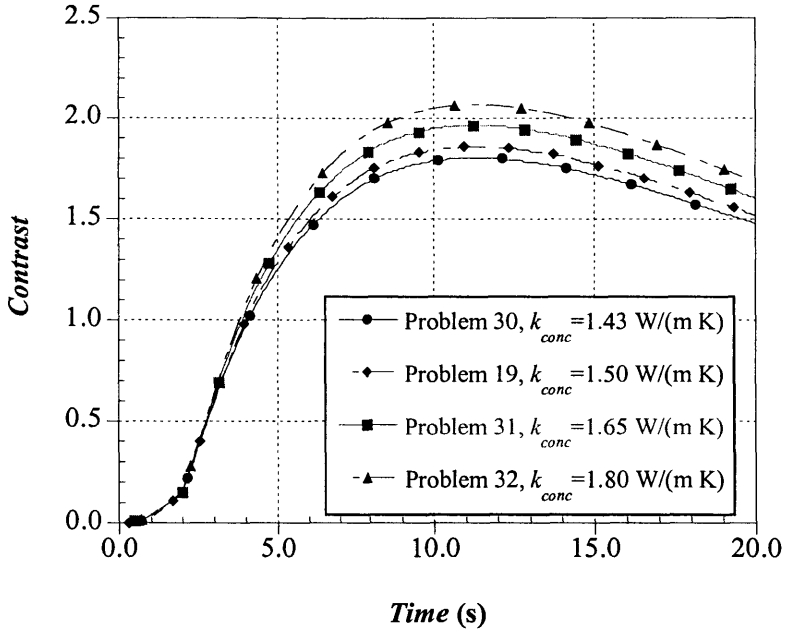

Fig. 4.46 Thermal contrast for problems 19 and 30 through 32 (k_{conc} = 1.43 W/m·K through 1.8 W/m·K)

4.4.4d Effects of the Specific Heat of Concrete

The next set of analyses involved the study of the effect of the specific heat of the concrete substrate on the thermal response of the test object. As shown in Table 4.14, the specific heat of the concrete was varied from 800 J/kg·K to 1,040 J/kg·K. The change in the specific heat did not affect the maximum surface temperatures reached by the test object. The maximum surface temperature was 51.6 °C.

Similarly to the case of changes in the thermal conductivity of concrete, the temperature above the defect were not affected by changes in the specific heat of the substrate. Background surface temperatures, however, decreased with increasing specific heat. Physically, the decrease of background temperature with increasing specific heat may be explained by the fact that materials with higher specific heat require a larger amount of thermal energy to raise their temperature by the same amount. Since the input energy was maintained constant in these simulations, lower temperatures were observed in the concrete and, hence, in the FRP.

Table 4.14 Results for simulations involving changes in the specific heat of concrete.

Problem	c_{conc} (W/m·K)	T_{max} (°C)	Maximum Signal		Maximum Contrast	
			t_s (s)	ΔT_{max} (°C)	t_c (s)	$\Delta T_{max}/\Delta T_{backg}$
19	800	51.6	5.75	9.92	11.25	1.86
33	880	51.6	5.75	10.12	11.25	1.96
34	960	51.6	5.75	10.30	11.25	2.07
35	1,040	51.6	5.65	10.46	11.25	2.17

The reduction in background surface temperature produced an increase in the thermal signal as a function of specific heat (Fig. 4.47). From the results shown in Table 4.14, it was found that the maximum thermal signal increased linearly with specific heat according to the equation:

$$\Delta T_{max} = 0.002c_{conc} + 8.15 \tag{4.27}$$

where, ΔT_{max} was the maximum signal and c_{conc} was the specific heat of the concrete substrate. The average increase in thermal signal was 0.2 °C per 10% increase in specific heat. For this particular set of simulations, the time for maximum signal remained constant at 5.75 s.

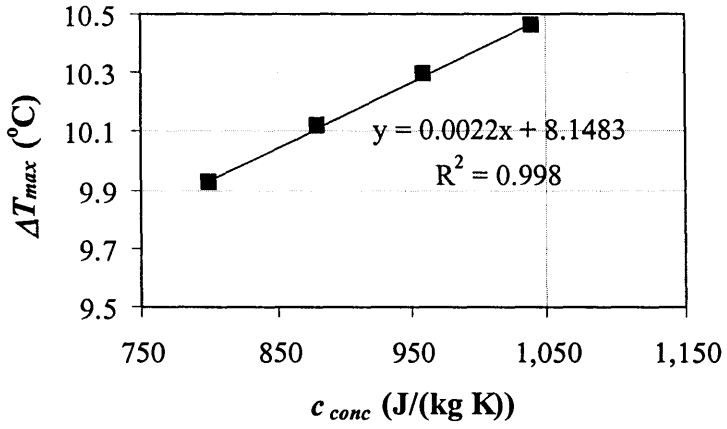

Fig. 4.47 Maximum signal as a function of the specific heat of concrete

As shown in Table 4.14, the thermal contrast increased linearly with increasing specific heat as well. The relationship was also found to be linear according to the following equation

$$Contrast = 0.0013c_{conc} + 0.834 \tag{4.28}$$

where, c_{conc} was the specific heat of concrete. The thermal contrast increased by 0.1 for a 10% increase in the specific heat of the concrete substrate.

4.4.4e Combined Effects of Changes in FRP and Concrete Properties

The final set of analysis of this parametric study involved different combinations of thermal conductivity and specific heat for FRP and concrete. These combinations are shown in Table 4.10 for simulations 36 to 43. The results, which are shown in Table 4.15, provide further insight into the thermal response of the test object due to variations in the thermal properties of the FRP and concrete.

Table 4.15 Results for problems 36 through 43 in which the thermal properties of FRP and concrete were varied

Combination	Problem	T_{max} (°C)	Signal		Contrast	
			ΔT_{max} (°C)	t_s (s)	$\Delta T_{max}/\Delta T_{backg}$	t_c (s)
low k_{FRP}-low k_{conc}	36	51.6	9.82	5.75	1.80	11.25
low k_{FRP}-high k_{conc}	37	51.6	10.29	5.75	2.06	11.25
high k_{FRP}-low k_{conc}	38	46.7	10.16	4.23	1.68	7.83
high k_{FRP}-high k_{conc}	39	46.7	10.68	4.24	1.92	7.84
low c_{FRP}-low c_{conc}	40	55.0	12.03	5.05	2.04	9.75
low c_{FRP}-high c_{conc}	41	55.0	12.64	4.95	2.37	9.75
high c_{FRP}-low c_{conc}	42	51.6	9.92	5.75	1.86	11.25
high c_{FRP}-high c_{conc}	43	51.6	10.46	5.75	2.16	11.25

The expected maximum signal and maximum contrast, due to the various combinations, were also estimated using the principle of superposition. This method resulted in estimations of the responses of test object that were within a 1% of the simulations. For example, problem 38 involved modifying the material properties in the two directions of the "control" test object (problem 19) by increasing k_{FRP} to 15.75 W/m·K and 1.8 W/m·K (problem 24) and reducing k_{conc} to 1.425 W/m·K (problem 30). The estimation was obtained using the signal results from problem 19 as a reference. The maximum signal difference ΔT_1 between the results of problem 24 and 19 was computed (see Table 4.11). The same procedure was applied to problems 30 and 10 (see Table 4.13) and ΔT_2 was obtained. The value of ΔT_1 was 0.36 °C and the value of ΔT_2 was 0.10 °C. Addition of these temperature differences to the maximum thermal signal 9.92 °C for problem 19 resulted in an estimation of the maximum thermal signal (Eq. 4.29) of 10.18 °C for problem 38.

$$\Delta T_{max}\big|_{new} = \Delta T_{max}\big|_{problem\ 19} + \Delta T_1 + \Delta T_2 \tag{4.29}$$

The maximum signal from the finite element simulation for problem 38 is 10.16 °C. Thus, for this particular example, the error between the estimation and the FEM output was only 0.02 °C. The maximum error occurred in the estimation of the ΔT_{max} of problem 39, in which the error

was 0.04 °C. The same procedure could be used in the estimation of the thermal contrast, with similar results.

The results shown in Table 4.15 indicate that the maximum surface temperature is affected mostly by the material properties of the FRP. Moreover, higher surface temperatures are obtained when the test object has low k_{FRP} and/or low c_{FRP}. Since one of the concerns in testing composites using IR thermography is to control T_{max}, more care would be needed when testing FRP composites with low thermal conductivity and low specific heat.

The results in Table 4.15 also indicate that the highest value of maximum thermal signal occurs with high k_{FRP} and high $k_{concrete}$ and the lowest value occurs with low k_{FRP} and low $k_{concrete}$. The maximum contrast is obtained, however, with low k_{FRP} and high $k_{concrete}$ and the lowest contrast occurs with high k_{FRP} and low $k_{concrete}$.

The effects of the specific heat differ from the effects of the thermal conductivity. The highest maximum thermal signal and highest thermal contrast are obtained with low c_{FRP} and high $c_{concrete}$, while the lowest maximum signal and lowest contrast are obtained with high c_{FRP} and low concrete.

The results also verified that the times for maximum signal and maximum contrast are affected only by the thermal conductivity and specific heat of the FRP, not by the thermal properties of the concrete.

4.4.5 Summary

Four different sets of analyses were performed to investigate the effect of material thermal properties in the thermal response of the flawed test object. The focus of the parametric study was two-fold:

- gain an understanding of thermal diffusion behavior of different values of thermal conductivity and specific heat,

- establish if accurate determination of the material thermal properties of the structural components is required for quantitative IR thermography testing of FRP laminates applied to concrete.

The test object presented a debond between the FRP composite and the concrete substrate. The thermal conductivity and specific heat of the composite and the concrete were varied to investigate the effect of these material properties on the thermal response. The models were subject to a square-wave thermal pulse of 2 s duration. The conclusions for this parametric study are as follows:

- The maximum surface temperature decreases nonlinearly with increasing k_{FRP}, and linearly with increasing c_{FRP}. The thermal properties of the concrete substrate do not affect the maximum surface temperature above the flaw.

- The maximum thermal signal varies nonlinearly (4^{th} order polynomial) with increasing thermal conductivity of the FRP. The maximum signal reaches a peak value and decreases with further increase in k_{FRP}.

- The maximum thermal signal decreases linearly with increasing c_{FRP}.

- The maximum thermal signal increases linearly with increasing $k_{concrete}$ and/or $c_{concrete}$.

- The maximum thermal contrast decays linearly with increasing k_{FRP} and/or c_{FRP}.

- The maximum thermal contrast increases linearly with increasing $k_{concrete}$ and/or $c_{concrete}$.

- The time for maximum thermal signal is only affected by the thermal properties of the FRP layers. The time for maximum thermal signal decreases nonlinearly with increasing thermal conductivity of the FRP. The time for maximum thermal signal increases with increasing c_{FRP}.

- The time for maximum thermal contrast is only affected by the thermal properties of the FRP composite. The time for maximum thermal contrast decays nonlinearly (power function) with increasing k_{FRP} and increases linearly with increasing c_{FRP}.

- Test objects with high k_{FRP}, high $k_{concrete}$, high c_{FRP}, and high $c_{concrete}$ result in the highest thermal signal and thermal contrast while minimizing the maximum surface temperature.

- The greatest change in maximum thermal signal was observed with changing specific heat of the FRP. This change was on the order of 2 °C. Most of the variations in maximum thermal signal due to changes in k_{FRP}, $k_{concrete}$, and $c_{concrete}$ were smaller than 0.6 °C.

In summary, while variations in the thermal properties of the FRP and concrete resulted in systematic variations in thermal response, none of the test parameters (maximum surface temperature, thermal signal, and contrast) were very sensitive to these variations. Thus, it would appear that the success of infrared thermography testing will not depend strongly on the specific values of the thermal properties of the FRP or concrete substrate.

The next series of studies will examine the effects of the depth of the flaw.

4.5 Parametric Study No.3: Effect of the Depth of the Flaw

In the use of FRP layers to strengthen concrete or masonry structures, defects may arise between the FRP layers (delaminations) or at the FRP/concrete interface (debonds). In addition, failure planes may occur in the concrete if the shear stresses needed to transfer load to the FRP, exceed the capacity of the concrete (spalls). Thus, it is desirable to investigate how the location of a flaw affects the thermal response and to establish whether it may be feasible to determine the depth of the flaw from the characteristics of the thermal evolution. The third parametric study had the following objectives:

- understand the effects of debonds on the thermal response,
- understand the effects of delaminations on the thermal response,
- understand the effects of concrete spalls on the thermal response,
- investigate the feasibility of estimating flaw depth from the measured thermal response.

Seven different sets of analyses were performed which included 21 finite element models.

4.5.1 Geometry of Model

The basic geometry of the test object corresponded to that of parametric studies No.1 and No.2, that is, a 100 mm long by 20 mm thick concrete slab covered with carbon FRP. Each ply of CFRP was 0.5 mm thick. The test object contained an internal flaw 25 mm long and 0.1 mm thick. The thermal contact resistance corresponded to 4.17×10^{-3} m^2/W. Plane two-dimensional modeling was used; thus, the test object is infinite in the z-direction. The internal flaw was located at the center of the model. The simulation was simplified using plane symmetry about the center of the specimen.

The test object was meshed using 2-D quadrilateral thermal solid elements containing 4 nodes. The model was meshed using mapped meshing with global element size of 0.5 mm. Similarly to the previous parametric studies, mesh refinement was applied in the thickness direction. The mesh refinement consisted of thin elements at the FRP layers, the defect, and at the concrete interface with the FRP. The element size was increased towards the bottom of the slab away from the heated surface. Thus, the meshing criterion used in the current parametric study was the same as in parametric study No.2.

For flaws located near the surface, the mesh configuration used in the previous parametric study showed some thermal gradient irregularities at the elements surrounding the tip of the flaw. To justify the use of the chosen mesh, a sensitivity analysis was performed to determine the accuracy of the results. The global element size was decreased to 0.25 mm, and this reduced the heat flux irregularities. The computational time, however, increased drastically and the differences in surface temperature changed only by 0.02 °C. The small difference in temperature results justified the use of the larger mesh configuration, regardless of the irregularities at the discontinuity.

The internal flaw (air void) was located at different depths and interfaces within the test object. The first set of simulations involved the investigation of debonds at the FRP/concrete interface. For this first set of problems, the number of FRP plies was increased from 1 ply to 7 plies as indicated in Table 4.16.

Table 4.16 Geometry for problem set involving debonds

Problem	Number of plies	Depth of debond
44	1	0.5 mm
45	2	1.0 mm
46	3	1.5 mm
47	5	2.5 mm
48	6	3.0 mm
49	7	3.5 mm

The second set of simulations involved delaminations between FRP layers. All the models in this set contained 5 layers of FRP. The depth of the internal flaw varied from 0.5 mm (delamination at top interface) to 2.5 mm (debond between FRP and concrete). Table 4.17 summarizes the geometrical characteristics.

Table 4.17 Geometry for problem set involving delaminations

Problem	Number of plies	Location of flaw	Depth of delamination
47	5	Between 5^{th} and concrete	2.5 mm
50	5	Between 4^{th} and 5^{th} layer	2.0 mm
51	5	Between 3^{rd} and 4^{th} layer	1.5 mm
52	5	Between 2^{nd} and 3^{rd} layer	1.0 mm
53	5	Between 1^{st} and 2^{nd} layer	0.5 mm

The third and fourth sets of simulations involved flaws or spalls in the concrete substrate. The third set of simulations examined on the effect of the number of FRP plies on the thermal response. As shown in Fig. 4.48, the concrete spall was located 2 mm below the FRP/concrete interface and the number of FRP plies was varied from 1 to 5 layers. The fourth set of problems focused on the effect of concrete cover. For this set of simulations, the number of FRP plies was kept constant at 2 plies. As shown in Fig. 4.49, the depth of the flaw was increased from 0.0 mm (debond) to 2.0 mm from the FRP/concrete interface.

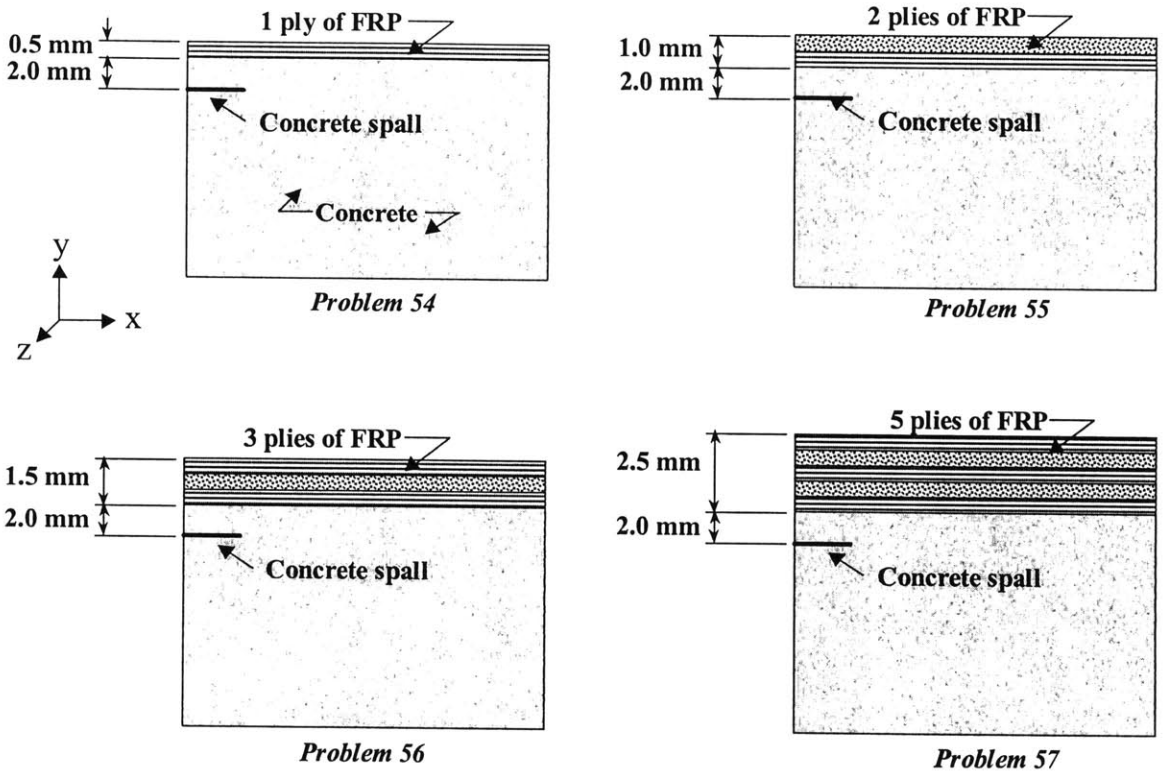

Fig. 4.48 Geometry of models for third set of problems involving flaw in concrete with different numbers of FRP layers

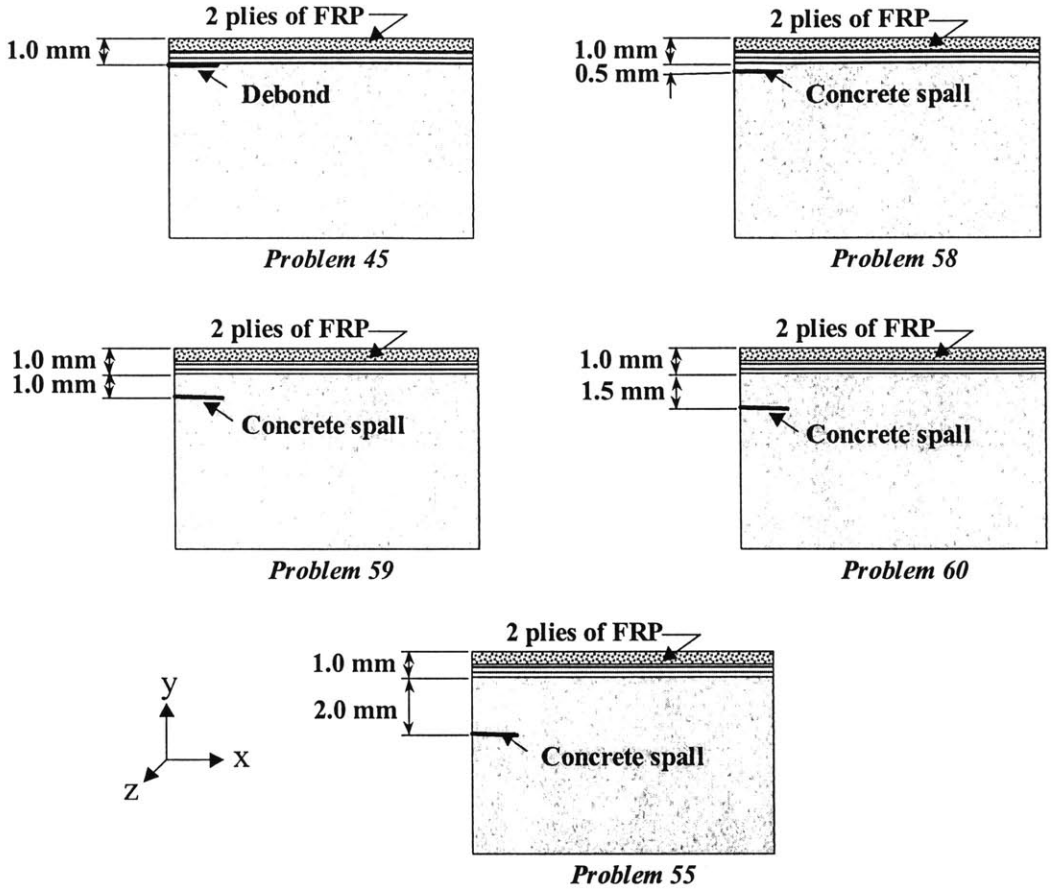

Fig. 4.49 Geometry of models for fourth set of problems involving varying flaw depths in concrete with 2 layers of FRP

The next three sets of simulations focused on the response due to flaws at any depth in three different FRP/concrete structures. As shown in Tables 4.18, 4.19, and 4.20, each set of simulations contained 5, 3, or 2 FRP plies. For each set, the depth of the flaw was varied to simulate delaminations, debonds, and concrete spalls. The purpose of these simulations was to examine whether there was a simple relationship for the thermal response due to any kind of flaw for a given test object

Table 4.18 Geometry for problems involving 5 layers of FRP

Problem	Number of plies	Type of flaw & location	Depth of flaw
53	5	Delamination between 1st and 2nd ply	0.5 mm
52	5	Delamination between 2nd and 3rd ply	1.0 mm
51	5	Delamination between 3rd and 4th ply	1.5 mm
50	5	Delamination between 4th and 5th ply	2.0 mm
47	5	Debond at interface	2.5 mm
57	5	Concrete spall 2 mm below interface	4.5 mm

Table 4.19 Geometry for problems involving 3 layers of FRP

Problem	Number of plies	Type of flaw & location	Depth of flaw
62	3	Delamination between 1st and 2nd ply	0.5 mm
63	3	Delamination between 2nd and 3rd ply	1.0 mm
46	3	Debond at interface	1.5 mm
64	3	Concrete spall at 1 mm below interface	2.5 mm
65	3	Concrete spall at 2 mm below interface	3.5 mm

Table 4.20 Geometry for problems involving 2 layers of FRP

Problem	Number of plies	Type of flaw & location	Depth of flaw
61	2	Delamination between 1st and 2nd ply	0.5 mm
45	2	Debond at interface	1.0 mm
58	2	Concrete spall at 0.5 mm below interface	1.5 mm
59	2	Concrete spall at 1.0 mm below interface	2.0 mm
60	2	Concrete spall at 1.5 mm below interface	2.5 mm
55	2	Concrete spall at 2.0 mm below interface	3.0 mm

4.5.2 Material Properties

The material properties of the model were those of carbon FRP (CFRP) for the bonded composite, concrete for the substrate, and air for the defect (see Table 4.2). The CFRP layer in direct contact with the concrete had the fibers running in the x-direction. The direction of the fiber alternated between z- and x-direction for additional layers of FRP.

4.5.3 Thermal Loading and Boundary Conditions

Again, the analysis was defined as a transient heat transfer problem. A square pulse of intensity 20,000 W/m^2 and duration 2 seconds was applied at the top surface of the model. Adiabatic conditions ($dT/dx = 0$ and $dT/dy = 0$) were assumed for the remaining surfaces. The initial temperature of the test object was 23 °C.

The same time stepping was prescribed for all the problems of this parametric study. The initial time step was 0.009 s. The analysis was performed using Ansys automatic stepping with the maximum and minimum time steps set to 0.1 s and 0.008 s, respectively. The simulation output was recorded at every time step.

4.5.4 Results

4.5.4a Debonds

The first set of simulations involved the study of debonds at the FRP/concrete interface. The number of plies was increased from 1 ply to 7 plies. Each ply of FRP had a thickness of 0.5 mm. Table 4.21 summarizes the results for this set of simulations.

Table 4.21 Results for simulations involving debonds (first set of problems in parametric #3)

Problem	Depth, d (mm)	T_{max} (°C)	Maximum Signal		Maximum Contrast	
			t_s (s)	ΔT_{max} (°C)	t_c (s)	$\Delta T_{max}/\Delta T_{backg}$
44	0.5	64.6	2.44	20.85	3.94	2.02
45	1.0	51.7	4.45	8.16	8.05	1.23
46	1.5	49.1	7.35	4.41	12.05	0.84
47	2.5	48.6	14.65	1.86	22.55	0.48
48	3.0	48.6	19.55	1.36	29.53	0.40
49	3.5	48.6	23.93	0.97	35.55	0.32

The data from Table 4.21 reveals some interesting details regarding the effect of debond depth on the thermal response. For example, as shown in Fig. 4.50, the maximum surface temperature decreases nonlinearly with flaw depth. For a depth of 2.5 mm or more, the maximum surface temperature is not affected by the depth of the debond.

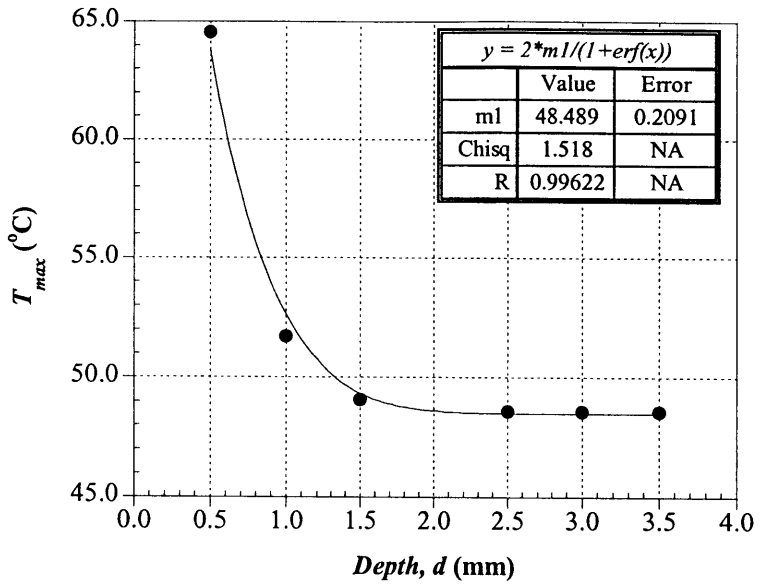

Fig. 4.50 Effect of debond depth on the maximum surface temperature

The maximum surface temperature can be estimated using Eq. 4.30

$$T_{max} = \frac{2T_{\infty}}{1 + erf(d)} \tag{4.30}$$

where, *erf(d)* is the error function for the depth of the flaw and T_{∞} is the asymptotic temperature reached when the flaw is deep in the material. As a reminder, the error function for the depth of the flaw is

$$erf(d) = \frac{2}{\pi}\int_{0}^{d} e^{-t^2} dt \tag{4.31}$$

The best fit value of T_{∞} is found to be close to the theoretical surface temperature for a semi-infinite solid heated with a heat flux impulse (Carslaw et al., 1959)

$$T_{\infty} = \frac{2q}{k}\sqrt{\frac{\alpha\tau}{\pi}} + T_o \tag{4.32}$$

where, q is the magnitude of the input heat flux, k is the thermal conductivity of FRP, α is the thermal diffusivity of FRP, τ is the pulse duration, and T_o is the initial temperature of the test object, 23 °C.

The results for the maximum thermal signal ΔT_{max} also showed a nonlinear relationship with flaw depth. Figure 4.51 illustrates the signal versus time behavior for the first set of problems. It is seen that debonds located near the surface result in maximum thermal signal (ΔT_{max}) and short time for maximum signal (t_s), while deep debonds result in low ΔT_{max} and long t_s.

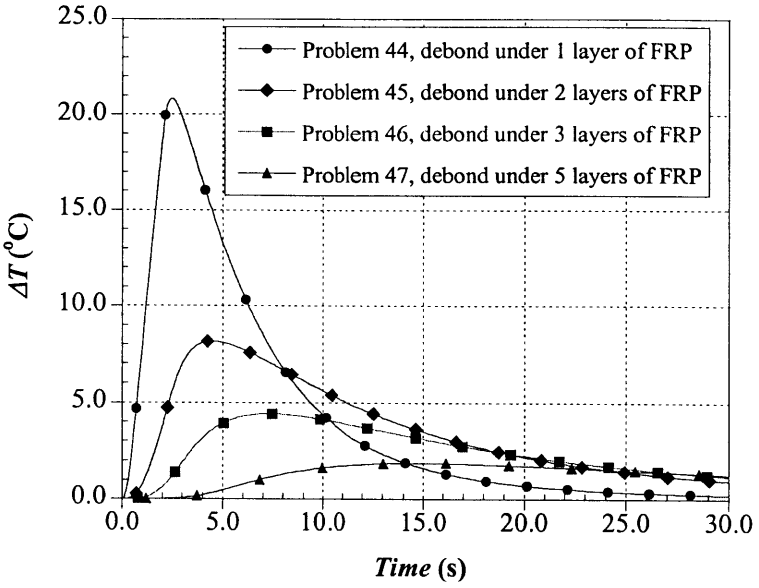

Fig. 4.51 Thermal signal as a function of debond depth

The variation of the maximum thermal signal with debond depth could be represented by the following power function:

$$\Delta T_{max} = 7.64\, d^{-1.57} \tag{4.33}$$

Figure 4.52 illustrates the FEM output and curve fit for the maximum signal. Figure 4.52 shows that the maximum thermal signal drops off quickly with increasing depth. It may be difficult to discern the presence of debonds with more than 3 mm of FRP.

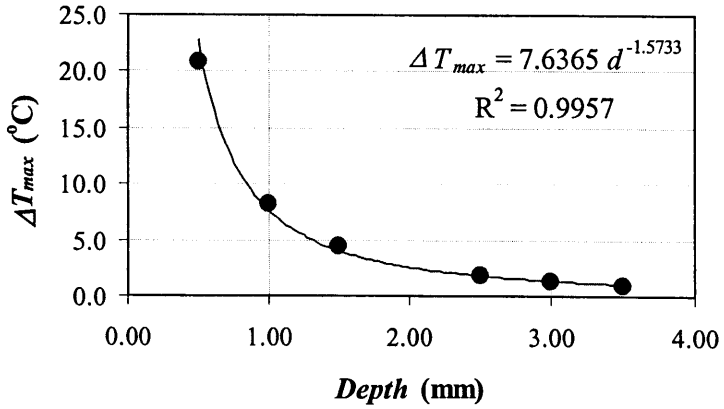

Fig. 4.52 Maximum thermal signal as a function of debond depth

As shown in Fig. 4.53, the time for maximum signal increased with increasing depth of the debond and the variation could be approximated by the following quadratic function

$$t_s = 1.08d^2 + 2.97d + 0.54 \tag{4.34}$$

This strong dependence between t_s and the depth of the debond indicates that the time for maximum signal may be a good indicator of relative flaw depth.

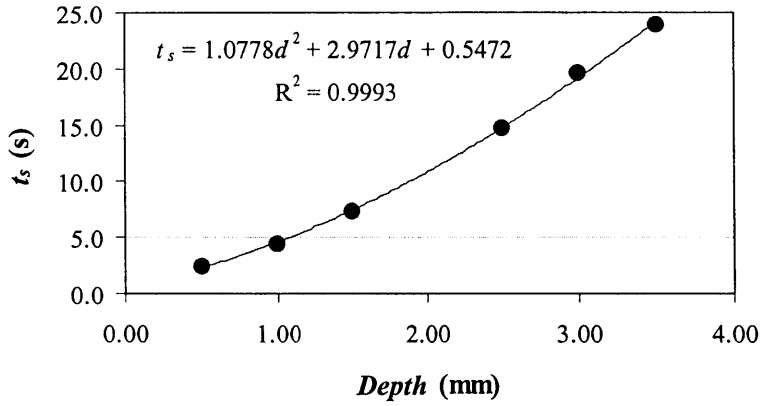

Fig. 4.53 Time for maximum signal as a function of debond depth

The maximum contrast also decreased nonlinearly with of the depth of the debond. Again, the simulation output could be fitted by a power function, as follows:

$$Max\,contrast = 1.14d^{-0.95} \tag{4.35}$$

while the time for maximum contrast could be fitted with a quadratic equation, as follows:

$$t_c = 1.18d^2 + 5.89d + 0.76 \tag{4.36}$$

The time for maximum contrast was also strongly dependent on debond depth and varied from 3.94 s for the test object with only one layer of FRP to 35.55 s for the test object with 7 layers of fiber composite.

4.5.4b Delaminations

The next set of problems focused on the effect of the depth of delaminations. All the simulations involved a test object containing 5 plies of FRP. The depth of the delamination was varied from 0.5 mm to 2.5 mm. Table 4.22 summarizes the results for this set of simulations.

Table 4.22 Results for simulations involving debonds (second set of problems in parametric #3)

Problem	Depth, d (mm)	T_{max} (°C)	Maximum Signal		Maximum Contrast	
			t_s (s)	ΔT_{max} (°C)	t_c (s)	$\Delta T_{max}/\Delta T_{backg}$
47	2.5	48.6	14.65	1.86	22.55	0.48
50	2.0	48.6	11.55	2.60	18.85	0.59
51	1.5	49.1	7.90	3.86	13.75	0.70
52	1.0	51.8	4.64	6.95	9.24	0.91
53	0.5	64.9	2.53	18.35	3.93	1.41

The thermal response was similar to that produced by debonds. For example, the maximum temperature response followed the same function as described for debonds. Thus, the maximum temperature can be estimated using Eqns. 4.30, 4.31, and 4.32. The maximum thermal signal as a function of depth was characterized using the following power function

$$\Delta T_{max} = 6.89 d^{-1.42} \tag{4.37}$$

Figure 4.54 illustrates the FEM results and curve fit for the maximum signal resulting from delaminations at various depths.

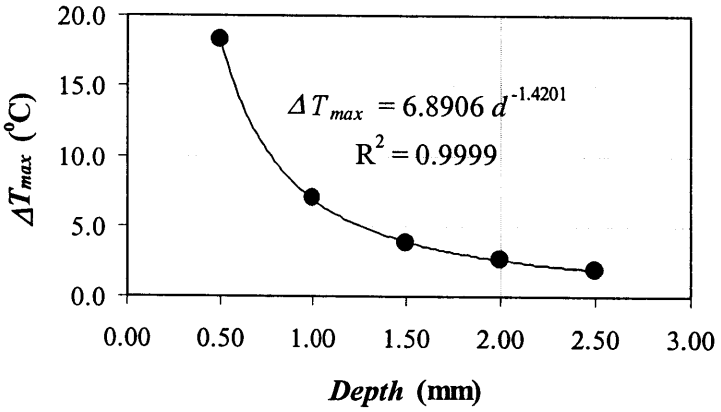

Fig. 4.54 Maximum thermal signal as a function of delamination depth

As shown in Fig. 4.55, the time for maximum signal was slightly longer for delaminations than for debonds located at the same depth. The difference, however, was only on the order of 0.5 s. The time for maximum signal increased quadratically following the next equation:

$$t_s = 0.69 d^2 + 4.19 d + 0.10 \tag{4.38}$$

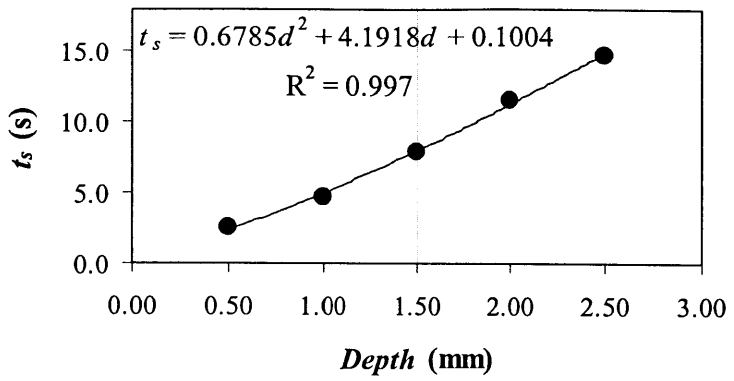

Fig. 4.55 Time for maximum signal as a function of delamination depth

The difference in contrast varied from 1.41 to 0.48 for delaminations buried between 0.5 and 2.5 mm, respectively. The maximum thermal contrast also changed as a power function. The best fitting function was

$$Max\,Contrast = 0.92d^{-0.56} \tag{4.39}$$

Both the maximum signal and maximum contrast values were lower than those values found for debonds at the same depth. The behavior can be explained by the fact that the background temperatures are higher for the delamination problems than for debonds. As a reminder, the thermal conductivity and diffusivity of concrete are higher than those of FRP. As a result, the background temperature of the simulations with debonds decreases at a higher rate than the background temperature of a delaminated test object.

The times for maximum signal and maximum contrast were longer for delaminations than for debonds located at the same depth. Some of these differences were on the order of 1 s to 1.5 s. An interesting observation was that the time for maximum contrast, although it is a quadratic function of depth, could be approximated as a linear function of depth without introducing a significant error; the linear function is as follows

$$t_c = 9.37d - 0.39 \tag{4.40}$$

Figure 4.56 shows the FEM output and fitting function for the time for maximum contrast due to variations in delamination depth.

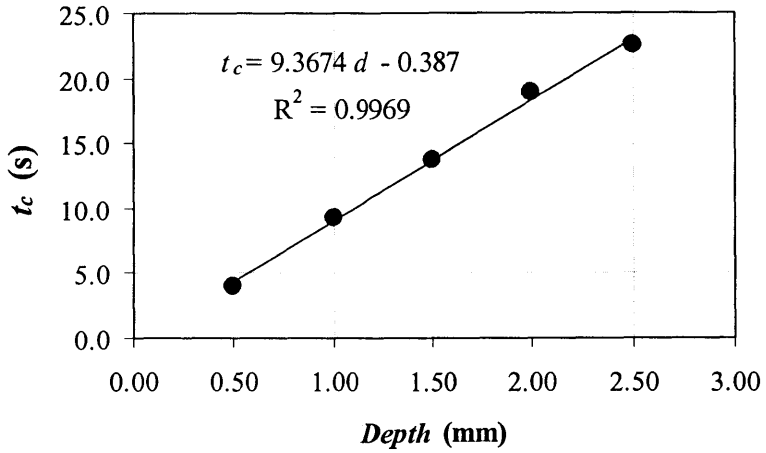

Fig. 4.56 Time for maximum contrast as a function of delamination depth

4.5.4c Concrete Spalls

The next set of simulations involved the study of concrete spalls. The study was divided into two different sets of models. First, the investigation focused on the case where the spall is located at 2 mm from the concrete/FRP interface, and the number of plies of FRP was increased from 1 ply to 5 plies. For the second set of problems, there were two plies FRP and the depth of the flaw in the concrete was varied. To ease the explanation of results the set of simulations are called "set No.3" and "set No.4", respectively.

Tables 4.23 and 4.24 summarize the results for these two sets of simulations.

Table 4.23 Results for simulations involving concrete spalls (third set of problems in parametric #3)

Problem	**Depth, d (mm)**	T_{max} (°C)	**Maximum Signal**		**Maximum Contrast**	
			t_s (s)	ΔT_{max} (°C)	t_c (s)	$\Delta T_{max}/\Delta T_{backg}$
54	2.5	46.2	11.76	2.22	19.06	0.62
55	3.0	48.0	15.90	1.66	24.95	0.53
56	3.5	48.5	19.85	1.22	29.55	0.42
57	4.5	48.6	30.50	0.72	43.15	0.29

Table 4.24 Results for simulations involving concrete spalls (forth set of problems in parametric #3)

Problem	Depth, d (mm)	T_{max} (°C)	Maximum Signal		Maximum Contrast	
			t_s (s)	ΔT_{max} (°C)	t_c (s)	$\Delta T_{max}/\Delta T_{backg}$
45	1.0	51.7	4.45	8.16	8.05	1.23
58	1.5	48.8	7.05	4.56	12.05	0.91
59	2.0	48.2	9.52	3.06	16.05	0.74
60	2.5	48.1	12.65	2.20	20.35	0.62
55	3.0	48.0	15.90	1.66	24.95	0.53

The first observation indicated that the maximum surface temperature increases with increasing depth of the flaw for set No.3 while it decreases for set No.4. For both cases, the behavior is easily explained as a function of the thermal properties of the materials. For the previous sets of simulations (debonds and delaminations), the maximum temperature was highly related to the location of the flaw. For the cases involving concrete spalls, however, the location of the defect has a lesser effect on the maximum temperatures observed in the FRP. The reason is that the flaw is buried too deep in the test object to affect the thermal response at early times during the test. The thickness of the FRP and concrete cover has an important role on the development of maximum surface temperature. For example, the maximum surface temperature for set No.3 increases as the thickness of FRP increases. The reason for the behavior is that FRP has lower k and α than concrete, thus there is a lower rate of diffusion. With increasing number of plies, the heat tends to concentrate at the upper layers of the FRP instead of being diffused through the concrete. The opposite is true for set No.4. As concrete cover over spall increases, the thermal energy diffuses through the test object more readily and the maximum surface temperature decreases with flaw depth.

The determination of the theoretical surface temperatures for concrete spalls is more complex than for debonds or delaminations. The reason for the complexity is the introduction of composite (FRP/concrete) layers. One-dimensional solutions for this problem were developed by previous researchers (Balagueas et al., 1986) and could be used to estimate the maximum surface temperature reached by the 2-D test object. The solution for a two-layered composite material with perfect contact between the two layers can be expressed as

$$T(t) = \frac{1}{\rho_1 c_1 L_1 + \rho_2 c_2 L_2}\left[1 + \frac{2(x_1\omega_1 + x_2\omega_2)}{(x_1 + x_2)}\right]$$

$$\sum_{k=1}^{\infty} \frac{\sum_{i=1}^{2} x_i \cos(\omega_i\gamma_k) + (-1)^i \mathrm{R}\gamma_k \sin(\omega_i\gamma_k)}{\sum_{i=1}^{2} x_i\omega_i \cos(\omega_i\gamma_k) - (-1)^i \mathrm{R}\cos(\omega_i\gamma_k) + (-1)^i \mathrm{R}\gamma_k\omega_i \sin(\omega_i\gamma_k)} f(\gamma_k, Fo_2, Fo_{2,\tau}) \tag{4.41}$$

where,

$$f(\gamma_k, Fo_2, Fo_{2,\tau}) = \frac{1}{\gamma_k^2(\tau/n_2^2)}\left[exp\left(\gamma_k^2 \frac{\tau}{n_2^2}\right) - 1\right] exp\left(-\gamma_k^2 \frac{t}{n_2^2}\right) \tag{4.42}$$

$$x_i = e_{12} - (-1)^i, \quad i = 1,2 \tag{4.43}$$

$$\omega_i = n_{12} - (-1)^i, \quad i = 1,2 \tag{4.44}$$

$$R = \frac{e_1}{hn_2} = \frac{e_1 R}{n_2} \tag{4.45}$$

with,

$$e_i = \sqrt{k_i \rho_i c_i}, \quad i = 1,2 \tag{4.46}$$

$$e_{12} = e_1/e_2 \tag{4.47}$$

and,

$$n_i = L_i/\sqrt{\alpha_i}, \quad i = 1,2 \tag{4.48}$$

$$n_{12} = n_1/n_2 \tag{4.49}$$

where, k is the thermal conductivity, α is the thermal diffusivity, L is the thickness of the material, R is the thermal resistance ($R=k/L$), and γ_k is the kth positive root of

$$\sum_{i=1}^{2} x_i \sin(\omega_i \gamma) - (-1)^i R\gamma \cos(\omega_i \gamma) = 0 \tag{4.50}$$

The maximum surface temperatures only varied by 2.4 °C for problem set No.3 and 3.7 °C for problem set No.4. Simple equations for estimation of maximum surface temperatures could be attained using again the error function used in the previous sets of analyses. For the cases of concrete spalls, however, the use of equivalent depths and material properties must be used in order to simplify the process. For problem set No.3 the material properties of FRP dominated the thermal response of the test object. In this case, however, the use of an equivalent depth was required to generate the estimation equation

$$T_{max} = T_\infty \, erf(d_{equiv}) \tag{4.51}$$

where, $erf(d_{equiv})$ is the error function of the equivalent depth of the flaw and T_∞ is the asymptotic temperature reached when the flaw is deep in the material (Eq. 4.32). For this particular test object, the equivalent depth (in mm) is

$$d_{equiv} = d - 1.1 \tag{4.52}$$

The determination of d_{equiv} was done empirically.

Figure 4.57 shows the finite element output and the estimation curve expressed in Eq 4.51 for the first set of concrete spall problems.

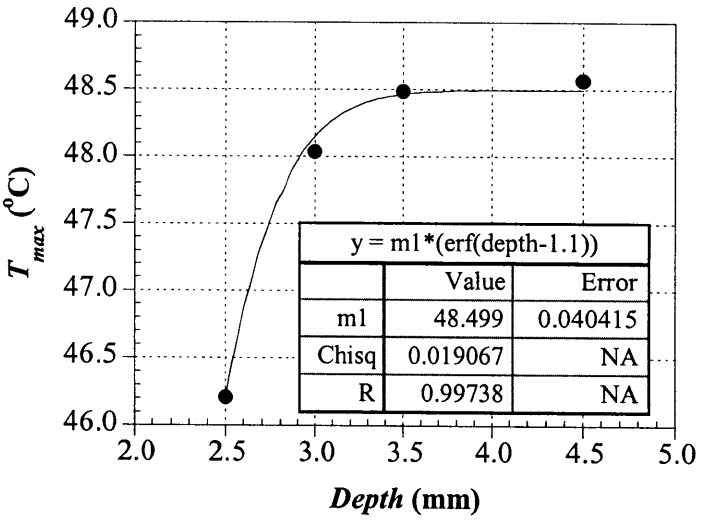

Fig. 4.57 Maximum surface temperature as a function of depth for first set of concrete spall problems (variable number of plies)

For problem set No.4 the material properties of both concrete and FRP affected the thermal response of the test object. The maximum surface temperature was estimated using Eq. 4.30. The asymptotic temperature, however, was a function of equivalent material properties.

$$T_{\infty} = \frac{2q}{k_{equiv}} \sqrt{\frac{\alpha_{equiv}\,\tau}{\pi}} + T_o \tag{4.53}$$

where,

$$k_{equiv} = 0.75\,k_{FRP} + 0.25\,k_{concrete} \tag{4.54}$$

$$\alpha_{equiv} = 0.75\,\alpha_{FRP} + 0.25\,\alpha_{concrete} \tag{4.55}$$

Figure 4.58 illustrates the finite element output and the estimation curve expressed in Eqs. 4.30 and 4.52 for the second set of concrete spall problems (problem set No.4).

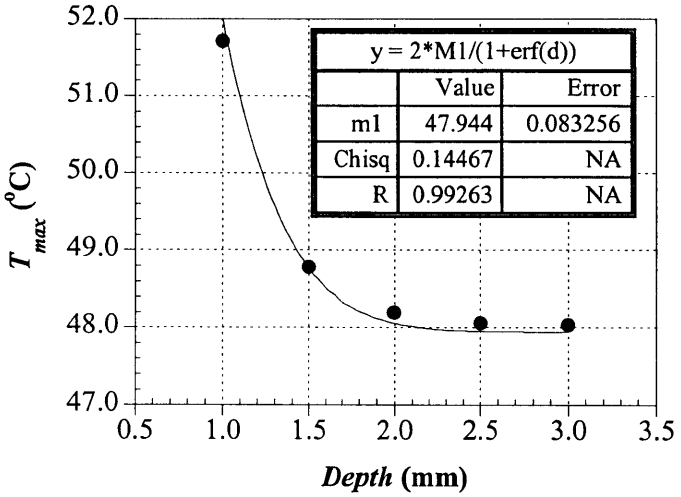

Fig. 4.58 Maximum surface temperature as a function of depth for second set of concrete spall problems

The results for the maximum signal and maximum contrast displayed nonlinear behavior similar to that for debonds and delaminations. The change in magnitude, however, was smaller than the previous type of flaws. For example, the change in maximum thermal signal for set No.3 was only 1.5 °C for an increase in depth of 2 mm. The change in maximum contrast was 0.33 for this case. The change in maximum signal and maximum contrast was slightly higher for the second set of concrete spalls problems. For this case, the decrease in maximum thermal signal and contrast was 6.5 °C and 0.70, respectively, for an increase in depth of 2 mm.

The decrease of the maximum thermal signal and contrast could be described by power functions. For the first set of concrete spalls (problem case No.3) the thermal signal and thermal contrast decreased as

$$\Delta T_{max} = 12.51\, d^{-1.86} \tag{4.56}$$

$$Max.\,Contrast = 1.95\, d^{-1.24} \tag{4.57}$$

Figures 4.59 and 4.60 show the maximum signal and maximum contrast, respectively, as a function of the flaw depth.

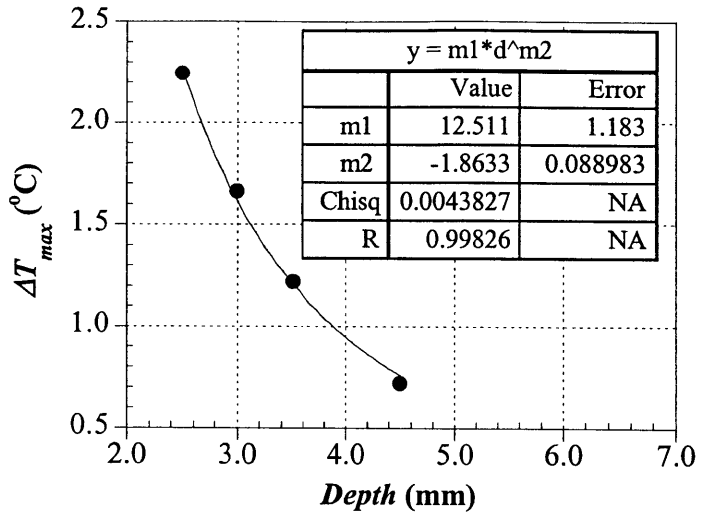

Fig. 4.59 Maximum signal as a function of flaw depth for first set of concrete spall problems

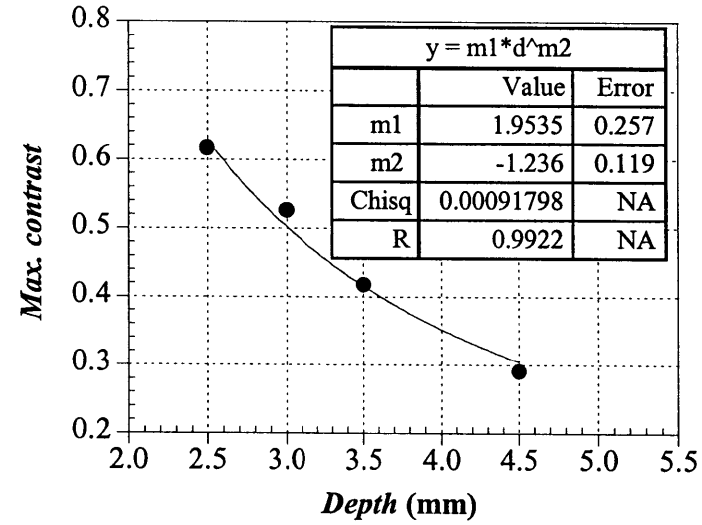

Fig. 4.60 Maximum contrast as a function of flaw depth for first set of concrete spall problems

As shown in Figs. 4.61 and 4.62, the maximum signal and maximum contrast for the second set of concrete spalls (case No.4) followed the following functions

$$\Delta T_{max} = 8.16\, d^{-1.43} \tag{4.58}$$

$$Max.\,contrast = 1.23\, d^{-0.76} \tag{4.59}$$

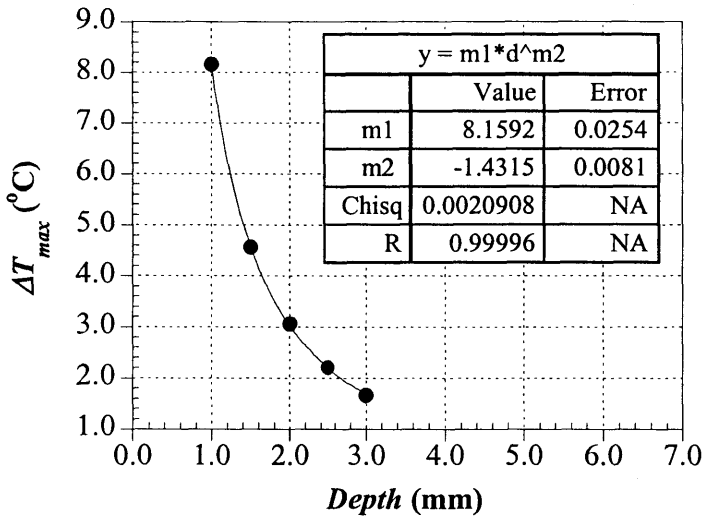

Fig. 4.61 Maximum signal as a function of flaw depth for second set of concrete spall problems

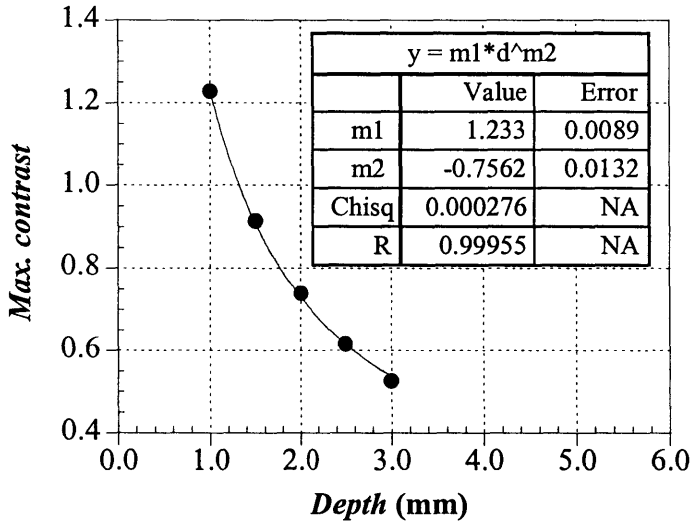

Fig. 4.61 Maximum signal as a function of flaw depth for second set of concrete spall problems

As shown in Figs. 4.63 and 4.64, the time for maximum signal and maximum contrast for problem set No.3 could be fitted by the following quadratic functions

$$t_s = 1.129\,d^2 + 1.411\,d + 1.272 \tag{4.60}$$

$$t_c = 1.178\,d^2 + 3.646\,d + 2.807 \tag{4.61}$$

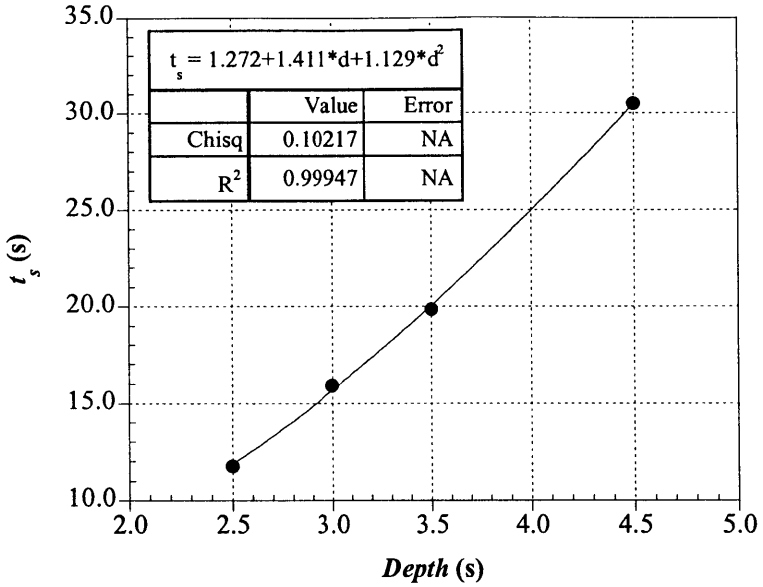

Fig. 4.63 Time for maximum signal for problem set No.3 (spall at 2 mm with varying number of FRP layers)

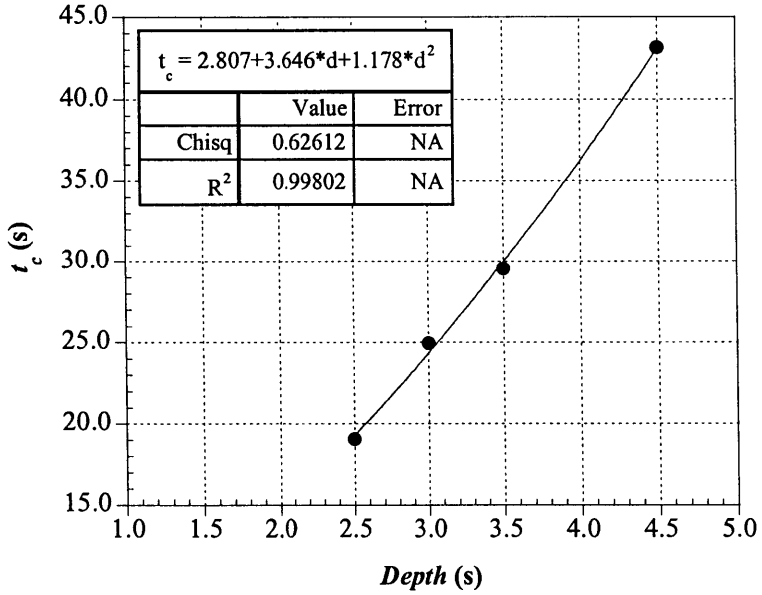

Fig. 4.64 Time for maximum contrast for problem set No.3 (spall at 2 mm with varying number of FRP layers

The time for maximum signal and maximum contrast could also be fitted using the following quadratic functions and as is illustrated in Figs. 4.65 and 4.66.

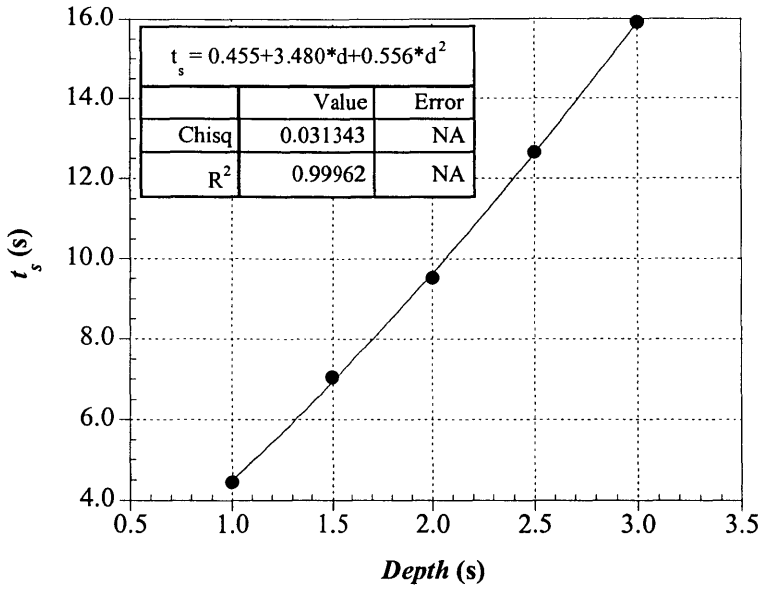

Fig. 4.65 Time for maximum signal for problem set No.4 (2 layers of FRP and varying spall depth)

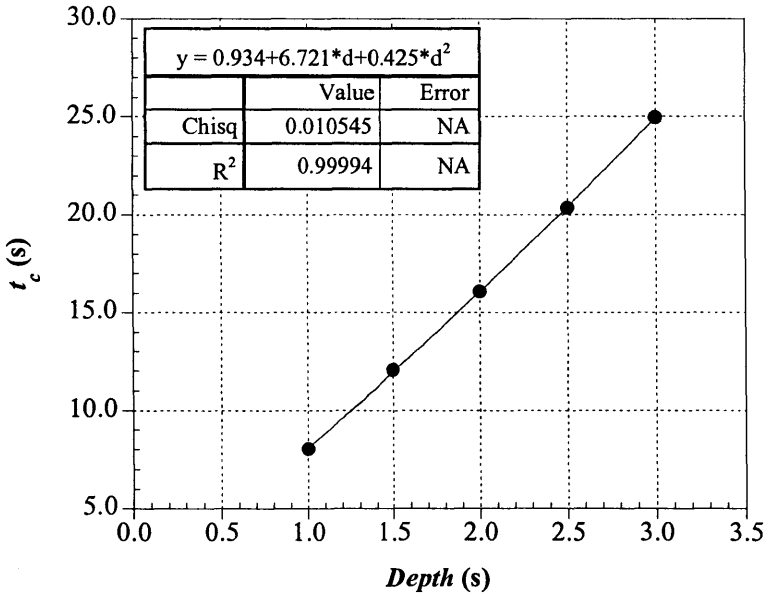

Fig. 4.66 Time to maximum contrast for problem set No.4 (2 layers of FRP and varying spall depth)

Summarizing, this section of the analysis provided some understanding of the effect of flaw depth on the thermal response:

- The maximum surface temperature is the same for delaminations and debonds located at the same depth.

- The maximum surface temperature decreases nonlinearly with increasing depth. The behavior of maximum surface temperatures can be described using the error function.

- Debonds and delaminations located at the same depth result in approximately equivalent values of maximum signal.

- Concrete spalls result in higher maximum thermal signals and contrasts than delaminations and debonds located at the same depth.

- The time for maximum signal and maximum contrast increases with the depth of the flaw. The time for detection increases nonlinearly for debonds and delaminations and approximately linearly for concrete spalls.

- Debonds are detected sooner than delaminations located at the same depth. For test objects with flaws at the same depth, the time for maximum contrast and signal increases with the number of FRP plies. The reason is that FRP has lower diffusivity than concrete. Hence, the higher the thickness of FRP the slower the rate of diffusion. The increase in time, though, is less than one second.

- For the case of concrete spalls located at the same depth, the more layers of FRP the lower the maximum surface temperatures and the higher the maximum thermal signal.

- Concrete spalls take a couple of seconds less for maximum signal compared with debonds.

4.5.4d Estimation of Depth

The FEM results reveal that the thermal response is a function of both the thickness of the FRP layer and the depth of the flaw. For the purpose of estimation, a simple procedure was developed to predict the maximum thermal signal and contrast as a function of its depth.

Three sets of problems were completed involving three different test objects with flaws at varying depths. Set problems No.5, No.6, and No.7 involved a test objects with 5, 3, and 2 plies of FRP, respectively. For each set of problems, the depth of the flaw was varied to include delaminations, debonds, and concrete spalls at different depths.

The results revealed thermal behaviors that followed the trends of power functions. Thus the basic form of the thermal response (ΔT_{max} or maximum contrast) is

$$Thermal\ response = \gamma\, d^{\varepsilon} \tag{4.62}$$

where, d is the depth of the flaw, γ is the coefficient, and ε is the exponent.

The best fitting power functions for problem sets No.5, No.6, and No.7 are presented in Table 4.22.

Table 4.22 Summary for set of FEM involving problem sets No.5 through No.7.

No. of plies	Thickness of FRP, d_{FRP}	ΔT_{max} (°C)	*Max.contrast*	t_s (s)	t_{ct} (s)
5	2.5 mm	$\frac{6.89}{d^{1.46}}$	$\frac{0.90}{d^{0.71}}$	$5.15d^{1.15}$	$8.72d^{1.08}$
3	1.5 mm	$\frac{7.34}{d^{1.39}}$	$\frac{1.03}{d^{0.67}}$	$5.03d^{1.06}$	$8.58d^{0.96}$
2	1.0 mm	$\frac{7.77}{d^{1.37}}$	$\frac{1.16}{d^{0.68}}$	$4.82d^{1.03}$	$8.42d^{0.95}$

The equations displayed in Table 4.22 indicate that the coefficients of the maximum thermal signal, contrast, and times for detection decrease with increasing number of FRP plies. The exponents, however, show increasing trends with increasing number of FRP plies.

Based on this data, an estimation procedure was developed. The steps are as follow:

- Establish the depth of the FRP layer (in mm).
- Find the coefficient and exponents for the maximum signal, contrast, time for maximum signal, and time for maximum contrast.

  For the maximum thermal signal:

$$\gamma_{signal} = 7.76\, d_{FRP}^{-0.13} \tag{4.63}$$

$$\varepsilon_{sin\,al} = -0.0648 d_{FRP} - 1.3004 \tag{4.64}$$

  For the maximum thermal contrast:

$$\gamma_{contrast} = 1.1613\, d_{FRP}^{-0.275} \tag{4.65}$$

$$\varepsilon_{contrast} = -0.0537 d_{FRP} - 0.615 \tag{4.66}$$

  For the time for maximum signal:

$$\gamma_{tsignal} = 4.8489\, d_{FRP}^{0.0697} \tag{4.67}$$

$$\varepsilon_{tsignal} = 0.0816 d_{FRP} + 0.943 \tag{4.68}$$

For the time for thermal contrast:

$$\gamma_{tcontrast} = 8.4324\, d_{FRP}^{0.037} \tag{4.69}$$

$$\varepsilon_{tcontrast} = 0.867\, d_{FRP} + 0.852 \tag{4.70}$$

where, d_{FRP} is the thickness of the FRP layer, γ is the coefficient, and ε is the exponent.

- The coefficients and exponents determined in the previous step provide the exponential equations for the thermal signal, contrast, time for maximum signal, and time for maximum contrast for flaws at any depth. These flaws include delaminations, debonds, and concrete spalls. Therefore,

$$\Delta T_{max} = \gamma_{signal}\, d^{\varepsilon_{signal}} \tag{4.71}$$

$$Max.\ contrast = \gamma_{contrast}\, d^{\varepsilon_{contrast}} \tag{4.72}$$

$$t_{signal} = \gamma_{tsignal}\, d^{\varepsilon_{tsignal}} \tag{4.73}$$

$$t_{contrast} = \gamma_{tcontrast}\, d^{\varepsilon_{tcontrast}} \tag{4.74}$$

where, d is the depth of the flaw, ΔT_{max} is the maximum thermal signal, t_{signal} is the time to maximum signal, and $t_{contrast}$ is the time to maximum contrast.

- Inversion of Eqs. 4.69 through 4.72 allow the estimation of the depth of the flaw based on the thermal response of the test object.

$$d = exp\left[\frac{ln(\Delta T_{max}) - ln(\gamma_{signal})}{\varepsilon_{signal}}\right] \tag{4.75}$$

$$d = exp\left[\frac{ln(Max.\ contrast) - ln(\gamma_{contrast})}{\varepsilon_{contrast}}\right] \tag{4.76}$$

$$d = exp\left[\frac{ln(t_{signal}) - ln(\gamma_{tsignal})}{\varepsilon_{tsignal}}\right] \tag{4.77}$$

$$d = exp\left[\frac{ln(t_{contrast}) - ln(\gamma_{tcontrast})}{\varepsilon_{tcontrast}}\right] \tag{4.78}$$

It is important to note that these equations are appropriate for the test object under study.

As illustrated in Fig. 4.67, plots of the time for maximum signal as a function of flaw depth for test objects with 5, 3, and 2 plies could also be used to estimate the depth of the flaw. This procedure is simpler and it provides an adequate estimate of the flaw depth.

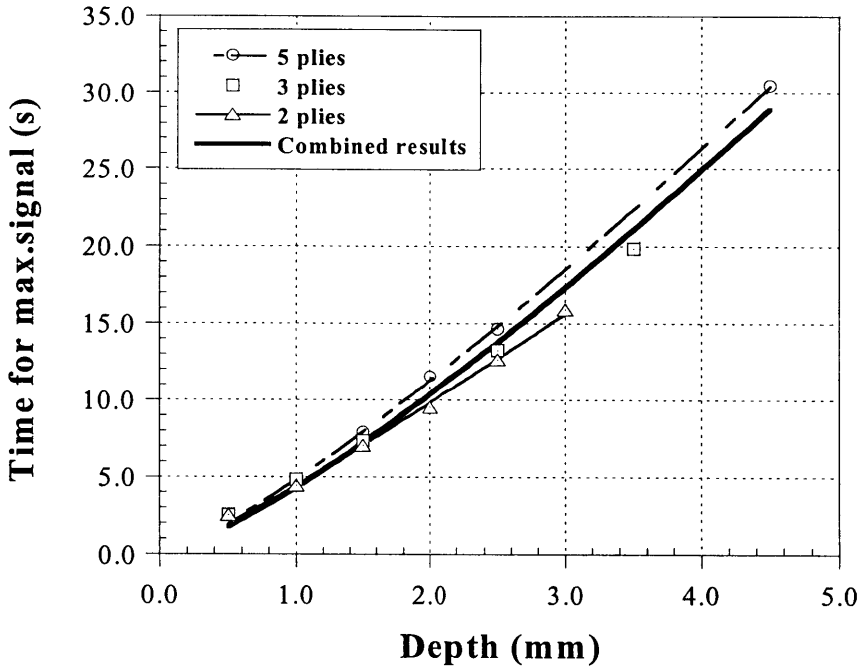

Fig. 4.67 Time for maximum signal as a function of flaw depth for test objects with 5, 3, and 2 layers of FRP

For example, for a 10 s time for maximum signal, the estimated flaw depth is 1.8 mm for the case of a 5-ply test object, while 2.0 mm for test objects containing 2 layers of FRP (Fig. 4.68). For this case, the estimation of flaw depth varies only by 0.2 mm. This value is less than the thickness of an FRP layer. For a long detection period, lets say 20 s for maximum signal, the estimated flaw depth is 2.5 mm for test objects containing 5 layers of FRP and 2.9 mm for test objects containing 2 layers of FRP. The estimation of the flaw depth varied slightly by only 0.4 mm, again, less than the thickness of an FRP layer.

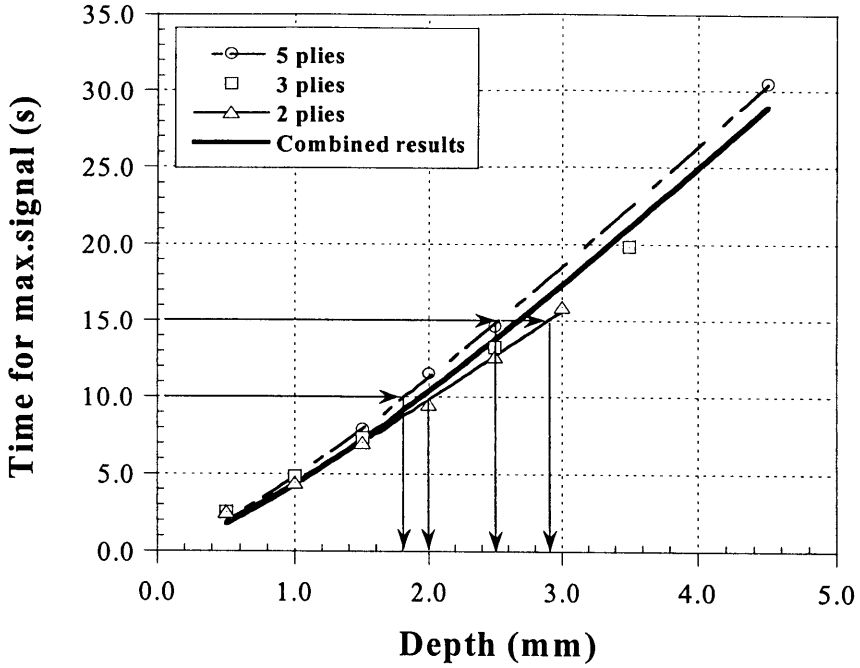

Fig. 4.68 Example of estimation of flaw depth

4.5.5 Summary

The third parametric study focused on the effect of flaw depth on the thermal response. The parametric study had the following objectives:

- understand the effect of delamination, debonds, and concrete spalls in the thermal response
- develop a simplified estimation of the thermal responses as a function of the depth of the internal flaw.

Five sets of analyses, including 21 FEM simulations, were performed to evaluate the effect of flaw depth on the thermal response of the test object. Two different parameters were varied through the course of the parametric study: the depth of the flaw and the number of FRP plies. These changes made possible the study of delaminations, debonds, and concrete spalls located at varying depths.

Several conclusions were reached from the results:

- The maximum surface temperature decreases nonlinearly with increasing depth. The behavior of maximum surface temperatures can be described using error functions.
- The maximum surface temperature is the same for debonds and delaminations located at the same depth.

- Debonds provide higher thermal signal and contrast than delaminations located at the same depth.

- Concrete spalls develop higher thermal signal and contrast than delaminations and debonds located at the same depth.

- For flaws at the same depth, the thermal signal decreases with increasing thickness of FRP.

- The time for maximum signal and maximum contrast increases with the depth of the flaw. The time for detection increases nonlinearly for debonds and delaminations and near-linearly for concrete spalls.

- Debonds are detected sooner than delaminations located at the same depth. For test objects with flaws at the same depth, the time for maximum contrast and signal increases with the number of FRP plies. For the case of concrete spalls located at the same depth, the more layers of FRP the lower the maximum surface temperatures and the higher the maximum thermal signal.

- Concrete spalls take a couple of seconds less to be detected compared with debonds.

The investigation has led to a simple procedure for estimating the thermal response as a function of the thickness of FRP material and the depth of the internal flaw. The next series of studies involve the investigation of the effect of thermal severity (resistance) of the internal flaw.

4.6 Parametric Study No.4: Effect of the Thickness of the Flaw

The thermal resistance of subsurface flaws is an additional parameter that affects the thermal response of the test object and thus the response parameters at its surface. The thermal resistance of the flaw is directly proportional to the thickness of the flaw. Thus, it is helpful to investigate the effect of the thickness of internal flaws in the thermal response.

The fourth parametric study had the following objectives:

- Understand the effects of flaw thickness on the thermal response

- Establish minimum thickness of detectable flaw

Three different sets of problems were performed which included a total of 15 simulations.

4.6.1 Geometry of Model

The test object consisted of a 50 mm long by 20 mm thick concrete slab with 3 layers of FRP bonded to its surface. Each layer of FRP was 0.5 mm thick. Each layer of FRP was oriented at 90 degrees with respect to the adjacent ply. The test object contained a 25 mm long internal flaw. The flaw was located at the center of the test object. The thickness of the flaw was varied

from 0.4 mm to 1 μm. The depth of the flaw was varied as well to include delaminations, debonds, and concrete spalls. The delamination was located at a depth of 0.5 mm, the debond at 1.5 mm and the concrete spall at 2.5 mm.

Plane two-dimensional modeling was used. The model was simplified using plane symmetry about the center of the test object. The model was meshed using 2-D quadrilateral thermal solid elements, each containing 4 nodes with one degree of freedom (temperature). The test object was meshed using a global mesh size of 0.5 mm. Mesh refinement was applied in the thickness direction (y-axis), which was the primary direction of heat flow. The thinner elements were located at the FRP layers, the flaw, and the interface between the FRP and the concrete. The element size increased towards the bottom of the concrete slab away from the heated top surface. The meshing criterion was similar to that of parametric study No.2.

As previously mentioned, the thickness of the air flaws was varied between 0.4 mm and 1 μm. These variations corresponded to thermal resistances ranging from 1.7×10^{-2} $m^2 \cdot °C/W$ to 4.0×10^{-5} $m^2 \cdot °C/W$.

The simulations were divided into 3 groups. The first set of simulations involved the investigation of the effect of thickness of delaminations on the thermal response. The second set of models involved the study of the effect of thickness of debonds. The third and final set involved the investigation of the effect of the thickness of concrete spalls.

For the first set of problems the thickness of the air flaw was varied from 0.4 mm to 1 μm which represented a thermal resistance of 1.7×10^{-2} $m^2 \cdot °C/W$ to 4.0×10^{-5} $m^2 \cdot °C/W$, as indicated in Table 4.23.

Table 4.23 Geometry for problem set involving delaminations

Problem	**Flaw depth (mm)**	**Flaw thickness (mm)**	**Thermal Resistance ($m^2 \cdot °C/W$)**
66	0.5	0.4	16.67×10^{-3}
67	0.5	0.2	8.33×10^{-3}
68	0.5	0.1	4.17×10^{-3}
69	0.5	0.05	2.08×10^{-3}
70	0.5	0.025	1.04×10^{-3}
71	0.5	0.001	0.04×10^{-3}

The second set of simulations involved debonds between the FRP and the concrete. Again, the thickness of the air flaws varied between 0.4 mm and 1 mm. Five different models were performed as indicated in Table 4.24.

Table 4.24 Geometry for problem set involving debonds

Problem	Flaw depth (mm)	Flaw thickness (mm)	Thermal resistance ($m^2 \cdot °C/W$)
72	1.5	0.4	16.67×10^{-3}
73	1.5	0.2	8.33×10^{-3}
74	1.5	0.1	4.17×10^{-3}
75	1.5	0.05	2.08×10^{-3}
76	1.5	0.001	0.04×10^{-3}

The final set of simulations focused on concrete spalls located at a depth of 1.0 mm below the FRP/concrete interface. Due to the depth of the air flaw, detection of thinner air voids was not expected. Thus, the thickness of the spalls was varied from 0.4 mm to 0.05 mm for this particular set of models. Table 4.25 summarizes the geometry of the models.

Figure 3.69 summarizes the geometry of the three different sets of simulations.

Table 4.25 Geometry for problem set involving concrete spalls

Problem	Flaw depth (mm)	Flaw thickness (mm)	Thermal resistance ($m^2 \cdot °C/W$)
77	2.5	0.4	16.67×10^{-3}
78	2.5	0.2	8.33×10^{-3}
79	2.5	0.1	4.17×10^{-3}
80	2.5	0.05	2.08×10^{-3}

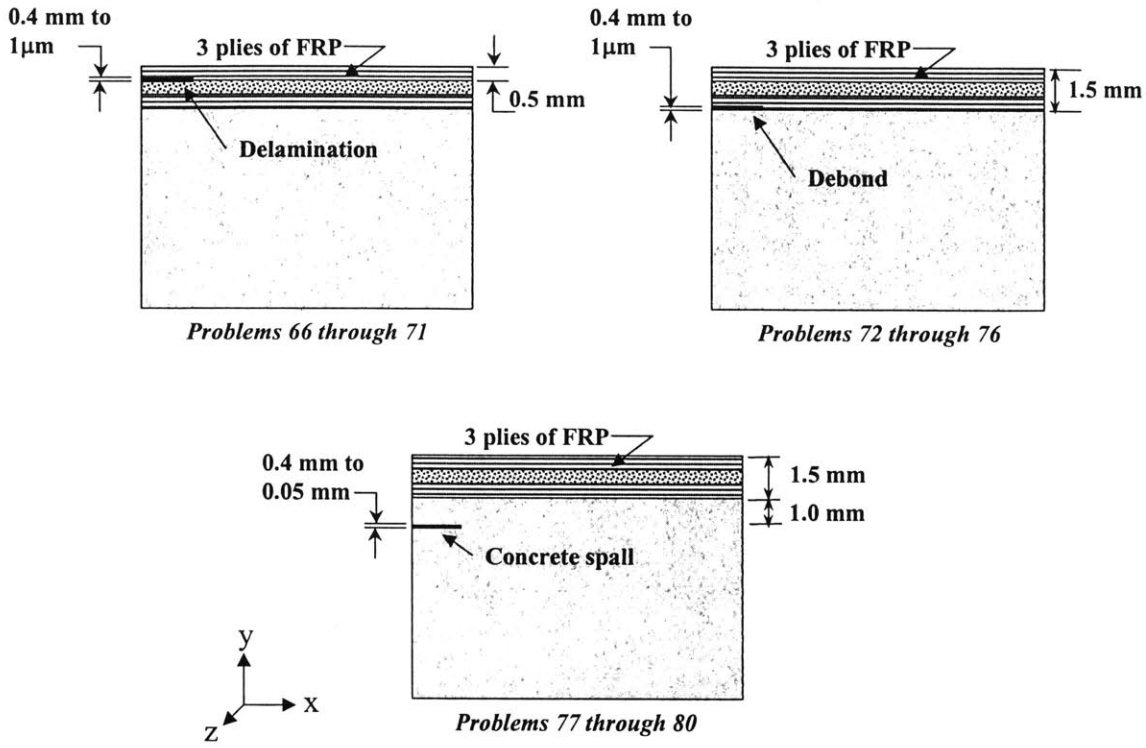

Fig. 4.69 Summary of simulations' geometry

4.6.2 Material Properties

The material properties of the model were those of concrete for the substrate, carbon FRP for the bonded composite, and air for the flaws (Table 4.2). As in previous parametric studies, the CFRP layer in direct contact with the substrate had fibers running in the x-direction. Each subsequent layer had its fiber direction rotating 90° about the y-axis.

4.6.3 Thermal Loading and Boundary Conditions

As in previous simulations, the analysis was defined as a transient heat transfer problem. A square pulse of intensity 20,000 W/m^2 with duration 2 s was applied to the top surface of the model. Adiabatic conditions ($dT/dx = 0$ and $dT/dz = 0$) applied to the remaining free surfaces and at the axis of symmetry. The initial temperature of the model was 23 °C.

Similarly to previous models, the simulations were performed using Ansys automatic time stepping. The maximum and minimum time steps were 0.1 s and 0.008 s, respectively. The initial time step was 0.009 s. The FEM output was recorded at every time step.

4.6.4 Results

4.6.4a Delaminations

The first set of models focused on the study of delaminations of different thickness. The delaminations were located at the top layer of FRP. The thickness of the air flaw was decreased from 0.4 mm, which represented a very severe flaw, to 1 μm, which represented a very moderate defect. Table 4.26 summarizes the results of the first set of simulations, which include problems 66 through 71.

Table 4.26 Results for simulations involving delaminations
(first set of problems in parametric No.4)

Problem	Thickness (mm)	R_{flaw} (m^2·°C/W)	T_{max} (°C)	Maximum Signal		Maximum Contrast	
				t_s (s)	ΔT_{max} (°C)	t_c (s)	$\Delta T_{max}/\Delta T_{backg}$
66	0.4	16.67×10^{-3}	88.6	2.73	44.4	6.63	4.71
67	0.2	8.33×10^{-3}	71.2	2.73	27.2	5.73	2.68
68	0.1	4.17×10^{-3}	64.9	2.53	18.5	4.43	1.54
69	0.05	2.08×10^{-3}	59.7	2.34	12.2	3.44	0.86
70	0.025	1.04×10^{-3}	55.5	2.24	7.4	2.84	0.46
71	0.001	0.04×10^{-3}	48.8	2.08	0.3	2.35	0.02

Table 4.26 indicates both thickness of the air flaw and its equivalent thermal resistance, R_{flaw}. Although the primary source of flaws in FRP composites bonded to concrete is air (e.g. bubbles entrapped in the epoxy matrix or cracks in the concrete), the results of the study can be generalized to any material by using the equivalent thermal resistance of the air flaw modeled in the study. Thermal resistance allows the representation of flaws of any thickness and any material, not just air flaws. Thermal resistance of a flaw is defined as (Özişik, 1985)

$$R_{flaw} = \frac{\Delta z}{k_{flaw}} \tag{4.79}$$

where Δz is the thickness of the flaw and k_{flaw} is the thermal conductivity of the flaw.

The results summarized in Table 4.26 indicate some interesting aspects of the effect of flaw thickness or thermal resistance on the thermal response. The data reveal that the thermal response varies nonlinearly due to changes in the thermal resistance of the flaw. In general, thermal responses increase with increasing flaw thickness.

The maximum surface temperature, T_{max}, increases nonlinearly with increasing thermal resistance. The variation of T_{max} with thermal resistance of the flaw could be represented as a power function:

$$T_{max} = 47.2 + 266 R_{flaw}^{0.5} \tag{4.80}$$

where R_{flaw} is the thermal resistance of the flaw.

The results for the thermal signal as a function of time are presented in Figure 4.70. Qualitatively, the results demonstrate that while the magnitude of the signal varies significantly with increasing resistance, changes in the time for maximum signal are negligible.

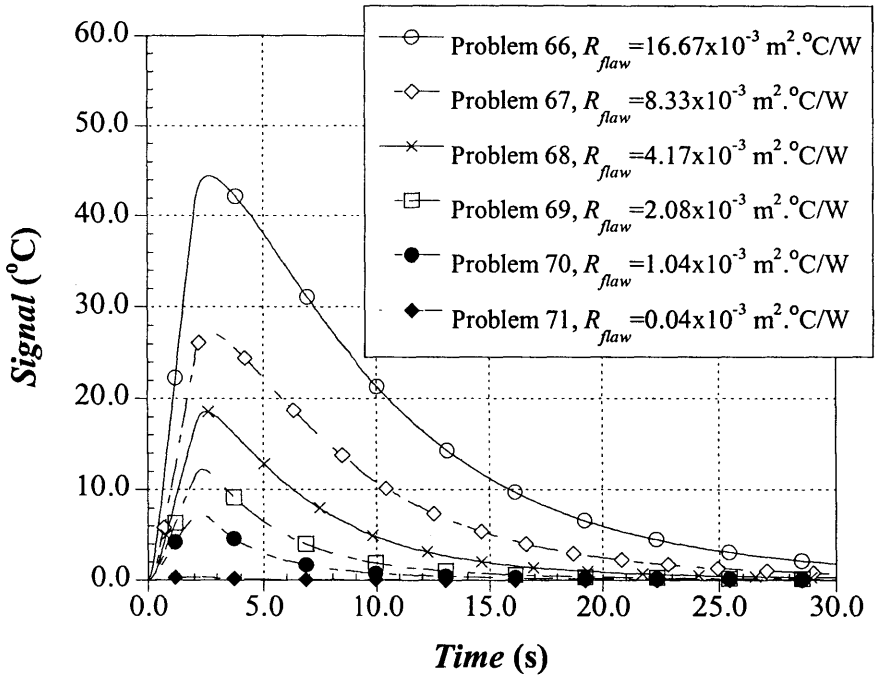

Fig. 4.70 Thermal signal for simulations involving delaminations of different thickness (Problems 66 through 71)

The maximum thermal signal as a function of thermal resistance could also be represented using a power function. The expression that fits the FEM output is

$$\Delta T_{max} = 606 R_{flaw}^{0.64} \tag{4.81}$$

The FEM output and power fit are presented in Figure 4.71.

The time for maximum signal also increases nonlinearly with increasing thermal resistance of the flaw. As previously mentioned, changes in t_s are negligible since t_s only increases by a fraction of a second for changes in thermal resistance between 16.67×10^{-3} m^2.°C/W and 0.04×10^{-3} m^2.°C/W. Once the thickness of the flaw becomes significant (i.e. thicker than 0.2 mm) the time for maximum signal does not vary for the case of a delamination in the upper layer of FRP. The increase in time for maximum signal can be represented as a power function:

$$t_s = 2.0 + 7.9 R_{flaw}^{0.5} \tag{4.82}$$

It is important to note that equation 3.82 represents the increase in t_s for problems 67 through 71. Problem 66 is not considered since t_s becomes asymptotic for large values of R_{flaw}. Figure 4.72

presents the FEM output and the power fit of the time for maximum signal for problems 67 through 71.

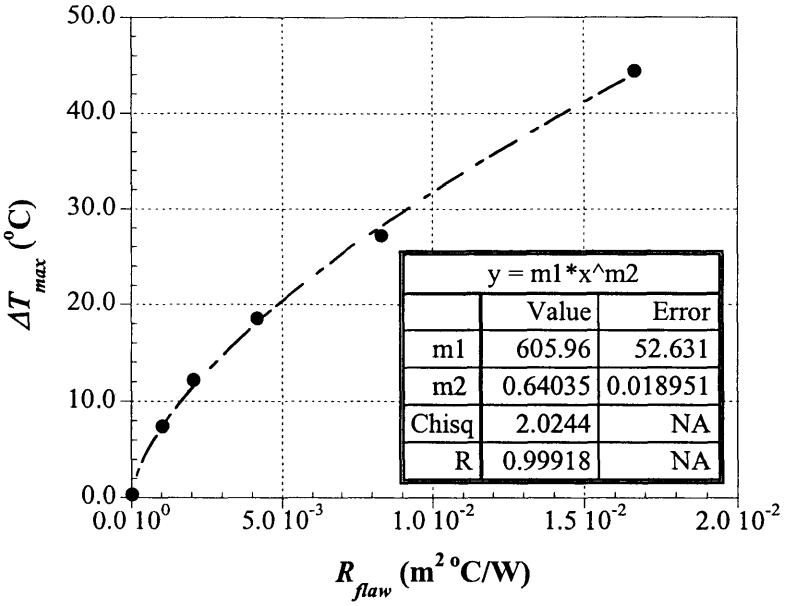

Fig. 4.71 Maximum thermal signal as a function of thermal resistance of the flaw (Problems 66 through 71)

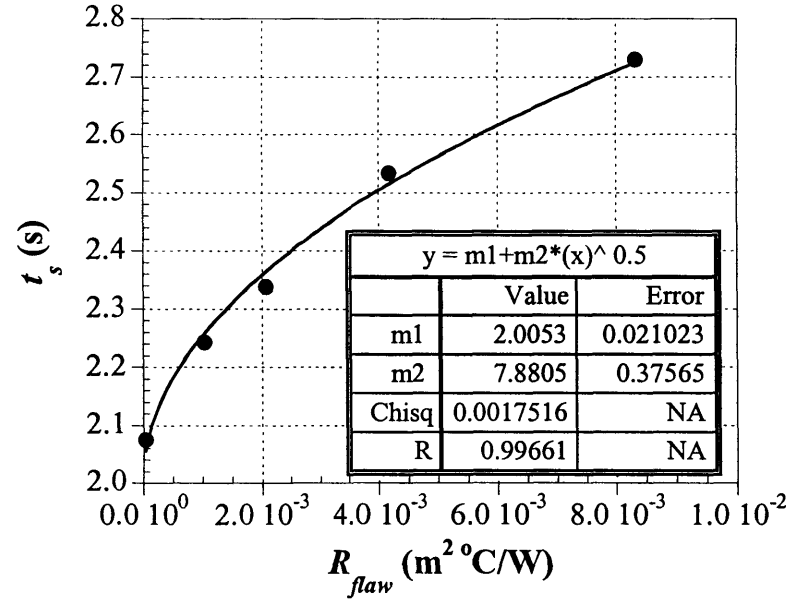

Fig. 4.72 Time for maximum signal as a function of flaw thermal resistance (Problems 67 through 71)

The thermal contrast versus time curves for simulations 67 through 71 are presented in Figure 4.73. The results show that both, the magnitude and the time to maximum contrast are affected by changes in the thermal resistance of the flaw.

Figure 4.73 reveals that the maximum thermal contrast increases with increasing thermal resistance of the flaw. The increase in maximum thermal contrast as a function of the thermal resistance of the flaw can be represented with the following equation:

$$Contrast = 139R_{flaw}^{0.82} \tag{4.83}$$

Figure 4.74 shows the maximum thermal contrast versus thermal resistance for the first set of simulations.

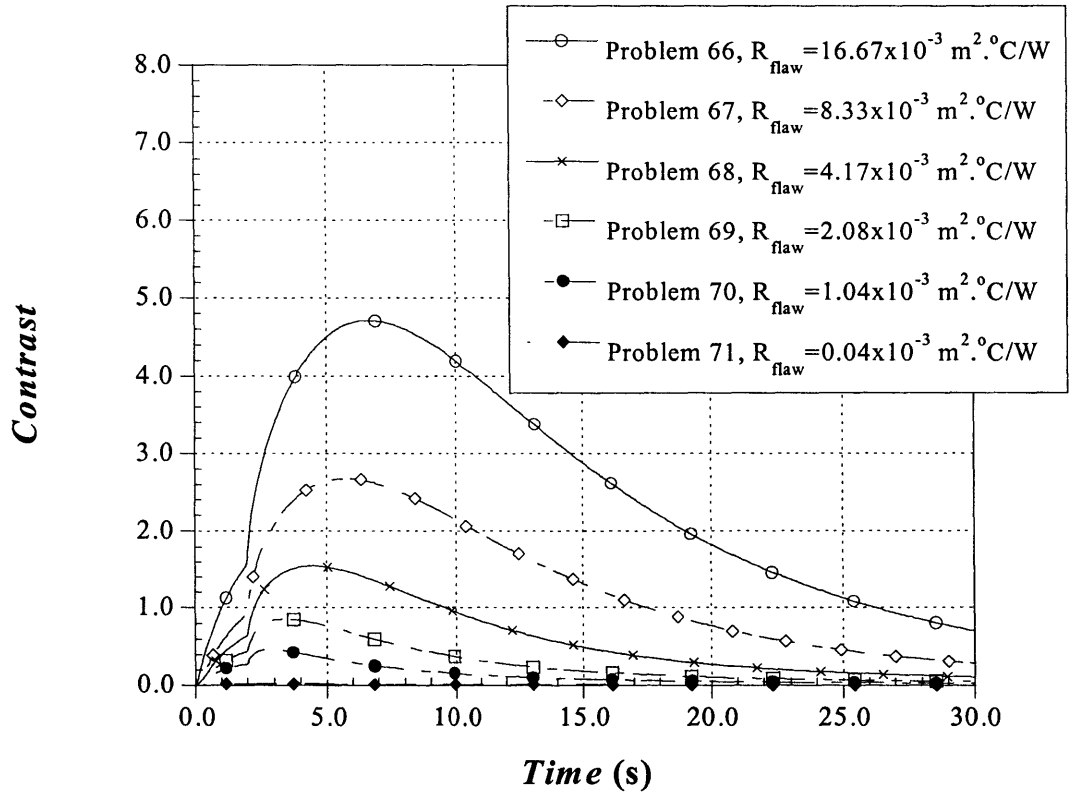

Fig. 4.73 Thermal contrast for simulations involving delaminations of different thickness (Problems 66 through 71)

The time for maximum contrast, t_c, is more sensitive to changes in thermal resistance than the time for maximum signal. For example, the time for maximum contrast increases by 4.3 s for test objects with R_{flaw} ranging from 0.04×10^{-3} m^2·°C/W to 16.67×10^{-3} m^2·°C/W. The increase in t_c is nonlinear and could be represented using the following power function:

$$t_c = 1.8 + 41.3R_{flaw}^{0.5} \tag{4.84}$$

Figure 4.75 illustrates the output from the FEM simulations and the power fit for t_c versus R_{flaw}.

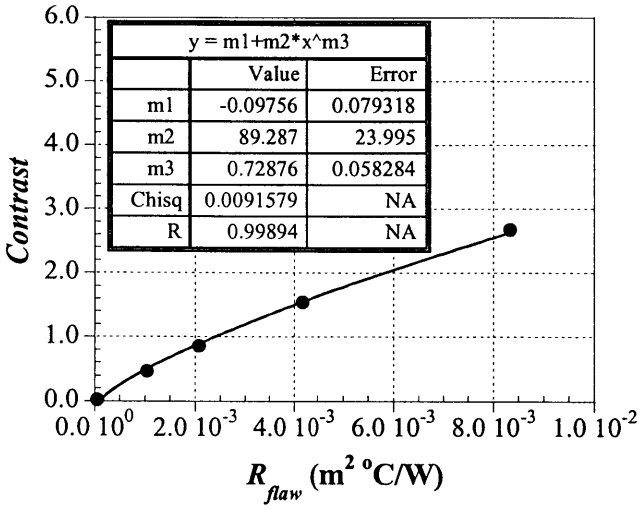

Fig. 4.74 Maximum contrast as a function of thermal resistance of the flaw (Problems 66 through 71)

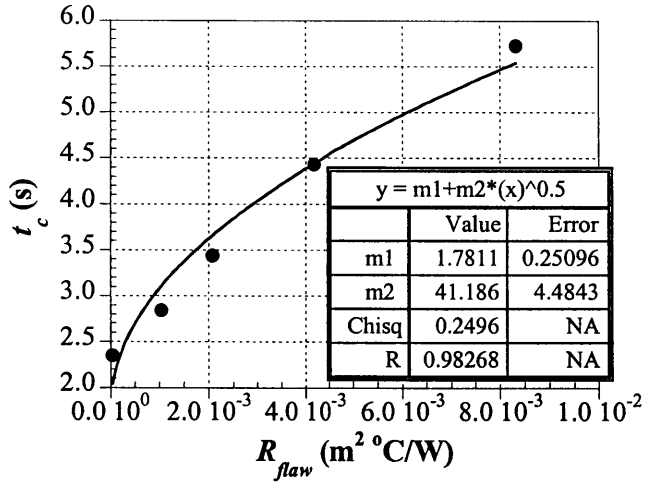

Fig. 4.75 Time for maximum contrast as a function of flaw thermal resistance (Problems 66 through 71)

4.6.4b Debonds

The second set of models focused on the study of debonds of different thickness. The thickness of the air flaw was decreased from 0.4 mm, a very severe flaw, to 1 μm, an extremely moderate defect. Table 4.27 summarizes the results of the second set of simulations, which include problems 72 through 76.

Table 4.27 Results for simulations involving debonds (second set of problems in parametric No.4)

Problem	Thickness (mm)	R_{flaw} ($m^2.°C/W$)	T_{max} (°C)	Maximum Signal		Maximum Contrast	
				t_s (s)	ΔT_{max} (°C)	t_c (s)	$\Delta T_{max}/\Delta T_{backg}$
72	0.4	16.67×10^{-3}	49.7	9.55	8.17	18.25	1.95
73	0.2	8.33×10^{-3}	49.3	8.55	6.10	14.32	1.31
74	0.1	4.17×10^{-3}	49.1	7.35	4.41	12.05	0.84
75	0.05	2.08×10^{-3}	48.9	6.45	2.91	9.85	0.49
76	0.001	0.04×10^{-3}	48.5	4.85	0.09	6.85	0.01

The results summed up in Table 4.27 show that similarly to delaminations, thermal responses vary nonlinearly with increasing thermal resistance. For example, the maximum surface temperature increases nonlinearly with increasing R_{flaw}. The change in maximum surface temperature, however, is only 1.2 °C for an increase from 0.04 $m^2.°C/W$ to 16.67 $m^2.°C/W$ in thermal resistance of the flaw. The change in maximum surface temperature is illustrated in Figure 4.76.

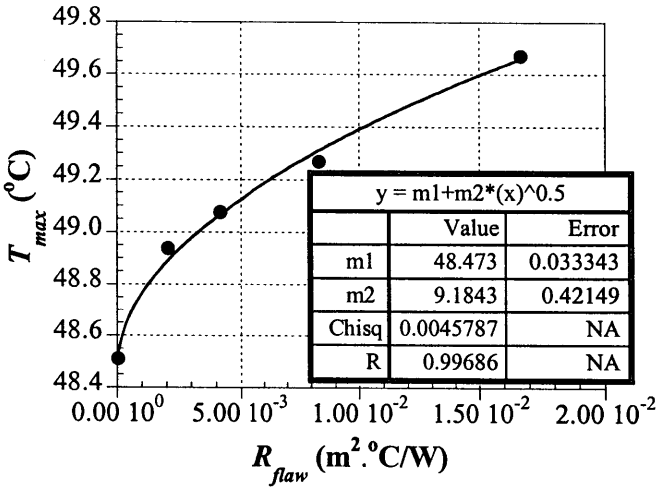

Fig. 4.76 Maximum surface temperature as a function of flaw thermal resistance (Problems 72 through 76)

The FEM output suggests that the effect of R_{flaw} in the thermal signal is lower for debond that it is for delaminations. The thermal signal as a function of time is presented in Figure 4.77.

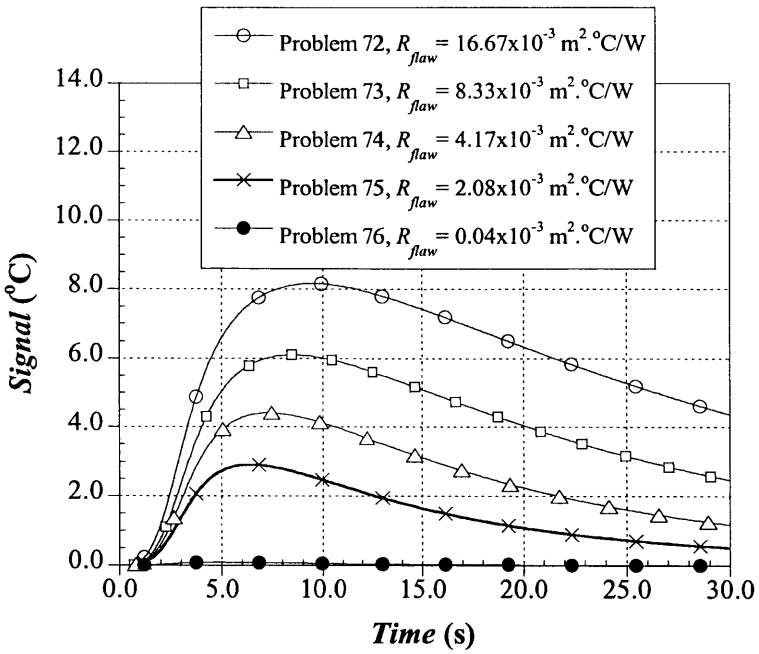

Fig. 4.77 Thermal signal for simulations involving debonds of different thickness (Problems 72 through 76)

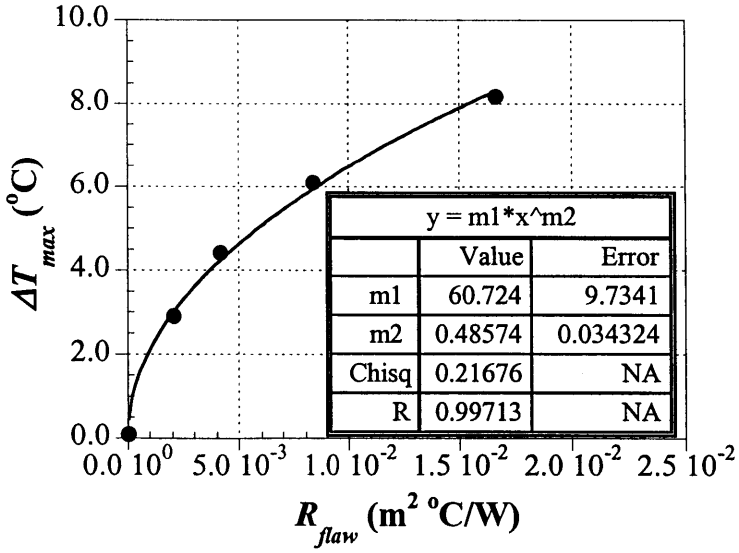

y = m1*x^m2		
	Value	Error
m1	60.724	9.7341
m2	0.48574	0.034324
Chisq	0.21676	NA
R	0.99713	NA

Fig. 4.78 Maximum Signal as a function of flaw thermal resistance (Problems 72 through 76)

The effect of thermal resistance of debonds in the maximum thermal signal follows similar trends to the case of delaminations. The maximum signal increases nonlinearly with increasing R_{flaw}. The overall change in ΔT_{max} is on the order of 8.1 °C for increases of R_{flaw} between 0.04 m^2·°C/W to 16.67 m^2·°C/W. The FEM output could be expressed as the following power function:

$$\Delta T_{max} = 60.9\, R_{flaw}^{0.49} \tag{4.85}$$

The FEM results and power function fit are presented in Figure 4.78.

The time for maximum signal also increases nonlinearly with increasing flaw thermal resistance. The influence of R_{flaw}, however, is higher on the time to detect debonds than the time to detect delaminations. For example, an increase in R_{flaw} from 0.04 $m^2 \cdot °C/W$ to 16.67 $m^2 \cdot °C/W$ produces an increase in t_s of 4.7 s. Figure 4.79 illustrates the results from the FEM simulations and the power fit, which could be expressed as

$$t_s = 4.7 + 39.2 R_{flaw}^{0.5} \tag{4.86}$$

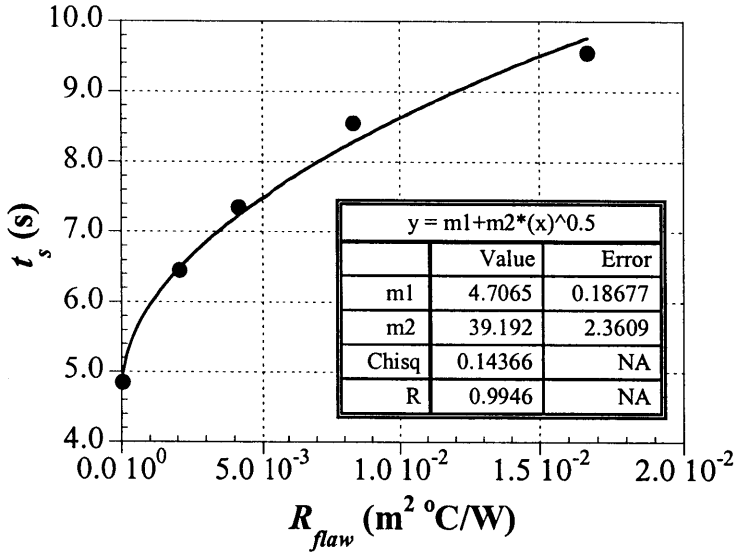

Fig. 4.79 Time for maximum signal as a function of flaw thermal resistance (Problems 72 through 76)

The summary of the results also indicates that variations in the thermal contrast are less pronounced for debonds than for delaminations. Figure 4.80 illustrates the thermal contrast as a function of time for the second set of simulations involving the effect of R_{flaw}.

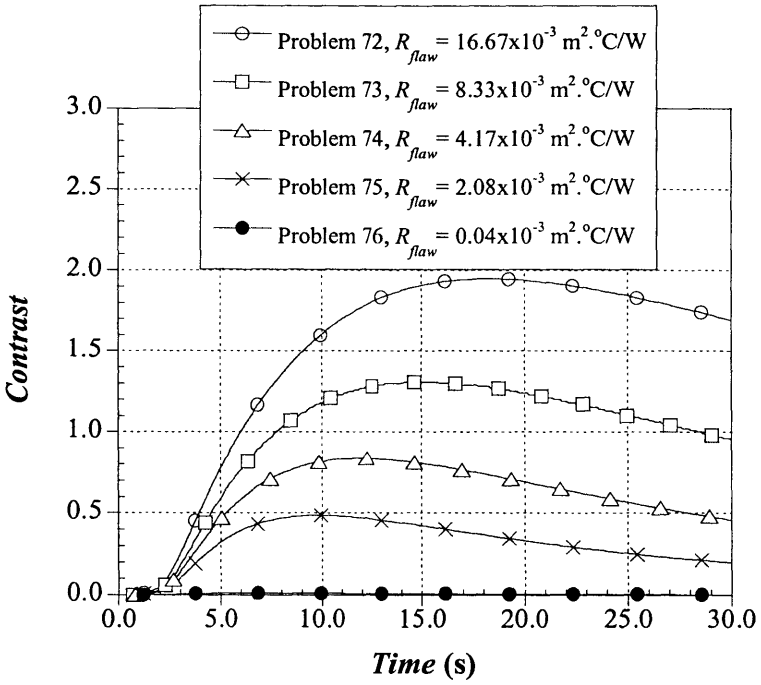

Fig. 4.80 Thermal contrast for simulations involving debonds of different thickness (Problems 72 through 76)

The change in thermal contrast varies between 0.10 and 1.95 for values of thermal resistance between 0.04 m^2·°C/W to 16.67 m^2·°C/W. The effect of flaw thermal resistance on the magnitude of the maximum contrast is illustrated in Figure 4.81. The change in maximum contrast as a function of R_{flaw} could be expressed as the following power function

$$Max.Contrast = 26.4 R_{flaw}^{0.63} \tag{4.87}$$

As expected from the conclusions of parametric study No. 3, the time for contrast was longer for debonds than for delaminations. The time for maximum contrast also increases nonlinearly with increasing R_{flaw}. The increase in time varies between 6.85 s and 18.25 s for test objects containing flaws with thermal resistance ranging from 0.04×10^{-3} m^2·°C/W and 16.67×10^{-3} m^2·°C/W. The FEM output is presented in Figure 4.82.

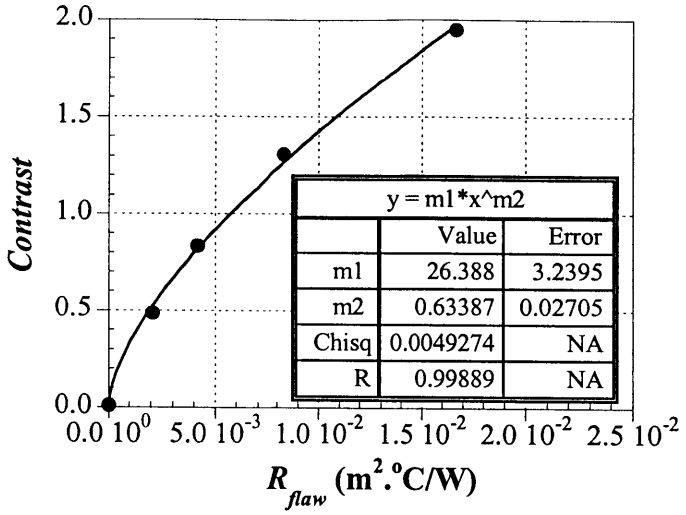

Fig. 4.81 Thermal contrast as a function of flaw thermal resistance (Problems 72 through 76)

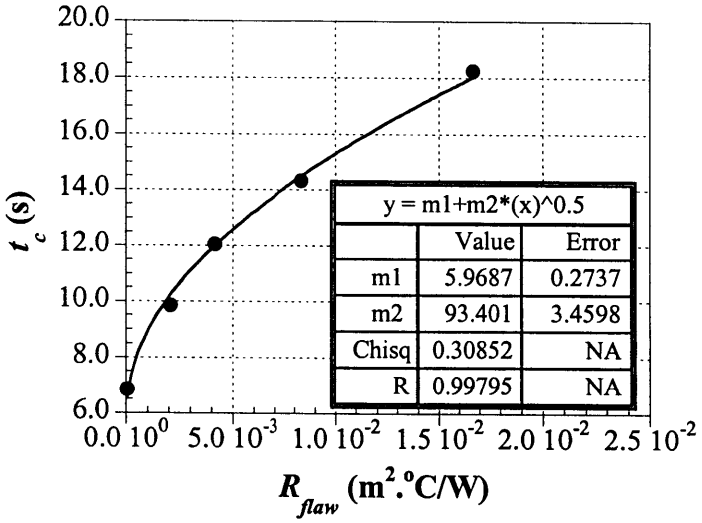

Fig. 4.82 Time for maximum contrast as a function of flaw thermal resistance (Problems 72 through 76)

Analysis of the FEM output suggests that the time for maximum contrast could fit a power function as it is indicated in Figure 4.82 and in Equation 4.88

$$t_c = 6.0 + 93.5R_{flaw}^{0.5} \tag{4.88}$$

4.6.4c Concrete Spalls

The third set of simulations concentrated on the study of concrete spalls and the effect that their thickness have on the thermal response. This set of studies involved test objects with flaw thickness between 0.4 mm and 0.05 mm. Thinner flaws were not considered since they were not expected to be detected. Results of the simulations for problems 78 through 80 are presented in Table 4.28.

Table 4.28 Results for simulations involving concrete spalls (third set of problems in parametric No.4)

Problem	Thickness (mm)	R_{flaw} ($m^2 \cdot °C/W$)	T_{max} (°C)	Maximum Signal		Maximum Contrast	
				t_s (s)	ΔT_{max} (°C)	t_c (s)	$\Delta T_{max}/\Delta T_{backg}$
77	0.4	16.67×10^{-3}	48.5	16.5	3.89	29.3	1.26
78	0.2	8.33×10^{-3}	48.5	14.8	2.98	24.3	0.88
79	0.1	4.17×10^{-3}	48.5	12.9	2.14	19.8	0.57
80	0.05	2.08×10^{-3}	48.5	11.3	1.39	16.4	0.34

Observation of the simulation output indicates that variations in flaw thermal resistance have less effect in concrete spalls than in any other kind of defect.

The maximum surface temperature varies insignificantly with increasing thermal resistance of concrete spalls. The changes in T_{max} are only on the order of 2×10^{-2} °C for variations in R_{flaw} between 2.08×10^{-3} $m^2 \cdot °C/W$ and 16.67×10^{-3} $m^2 \cdot °C/W$.

Finite-element output data were recorded at every time step of the transient analysis. The thermal signal as a function of time is presented in Figure 4.83.

Changes in the maximum signal as a function of thermal resistance of the flaw are quite small. For instance, the maximum signal varies only by 2.5 °C with increases in R_{flaw} between 2.08×10^{-3} $m^2 \cdot °C/W$ and 16.67×10^{-3} $m^2 \cdot °C/W$. The variation in maximum signal is, again, nonlinear and could be represented as the following power function:

$$\Delta T_{max} = 26.2\, R_{flaw}^{0.46} \tag{4.89}$$

The FEM output and its power fit function are presented in Figure 4.84.

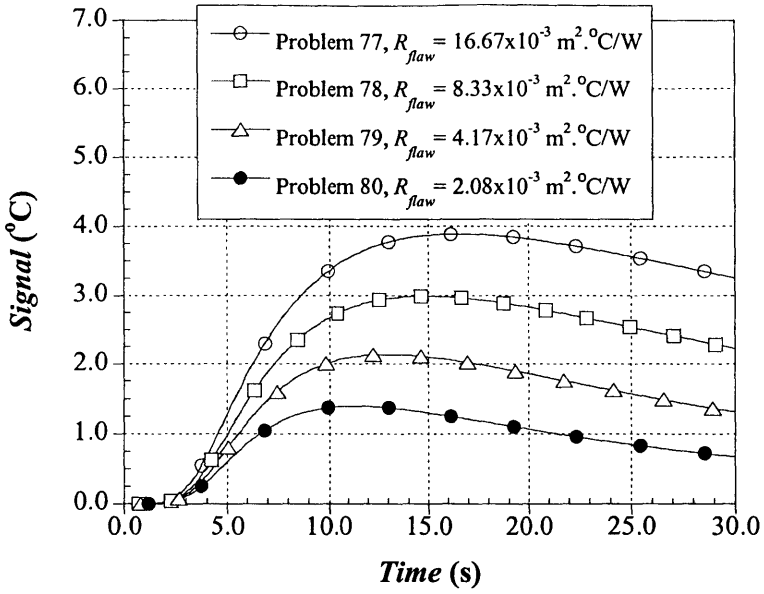

Fig. 4.83 Thermal signal for simulations involving concrete spalls of different thickness (Problems 77 through 80)

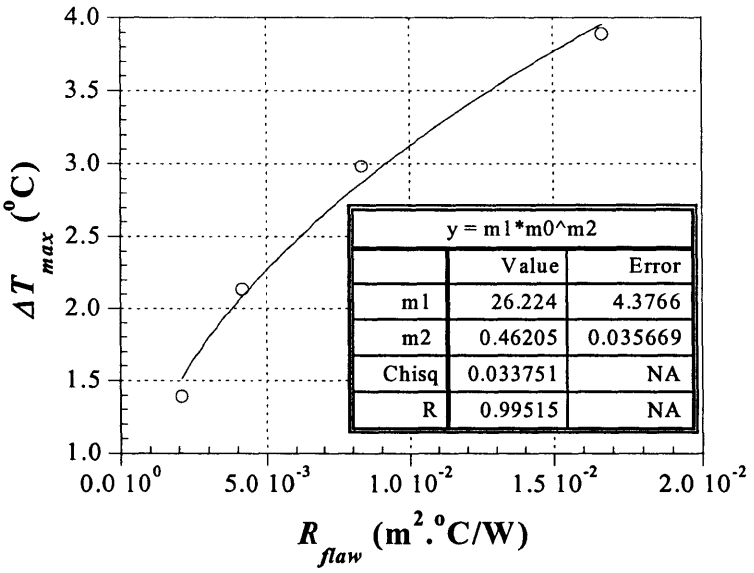

Fig. 4.84 Maximum thermal signal as a function of flaw thermal resistance (Problem 77 through 80)

The time for maximum signal varies more significantly for concrete spalls than for other kinds of defect (e.g. delaminations and debonds). Changes of 5.2 s are reported for t_s ranging from 2.08 m^2·°C/W to 16.67 m^2·°C/W. Similarly to debonds and delaminations, the variation in t_s for concrete spalls varies as a power function. The equation that could be used to represent the time for maximum signal is

$$t_s = 8.82 + 61.8\ R_{flaw}^{0.5} \tag{4.90}$$

Equation 4.90 and the FEM output data are presented in Figure 4.85.

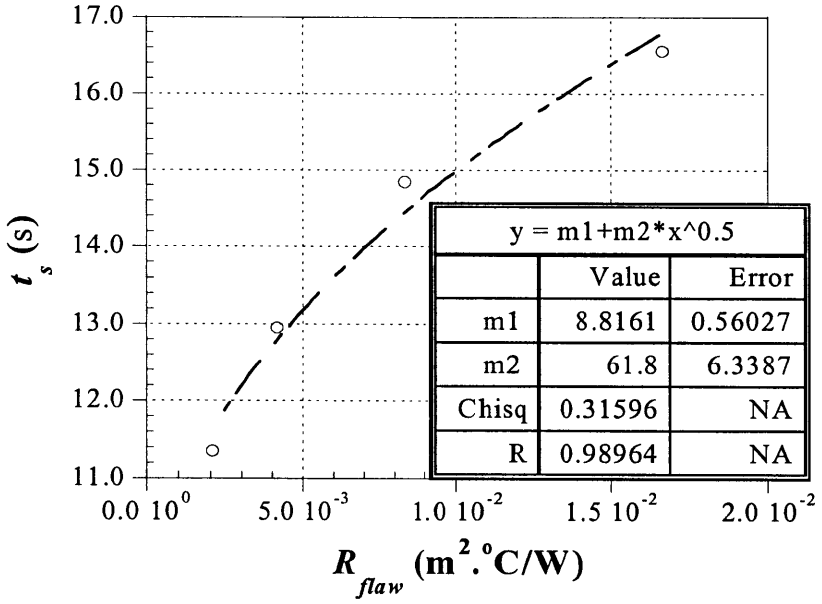

Fig. 4.85 Time for maximum signal as a function of flaw thermal resistance (Problems 77 through 80)

The thermal contrast for the third set of simulations was computed for every time step of the analysis. The output for thermal contrast as a function of time is presented in Figure 4.86.

Figure 4.86 also illustrates that the magnitude of the maximum contrast increases with increasing R_{flaw}. The values of maximum contrast are presented in Table 3.28. The increase in maximum contrast could be expressed as a power function of the flaw thermal resistance:

$$Max.\ Contrast = 26.4\ R_{flaw}^{0.63} \tag{4.91}$$

The output summarizing the effect that R_{flaw} had on the maximum thermal contrast is presented in Figure 4.87.

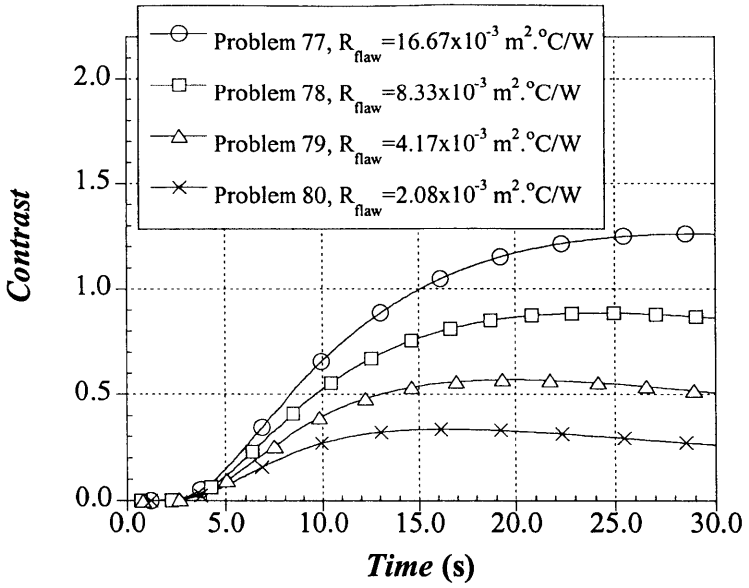

Fig. 4.86 Thermal contrast for simulations involving concrete spalls of different thickness (Problems 77 through 80)

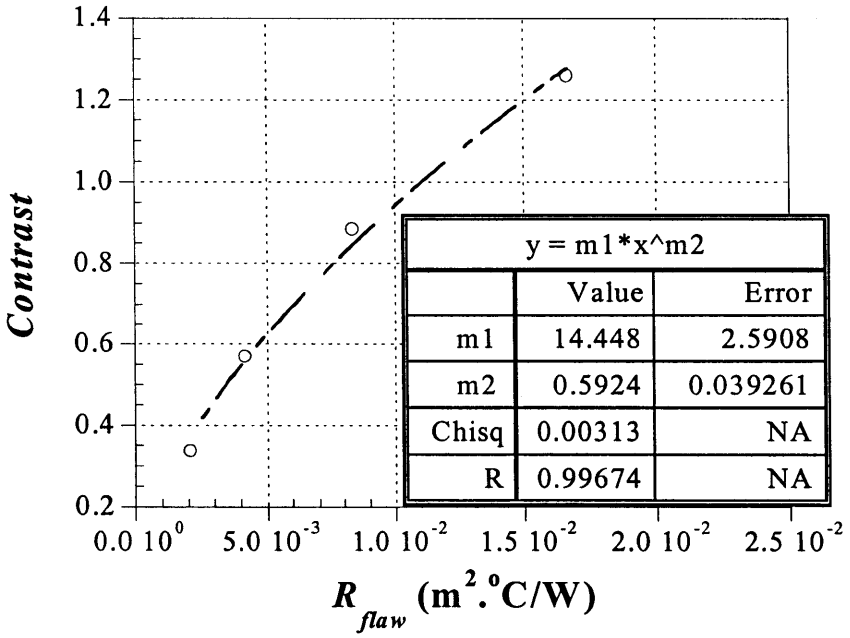

Fig. 4.87 Maximum thermal contrast as a function of flaw thermal resistance (Problems 77 through 80)

Figure 3.86 also illustrates that the time for maximum contrast t_c increases with increasing the flaw thermal resistance of the flaw. Further analysis indicated that the change of time for maximum contrast is greater for concrete spalls than for delaminations or debonds. For example,

for the case of concrete spalls, t_c varied by 12.9 s for an increase in R_{flaw} from 2.08×10^{-3} m^2·°C/W to 16.67×10^{-3} m^2·°C/W. Similar increases in R_{flaw} of delaminations only produced increases in t_c on the order of 3.2 s. Similarly to other kind of flaws, the increase in time for maximum signal for concrete spalls could also be expressed as a power function. The power function that fits the FEM output is

$$t_c = 9.8 + 154.2 R_{flaw}^{0.5} \tag{4.92}$$

Equation 4.92 and the FEM output of time for maximum contrast as a function of R_{flaw} are presented in Figure 4.88.

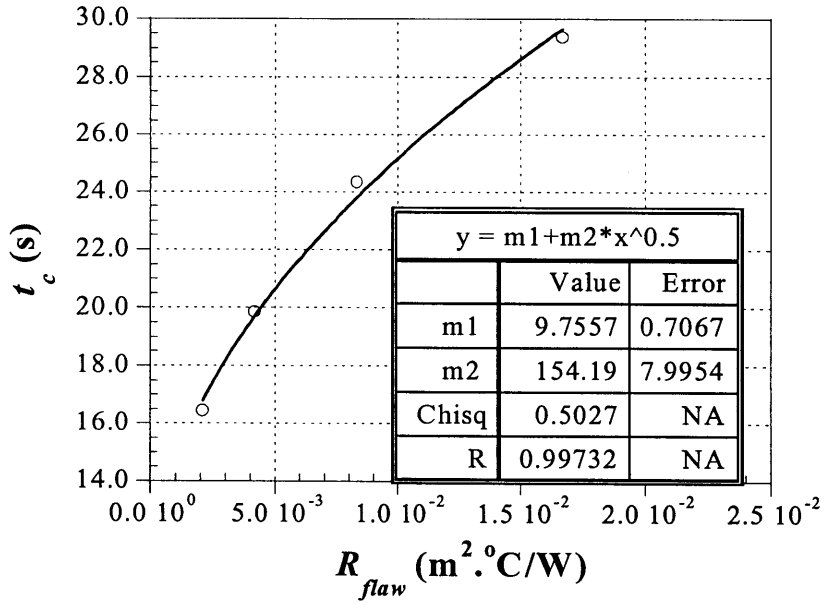

Fig. 4.88 Time for maximum contrast as a function of flaw thermal resistance (Problems 77 through 80)

4.6.4d Minimum Flaw Thickness

The minimum flaw thickness required for detection was also estimated for three different cases: ΔT_{max} equal to 0.1 °C, 5.0 °C, and 10.0 °C. The case of a maximum signal of 0.1 °C corresponds to the thermal sensitivity expected from most IR detectors. The second and third cases were considered to compensate for the fact that values reported by the FEM analysis are ideal since perfect layer interface was considered. The minimum thermal resistance of detectable flaws was computed using Equations 4.81, 4.85, and 4.89. The results from the calculations are presented in Table 4.29. Figure 4.89 presents the results of the minimum thickness of detectable flaws as a function of their depth.

Table 4.29 Minimum thermal resistance and thickness for detectable flaw

ΔT_{max} (°C)	Delamination (d = 0.5 mm)		Debond (d = 1.5 mm)		Spall (d = 2.5 mm)	
	R_{flaw} (m^2·°C/W)	Δz (mm)	R_{flaw} (m^2·°C/W)	Δz (mm)	R_{flaw} (m^2·°C/W)	Δz (mm)
0.1	1.23×10^{-6}	2.95×10^{-5}	2.08×10^{-6}	4.99×10^{-5}	5.53×10^{-6}	1.33×10^{-4}
5.0	5.55×10^{-4}	1.33×10^{-2}	6.09×10^{-3}	1.46×10^{-1}	2.73×10^{-2}	6.55×10^{-1}
10.0	1.64×10^{-3}	3.94×10^{-2}	2.50×10^{-2}	6.00×10^{-1}	1.23×10^{-1}	2.95×10^{0}

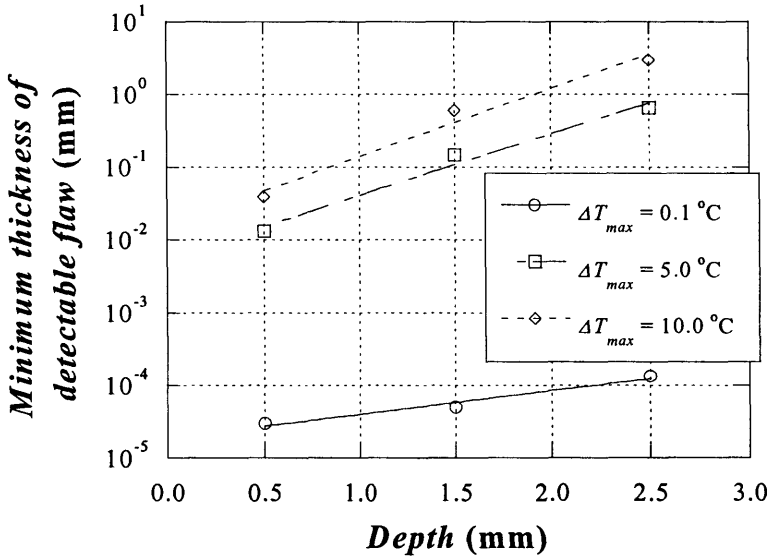

Fig. 4.89 Minimum thickness of detectable flaw as a function of flaw depth (mm)

The results presented in Figure 4.89 indicate that as the resolution of the signal increases (smaller ΔT_{max}), the minimum thickness for detectable flaws decreases. Exponential functions could be used to express the minimum thickness of detectable flaw. For the case of a thermal resolution of 0.1 °C (ΔT_{max} = 0.1 °C) the minimum width of detectable flaw could be expressed as

$$\Delta z_{min} = \left(1.88 \times 10^{-5}\right) e^{0.75 d_{flaw}} \tag{4.93}$$

where Δz_{min} is the minimum thickness of detectable flaws and d_{flaw} is the depth of the flaw.

For the case of a thermal resolution of 5.0 °C the following exponential function could be used to estimate the minimum thickness of detectable air flaws:

$$\Delta z_{min} = \left(5.83 \times 10^{-3}\right) e^{1.95 d_{flaw}} \tag{4.94}$$

Finally, for the case of a maximum thermal signal of 10.0 °C the following exponential function calculates the minimum thickness of detectable flaws:

$$\Delta z_{min} = \left(1.62 \times 10^{-2}\right) e^{2.16 d_{flaw}} \tag{4.95}$$

The results indicate that the minimum thickness of detectable flaws depends on the depth of the flaw and the maximum signal required to overcome noise in the measurement process. Moreover, very thin and "zero volume flaws may be undetectable using infrared thermography.

4.6.5 Summary

Summarizing, this section of the analysis rendered an understanding of the effect of flaw thickness or thermal resistance on the thermal response:

- The influence of flaw thermal resistance on the maximum surface temperature is significant in the case of delaminations but is very small on debonds and concrete spalls.
- The maximum surface temperature increases nonlinearly with increasing thermal resistance of the flaw. The behavior of the maximum surface temperature could be expressed as a power function.
- Flaws with higher thermal resistance produce higher thermal signal.
- Changes in maximum signal are more pronounced for flaws located closer to the surface.
- The time for maximum signal increases with increasing flaw thermal resistance.
- Variation in t_s with thermal resistance is greater for deeper than for shallow flaws.
- Flaws with higher thermal resistance generate higher thermal contrast.
- Increases in maximum contrast are more noticeable for delaminations close to the surface than for deeper flaws.
- Time for maximum contrast also increases nonlinearly with increasing flaw thermal resistance.
- The effect of flaw thermal resistance on the time for maximum contrast is greater for deep rather than shallow flaws.
- The effect of flaw thermal resistance on the different thermal parameters (T_{max}, ΔT_{max}, t_s, Contrast, and t_c) can be represented as power functions.
- The minimum thickness of detectable flaws depends on the depth of the flaw and the maximum signal required to overcome noise in the measurement process.
- Very thin and "zero volume flaws may be undetectable.

The next series of simulations involve the study of the effect and estimation of flaw size.

4.7 Parametric Study No.5: Effect of the Width of the Flaw and Estimation of Width of the Flaw

The size of debonds or delaminations could be the determining factor on the proper performance of the FRP composite bonded to concrete. With this concern, minimum requirements on allowable flaw size have been introduced by the International Conference of Building Officials Evaluation Services (ICBO ES).

Among the conditions of acceptance, the ICBO ES states that small air flaw of diameter up to 3.2 mm occur naturally on FRP systems. Flaws of this size and smaller do not require repair. Delaminations with areas of 13 cm^2 or smaller are also allowed. Flaws larger than 13 cm^2, however, should be repaired.

Based on the need to determine the size of the internal flaw, the final parameter investigated was the width of the flaw. The fifth parametric study had the following objectives:

- Understand the effects of flaw width on the thermal response
- Establish minimum width of detectable flaw.

Three different sets of problems were performed which included a total of 12 finite element models.

4.7.1 Geometry of Model

The test object consisted of a 50 mm long by 20 mm thick concrete slab. Three layers of carbon FRP were bonded to the top surface of the concrete. Each layer of FRP was 0.5 mm thick. Also, each layer of composite was oriented at 90° from its adjacent ply. An internal flaw was located at the center of the cross section of the flaw. The thickness of the flaw was 0.1 mm. The depth of the flaw was varied to include delaminations 0.5 mm deep, debonds 1.5 mm deep, and concrete spalls 2.5 mm deep. Using plane symmetry about the center of the test object, the test was simplified. Thus, flaws ranging from 3.0 mm to 25 mm wide were investigated by modeling flaws 1.5 mm to 12.5 mm wide in a half space. Figure 4.90 illustrates the geometry of the different models analyzed in this parametric study.

Plane two-dimensional modeling was again used in parametric study No.5. The model was meshed using 2-D quadrilateral thermal solid elements containing 4 nodes. Each node has one degree of freedom, temperature. The model was meshed using a global mesh size of 0.5 mm. Similarly to previous simulations, the mesh was refined in the y-direction. Thinner elements were located at the FRP layers, the flaw, and the concrete close to the interface with the FRP. The thickness of the elements increased towards the bottom of the concrete slab where the effect of the thermal front tends to dissipate.

The models were arranged into three different groups. The first group of simulations focused on the study of the effect of size or width on delaminations located 0.5 mm deep. The second set involved the investigation of the effect of the width of debonds which were located at a depth of 1.5 mm. The third, and lasts, group involved the study of concrete spalls located 2.5 mm from the surface of the test object.

In each set of models, the size of the half-flaw was varied between 12.5 mm and 1.5 mm. Table 4.30 summarizes the specific width and location of the subsurface flaws for the problems in Parametric No.5

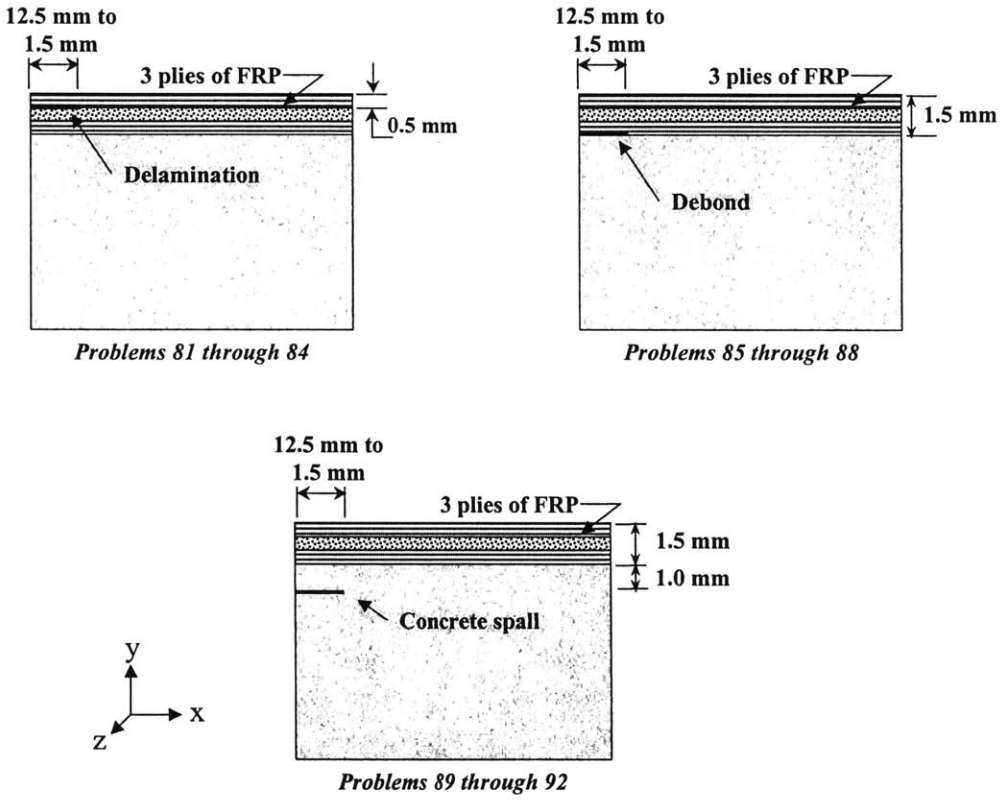

Fig. 4.90 Summary of geometry of models (Parametric No.5)

Table 4.30 Geometry for problem sets in Parametric No.5

Problem	Flaw depth (mm)	Actual flaw width (mm)	Simulation flaw width (mm)
81	0.5	25.0	12.5
82	0.5	14.0	7.0
83	0.5	5.0	2.5
84	0.5	3.0	1.5
85	1.5	25.0	12.5
86	1.5	14.0	7.0
87	1.5	5.0	2.5
88	1.5	3.0	1.5
89	2.5	25.0	12.5
90	2.5	14.0	7.0
91	2.5	5.0	2.5
92	2.5	3.0	1.5

4.7.2 Material Properties

The material properties of the simulations were those of concrete for the substrate, carbon FRP for the bonded composite, and air for the internal flaw. The physical and thermal properties of these materials are presented in Table 3.2.

4.7.3 Thermal Loading and Boundary Conditions

The models were defined as transient heat transfer analyses. The models were subjected to a uniform initial temperature of 23 °C. A square pulse of magnitude 20,000 W/m^2 and duration 2 s was applied to the top surface of the model. The remaining free surfaces were subjected to adiabatic conditions ($dT/dx = 0$ and $dT/dz = 0$). The simulations were ran for up to 30 s.

Automatic time stepping was chosen for all the models. The initial time step was 0.009 s, which conforms with the guidelines established by Ansys for the mesh size applied to the current set of models. The maximum and minimum time steps were 0.1 s and 0.008 s, respectively.

4.7.4 Results

4.7.4a Delaminations

The first set of simulations involved the study of the effect of delamination size on the thermal response. As previously mentioned, the delamination was located on the top layer of FRP. The actual width of the flaw was varied between 25.0 mm and 3.0 mm. As a reminder, only half of the test object was modeled in order to take advantage of symmetry and thus simplify the computation effort. Thus, the flaw width in the simulations was varied between 12.5 mm to 1.5 mm. For the purpose of clarity, the results are reported for the actual size of the flaw instead of the modeled width.

First, the model output was analyzed to compute the thermal response as a function of time. Figures 4.91 and 4.92 illustrate both, the thermal signal and thermal contrast as a function of time, respectively.

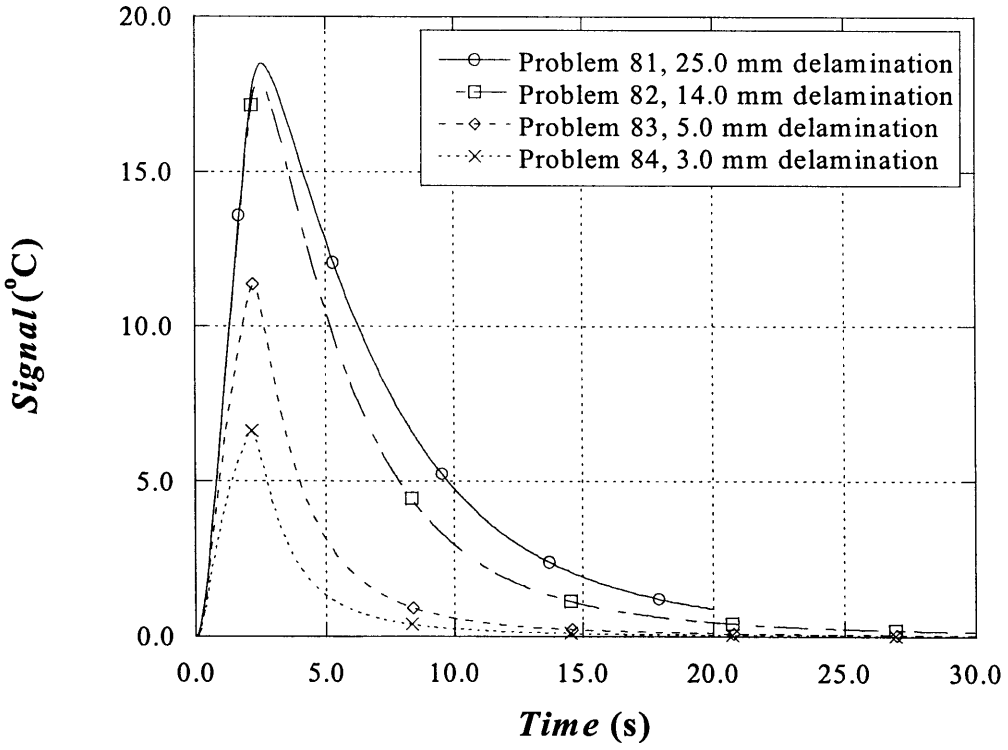

Fig. 4.91 Thermal signal for simulations involving delaminations of different widths (Problems 81 through 84)

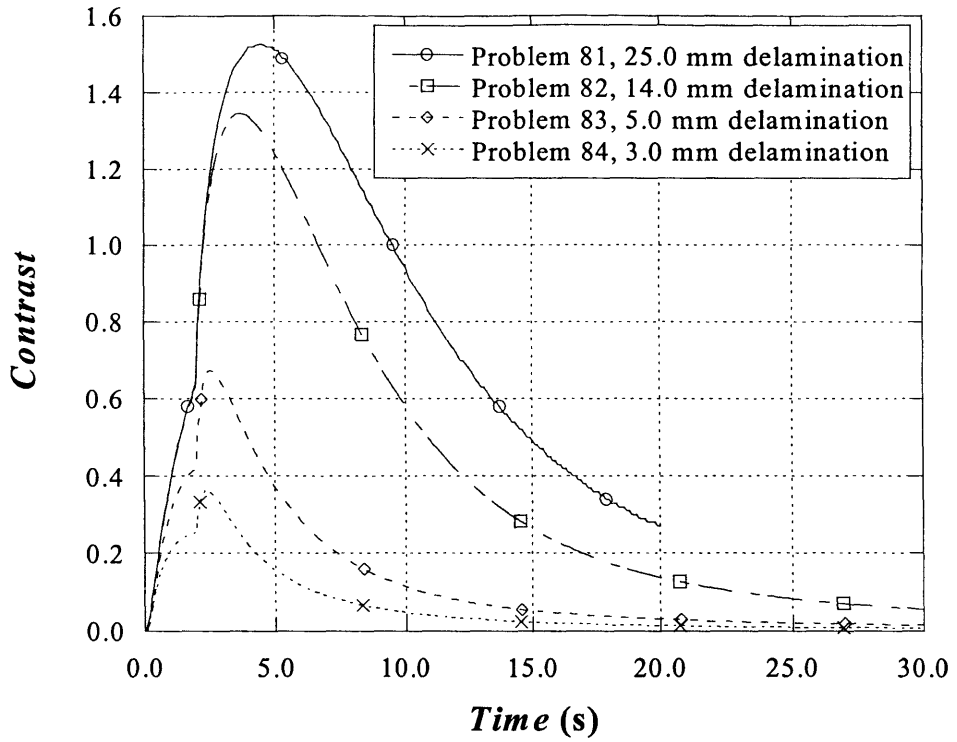

Fig. 4.92 Thermal contrast for simulations involving delaminations of different width (Problem 81 through 84)

Based on the transient response illustrated above, the thermal response parameters T_{max}, t_s, ΔT_{max}, t_c, and contrast were obtained. The computed parameters are presented in Table 4.31.

Table 4.31 Results of thermal responses for models involving delaminations

Problem	Depth (mm)	Width (mm)	T_{max} (°C)	Maximum Signal		Maximum Contrast	
				t_s (s)	ΔT_{max} (°C)	t_c (s)	$\Delta T/\Delta T_{backgr}$
81	0.5	25.0	64.9	2.5	18.5	4.4	1.53
82	0.5	14.0	64.6	2.4	17.9	3.7	1.35
83	0.5	5.0	59.4	2.2	11.3	2.6	0.67
84	0.5	3.0	55.0	2.1	6.6	2.4	0.36

The results summarized in Table 4.31 indicate that the maximum surface temperature increases nonlinearly with increasing delamination width or size. The increase in T_{max} varies by 9.9 °C for an increase in width of 22.0 mm. The surface temperature, however, became asymptotic for test objects containing flaws 14.0 mm or wider.

The FEM output for the maximum surface temperature is presented in Figure 4.93.

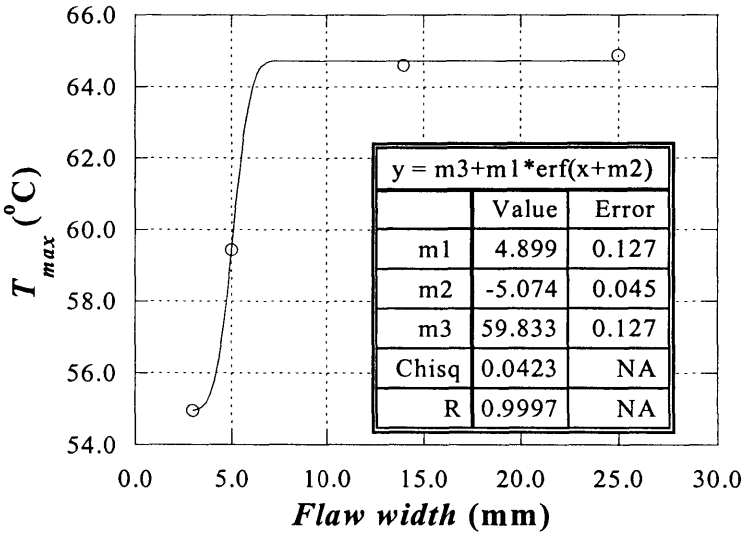

Fig. 4.93 Maximum surface temperature as a function of flaw width (Problems 81 through 84)

The results from Table 4.31 also indicates that the maximum signal increases with increasing flaw length. Figure 4.94 illustrates the FEM output for ΔT_{max}.

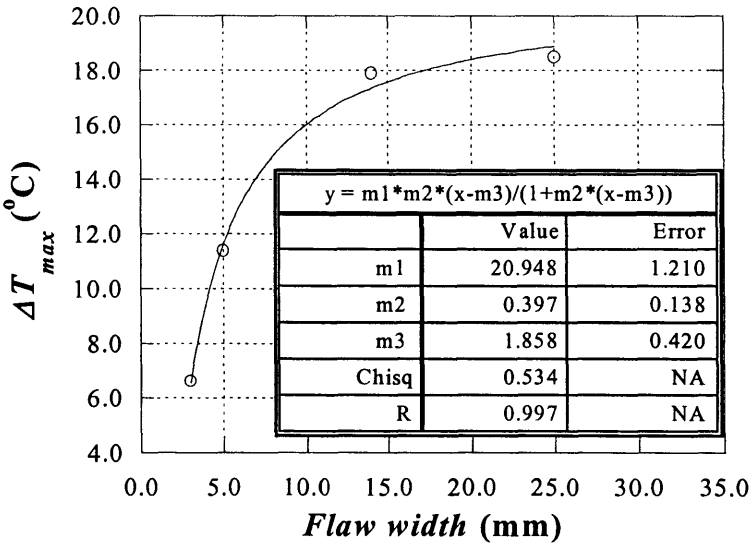

Fig. 4.94 Maximum signal as a function of flaw width (Problems 81 through 84)

The increase in maximum signal could be represented as a hyperbolic function of the following form:

$$\Delta T_{max} = 20.948 \frac{0.397(w - 1.858)}{1 + 0.397(w - 1.858)} \tag{4.93}$$

where w is the width of the internal flaw. The output indicates that the magnitude of the maximum signal increase from 6.6 °C to 18.5 °C with an increase in flaw width from 3.0 mm to 25.0 mm.

The time for maximum signal also increases with increasing flaw width. The change in t_s, however, is less than a second for the increase in width investigated in this study. Specifically, the time for maximum signal only increased from 2.1 s to 2.5 s. Thus, the effect of flaw width in t_s is negligible. The change in the time for maximum signal could be expressed as the following power function:

$$t_s = 1.043 + 0.922 w^{0.151} \tag{4.94}$$

The maximum thermal contrast shows the same hyperbolic trend than the maximum signal. The FEM output indicates that the maximum contrast increased from 0.33 to 1.18 when the width increased from 14.0 mm to 25.0 mm. The change in maximum thermal contrast as a function of flaw width is illustrated in Fig. 4.95.

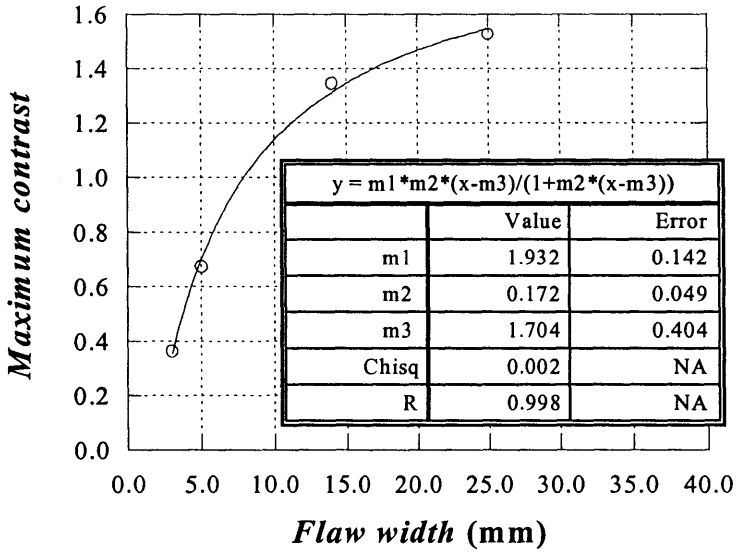

Fig. 4.95 Maximum contrast as a function of flaw width
(Problems 81 through 84)

Like the case of maximum signal, the increase in maximum signal as a function of flaw width could be expressed as a hyperbolic function

$$Max.\ Contrast = 1.932 \frac{0.172\ (w - 1.704)}{1 + 0.172\ (w - 1.704)} \tag{4.95}$$

The time for maximum contrast is higher than the time for maximum signal. This behavior is also reported in previous parametric studies. The FEM output of this investigation indicates that t_c increases with increasing flaw width. The increase in t_c is 2 s when the flaw width increased from 3.0 mm to 25.0 mm. The output is presented in Figure 4.96.

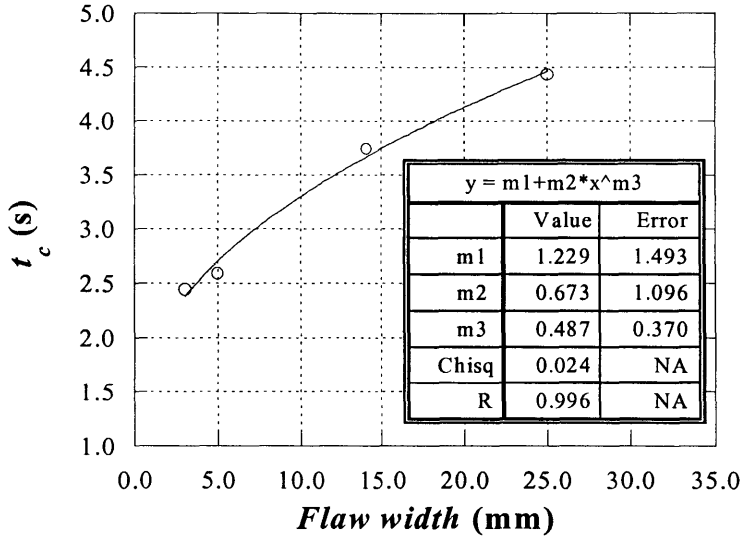

Fig. 4.96 Time for maximum contrast as a function of flaw width (Problems 81 through 84)

The simulation output could be represented as the following power function

$$t_c = 1.229 + 0.673 w^{0.487} \tag{4.96}$$

Analysis of the FEM output is also performed to estimate the width of the flaw. The distance versus surface temperature plot was constructed to estimate the size of the internal flaw. As can be observed on Fig. 4.97, a typical temperature-distance plot has an inflection point. The location of the inflection point may be used to estimate the location of the edge of the subsurface flaw.

The location at which the inflection point is located in the distance vs. temperature curve can be computed by setting the second derivative of the curve equal to zero

$$\frac{\partial^2 T}{\partial x^2} = 0 \quad at\ w_{estimate} \tag{4.97}$$

where T is the surface temperature, x is the distance from the center line along the x-axis, and $w_{estimate}$ is the estimation of the distance of the edge of the flaw from the center line.

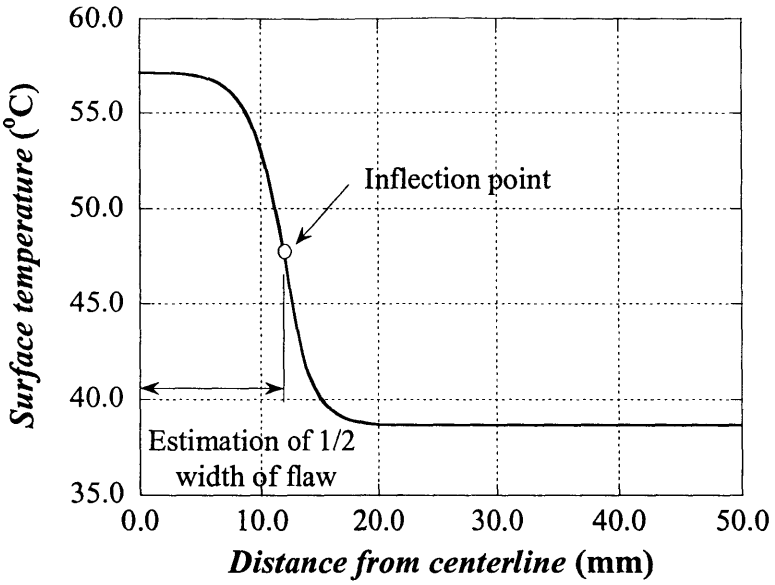

Fig. 4.97 Estimation of width of flaw

The surface temperature output is plotted for all four simulations in Fig. 4.98. The location of the inflection points from each curve could be computed numerically. This approach provides a good estimate of the size of the defect. The results of the estimation using the location of the inflection point are presented in Table 4.32.

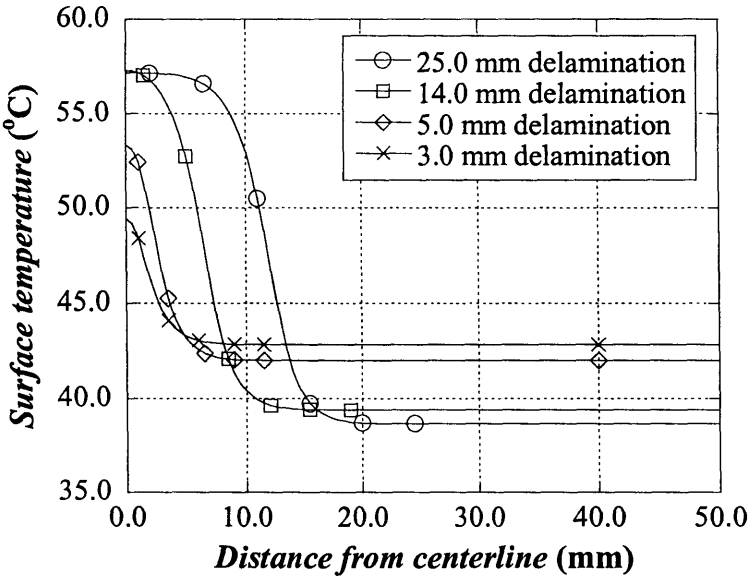

Fig. 4.98 Estimation of flaw width for simulations involving delaminations (Problems 81 through 84)

Table 4.32 Estimation of flaw width for simulations involving delaminations

Problem	Actual flaw width (mm)	Estimated flaw width (mm)	% Error
81	25.0	24.0	4
82	14.0	13.1	6
83	5.0	4.6	8
84	3.0	3.1	-3

Therefore, the analysis of the FEM output indicates that delaminations of different width are easily detected. Although the thermal signal decreases with decreasing w, small delaminations 5.0 mm wide produce ΔT_{max} on the order of 7 °C. Additionally, the estimation of their size renders errors smaller than 8%. The range of error appears acceptable for the purpose of the evaluation of delaminations, since the width estimations are within a millimeter from the actual width of the flaw.

4.7.4b Debonds

The second set of simulations corresponded to test objects containing debonds of different length. Debond length was varied between 25.0 mm and 3.0 mm.

The simulation output was recorded at every time step of the transient analysis. The surface temperature above the flaw and in the background was recorded in order to calculate the thermal signal and contrast as a function of time. Figures 4.99 and 4.100 illustrate the time history output for the thermal signal and thermal contrast, respectively.

Observation of the simulation output illustrated in Figures 4.99 and 4.100 yields the required thermal response parameters. Table 4.33 summarizes the response parameters for the set of simulations involving debonds.

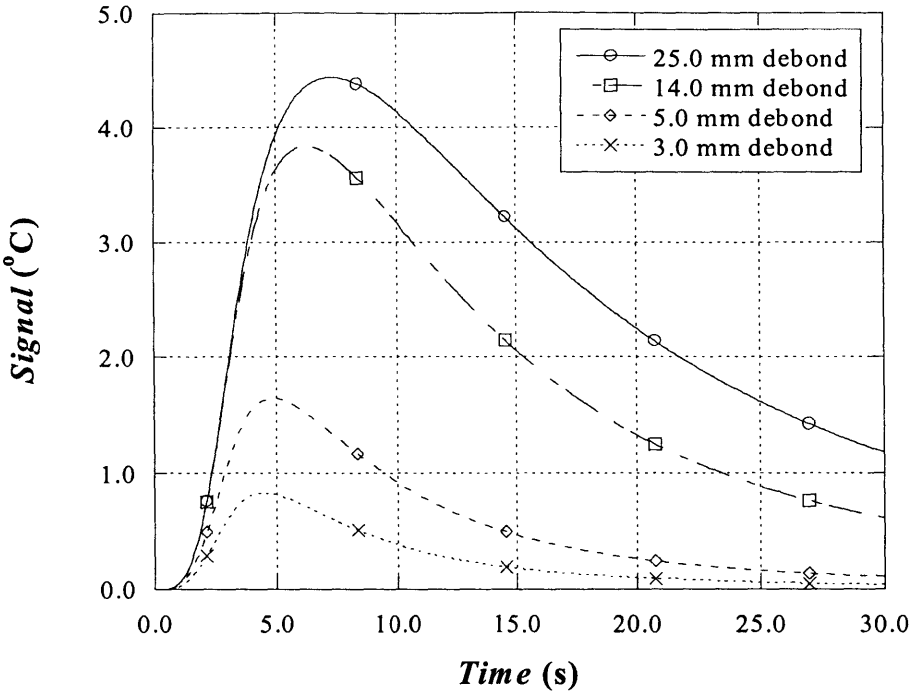

Fig. 4.99 Thermal signal for simulations involving debonds of different width (Problems 85 through 88)

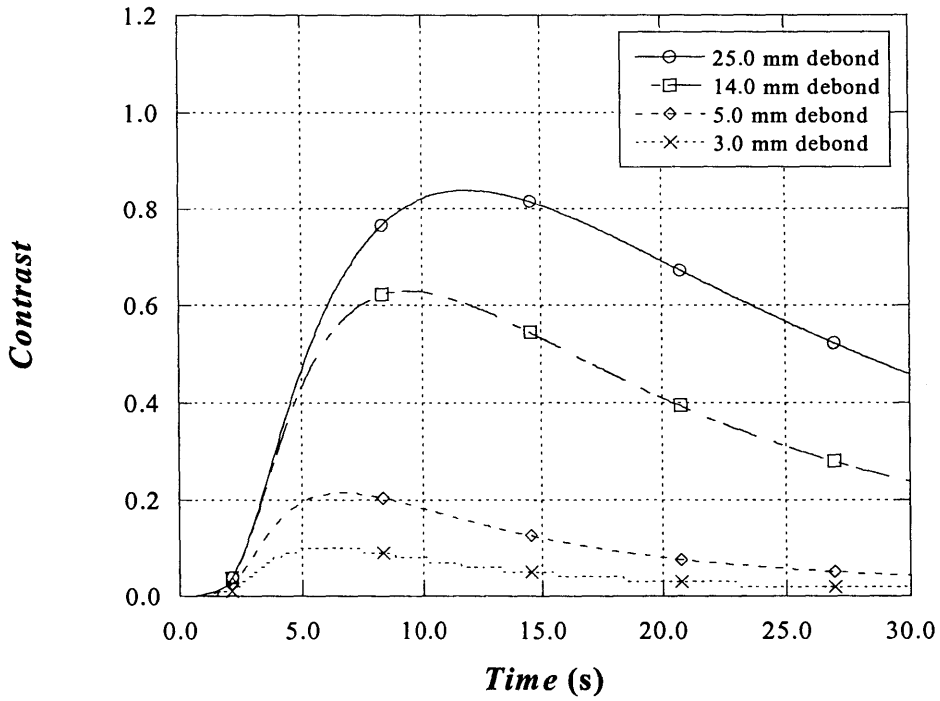

Fig. 4.100 Thermal contrast for simulations involving debonds of different width (Problems 85 through 88)

Table 4.33 Results of thermal responses for models involving debonds

Problem	Depth (mm)	Width (mm)	T_{max} (°C)	Maximum Signal		Maximum Contrast	
				t_s (s)	ΔT_{max} (°C)	t_c (s)	$\Delta T/\Delta T_{backgr}$
85	1.5	25.0	49.1	7.3	4.4	11.8	0.84
86	1.5	14.0	49.1	6.2	3.8	9.4	0.63
87	1.5	5.0	48.9	4.8	1.6	6.6	0.22
88	1.5	3.0	48.7	4.4	0.8	5.9	0.10

The results show that the maximum surface temperature increases nonlinearly with increasing width of the flaw. For the simulations involving debonds, T_{max} increases only by 0.4 °C with an increase in flaw width from 3.0 mm to 25.0 mm. The surface temperature becomes asymptotic at 49.07 °C for flaws wider than 4.0 mm. The FEM output is presented in Figure 4.101.

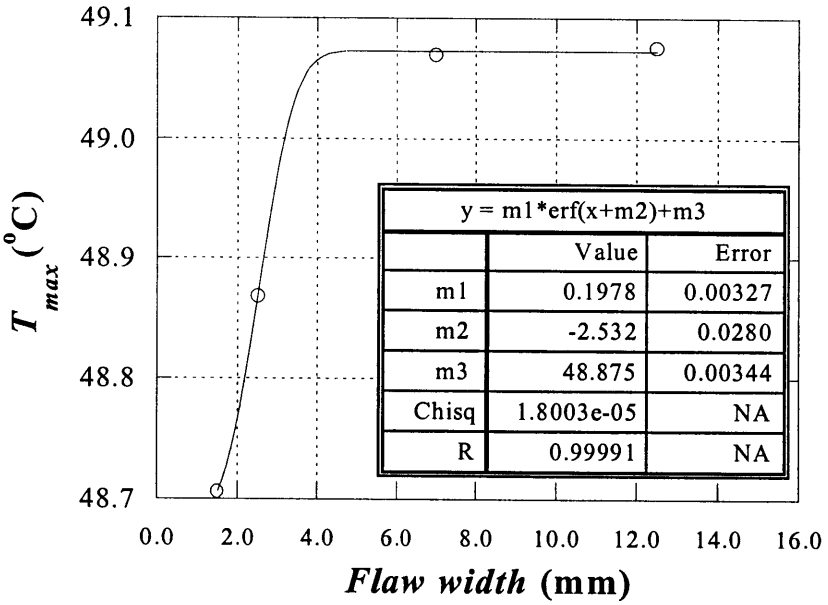

Fig. 4.101 Maximum surface temperature as a function of flaw width (Problems 85 through 88)

The results listed in Table 4.32 also show that the maximum thermal signal increases with increasing flaw width. The FEM output and its corresponding best-fit curve are presented in Fig. 4.102.

The increase in ΔT_{max} for debonds could be expressed as the following hyperbolic function of the width of the flaw:

$$\Delta T_{max} = 5.947 \frac{0.136\,(w - 1.897)}{1 + 0.136\,(w - 1.897)} \tag{4.98}$$

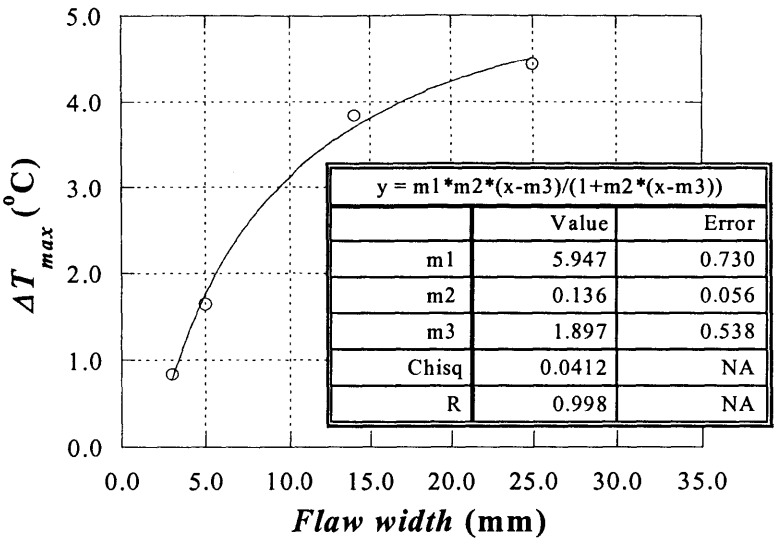

Fig. 4.102 Maximum signal as a function of flaw width
(Problems 85 through 88)

The time to reach the maximum signal also increases with increasing flaw width. The time for maximum signal, however, increases more significantly for debonds than for delaminations. For example, t_s increases from 4.4 s to 7.3 s for debonds 3.0 mm to 25.0 mm wide. The simulation output is presented in Figure 4.103.

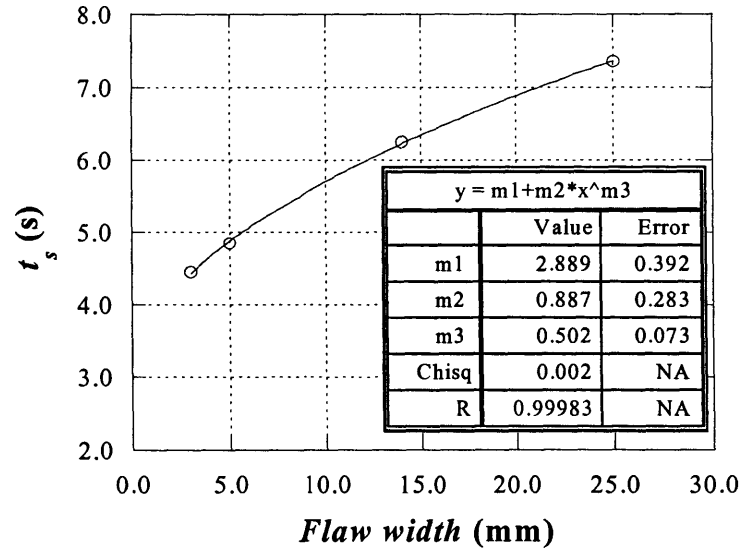

Fig. 4.103 Time for maximum signal as a function of
flaw width (Problems 85 through 88)

The change in t_s as a function of flaw width could be expressed as the following power function:

$$t_s = 2.889 + 0.887\, w^{0.502} \tag{4.99}$$

Similarly to other response parameters, the maximum thermal contrast increases with increasing flaw width. Moreover, the maximum contrast increases from 0.09 for the test object containing a 3.0 mm wide flaw to 0.01 for the test object having a flaw 25.0 mm wide. Figure 4.104 illustrates the maximum contrast output extracted from the simulations. The output could be expressed as the following hyperbolic function:

$$Max.\ Contrast = 1.416\frac{0.064\,(w-1.932)}{1+0.064\,(w-1.932)} \tag{4.100}$$

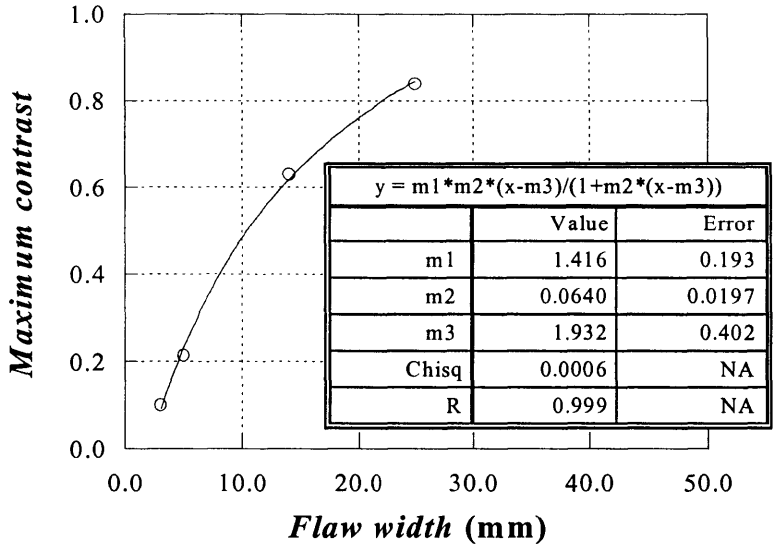

Fig. 4.104 Maximum contrast as a function of flaw width
(Problems 85 through 88)

Finally, the time for maximum contrast also increases with increasing flaw width. The increase could be expressed as the following power function:

$$t_c = 3.707 + 1.113\,w^{0.619} \tag{4.101}$$

Figure 4.105 reproduces the FEM output for t_c and Eq. 4.101

Similar to the case of delaminations, the surface temperature along the x-axis is plotted in order to estimate the width of the flaw. Figure 4.106 represents the distance versus surface temperature for the simulations involving debonds.

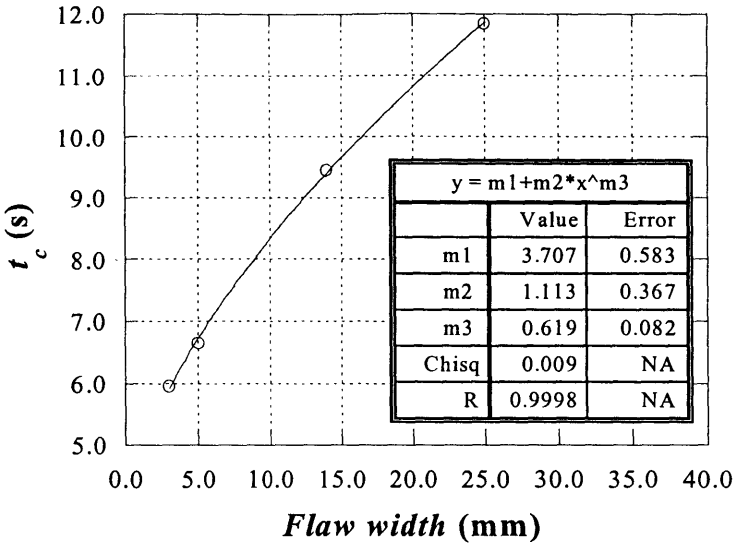

Fig. 4.105 Time for maximum contrast as a function of flaw width (Problems 85 through 88)

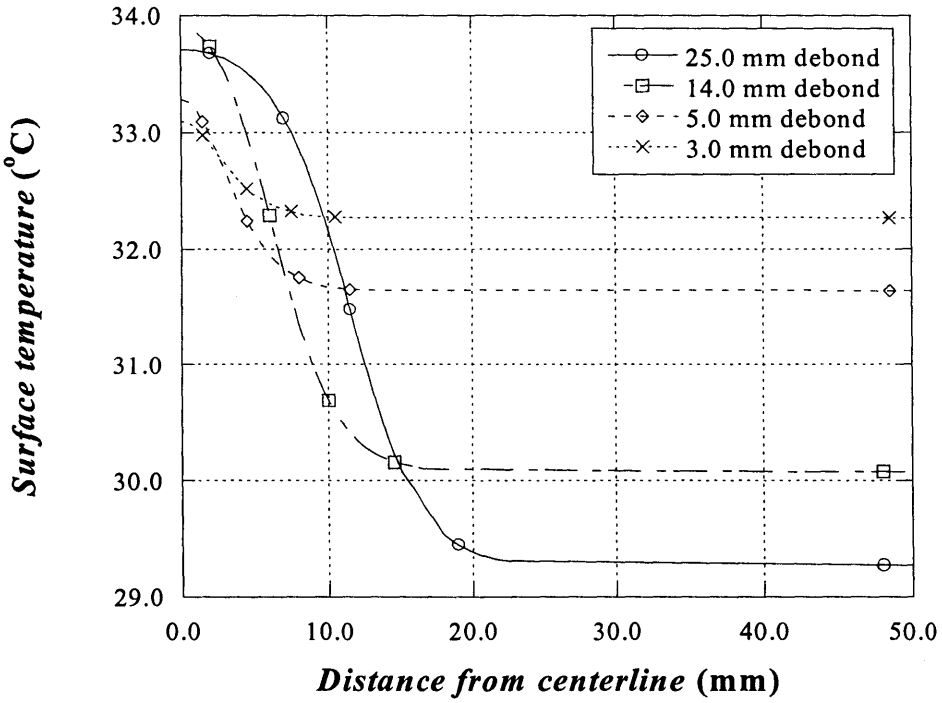

Fig. 4.106 Estimation of flaw width for simulation involving debonds (Problems 85 through 88)

The flaw size is estimated by determining the location at which the second derivative of the curve was equal to zero. The results of the estimation are presented in Table 4.34.

Table 4.34 Estimation of flaw width for simulations involving debonds

Problem	Actual flaw width (mm)	Estimated flaw width (mm)	% Error
85	25.0	23.2	7
86	14.0	12.5	11
87	5.0	5.7	-14
88	3.0	4.9	-63

The results from the width estimation provide some interesting facts. For example, the output presented in Table 4.34 indicate that the flaw width was underestimated for the cases of flaws 25.0 mm and 14.0 mm wide. On the other hand, the width is overestimated for the smallest flaws. The over- or underestimation is only on the order of 2.00 mm for the poorest case. This level of error could be considered negligible in the evaluation of the bond between FRP composites and concrete.

4.7.4c Concrete Spalls

The last set of simulations involved the evaluation of the effect of spall width on the thermal response. The concrete spall was located 2.5 mm from the surface of the test object, that is, 1.0 mm below the interface between the FRP and the concrete.

The first step on the analysis of the FEM output was to investigate the transient behavior of the thermal signal and thermal contrast. The thermal signal and thermal contrast as a function of time are presented in Figures 4.107 and 4.108.

The thermal response was analyzed to identify the response parameters: T_{max}, ΔT_{max}, t_s, maximum contrast, and t_c.

Table 4.35 lists the response parameters for the last set of simulations.

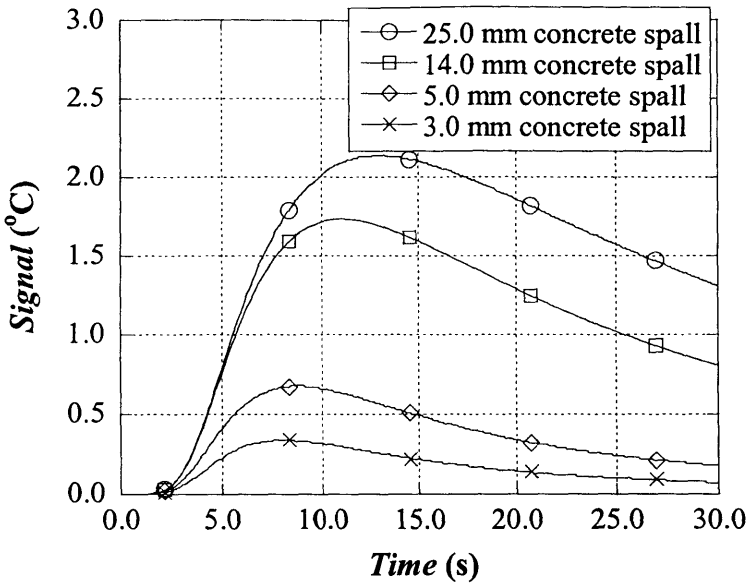

Fig. 4.107 Thermal signal for simulations involving concrete spalls of different width (Problems 89 through 92)

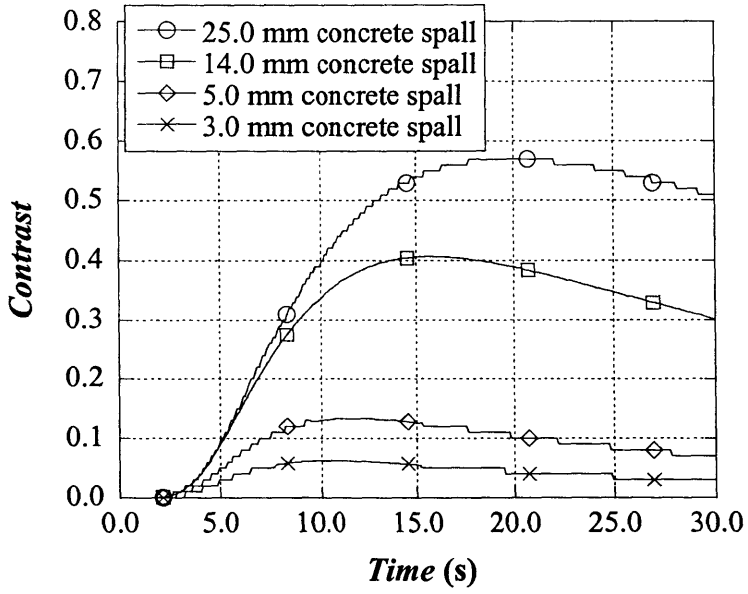

Fig. 4.108 Thermal contrast for simulations involving concrete spalls of different width (Problems 89 through 92)

Table 4.35 Results of thermal responses for models involving concrete spalls

Problem	Depth (mm)	Width (mm)	T_{max} (°C)	Maximum Signal		Maximum Contrast	
				t_s (s)	ΔT_{max} (°C)	t_c (s)	$\Delta T/\Delta T_{backgr}$
89	2.5	25.0	48.5	12.9	2.1	19.6	0.57
90	2.5	14.0	48.5	11.0	1.7	15.7	0.41
91	2.5	5.0	48.5	8.7	0.6	11.6	0.13
92	2.5	3.0	48.5	7.9	0.3	10.6	0.06

As Table 4.35 indicates, the maximum surface temperature is not affected by changes in the width of the concrete spalls. The width of the flaw, however, affects the magnitude of maximum signal. It is important to note that the maximum signal only reaches a magnitude of 2.1 °C for the largest spall simulated and 0.3 °C for the smallest flaw. This behavior suggested that small concrete spalls may be difficult to detect.

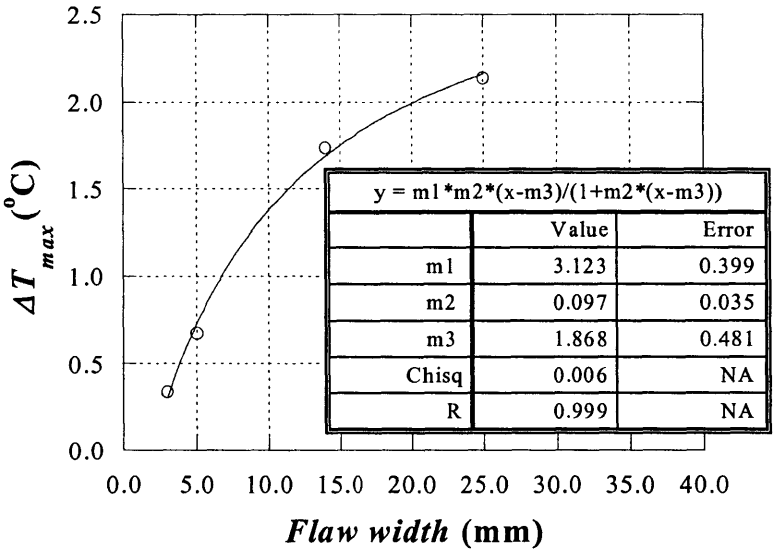

Fig. 4.109 Maximum signal as a function of flaw width (Problems 89 through 91)

The maximum thermal signal as a function of the spall width is presented in Figure 4.109. Similar to the cases of delaminations and debonds, ΔT_{max} for concrete spalls could be expressed as the following hyperbolic function

$$\Delta T_{max} = 3.123 \frac{0.097\,(w - 1.868)}{1 + 0.097\,(w - 1.868)} \tag{4.102}$$

The time to reach the maximum thermal signal increases nonlinearly with increasing flaw width. The output recorded for the last set of simulations is presented in Figure 4.110.

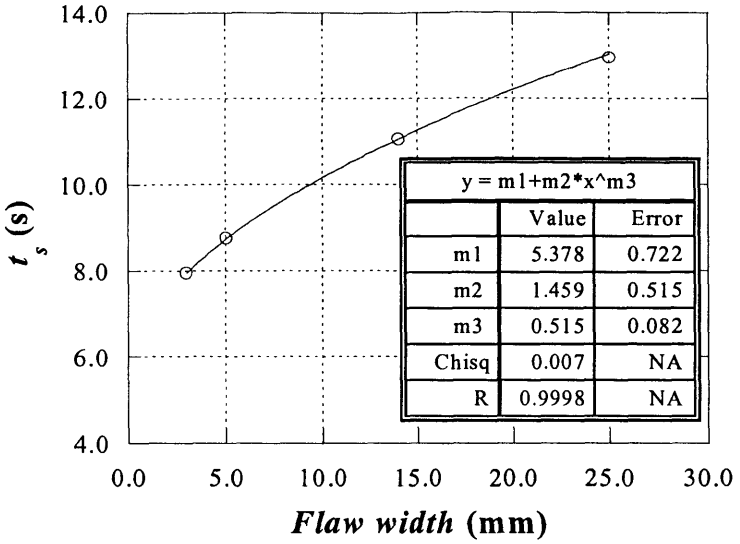

Fig. 4.110 Time for maximum signal as a function of flaw width (Problems 89 through 92)

The increase in t_s as a function of flaw width could be represented with the following power function:

$$t_s = 5.378 + 1.459\, w^{0.515} \tag{4.103}$$

Examination of the thermal contrast indicates that the magnitude of the maximum contrast also increases nonlinearly with increasing width of the flaw. The output of the maximum contrast as a function of spall width is presented in Figure 4.111.

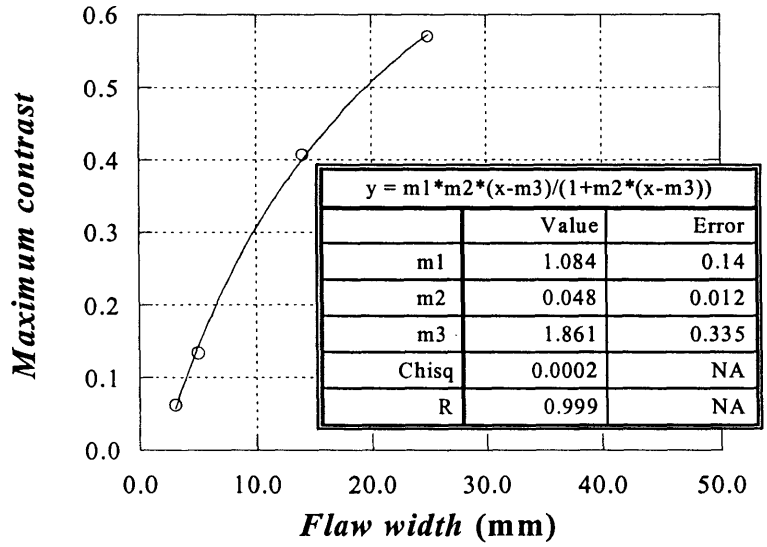

Fig. 4.111 Maximum contrast as a function of flaw width (Problems 89 through 92)

As illustrated in Figure 4.111, the output for maximum contrast could be expressed as the following hyperbolic function of the flaw width

$$Max.\,Contrast = 1.084\,\frac{0.048\,(w-1.861)}{1+0.048\,(w-1.861)} \tag{4.104}$$

The maximum contrast is reached at time t_c. The time for maximum contrast increases with increasing width of the concrete spall. The time rises from 10.6 s to 19.6 s for flaws that were 3.0 mm and 25.0 mm wide, respectively.

The output for the four simulations involving concrete spalls is presented in Figure 4.112.

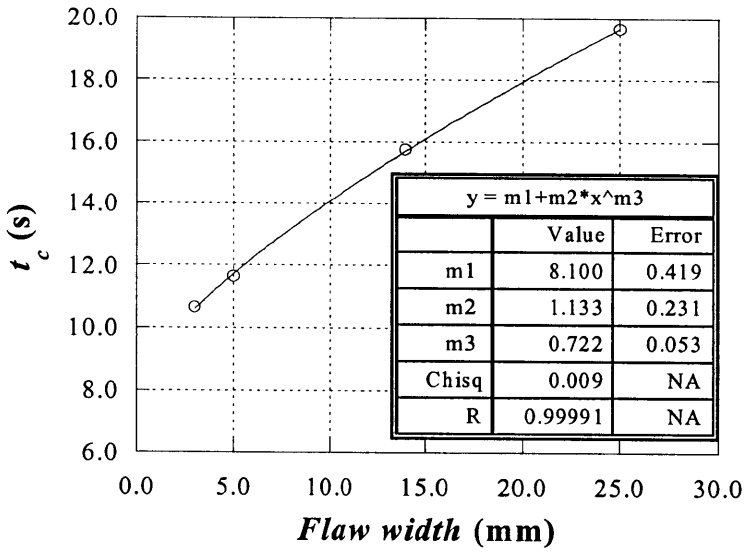

Fig. 4.112 Time for maximum contrast as a function of flaw width (Problems 89 through 92)

For the simulations involving concrete spalls, the time for maximum contrast could be expressed as the following power function:

$$t_c = 8.100 + 1.133\,w^{0.722} \tag{4.105}$$

For the purpose of width estimation, the surface temperature output is evaluated at time t_s. The surface temperature is plotted as a function of the distance from the centerline of the flaw as presented in Figure 4.113.

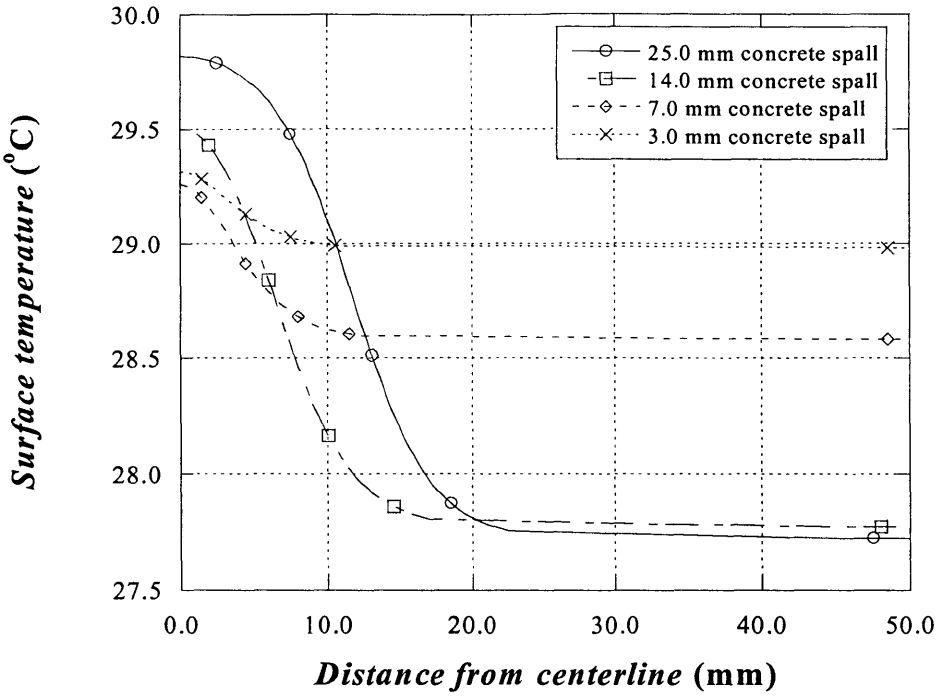

Fig. 4.113 Estimation of flaw width for simulations involving spalls (Problems 89 through 92)

The location of the inflection point on each curve provides the estimation of the half-width of the corresponding subsurface flaw. The calculated flaw width and the percent error corresponding to its comparison to the actual width of the flaw are presented in Table 4.36.

Table 4.36 Estimation of flaw width for simulations involving concrete spalls

Problem	Actual flaw width (mm)	Estimated flaw width (mm)	% Error
89	25.0	23.3	7
90	14.0	12.7	9
91	5.0	6.7	-34
92	3.0	6.0	-100

The results listed in Table 4.36 show that the width of larger concrete spalls (14.0 mm to 25.0 mm) tends to be underestimated while the width of smaller spalls (5.0 mm to 3.0 mm) tends to be overestimated. The larger percent error is observed on the smallest spall. The 3.0 mm wide spall is estimated to be 6.0 mm wide, thus the overestimation was 100%.

Large sized flaws are the most critical for the adequate performance of the structures, thus their detection and characterization is essential. The results reveal that special consideration should be

taken with large spalls since their width tends to be underestimated. The error in estimation, however, is less than 10%.

For the case of small concrete spalls, the results demonstrate that their width tend to be overestimated. The results for problem 92 indicate an error in estimation of 100%, which corresponds to a 3.0 mm overestimation.

4.7.4d Comparison of width estimations

The results presented in the previous sections indicate that flaw width may be under or over estimated depending on the size of the flaw. For example, the width of large flaws tends to be underestimated while the width of smaller flaws tends to be overestimated.

For the purpose of analysis, the estimation error for each simulation was plotted as a function of the actual width of the flaw. Table 4.37 presents the estimation error for each kind of flaw. The data are illustrated in Figure 4.114.

Table 4.37 Estimation error of flaw width

Problem	Depth (mm)	Actual width (mm)	Estimated width (mm)	Estimation error (mm)
81	0.5	25.0	24.0	-1.0
82	0.5	14.0	13.1	-0.9
83	0.5	5.0	4.6	-0.4
84	0.5	3.0	3.1	+0.1
85	1.5	25.0	23.2	-1.8
86	1.5	14.0	12.5	-1.5
87	1.5	5.0	5.7	+0.7
88	1.5	3.0	4.9	+1.9
89	2.5	25.0	23.3	-1.7
90	2.5	14.0	12.7	-1.3
91	2.5	5.0	6.7	+1.7
92	2.5	3.0	6.0	+3.0

Plotting the output provided some insight into the behavior. For example, the estimation of error could be expressed as a hyperbolic function of the actual flaw width. The results presented in Figure 4.114 illustrate that the error in estimation increases with the depth of the flaw. That is, the estimation of delamination width is more accurate and precise than the estimation of debonds and concrete spalls. As illustrated in Figure 4.115, the reason for the smaller error in the estimation of delaminations is that the 2-dimensional effect of the thermal wave is less pronounced than for spalls. Estimation errors also tend to be larger for wider flaws than for smaller flaws.

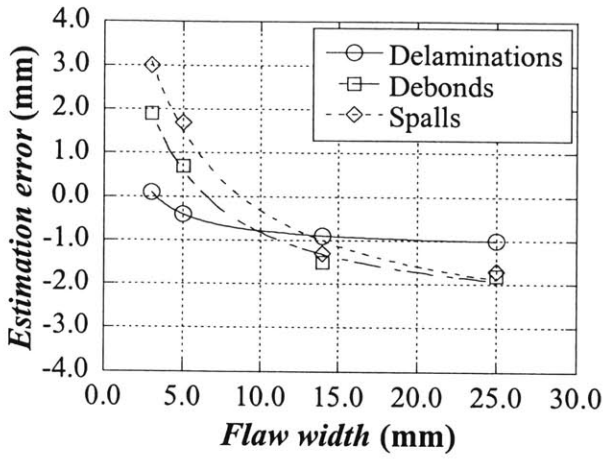

Fig. 4.114 Estimation error as a function of flaw width

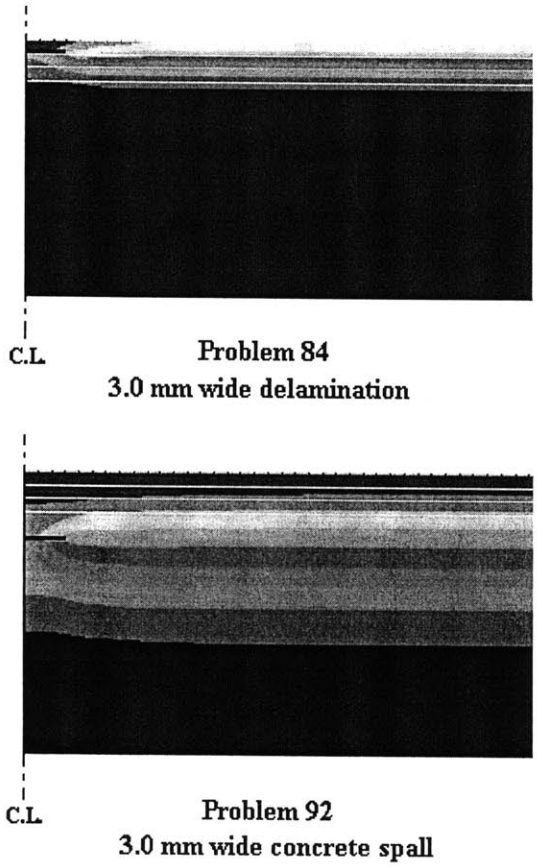

Fig. 4.115 Thermal fronts at time for maximum signal for simulations containing 3.0 mm wide delaminations and concrete spalls (Problems 84 and 92)

For the purpose of comparison, the estimation error is plotted as a function of estimated flaw width. The error as a function of estimated flaw width is presented in Figure 4.116 for the delaminations, debonds, and concrete spalls investigated in this parametric study.

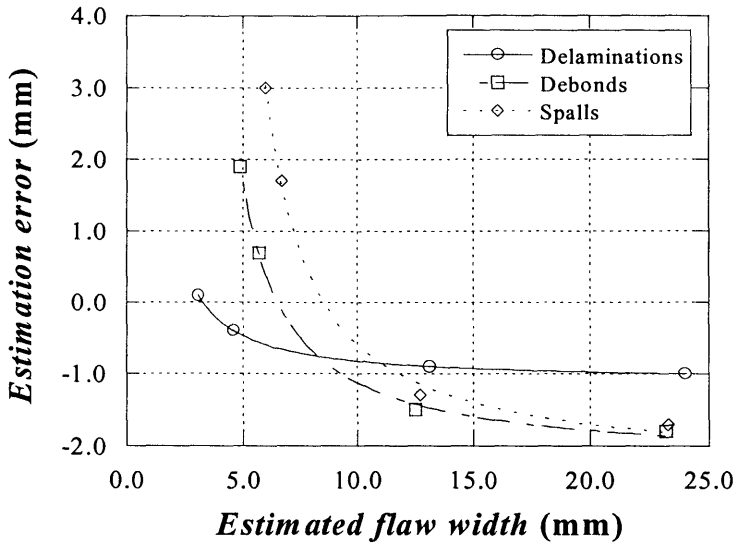

Fig. 4.116 Estimation error as a function of estimated flaw width

The output plotted in Figure 4.116 could be expressed as the following hyperbolic functions:

$$Error_{delamination} = -1.11 \frac{0.43\left(w_{estimate} - 3.29\right)}{1 + 0.43\left(w_{estimate} - 3.29\right)} \tag{4.106}$$

for delaminations,

$$Error_{debonds} = -2.24 \frac{0.29\left(w_{estimate} - 6.49\right)}{1 + 0.29\left(w_{estimate} - 6.49\right)} \tag{4.107}$$

for debonds, and

$$Error_{spalls} = -2.35 \frac{0.23\left(w_{estimate} - 8.51\right)}{1 + 0.23\left(w_{estimate} - 8.51\right)} \tag{4.108}$$

for concrete spalls.

These equations indicate that, for each case, there is an estimated flaw width at which the estimation error is 0 mm. The estimated flaw width at which the estimation error is zero is 3.3 mm, 6.5 mm, and 8.5 mm for delaminations, debonds, and concrete spalls, respectively. The equations could also be used to determine what is the estimation error for a determined flaw width. For example, analysis of the maximum signal may indicate that a given debond is located at a depth of 1.5 mm (as per parametric study No.3). Thus, Equation 4.107 could be used to calculate what error is expected on the estimation of the width of the flaw.

If analysis of the surface temperature data suggests that the estimated flaw width is 12.0 mm, Equation 4.107 could identify that the error in the width estimation is –1.4 mm. Since the actual width of the flaw was established as

$$w = w_{estimate} - error \tag{4.109}$$

where w was the actual width of the flaw, and $w_{estimate}$ was the estimated width, the actual width of the debond could be expected to be 13.4 mm.

An additional question that needs addressing is the minimum width of detectable flaws. The width of detectable flaws is highly influenced by the thermal sensitivity of the camera and environmental noise, among others. Thus, calculation of the minimum detectable flaw is based on the required maximum thermal signal.

The minimum detectable flaw was estimated for three different cases: ΔT_{max} equal to 0.1 °C, 1.0 °C, and 2.0 °C. The first case, ΔT_{max} equal to 0.1 °C, corresponds to the thermal sensitivity of most IR cameras. Since, the values reported by the FEM analysis are ideal, that is, with perfect layer interface and without ambient noise, the cases with ΔT_{max} equal to 1.0 °C and 2.0 °C were also considered. The minimum width of detectable flaws could be computed using Equations 4.93, 4.98, and 4.102. The results from the calculations are presented in Figure 4.117.

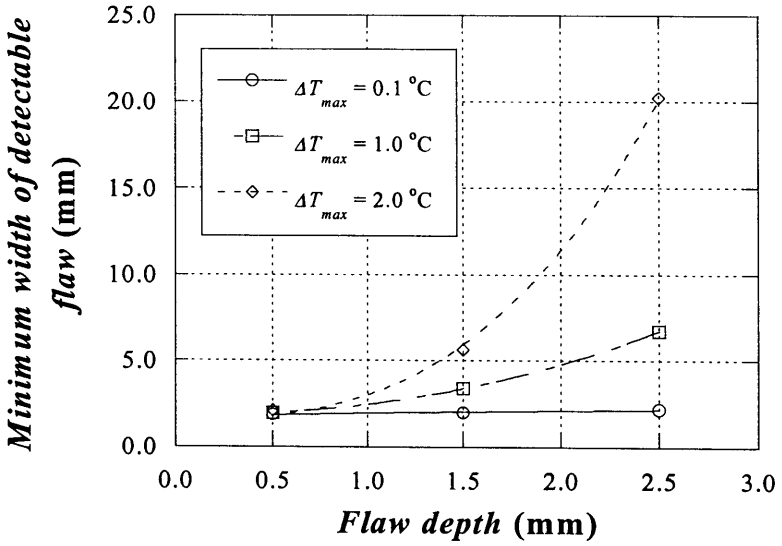

Fig. 4.117 Minimum width of detectable flaw as a function of flaw depth (mm)

Observation of the results presented in Figure 4.117 indicated that as the resolution of the signal increases (smaller ΔT_{max}), the minimum width for detectable flaws decreases. Power functions could be used to express the minimum width of detectable flaw. For the case of a thermal resolution of 0.1 °C (ΔT_{max} = 0.1 °C) the minimum width of detectable flaw could be expressed as

$$w_{min} = 1.61 + 0.36 d_{flaw}^{0.53} \tag{4.110}$$

where w_{min} is the minimum width of detectable flaws and d_{flaw} in millimeters, is the depth of the flaw in millimeters.

For the case of a thermal resolution of 1.0 °C the following power function could be used to estimate the minimum width of detectable flaws:

$$w_{min} = 1.86 + 0.61 d_{flaw}^{2.27} \tag{4.111}$$

Finally, for the case of a thermal resolution of 2.0 °C the following power function estimates the minimum width of detectable flaws:

$$w_{min} = 1.68 + 1.33 d_{flaw}^{2.87} \tag{4.112}$$

The results indicate that near-the-surface delaminations should be easily detected up to widths of 2 mm. The minimum width required for detection increases with increasing depth. For concrete spalls buried 2.5 mm from the surface, the minimum width varies from 2 mm with ΔT_{max} = 0.1 °C to 20 mm with ΔT_{max} = 2 °C.

4.7.5 Summary

The final parametric study focused on the evaluation of the effect of flaw width in the thermal response and the estimation of flaw width.

The conclusions reached are as follows:

- All response parameters, T_{max}, ΔT_{max}, t_s, maximum contrast, and t_c, increase nonlinearly with increasing flaw width.
- The increase in T_{max} could be expressed as an error function of the flaw width. The change in T_{max} for concrete spalls, however, was negligible.
- The increase in ΔT_{max} as a function of the width of the flaw could be expressed as a hyperbolic function. The effect of flaw width in the minimum signal is more evident for delaminations than for debonds or spalls.
- The increase in t_s as a function of the flaw could be expressed as a power function.
- Changes in t_s are negligible for near the-surface delaminations (less than 0.5 s for increases in w from 3 mm to 25 mm).
- The effect of flaw width is more pronounced on concrete spalls than on debonds or delaminations.

- The increase in maximum contrast could be expressed as a hyperbolic function of the flaw width.
- The increase in t_c could be expressed as a power function of the flaw width.
- The effect of the width of the flaw on t_c is more evident as the depth of the flaw increases.
- The width of the flaw can be estimated by locating the position at which $d^2T/dx^2 = 0$ from the surface temperature data.
- The error in width estimation decreases nonlinearly with increasing width. Moreover, the error changes signs, changing from over- to underestimations, as the width of the flaw increases.
- The minimum flaw width required to detect the flaw increases nonlinearly with increasing depth. The minimum width is also a function of the resolution of the IR equipment. That is, the higher the resolution of the IR detector, the smaller the width of the flaw that can be detected.
- The most difficult flaws to detect and characterize are concrete spalls. Small spalls are difficult to detect (small ΔT_{max}) and their size is difficult to estimate (large estimation error).

4.8 Summary on Single-Factor Parametric Studies

This chapter focused on the evaluation of the effect of various parameters on the thermal response. Finite element analysis was the chosen analytical tool. Five different parametric studies were conducted using ANSYS 5.6. The parameters investigated were the effect of the thermal input, effect of thermal material properties, effect of the depth of the flaw, effect of the thickness of the flaw, and effect of the width of the flaw.

In addition to investigating the effect of the various single-parameters on thermal response, the objectives of the parametric study also involved:

- optimize heating time and intensity for maximum thermal signal,
- establish if accurate determination of material thermal properties is required for quantitative IR thermography of FRP laminates applied to concrete,
- investigate the feasibility of estimating flaw depth from the measured thermal response,
- establish minimum thickness of detectable flaw,
- establish minimum width of detectable flaw.

The conclusions indicated that the thermal input could be optimized. Given a specific heat flux, the selection of the pulse duration is governed by the surface temperature that can be tolerated

and the required input energy for the desired signal. For a given flaw geometry, the maximum signal is a linear function of the input energy E (J/m^2). The surface temperature that can be tolerated is a function of energy as well as of the pulse duration.

The results from the second parametric study demonstrated that changes in the thermal properties of the constituent materials resulted in variations in the thermal response. The response parameters, however, were not very sensitive to the variations.

The investigation of the effect of flaw depth led to a simple procedure for estimating the response parameters as a function of the thickness of the FRP and the depth of the flaw. The results proved that the depth of the flaw could be estimated based on the time for maximum signal.

The fourth parametric study concluded with the estimation of the minimum thickness for detectable flaws. The minimum flaw thickness required for detection was estimated for three different maximum thermal signals. For each case, the minimum thickness of the flaw increased linearly with increasing depth.

Finally, the effect of flaw width was investigated. In addition to the effect of flaw width on the response parameters, the minimum flaw width required for detection was also examined. The results indicated that the minimum flaw width required to detect a flaw increases nonlinearly with increasing depth. Similar to the case of minimum thickness, the determination of minimum width is a function of the maximum thermal signal. The required maximum thermal signal depends on the thermal resolution of the IR detector. Ambient noise should also be considered since the simulations performed in this study assume perfect conditions (no convection losses, perfect material interface, etc.)

4.9 Multi-Factor Parametric Study

The previous parametric studies provided information regarding the effect of single parameters on the thermal response of the FRP/concrete assembly. A ranking of the most important factors and the interaction between them, however, is desired. The following parametric study answers which is the most important factors or interactions affecting three thermal responses: time for maximum signal, magnitude of maximum signal, and maximum surface temperature. The screening study would allow the determination of what factors and to what degree affect each of the thermal responses.

4.9.1 Design of Screening FEM Experiment

The purpose of the screening FEM experiment was the following:

- Determine important parameters and interactions affecting the thermal response
- Determine ranking of parameters and interactions affecting the thermal response

The following material parameters and their interactions were investigated: Depth, thickness, and width of flaw. Additional factors such as thermal input, and material properties of the constituents were kept fixed. Thus the screening experiment was designed to investigate three factors with 2 levels each. An additional "center-point" simulation was added for modeling purposes. The additional center point could provide the output needed to model nonlinear behavior of the response. The chosen design was a full factorial experiment (2^3) with and extra center point.

In the design and planning of experiments that involve the simultaneous variation of various physical parameters or *factors*, it is customary to use the expression *Full Factorial Experimental Design* (Wu et al., 2000). Other related expressions commonly used in experimental design are also *Latin-Square Experimental Design*, *Taguchi Experimental Design*, and so forth. Each of these expressions corresponds to a particular kind of experimental design. A *full factorial experimental design* is analogous to a *full parametric analysis* in engineering science, except that it involves not only the variation of parameters affecting a given physical problem, but the specification of how the experiments ought to be carried out, and what factors need be varied. The term "full factorial design" is used in this special context in the following section.

The advantages of choosing a full factorial design are the ability to estimate all interaction and main effects, it allows study of discrete and continuous factors, it is orthogonal in geometry, and it could generate a perfect fit model. The main disadvantage of this design is that is expensive in the number of runs and time. Nine runs were required to investigate the effect of the parameters on each thermal response.

The thermal responses under study were time for maximum signal t_s, magnitude of maximum signal ΔT_{max}, and maximum surface temperature T_{max}.

The test object selected for the study consisted of 3 layers of FRP composite bonded to a concrete semi-infinite slab. An air flaw was added at different depths of the FRP and at the interface with the concrete. Two different depths, thicknesses, and widths were applied to the flaw. The levels of each factor were coded either – or +. The levels were coded as follows in Table 4.38.

The full factorial design was constructed using Yates' order. Yates order guarantees that the design of the experiment is balanced and fair to any single factor and pair of factors. This design also provides an unbiased estimate of the main effects and allows the estimation of interactions between factors. Yates order construction was also chosen because is extensible in case additional factors want to be added to the experiment.

An outline of the design and levels is presented in Table 4.39. No randomization was applied to the run sequence.

Table 4.38 Coding of levels

Factor	Level	
	−	+
Depth of flaw, x1	1.5 mm (debond)	0.5 mm (top delamination)
Thickness of flaw, x2	0.1 mm	0.2 mm
Width of flaw, x3	14 mm	25 mm

Table 4.39 Design of full factorial plus center-point parametric study

Problem	x_1 (depth of flaw)	x_2 (thickness of flaw)	x_3 (width of flaw)
1	−	−	−
2	+	−	−
3	−	+	−
4	+	+	−
5	−	−	+
6	+	−	+
7	−	+	+
8	+	+	+
9 (center point)	0	0	0

Finite element analysis again was the chosen analytical tool. Three separate thermal responses were obtained from each simulation, providing the data for three different studies. The thermal responses obtained were the time for maximum signal t_s, the magnitude of the maximum signal ΔT_{max}, and the maximum surface temperature T_{max}.

4.9.2 Numerical Simulations

The test object consisted of a 50 mm long by 20 mm thick concrete slab with 3 layers of FRP bonded to its surface. Each layer of FRP was 0.5 mm thick. Each layer of FRP was oriented at 90 degrees to respect to the adjacent ply. The test object contained an internal air flaw. The flaw was located at the center of the test object. The thickness of the flaw was varied from 0.2 mm to 0.1 mm. The depth of the flaw was varied as well to include 0.5 mm deep delaminations, and 1.5 mm deep debonds. The length of the flaw was varied fro 7.0 mm to 12.5 mm

All the simulations were conducted using ANSYS 5.6. Plane two-dimensional modeling was used. The model was simplified using plane symmetry about the center of the test object. The model was meshed using 2-D quadrilateral thermal solid elements containing 4 nodes each with one degree of freedom (temperature). The test object was meshed using a global mesh size of 0.5 mm. Mesh refinement was applied in the thickness direction (y-axis), which was the primary direction of heat flow. The thinner elements were located at the FRP layers, the flaw, and the interface between the FRP and the concrete. The element size increased towards the bottom of the concrete slab away from the heated top surface. The meshing criterion was similar to that of the single-factor parametric studies.

The material properties of the model were those of concrete for the substrate, carbon FRP for the bonded composite, and air for the flaws (Table 4.2). As in previous parametric studies, the CFRP layer in direct contact with the substrate had fibers running in the x-direction. Each subsequent layer had its fiber direction rotating 90° about the y-axis.

Again, the analysis was defined as a transient heat transfer problem. A square pulse of intensity 20,000 W/m^2 with duration 2 s was applied to the top surface of the model. Adiabatic conditions ($dT/dx = 0$ and $dT/dz = 0$) applied to the remaining free surfaces and at the axis of symmetry. The initial temperature of the model was 23 °C.

The simulations were performed using Ansys automatic time stepping. The maximum and minimum time steps were 0.1 s and 0.008 s, respectively. The initial time step was 0.009 s. The FEM output was recorded at every time step.

4.9.3 FEM Output

The results of the simulations were evaluated for three different thermal responses. The thermal responses recorded were t_s, ΔT_{max}, and T_{max}. The results from the simulations are presented in Table 4.40.

Table 4.40 FEM outputs for single-factor parametric study

	Design of Study			Results		
Problem	x_1	x_2	x_3	t_s (s)	ΔT_{max} (°C)	T_{max} (°C)
1	−	−	−	6.25	3.83	49.1
2	+	−	−	2.44	17.9	64.6
3	−	+	−	6.85	5.12	49.3
4	+	+	−	2.54	26.1	71.7
5	−	−	+	7.35	4.44	49.1
6	+	−	+	2.53	18.5	64.9
7	−	+	+	8.55	6.10	49.3
8	+	+	+	2.73	27.2	71.2
9	0	0	0	5.14	9.1	52.3

4.9.4 Analysis of Results for t_s

The first thermal response evaluated was the time for maximum signal. The effect from each factor on the thermal response was computed by subtracting the group averages as indicated in the following equation

$$\hat{\beta}_i = \bar{y}_+ - \bar{y}_- \tag{4.113}$$

where $\hat{\beta}_i$ was the measure of the effect of the factor or interaction, $\bar{y}_+$ was the average of the responses for the levels identified as "+", and $\bar{y}_-$ was the average of the responses for the levels identified as "−". The results of the computation of the effect of each factor and the interactions are presented in Table 4.41.

Table 4.41 Estimate of the effects of the factors and their interactions in the time for maximum signal

Factor or Interaction	$\bar{y}_+$ (s)	$\bar{y}_-$ (s)	$\hat{\beta}_i$ (s)
x_1	2.5	7.3	-4.7
x_2	5.2	4.6	0.5
x_3	5.3	4.5	0.8
$x_1 \cdot x_2$	4.7	5.1	-0.4
$x_1 \cdot x_3$	4.6	5.2	-0.7
$x_2 \cdot x_3$	5.0	4.8	0.2
$x_1 \cdot x_2 \cdot x_3$	4.8	5.0	-0.1

The same results are presented in Fig. 4.118. Each graph plots a factor or interaction versus the average of the thermal response at levels "+" and "−". The slope of each line is an indicator of the effect of the factor on the time for maximum signal. The results indicate that factor x_1 (depth of flaw) is the parameter that affects the time for maximum signal the most.

The first step for deciding what factors or interaction have an important effect in the response was to compare the difference of the means ($\hat{\beta}_i$) to the minimum engineering significant response. The minimum engineering significant response is a value specified a priori by the researcher and is based on instrumentation capabilities and on engineering judgment. For this particular study, the minimum engineering significant response for t_s was selected as 0.5 s. Based on this assumption and comparing with the results presented in Table 4.41, only three single factors and one interaction should be considered to affect the response. The ranking of these factors and interactions from the highest effect to the lowest effect are the following:

1. x_1 (depth of flaw) → $\hat{\beta}_1 = -4.7$ s
2. x_3 (width of flaw) → $\hat{\beta}_3 = 0.8$ s
3. x_{13} (interaction between depth and width of flaw) → $\hat{\beta}_{13} = -0.7$ s
4. x_2 (thickness of flaw) → $\hat{\beta}_2 = 0.5$ s

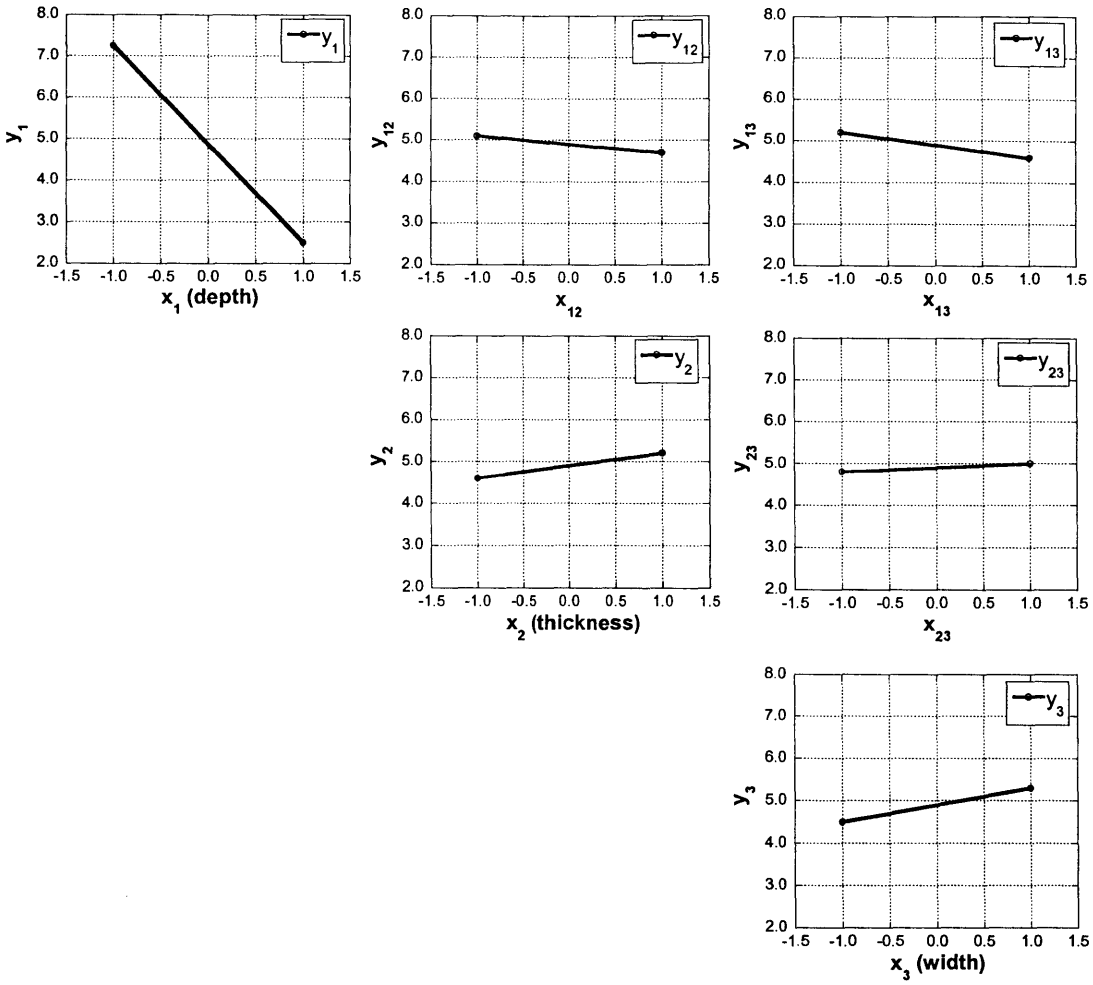

Fig. 4.118 Plots of means of factors and interactions for the time to maximum signal

The search for the important factors affecting a response, however, may be further refined by using a plot of the halfnormal probability. This criterion states that only the factors or interactions that deviate from the straight line fit to the points whose $\hat{\beta}_i$ are near zero are the factors that have an important effect on the response. The halfnormal probability plot for this study is presented in Fig. 4.119. The graph clearly indicates that only one factor, the depth of the flaw, has an important effect on the time for maximum signal.

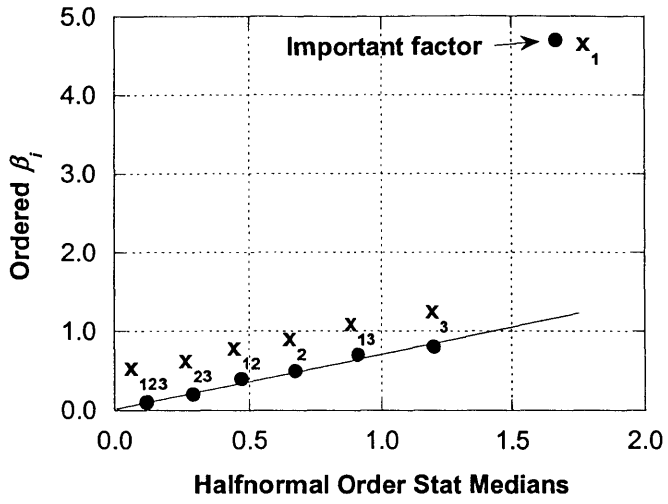

Fig. 4.119 Halfnormal probability plot for the time for maximum signal

4.9.5 Conclusions for t_s

The evaluation of the results from the first screening study highlights the importance of the depth of the flaw as the primary factor affecting the time for maximum signal. Even though the width and thickness of the flaw and the interaction between depth and width have some effect on the thermal response, the halfnormal probability analysis indicates clearly that the depth of the flaw is main parameter.

Nondestructive evaluation requires the solution to the inverse problem that is, determination of the characteristics of the flaw based on the given thermal response. The conclusion from this multi-parameter study suggests that the depth of the flaw may be estimated from the time for maximum signal alone. In this case, the estimation procedures described in Section 4.5.4d may provide an option for solving the inverse problem in the future.

4.9.6 Analysis of Results for ΔT_{max}

The second thermal response assessed was the magnitude of the thermal signal. The average value of the maximum thermal signal was 13.6 °C. The effect from each factor on the thermal response was evaluated using Eq. 4.113. The results from the calculation of the effects are presented in Table 4.42.

Table 4.42 Estimate of the effects of the factors and their interactions in the magnitude of the maximum signal

Factor or Interaction	$\bar{y}_+$ (°C)	$\bar{y}_-$ (°C)	$\hat{\beta}_i$ (°C)
x_1	22.4	4.9	17.6
x_2	16.1	11.2	5.0
x_3	14.0	13.2	0.8
$x_1 \cdot x_2$	15.4	11.9	3.5
$x_1 \cdot x_3$	13.6	13.6	0
$x_2 \cdot x_3$	13.8	13.5	0.2
$x_1 \cdot x_2 \cdot x_3$	13.6	13.6	0

The results of the effects summarized in Table 4.42 are illustrated in Fig. 4.120. The slope of each line is an indicator of the degree of influence that the factor or interaction has on the thermal response, ΔT_{max}.

The minimum engineering significant response for the magnitude of the maximum signal was 0.2 °C. This value was specified a priori based on the thermal sensitivity of most IR cameras.

The parameters were ranked based on the degree of influence on the thermal response and on the minimum engineering significant response. The following list presents the ranking of the factors:

1. x_1 (depth of flaw) → $\hat{\beta}_1 = 17.6$ °C
2. x_2 (thickness of flaw) → $\hat{\beta}_2 = 5.0$ °C
3. x_{12} (interaction between depth and thickness of flaw) → $\hat{\beta}_{12} = 3.5$ °C
4. x_3 (width of flaw) → $\hat{\beta}_3 = 0.8$ °C
5. x_{23} (interaction between thickness and width of flaw) → $\hat{\beta}_{23} = 0.2$ °C

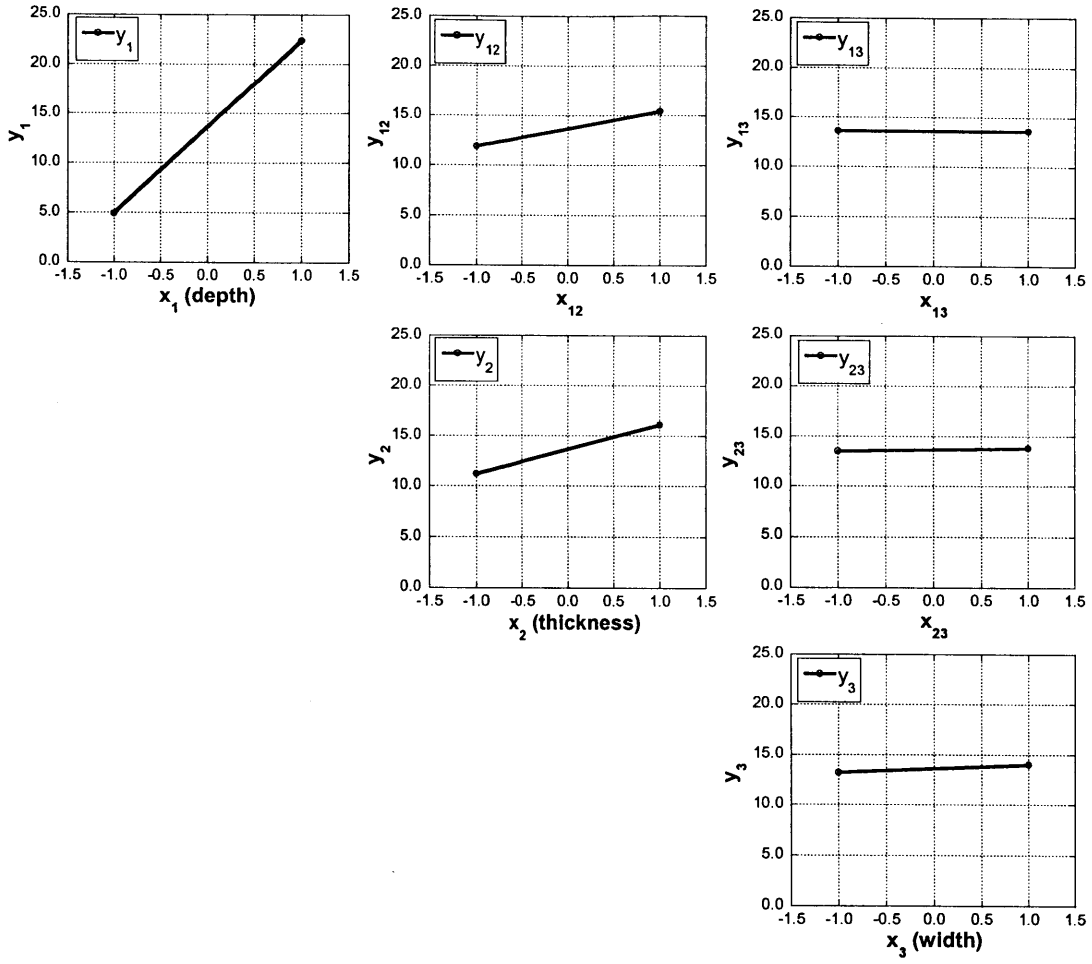

Fig. 4.120 Plot of means of factors and interactions for the maximum signal

The determination of the factors that have a significant influence on the magnitude of the maximum signal is further refined by examining the halfnormal probability plot of the results. The factors and interaction that have an important influence on the thermal response correspond to those that deviate from the straight line that best fit the values next to the axis origin. The factors and interactions that have an effect on the maximum signal are presented in Fig. 4.121. Using this method of determination of important factors, two parameters and one interaction, flaw depth flaw thickness and the interaction between them, have a relevant influence in the magnitude of the maximum signal.

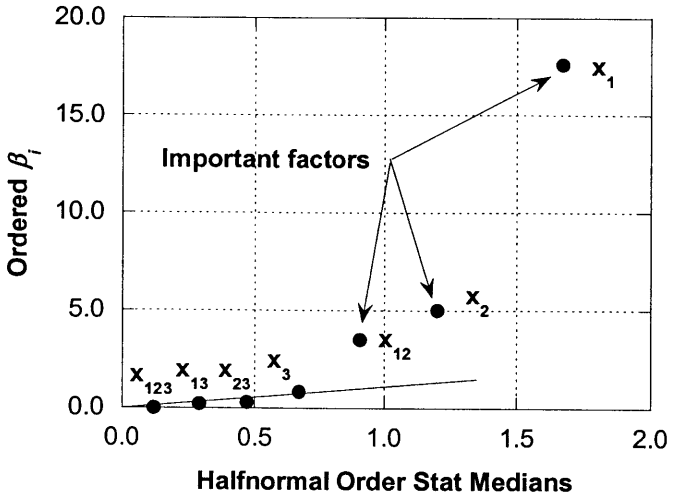

Fig. 4.121 Halfnormal probability plot for the maximum signal

A third analysis tool was used to evaluate the output. This method involved the observation of the degree of dispersion of the output related to each of the important parameters. While the plots of the means (Fig. 4.120) and the halfnormal probability plot (Fig. 4.121) explain what factors have an influence on the thermal response, the scatter plots (Fig. 4.122) clarifies the way in which the effect occurs. Factors with more localized data around the + or – levels and with larger differences in the means ($\hat{\beta}_i$) are said to be more influential on the response than factors with highly scattered data. The factors with tighter output can be predicted easily and reliably from the response. On the other hand, factors with highly scattered output are difficult to predict from the response.

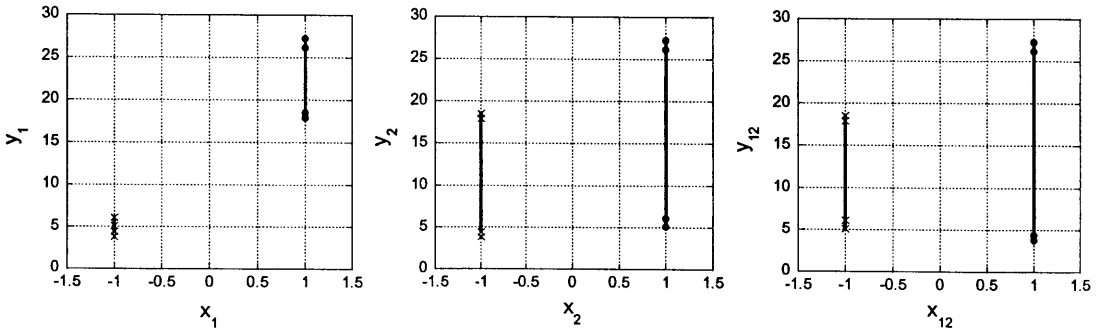

Fig. 4.122 Scatter plots of the important factors affecting ΔT_{max}

Figure 4.122 illustrates that of the 2 factors and one interaction that have an important effect on the response, only the depth of the flaw (x_1) have localized output around its + and – levels. The thickness of the flaw and the interaction between both factors have scatter outputs. This

dispersion effect would impede any attempt to attain a good model for the prediction of the maximum signal. Thus, solution of the inverse problem (determination of the factors from the response) should not rely on the magnitude of the maximum signal.

4.9.7 Conclusions for ΔT_{max}

The evaluation of the results from the second screening study confirms the importance of the depth of the flaw as the primary factor affecting the magnitude of the maximum signal. In this case, however, flaw thickness and the interaction between flaw depth and thickness are also important parameters influencing the thermal response.

The scatter plots illustrated the high dispersion of the output as a function of the thickness of the flaw and the interaction between flaw depth and thickness. The evaluation of the scatter plots indicates that the development of a good model to estimate maximum signal based on the important factors is problematical.

4.9.8 Analysis of Results for T_{max}

The final thermal response examined was the maximum surface temperature. The average value of the maximum surface temperature for the simulation was 58.7 °C. The effect from each factor on the maximum surface temperature was evaluated using Eq. 4.113. The results from the calculation of the effects are presented in Table 4.43.

Table 4.43 Estimate of the effects of the factors and their interactions in the magnitude of the maximum surface temperature

Factor or Interaction	$\bar{y}_+$ (°C)	$\bar{y}_-$ (°C)	$\hat{\beta}_i$ (°C)
x_1	68.1	49.2	18.9
x_2	60.4	56.9	3.5
x_3	58.7	58.7	0
$x_1 \cdot x_2$	60.3	57.0	3.3
$x_1 \cdot x_3$	58.7	58.7	0
$x_2 \cdot x_3$	58.6	58.8	-0.2
$x_1 \cdot x_2 \cdot x_3$	58.6	58.8	-0.2

The results of the effects $\hat{\beta}_i$ are also illustrated in Fig. 4.123. The slope of each line denotes degree of influence of the factor or interaction on the maximum surface temperature. The minimum engineering significant response for T_{max} was 0.2 °C. This value corresponds to the thermal sensitivity of most infrared detectors.

Based on the minimum engineering significant response, the factors and their interactions were ranked in decreasing order based on the degree of influence on the thermal response. The following list enumerates the ranking of the factors:

1. x_1 (depth of flaw) → $\hat{\beta}_1 = 18.8$ °C

2. x_2 (thickness of flaw) → $\hat{\beta}_2 = 3.5$ °C

3. x_{12} (interaction between depth and thickness of flaw) → $\hat{\beta}_{12} = 3.3$ °C

4. x_{23} (interaction between thickness and width of flaw) → $\hat{\beta}_{23} = -0.2$ °C

5. x_{123} (interaction between depth, thickness, and width of flaw) → $\hat{\beta}_{123} = -0.2$ °C

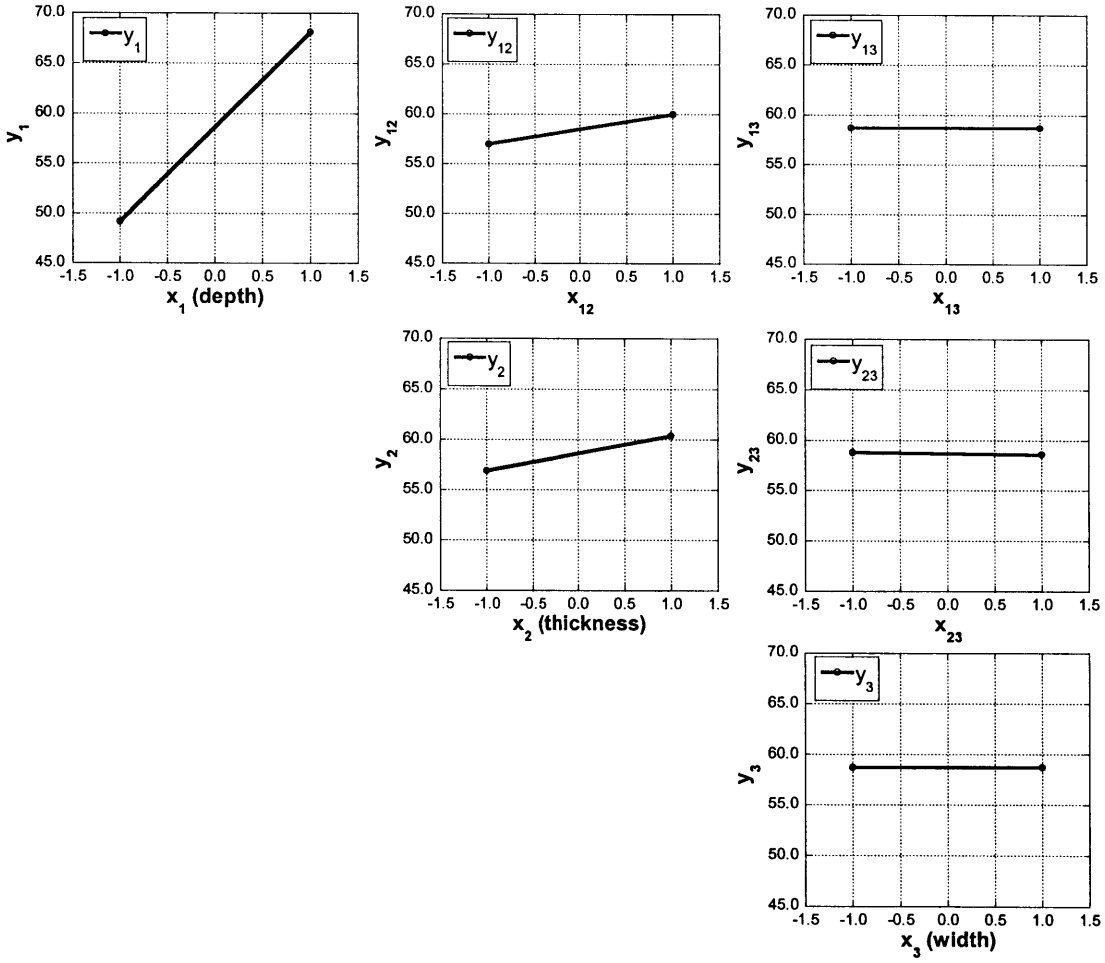

Fig. 4.123 Plot of means of factors and interactions for the maximum surface temperature

Next, the halfnormal probability of the $\hat{\beta}_i$s was plotted. The factors and interaction that have a significant effect on the maximum surface temperature are those that diverge from the straight line that best fit the values next to the axis origin. The factors and interactions that have an effect on the maximum surface temperature are presented in Fig. 4.124. Using this analytical tool, the

number of important factors was reduced to two factors (depth and thickness) and their interaction.

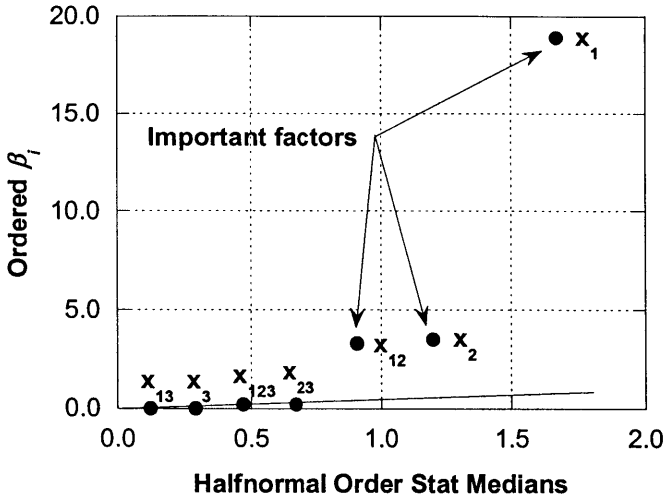

Fig. 4.124 Halfnormal probability plot for the maximum surface temperature

Next, the FEM output was plotted using scatter plots. The scatter plots for the two main factors and their interaction are presented in Fig. 4.125. The results are similar to those for the magnitude of the maximum signal. The graphs indicated that the only factor with localized output is the depth of the flaw. Both, the thickness of the flaw and the interaction between depth and thickness have dispersed outputs.

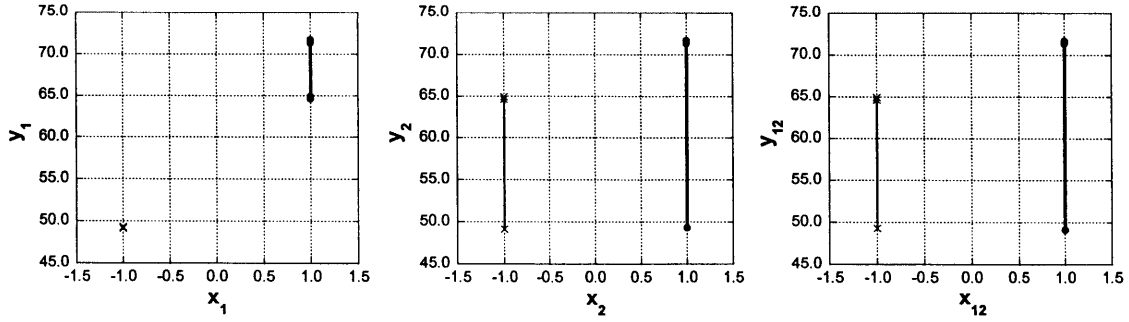

Fig. 4.124 Scatter plots of the important factors affecting T_{max}

The determination of an adequate model to estimate the maximum surface temperature from the significant factors is improbable due to the high dispersion of the output values for the flaw thickness and the interaction factor.

4.9.9 Conclusions for T_{max}

The evaluation of the results from the final screening study confirms the significance of the depth of the flaw as the primary factor affecting the maximum surface temperature. The thickness of the flaw and the interaction between flaw depth and thickness are also important parameters influencing the magnitude of the maximum surface temperature.

The analysis also showed a high level of dispersion of the response as a function of the thickness of the flaw and the interaction between flaw depth and thickness. This scattering indicates that the development of a simple model to estimate maximum surface temperature and based on the important factors is questionable.

4.9.10 Conclusions for the Multi-Factor Parametric Study

A screening multi-parameter study was conducted to determine what flaw geometry factors have a significant effect on the thermal responses. A full factorial design was used to investigate the effect of the factors and all their interactions. The factors investigated were the depth, thickness, and width of the flaw. The same study was conducted for three thermal responses: time to maximum signal, magnitude of maximum signal, and maximum surface temperature.

The investigation proved that the depth of the flaw is the only factor that has a significant effect on the time to maximum signal. Thus the study confirmed that the depth of the flaw could be estimated using the time for maximum signal. Similarly to previous analyses (section 4.6), the results also indicated that flaws located near the surface are more likely to be estimated accurately than deeper flaws.

The analysis also established that the magnitude of the maximum signal and the maximum surface temperatures are affected by the depth of the flaw, the thickness of the flaw, and their interaction. The large scatter of the thermal responses as a function of the thickness indicated that this factor would be difficult to characterize accurately.

4.10 Summary

Finite-element modeling was used as the analytical tool. This chapter investigated the effect of various parameters on the thermal response. The study focused on the evaluation of the various parameters that influence thermal evolution (the spatial and temporal variations of surface temperature). The investigation was subdivided into a single-factor parametric study and a multi-factor parametric study.

The first parametric study involved evaluation of single parameters that affect the thermal response. The objectives for the single-factor parametric study were the following:

- optimize heating time and intensity for maximum image contrast,
- determine the effects of material properties on the measurement of thermal signals,
- investigate the effect of flaw depth,

- examine the effect of type of flaw (delamination versus debond),
- study the effect of defect thickness on flaw detection and characterization; and
- determine minimum detectable flaw size.

The selection of the thermal pulse is governed by the desired maximum signal and by the maximum surface temperature that can be tolerated by the material.

The conclusions from the investigation indicated that for a given flaw geometry, the maximum surface temperature difference is a linear function of the input energy (expressed in J/m^2). Thus, a maximum value of input energy can be established for a given minimum signal. The maximum surface temperature is also a linear function of the input energy, but it also depends on the pulse duration. The selection of the pulse duration to produce the minimum input energy is governed by the maximum surface temperature that can be tolerated. These results have led to a simple approach for selecting the thermal input so as to obtain a desired thermal signal while limiting the surface temperature due to heating. The investigation also concluded that, based on the thermal input, variations in the pulse duration affect both the magnitude of the signal and the time to maximum signal, while variations in the magnitude of the heat flux only affect the magnitude of the signal.

The results from the study of the effect of material properties stated that, while variations in the thermal properties of the FRP and concrete resulted in systematic variations in thermal response, none of the response parameters were very sensitive to these variations. Thus, the success of infrared thermography testing will not depend strongly on the specific values of the thermal properties of the FRP or concrete substrate.

The third parametric study focused on the potential estimation of flaw depth based on the thermal response. The findings from the study of the effect of the depth of the flaw demonstrated that the thermal responses are a function of both the depth of the flaw and the number of FRP plies in the strengthened system. The time to maximum signal was the thermal response least affected by the number of FRP layers. Estimation of the depth of the flaw was demonstrated using the time to maximum signal.

The conclusions also showed that the influence of flaw thickness on the thermal responses is significant in the case of delaminations near the surface but is very small on debonds and concrete spalls.

The results also indicated that the width of the flaw could be estimated from the second derivative of the surface temperature profile. The investigation of the minimum detectable flaw demonstrated that the smallest detectable flaw is a function of the depth of the flaw and the maximum signal required to overcome noise in the measuring process.

A multi-factor parametric study was performed to determine which factors have an important effect in the thermal responses. The investigation proved that the depth of the flaw is the only factor that has a significant effect on the time to maximum signal. Thus the results confirmed that the depth of the flaw could be estimated using the time for maximum signal. On the other hand, the large scatter of the thermal responses as a function of the thickness indicated that this factor would be difficult to characterize accurately.

Chapter 5

Laboratory Studies

5.1 Introduction

The second component of the project focused on a series of laboratory studies aimed to define good testing and analysis procedures for IR thermography testing of FRP composites bonded to concrete. Verification of the FEM simulations was an additional purpose of the laboratory studies. Specifically, the objectives of the experimental program were the following:

- Determination of emissivity values of pultruded FRP laminates and hand lay-up FRP laminates;
- Comparison of FEM simulation with results from actual infrared testing;
- Study the potential of flaw width estimation;
- Evaluation and ranking of the importance of several parameters such as, flaw depth, flaw; thickness and flaw width, and their interactions;
- Determination a good model;
- Evaluation of test repeatability; and,
- Determination of adequate sampling rate.

The objectives were carried out by:

- Selection of adequate heating devices
- Measurement of heat flux input
- Construction of experimental setup
- Conducting controlled-flaw experiments

The results presented in this chapter focus on measurement of emissivity, measurement of heat flux, detection of debonds, comparison of FEM output and experimental data, estimation of the width of a debond in a controlled-flaw specimen, evaluation and ranking of several flaw parameters, determination of a good model for quantitative evaluation of the depth of subsurface flaws, assessment of test repeatability, and determination of suitable sampling rates. As such, the chapter focuses on measurement of various parameters required for infrared thermography and on the infrared thermography results obtained of simple controlled-flaw specimens.

5.2 Design of Experiments

The experimental program was subdivided into 5 different research focuses, each involving one experiment:

- The first part of the experimental study was qualitative in nature, and its focus was to evaluate the potential detection of simulated flaws embedded in the test object. A qualitative test was performed to determine what materials could be used successfully in the controlled-flaw specimens. A specimen having two bonded pultruded CFRP laminates and containing eight fabricated debonds was used for this experiment.

- The second test was quantitative and focused on the comparison of infrared thermography results and the output from FEM simulations. An air void contained in the specimen from the first experiment (pultruded CFRP bonded to concrete slab) was inspected.

- The purpose of the third experiment was to evaluate the potential estimation of the width or area of the flaw. For this purpose, the air void buried in the specimen fabricated with pultruded CFRP was investigated.

- The forth experiment involved a screening parametric investigation. Three flaw parameters were investigated: flaw depth, flaw thickness, and flaw width. To investigate these three parameters, a full factorial experimental design was planned.

  As explained in Chapter 4, in the design of experiments that involve the simultaneous variation of various physical parameters or *factors*, it is customary to use the term *Full Factorial Experimental Design*. A *full* factorial *experimental design* in the laboratory is analogous to a *full parametric analysis* in engineering science. The term "full factorial design" is used in this special context in this chapter. The primary advantage of choosing a full factorial design is the ability to estimate all interaction and main effects.

  The purpose of the screening experiment was the following:

  - Determination of important parameters and interactions affecting thermal response
  - Determination of ranking of parameters and interactions affecting thermal response
  - Determination of a potential good model

  Factors such as thermal input, and material properties of the constituents were kept fixed in the experimental design. Thus the screening experiment was designed to investigate three factors with 2 levels each. The chosen design was a full factorial experiment (2^3) with and two extra center points. Two additional "center-points" were added for modeling purposes. The additional center points could provide the output needed to model nonlinear behavior of the response. A full factorial design was selected because it provided all the information required to estimate the effect of the main factors and all interactions. It allows study of discrete and continuous factors, it is orthogonal in geometry, and it can generate a good model. The main disadvantage of this design is that is expensive in the number of runs and time.

The test object selected for the study consisted of 3 layers of FRP composite bonded to a concrete semi-infinite slab. An air flaw was added at different depths of the FRP and at the interface with the concrete. Two different depths, thicknesses, and widths were applied to the flaw. The levels of each factor were coded either– 1 or +1 (and in some cases,"– " or "+"). The levels were coded as follows in Table 5.1.

Table 5.1 Coding of levels

Factor	**Level**	
	−1	**+1**
Depth of flaw, x1	1.5 mm (debond)	0.5 (top delamination)
Thickness of flaw, x2	0.1 mm	0.2 mm
Width of flaw, x3	7 mm	12.5 mm

The full factorial design was constructed using Yates' order. Yates order construction is extensible in case additional factors need to be added to the experiment. Run randomization was carried out at the time the tests were performed. Randomization was introduced to ensure that uncontrolled variables did not bias the results. The design and running order of this experiment is presented in Table 5.2. For the coded levels for each factor, either "–" and "+" or –1 and +1 are used interchangeably.

The construction of the specimen and testing procedures for all the experiments are explained in the subsequent sections.

- The final experiment focused on the investigation of test repeatability and the effect of sampling rate.

Table 5.2 Design of full factorial plus center-points screening study

Case	x1 (depth of flaw)	x2 (thickness of flaw)	x3 (width of flaw)	Run Sequence
1	−	−	−	6
2	+	−	−	4
3	−	+	−	2
4	+	+	−	1
5	−	−	+	9
6	+	−	+	10
7	−	+	+	5
8	+	+	+	7
9 "center" point	0	−	0	8
10 "center" point	0	+	0	3

5.3 Testing Configurations

Depending on the objective of the experiments, two different configurations were used for testing. The first set of tests involved qualitative assessment of the presence of debonds in a controlled test specimen. The remaining experiments involved quantitative evaluation of several subsurface flaws. The test configuration for quantitative testing was more elaborate than the setup for qualitative testing.

Both detection and characterization of subsurface flaws require an external heat source to produce the desired transient heat transfer conditions. Moreover, a short duration, high intensity thermal pulse is ideal for producing highly transient behavior. As discussed in the previous chapter and in Starnes et al. (2002), selection of the input requires achieving a balance between the desired thermal signal (surface temperature differential between damaged and sound

material) and the maximum allowable surface temperature. This balance is achieved by selecting appropriate values of both the heat flux intensity and the heating period. The inspector may choose between using a short duration heating period with high intensity heat flux, or vice versa. The parametric studies described in the previous chapter also indicate that for civil engineering applications, lower intensity heat flux with a longer heating period (for example, seconds instead of microseconds) provides the balance needed in thermal signal and maximum surface temperature.

Both qualitative and quantitative testing techniques require an IR camera and a data acquisition system that allows viewing of the thermograms. Quantitative testing, however, requires the capability of recording and measuring the thermal response as a function of time. To fulfill this requirement a more involved testing setup was constructed. Additionally, the experimental setup included shutters for the heating system, external triggers, and data analysis software. A schematic of the test configuration for quantitative testing is presented in Fig. 5.2.

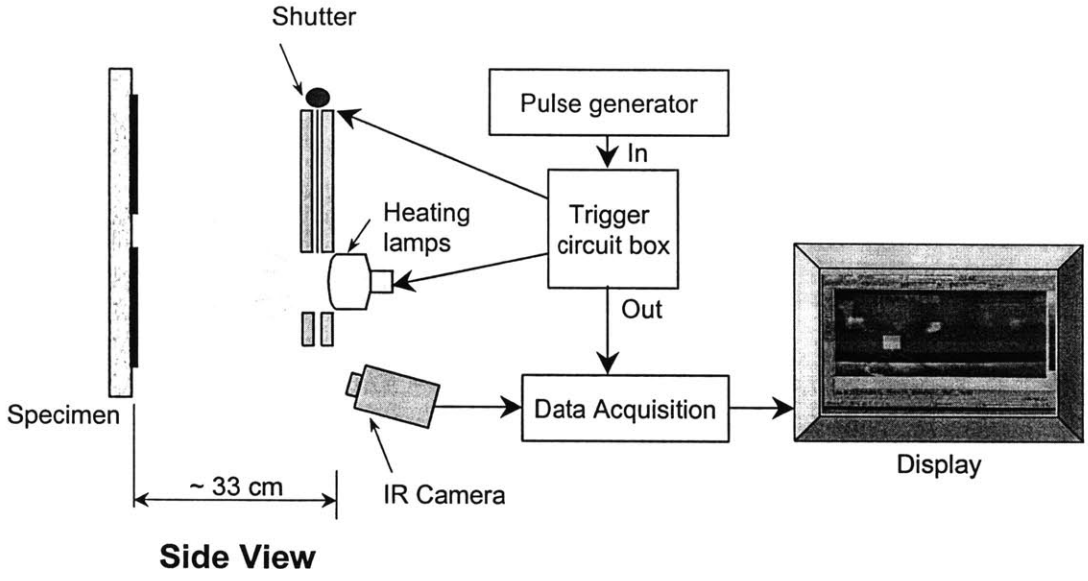

Fig. 5.2 Infrared thermography quantitative test configuration

The following subsections describe the qualitative and quantitative test configurations in a greater detail.

5.3.1 Qualitative Test

The purpose of qualitative testing is to detect the presence of subsurface anomalies. Qualitative testing does not require accurate measurement of the input thermal pulse and the time history of the thermal response. The qualitative test performed in this project involved the use of one 250-W infrared lamp. Heating, in this case, is done by sweeping an infrared heat lamp along the length of the FRP at a distance of 50 mm from the surface and at a speed of approximately 0.15 m/s. This technique is similar to the method used in practice (Hawkins et al., 1999).

No measurement was taken of the time history of the thermal response. The surface temperatures recorded by the infrared camera were logged with the aid of the data acquisition system. The infrared camera used for the qualitative test was an AGEMA Thermovision 900. Subsurface flaws were identified visually through the thermograms recorded by the data acquisition system. The data acquisition used was Researcher HS by Flir Systems. The specifications for this IR camera and the data acquisition are described further in the next section.

5.3.2 Quantitative Tests

The purpose of these studies is to provide the basis for quantitative infrared thermography in which not only the presence but also characteristics of a flaw can be established. The experimental configuration for quantitative testing included a heating module, IR cameras, data acquisition system, and analysis software capable of recording thermal behavior as a function of time.

5.3.2a Heat Sources

A heating module was fabricated to provide the heat flux pulse required for quantitative testing. Two 250-W infrared heating lamps mounted at 200 mm on center were used for the thermal input. An aluminum frame was made to hold the heating lamps and an aluminum shutter. The shutter was necessary to block radiation from the lamps after they were turned off. This was required so that the heat pulse would be similar to the step pulse used in the FEM simulations. The shutter was kept open during heating by suspending it from the top of the frame using an electromagnet. An illustration of the heating configuration is presented in Fig. 5.3.

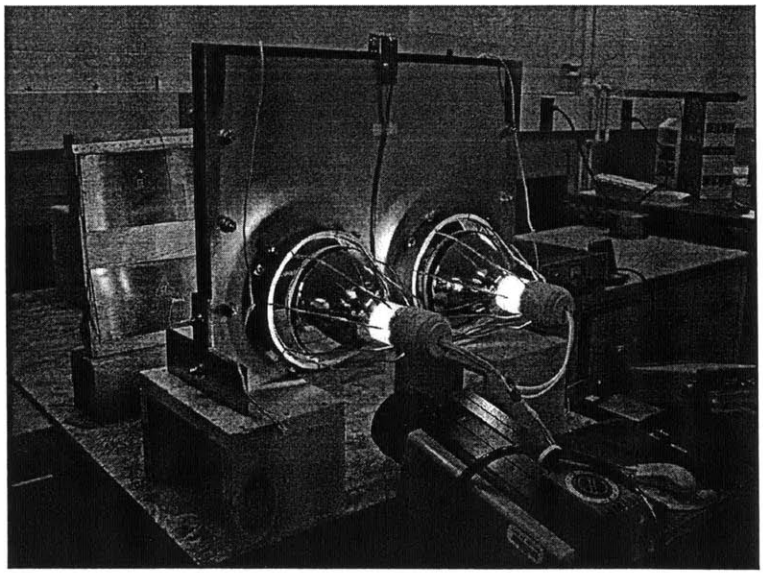

Fig. 5.3 Configuration of heating lamps for quantitative testing

A DC power supply, a pulse generator, and a trigger box were also needed for producing a "square" heat pulse. A waveform generator was connected to the heating lamps as well as to a

trigger box. At the end of the pulse, the trigger turned off the lamps and the current supplied to the electromagnet, and the shutter fell in front of the lamps. An additional function of the trigger was to externally trigger the data acquisition system at the beginning of the heat pulse. Figure 5.4 illustrate the pulse generator, DC power supply and trigger box used in the experiments.

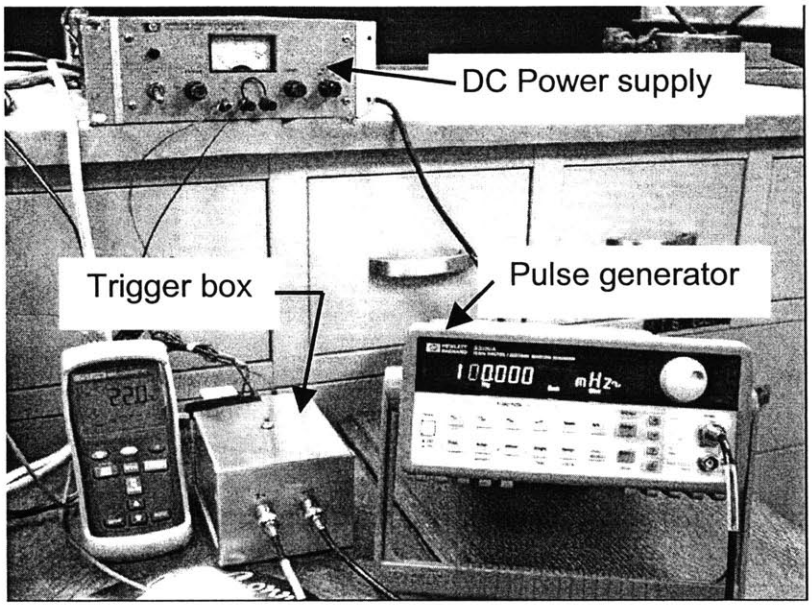

Fig. 5.4 Pulse generator, trigger box, and power supply

5.3.2b Infrared Cameras

Two different infrared cameras were used during the project. The initial experiments, those involving pultruded CFRP composites, were performed using an infrared camera with a nitrogen-cooled detector. An uncooled microbolometer was used for the final set of experiments.

Infrared Camera with Nitrogen-Cooled Detector

The infrared camera used in the first three sets of experiments was an AGEMA Thermovision 900. The infrared camera has a mercury-cadmium-telluride (HgCdTe or MCT) detector. The scanner operates in the long-wave infrared region with a spectral response between 8 μm and 12 μm. The detector has a sensitivity of 0.08 °C at 30 °C and a measurement accuracy of ±1 °C. As mentioned, this detector requires continuous cooling with liquid nitrogen (LN_2). The scanner was able to record data at a maximum sampling rate of 15 Hz.

Infrared Camera with an Uncooled Detector

The experiments involving wet lay-up composites were carried out using a FLIR ThermaCAM SC2000. This infrared camera has a focal plane array (FPA) uncooled microbolometer detector with 320 pixels × 240 pixels. The infrared camera operated in the long wavelength infrared

spectral band (7.5 μm and 13 μm), thus minimizing the atmospheric attenuation of the received radiation. The camera has an atmospheric filter with cut-on at 7.5 μm. The thermal sensitivity of the detector is 0.08 °C at 30 °C with a measurement accuracy of ±2 °C. The infrared camera allowed the recording of thermograms at a rate of 60 Hz.

5.3.2c Data Acquisition and Analysis Software

The primary data acquisition and analysis software for infrared measurements was Researcher High Speed from FLIR Systems. This software package provides up to 60 Hz digital video and data acquisition and retrieval. For quantitative testing, an external trigger was connected to the data acquisition system. Data acquisition was triggered at the time the heating lamps were turned on.

For heat flux measurement, a DataShuttle data acquisition system and QuickLog software from Omega were used to measure the heat flux incident on the heat flux sensor.

5.3.3 Specimens

Three different specimens were constructed for the experimental studies. The first specimen was constructed using pultruded CFRP laminates (Carbodur from Sika). The remaining two specimens were fabricated using wet lay-up CFRP fabric (M-Brace from Master Builders).

5.3.3a Specimen Fabricated with Pultruded CFRP Laminates

The controlled-flaw specimen was constructed by using a 610 mm × 250 mm × 45 mm precast concrete slab as the substrate. Two pultruded carbon FRP (CFRP) laminates (CarboDur®) were bonded to the substrate, as shown in Fig. 5.4. The laminates are available commercially and contained unidirectional carbon fibers. Each laminate had the following dimensions: 609 mm × 102 mm × 1.3 mm. First, the surface of the concrete slab was cleaned to remove any existing dust. The composite laminates were precut to the appropriate length and cleaned with acetone. The bonding epoxy (SikaDur®) used was that recommended by the manufacturer of the pultruded laminates. The bonding epoxy was applied over the concrete surface to a thickness of 1.6 mm using a spatula. Application of epoxy was avoided at the location at which the created flaws where going to be placed. Eight "flaws" were created by placing different materials at the interface between the concrete substrate and the FRP. Each flaw was approximately 25 mm × 25 mm in plan. The materials used to simulate flaws and their approximate thickness are summarized in Table 5.3. One of the objectives of the experimental work was to see whether there is a material that would produce results similar to an air void. The laminate was then applied to the concrete and pressed down using a rubber roller. The excess epoxy that was forced out on both sides of the laminate was removed. The specimen was kept undisturbed for one day to allow curing of the epoxy.

Two thermocouples were also placed in the bonding epoxy between the concrete and the FRP, as illustrated in Fig. 5.5. Additionally, a heat flux transducer with an internal thermocouple was placed on the surface of the specimen. The thermocouples and the heat flux transducer were linked to a data acquisition system.

Table 5.3 Summary of simulated flaws

Flaw No.	Material	Placement/construction	Approximate thickness (mm)
1	Air & plastic	Air-filled plastic	0.4
2	Air & wax	Lost wax process	0.6
3	Styrofoam		0.5
4	Masking tape		0.3
5	Low *k* fabric & plastic	Fabric wrapped in plastic	0.8
6	Air	Air void created with wire dam	0.6
7	Parafilm®		0.1
8	Ceramic paper & plastic	Ceramic paper wrapped in plastic	0.8

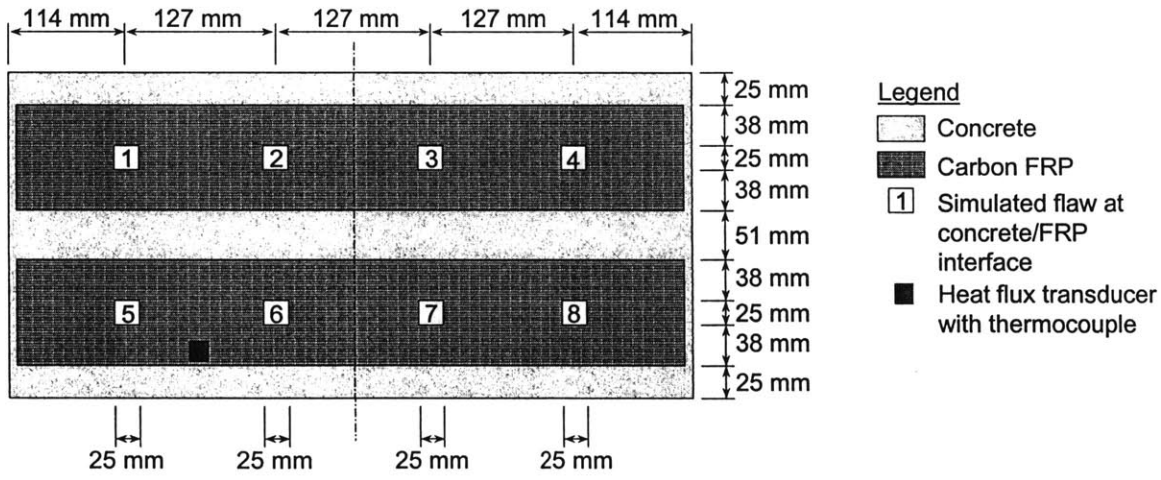

Fig. 4.5 Controlled-flaw test specimen

The heat flux sensor bonded to the surface of the specimen was an Episensor B04 from Vatell Corporation. Episensor is an inexpensive and flexible transducer. The sensor is 24.5 mm × 24.5 mm in area and contains 1600 thermocouples per square centimeter. It operates to a maximum of 150 °C. Figure 5.6 illustrates the heat flux sensor bonded to the surface of the CFRP laminate.

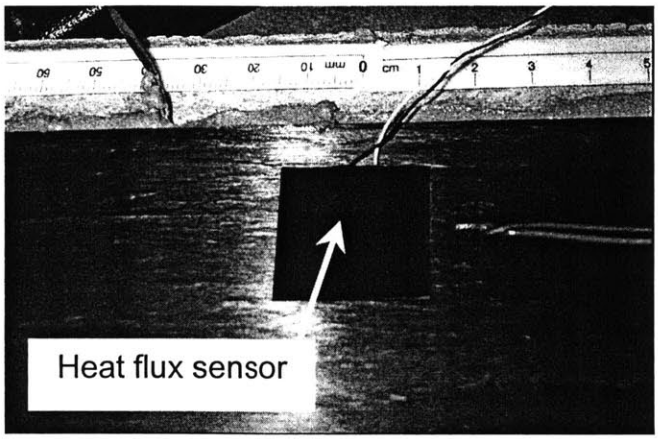

Fig. 5.6 Heat flux sensor bonded to FRP laminate

5.3.3b Specimens Fabricated with Wet-Lay Up CFRP Laminates

The second set of specimens involved wet lay-up composites bonded to concrete. The substrate was again a precast concrete slab. The dimensions of the concrete slab block were 610 mm × 250 mm × 45 mm. Two specimens were constructed by bonding MBrace™ carbon fiber sheets from Master Builders to the concrete slab. Both specimens were constructed with 3 layers of FRP bonded to the concrete. The material used to simulate internal flaws varied. One specimen contained flaws constructed with low *k* fabric (Nomex® III-Defender, material used on firefighter clothing). The second specimen had flaws created using Parafilm®. Parafilm® is a flexible film that consists primarily of polyolefins and paraffin waxes. Fig. 5.7 illustrates both

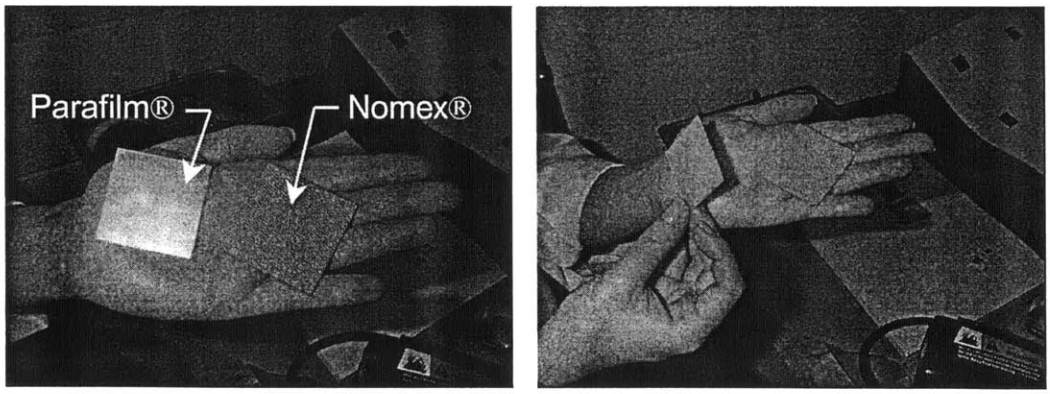

Fig. 5.7 Materials used as flaws in MBrace™ specimens

materials used as flaws in this set of experiments.

Both specimens were constructed following the same layout. Each specimen included all the flaws specified in the design of the experiments summarized in Tables 5.1 and 5.2. A plan view of the location of the flaws for both specimens is presented in Fig. 5.8.

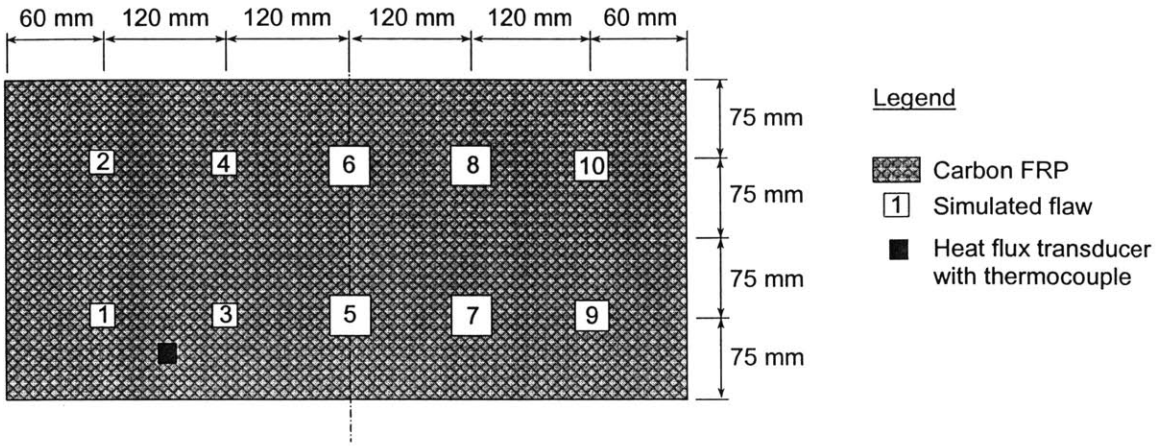

Fig. 5.8 Configuration of specimens constructed with hand lay-up FRP

The FRP reinforcement was bonded to the concrete slab using the procedures specified by the manufacturer of the composite system.

- First, the concrete substrate was prepared by cleaning the surface and applying a thin layer of MBrace putty using a trowel (Fig. 5.9).

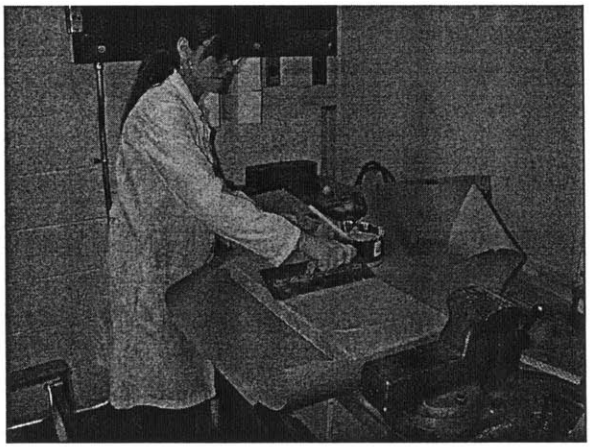

Fig. 5.9 Application of MBrace putty

The putty is a thick, paste-like epoxy which purpose is to fill holes and surface defects up to 5 mm deep. The putty was allowed to cure before proceeding to the following step.

- A coat of MBrace saturant, which is blue in color, was applied over the puttied surface. The saturant or resin is formulated to impregnate the fibers and hold the tow sheet in place until the reinforcement system cures. Application of saturant was avoided at the location were the first set of flaws (debonds) were going to be located (Fig. 5.10). The thickness of the layer of resin was 0.4 mm approximately.

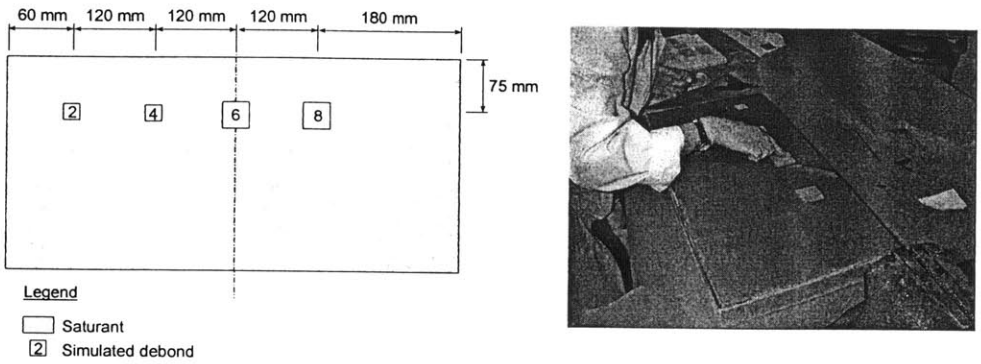

Fig. 5.10 Location (plan view) and placement of debonds

The first fiber sheet was cut to the proper size prior to placement. The sheet was placed on top of the resin. The direction of the fiber was along the longitudinal direction of the concrete slab. A trowel was pressed over the paper backing of the fiber sheet in order to remove possible air bubbles from the FRP laminate. The paper backing was removed to allow pressing of the fiber sheet with a ribbed roller. Rolling over the sheet in the direction of the fiber allowed impregnation and separation of the fibers to occur. Finally, a second coat of resin was applied and let to cure before proceeding to the application of the following layer. Figure 5.11 illustrates some of the procedures described in this paragraph.

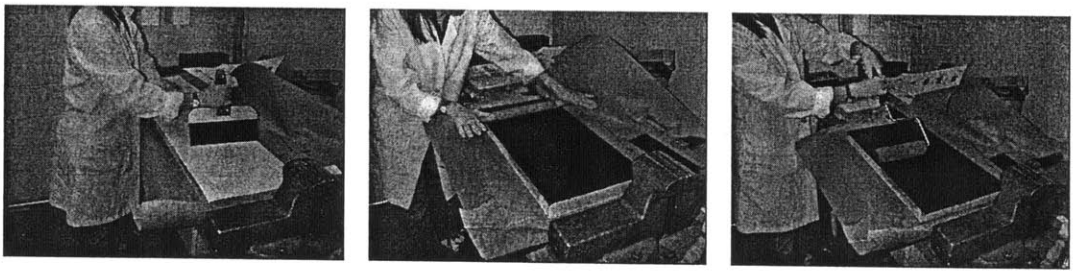

FRP sheet being pressed with trowel

FRP sheet being pressed with roller

Application of resin

Fig. 5.11 Application of first layer of FRP

- After 30 minutes, another coat of resin was applied. Again, care was taken to avoid placement of saturant on the area were the next set of flaws were to be located. Two bottom delaminations were designed to be located at this interface as illustrated in Fig. 5.12.

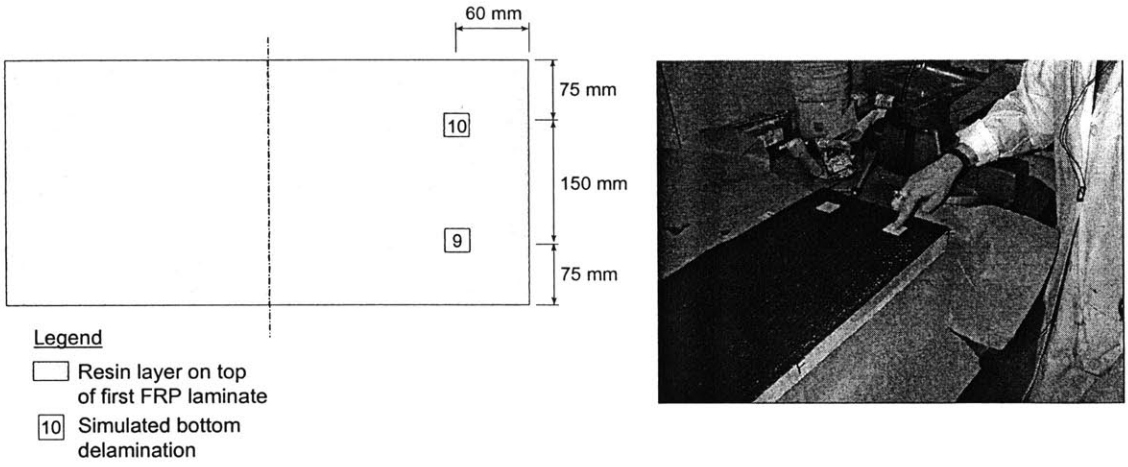

Fig. 5.12 Location (plan view) and placement of bottom delaminations

A sheet of fiber was applied on top of the resin. In this case, the fiber was running at 90° relative to the fiber sheet located below, that is, in the transversal direction. The fiber was again pressed with a trowel and a ribbed roller in the direction of the fiber. A coat of resin was applied on top of the fiber sheet and was allowed to cure for 30 minutes.

- After 30 minutes, another coat of saturant was applied. Again, care was taken to avoid placement of resin on the area were top delaminations were to be located. The location and actual placement of the created delaminations are presented in Fig. 5.13. A sheet of carbon fiber was placed on top of the resin (Fig. 5.14). In this case, the fiber ran in the longitudinal direction of the specimen. The final coat of resin was applied. The specimen was allowed to cure overnight.

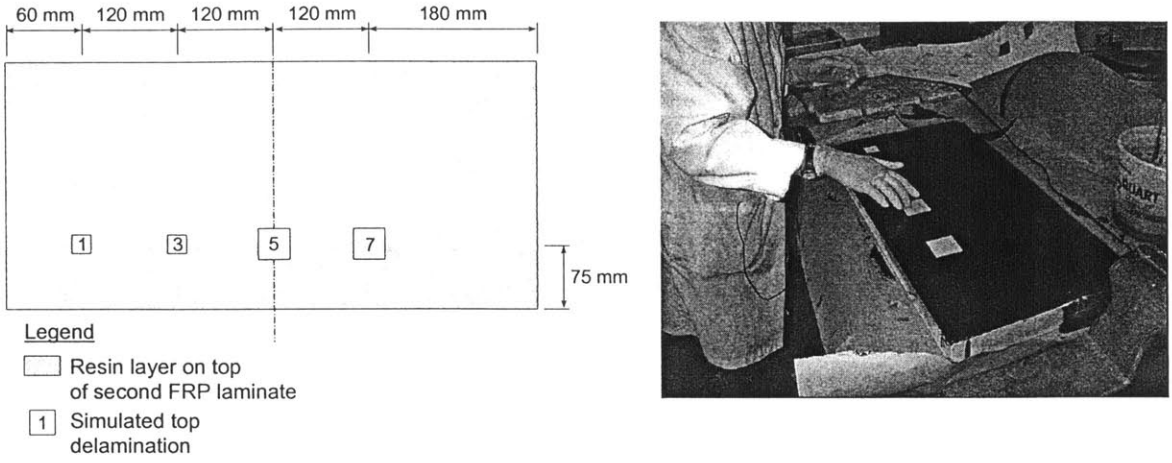

Fig. 5.13 Location (plan view) and placement of top delaminations

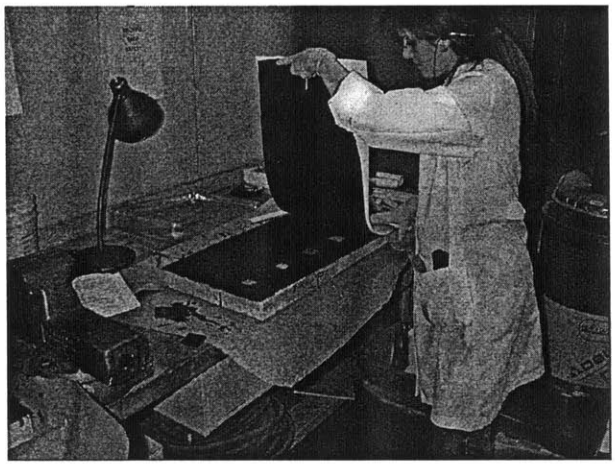

Fig. 5.14 Placement of last fiber sheet

Specimen Containing Flaws Created with Low *k* Fabric

One of the specimens was constructed using a low *k* fabric (Nomex®) as the material for the simulated flaws. The material had a thickness of 0.6 mm. The layout of the specimen followed the outline specified in Table 5.2 and in Fig. 5.8. Following the design of the experiment summarized in Table 5.2, the following levels were assigned to the parameters under study:

- Depth of flaw, x1 →
  - (−) indicates a top delamination with a depth of 0.5 mm approximately;
  - (+) indicates a debond with a depth of 1.5 mm approximately; and,
  - (0) indicates a bottom delamination at a depth of 1.0 mm approximately.

- Thickness of flaw, x2 → (−) indicates a thin flaw with a thickness of 0.6 mm approximately;
  (+) indicates a thick flaw with a thickness of 1.2 mm approximately; and,

  Using this material, no center point (0) was assigned to this parameter.
- Width of flaw, x3 → (−) indicates a small with a width of 25 mm;
  (+) indicates a large flaw with a width of 40 mm; and,
  (0) indicates a flaw that is 32.5 mm wide.

Specimen Containing Flaws Created with Thin Film

The second specimen was constructed using a thin film (Parafilm®) as the material for the simulated flaws. The material has a thickness of 0.13 mm. The layout of the specimen conformed to the outline specified in Table 5.2 and in Fig. 5.8. The following levels were assigned to the parameters under study:

- Depth of flaw, x1 → (−) indicates a top delamination with a depth of 0.5 mm approximately;
  (+) indicates a debond with a depth of 1.5 mm approximately; and,
  (0) indicates a bottom delamination at a depth of 1.0 mm approximately.
- Thickness of flaw, x2 → (−) indicates a thin flaw with a thickness of 0.13 mm approximately;
  (+) indicates a thick flaw with a thickness of 0.38 mm approximately; and,
  (0) indicates a flaw that is 0.25 mm wide.
- Width of flaw, x3 → (−) indicates a small with a width of 25 mm;
  (+) indicates a large flaw with a width of 40 mm; and,
  (0) indicates a flaw that is 32.5 mm wide.

5.4 Experiment #1: Qualitative Test

The first part of the experimental study was qualitative in nature, and was intended to evaluate the potential detection of each simulated flaw embedded in the test object. For this purpose, the entire surface of the specimen was heated and the surface temperature was recorded using the infrared camera and associated software. The qualitative nature of the test did not require measurement of applied heat flux. Heating, in this case, was done by sweeping an infrared heat lamp along the length of the FRP at a distance of 50 mm from the surface and at a speed of approximately 0.15 m/s. Observation of the thermogram shown in Fig. 5.15 shows that all eight flaws were detectable. The most visible flaws were numbers 5, 6 and 8, which corresponded to low-conductivity fabric, air, and ceramic paper, respectively (see Fig. 5.5). Flaw number 4

(masking tape) and flaw number 7 (Parafilm®) produced the smallest signals. The thermogram clearly indicates the location of the subsurface flaws and the sensors bonded to the surface of the specimen (i.e., heat flux sensor and thermocouple wires).

In practice, this quick technique could be used to easily detect and locate subsurface flaws. Actual characterization of the flaw, however, requires precise measurement of surface temperatures as a function of time and knowledge of some parameters such as absorbed heat flux. The next set of experiments involved quantitative testing of the FRP bonded to concrete.

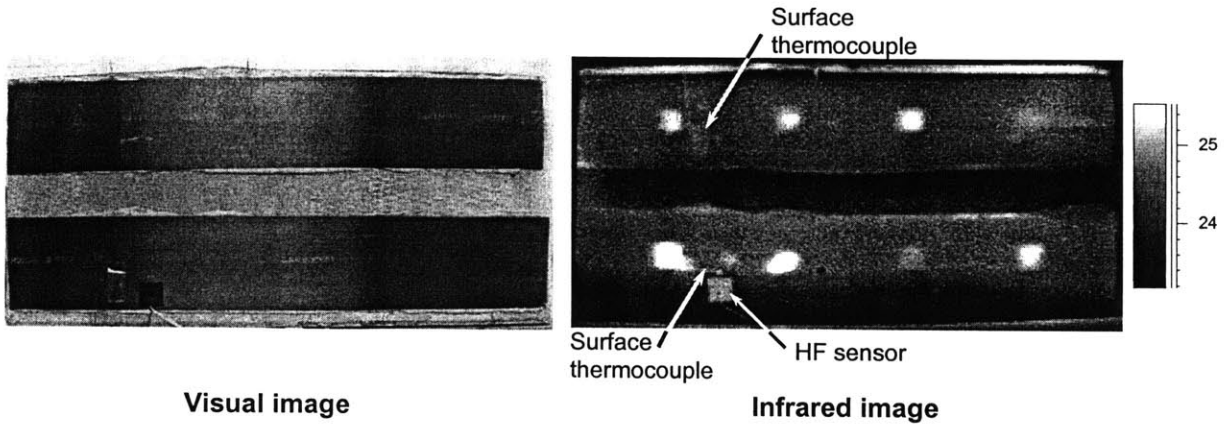

Fig. 5.15 Visual image and thermogram of test object during qualitative detection of internal flaws created artificially with different materials

5.5 Experiment #2: Comparison of IR Thermography and FEM Simulations

Experiment #2 concentrated on quantitative testing and comparison of the results with FEM simulations. Based on the qualitative test and focusing on comparison of test results with numerical simulations, the air-void flaw (flaw number 6) was selected for further study. The reason for the choice was twofold:

- the air void provided a significant thermal signal; and,
- the material properties of air are known, thus reducing uncertainty in the numerical modeling.

During the qualitative test, it was observed that the shape of air void was not square as intended. This meant that epoxy had flooded over the "wire dam" that was used to try to create a square-shaped void. Thus it was recognized that the thickness as well as the area of the flaw was different from intended. To estimate the thickness of the air void, seven measurements of the height of the FRP laminate were taken using a caliper. From the known laminate thickness, the mean value of the epoxy thickness was 0.9 mm and the standard deviation was 0.2 mm. The thickness of air void was thus assumed to be 0.9 mm.

5.5.1 Determination of Surface Emissivity for Pultruded FRP

Accurate determination of surface emissivity, and compensation for it, is key for the correct measurement of surface temperatures by using an infrared camera. The Stefan-Boltzmann principle (Eq. 2.1) relates the surface temperature of an object to the radiation emitted by it. This relationship, however, is affected by the characteristics of the surface of the material. The emissivity measures the capability of a material to emit radiation. In particular, emissivity is the ratio of the radiance of a body at a given temperature to the radiance of a black body at the same temperature (ASTM E 1316).

Standard methodology for determining emissivity is described in ASTM E 1933. First, the contact thermometer method described in the standard was used in this experimental study. Surface temperatures of the FRP laminate were measured using a copper/constantan thermocouple (ANSI Type T, special limits, 0.010 mm in diameter). Each thermocouple was embedded in the FRP so that half of the perimeter of the wire was in contact with the composite and the other half of the wire was in contact with air. A small notch was cut into the laminate and epoxy adhesive was used to hold the thermocouple in place.

In accordance with ASTM E 1933, the test specimen was heated so the surface reached at least 10 °C above ambient temperature. To avoid rapid cooling of the surface, the specimen was heated in an oven to a temperature of 45 °C. As a result, surface cooling of the surface was slow enough to allow for the estimation of the emissivity of the surface.

The data acquisition and analysis software calculate surface temperatures based on the following equation (Rinaldi, 2002):

$$W = \varepsilon \sigma T^4 + (1-\varepsilon)\sigma T_{amb}^4 \tag{5.1}$$

where W is the radiation emitted by the specimen, ε is the emissivity of the material being tested, σ is the Stefan-Boltzmann constant, and T_{amb} is the ambient temperature. Equation 5.1 allows the accurate measurement of the surface temperature by compensating for the atmospheric radiation emitted by the surroundings and recorded by the infrared detector. The "ambient temperature" should not be confused with the "atmospheric temperature." The atmospheric temperature is a measure of the actual temperature of the air in the surroundings of the test. Ambient temperature, however, corresponds to the temperature equivalent to the radiation emitted by the surroundings (objects and atmosphere) and reflected by the surface of the specimen under testing (Rinaldi, 2002). To measure it, the infrared camera is placed against the surface being measured and facing the direction of the testing. The emissivity of the IR image is set to 1.0 and the average temperature of the image is measured. The recorded average temperature is the "ambient temperature" required to calibrate the thermograms for quantitative testing.

The ambient temperature of the room in the direction against the surface of the specimen was measured and its value entered into the data analysis software. The value of T_{amb} was 24 °C.

To measure the emissivity of the laminate, the test specimen was located at a distance of 0.55 m from the infrared camera and placed perpendicular to the line of view of the camera. The perpendicular placement of the test object is an important consideration since emissivity varies with the angle of view. Surface temperatures next to the location of a thermocouple were taken with the infrared camera using spot meters, which are measurement tools used by the analysis software to determine the temperature at a point. Specifically, the spot meter averages the temperature of the pixels around the chosen point. Surface temperatures were measured at 3 points next to a thermocouple using 3 spot meters. The emissivity at each point was varied in order to match the temperature measured with the thermocouple and the temperature indicated by the camera. The measurements were repeated 55 times, for a total of 165 that ranged from 0.77 to 0.84 (Fig. 5.16), the average emissivity of the FRP laminate was 0.80, with a standard deviation of 0.016. Thus the expanded uncertainty interval is 0.80 ± 0.03, for a coverage coefficient of k=2.

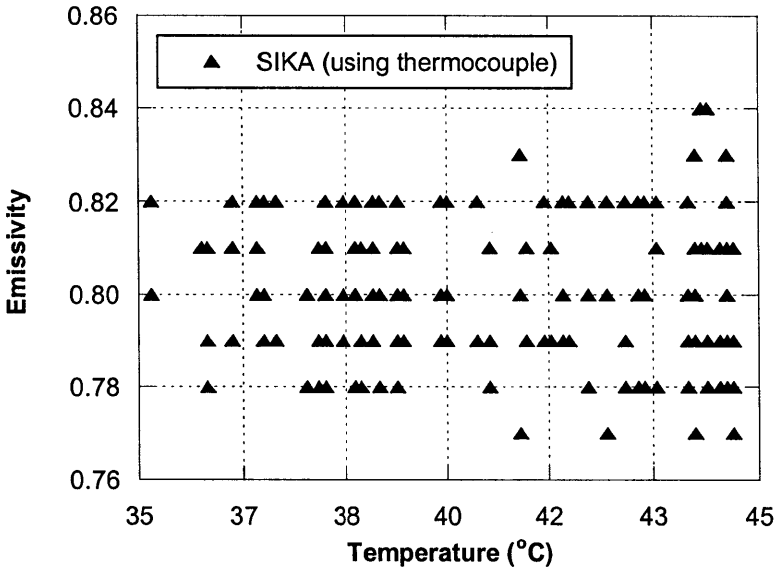

Fig. 5.16 Emissivity measurements using thermocouples for pultruded CFRP laminate

The *noncontact thermometer method* specified in ASTM E1933 was also used to determine the emissivity of the pultruded composite laminate. For this measurement, a small piece of electrical tape was applied to the surface of the specimen. Electrical tape has a typical value of emissivity equal to 0.95 (Mikron, 2002 and Rinaldi, 2002). Additionally, the ambient temperature of the room was calculated. The ambient temperature was 24 °C. The specimen was heated in an oven to a temperature of 43 °C. The specimen was removed from the oven to take the emissivity measurements. Since the electrical tape was bonded to the surface of the specimen, both the FRP and the tape had the same temperature. Two "area" measurement functions were used to measure the average temperature of the tape and the FRP adjacent to the tape. The temperature of the tape was measured using an emissivity equal to 0.95. The emissivity of the "area" measuring the FRP's temperature was adjusted to match the temperature of the tape. This computation is done automatically by the analysis software using an *Emissivity Calculation* tool.

A total of 18 measurements were recorded. The values ranged from 0.78 to 0.81 (Fig. 5.17). The average emissivity of the FRP laminate was 0.80, with a standard deviation of 0.01. Thus the expanded uncertainty interval is 0.80 ± 0.02.

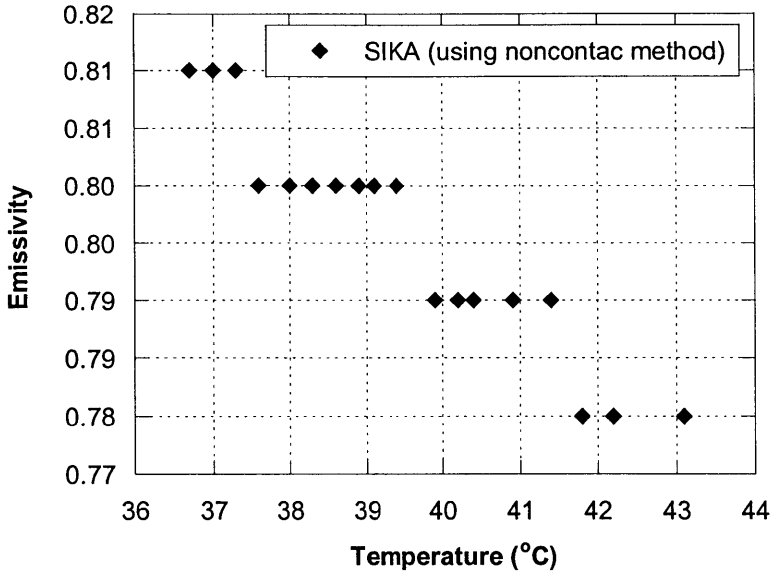

Fig. 5.17 Emissivity measurements using noncontact method for pultruded CFRP laminate

5.5.2 Determination of Heat Flux

Two sets of measurements were performed to determine the incident heat flux onto the surface of the test object. First, the heat flux distribution was measured along the surface of the specimen to determine the homogeneity of the heat flux produced by the heating module. The second set of tests involved the measurement of the heat flux pulse as a function of time.

5.5.2a Homogeneity of Heat Flux

The quantitative thermography method investigated in this research involves the application of uniform heat flux over the surface of the object being tested. The heat flux produced by the two-lamp heating module was measured to ensure this homogeneity.

The heating module was placed 0.33 m from the surface of the specimen. The heat flux sensor was placed on the surface of the specimen at the same height than the center of the heating lamps. The heat flux at the surface of the specimen was measured at intervals of 20 mm along a parallel line with respect to the 2 lamps. Thus for each test, the heat flux transducer was moved by 20 mm along the line of measurement. The configuration of the test is presented in Fig. 5.18.

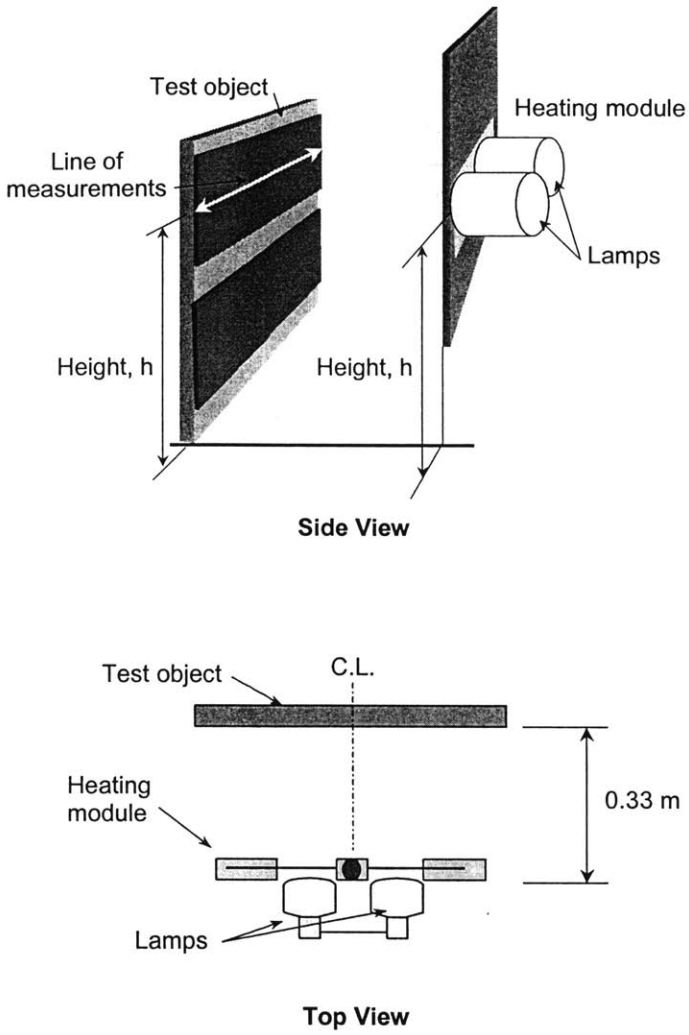

Fig. 5.18 Experimental setup for measurement of homogeneity of incident heat flux

Heat flux measurements were recorded at 16 different locations along the line of measurement thus covering a length of 0.3 m along the surface of the test object. For each measurement, the heat lamps were activated for 10 s. After 10 s, the lamps were turned off and the shutter fell in front of the lamps to shield any additional radiation. The measured heat flux at 10 s was used as the value of heat flux at the specific location along the line of measurement.

The values of the recorded data are presented in Table 5.4. The relevant location to test heat flux homogeneity was between the two lamps, since this is the area where the potential flaw would be located and measured. The results summarized in Table 5.4 and illustrated in Fig. 5.18 show some undulation of the data between the two lamps suggesting a small heterogeneity of the incident heat flux. Also, the highest heat fluxes were not located at the center of the lamps, as expected. These aspects could be due to the irregularity of the electrical filaments inside the lamps and the fact that there may be slight rotations of the lamps with respect to the surface of the test object. The average measured heat flux between the two lamps (measurements between

80 mm and 280 mm) was 1650 W/m^2 and the standard deviation was 80 W/m^2. Figure 5.18 illustrates the heat flux data.

Table 5.4 Heat flux distribution along line of measurement

Distance, mm	Heat flux, q (W/m^2)	Comments
0	1210	
20	1160	
40	1440	
60	1470	
80	1530	C.L. of lamp
100	1760	
120	1730	
140	1660	
160	1620	
180	1600	C.L. of module
200	1570	
220	1770	
240	1640	
260	1590	
280	1650	C.L. of lamp
300	1580	

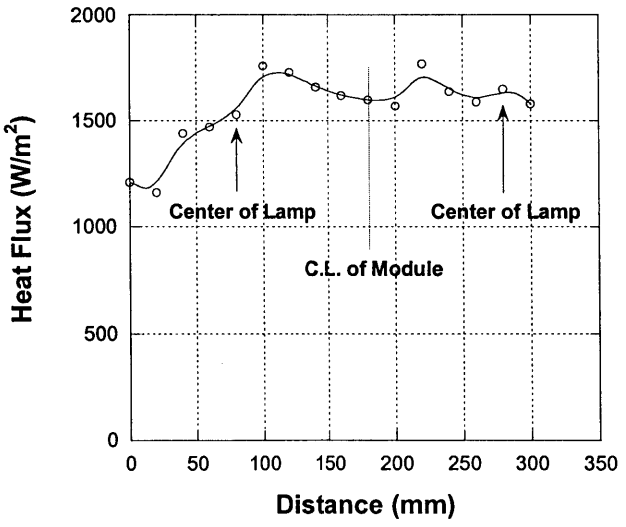

Fig. 5.18 Results of heat flux distribution measurements

The results reported that the heat flux in the area located between both lamps of the heating module provided the required uniform heating.

5.5.2b Heat Flux Pulse as a Function of Time

As previously stated, the surface temperature and thermal signal of the FRP laminate depend on the input thermal pulse. The input thermal pulse has two parameters that may be varied: the duration of the pulse and the magnitude of the heat flux. The pulse duration is easily controlled. For this particular experiment the pulse duration was adjusted to 10 s using a pulse generator and an external trigger. The lamps were triggered to turn on. After 10 s, the pulse generator sent a signal to the trigger circuit board to turn off the lamps and the electromagnet holding the shutter. The shutter fell and stopped heat flow to the test specimen.

The second parameter that needs to be determined is the magnitude of the thermal pulse. This parameter depends on the power of the heating source and its distance from the test object.

The incident heat flux was measured using a heat flux sensor placed on the surface of the FRP laminate. The sensor also included a thermocouple. Heat flux and temperature measurements from the sensor were recorded using a data acquisition system. The experiment was conducted with the heating lamps located 0.33 m from the surface of the FRP laminate. In order to record the heat flux that the specimen would be subjected to during thermography testing, the heat flux sensor was placed at the same position with respect to the heating lamps that the flawed specimen would be during thermography testing. For convenience, this position will be referred to as location A through the rest of this chapter.

Three heat flux measurements were obtained. The maximum magnitude of the heat flux was 1750 W/m^2 measured at 10 s. Table 5.5 summarizes the input heat flux data and Fig. 5.20 shows the shape of one of the heat pulses.

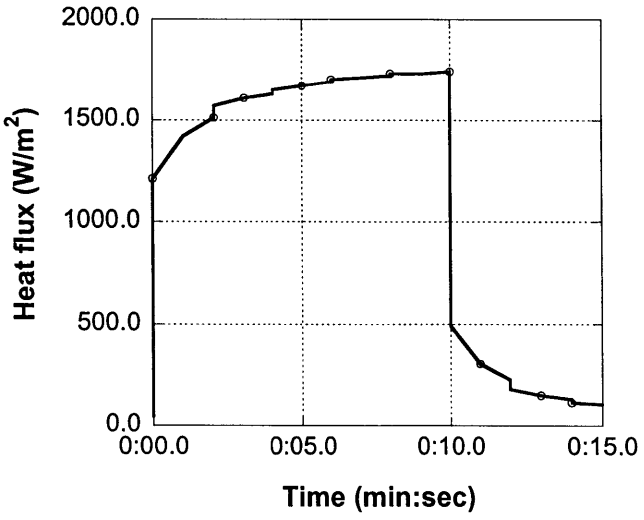

Fig. 5.20 Measured heat flux pulse (test #3)

Table 5.5 Heat flux measurements

Time (s)	Incident heat flux, $q_{incident}$ (W/m^2)		
	Test 1	Test 2	Test 3
0	0	0	0
1	1360	1400	1420
2	1480	1500	1570
3	1600	1610	1610
4	1640	1640	1650
5	1680	1680	1670
6	1690	1690	1690
7	1710	1710	1710
8	1720	1720	1730
9	1740	1740	1730
10	1750	1740	1740
11	350	340	310
12	250	240	220
13	160	160	150
14	120	140	130

An important consideration with respect to numerical simulations is that the heat flux sensor measures the incident heat flux, $q_{incident}$. This heat flux, however, needs to be adjusted to determine the amount absorbed by the FRP. The fraction of the incident heat flux absorbed by the surface of a material is referred to as absorptivity. Kirchhoff's law relates the absorptivity of a surface to its emissivity as follows (Özişik, 1985):

$$\varepsilon_\lambda(T) = \alpha_\lambda(T) \tag{5.2}$$

where $\varepsilon_\lambda(T)$ is the spectral emissivity for the emission of radiation at temperature T and $\alpha_\lambda(T)$ is the spectral absorptivity for radiation coming from a blackbody at temperature T. Thus the absorbed radiation can be expressed as

$$q_{absorbed} = \varepsilon\, q_{incident} \tag{5.3}$$

Therefore, the heat flux absorbed by the FRP was 80% of the incident heat flux measured by the sensor.

5.5.3 IR Thermography Test Procedure and Analysis

The heating module was placed at 0.33 m from the surface of the specimen and facing its surface. The specimen was placed so the air void was positioned at the same location relative to the heat lamps as was the heat flux sensor during heat flux measurement (position A as

mentioned in the previous section). The duration of the thermal pulse was set to 10 s. During the test, thermogram data were recorded at 15 Hz for a period of 60 s.

Two inspection procedures were investigated. The first procedure involved two tests. In the first test, the air void was at location A. In the second test, an unflawed region of the specimen was placed at location A. Temperature data were analyzed at the same location using the same spot meter. The signal as a function of time was obtained by subtracting the temperature data of the second measurement ($T_{background}$) from the temperature data from the first measurement (T_{defect}). This setup may seem unnecessary; it, however, ensured that both $T_{background}$ and T_{defect} were measured for the same heat flux input. This detail was important for comparison with analytical results. Additionally, it provided for comparison with the second quantitative thermography test to be described.

A 10-point averaging filter that computes a moving average of the temperature data was used to smooth the signal. The smoothed signal output is presented in Fig. 5.21. The maximum signal was 2.9 °C, and it occurred 12 s after the beginning of the test. This test produced a maximum surface temperature of 28.7 °C at the location of the flaw.

The second procedure involved one test. This would be similar to actual field-testing. The specimen was positioned so that the air void was at location A. The recorded data were analyzed by using two spot meters: one was placed above the center of the flaw to measure T_{defect}, the other was placed 15 mm from the apparent boundary of the air void (over undamaged material) to measure $T_{background}$. In this case, the maximum signal was 2.7 °C, and it also occurred 12 s after the start of heating. The maximum surface temperature was 28.4 °C. The smoothed signal as a function of time is presented in Fig. 5.22.

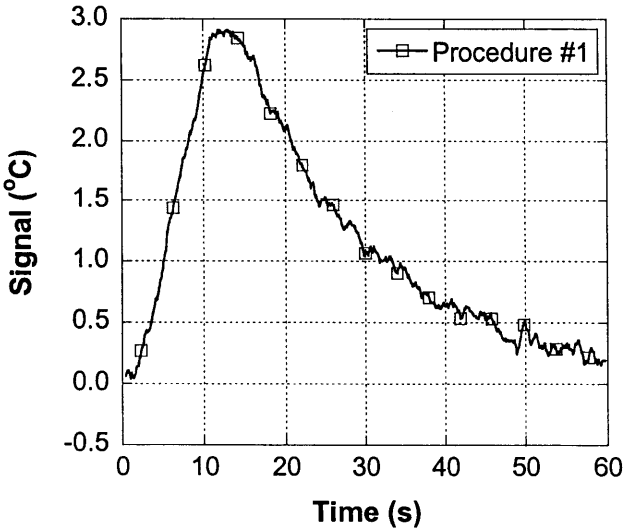

Fig. 5.21 Thermal signal for IR test #1 of air void

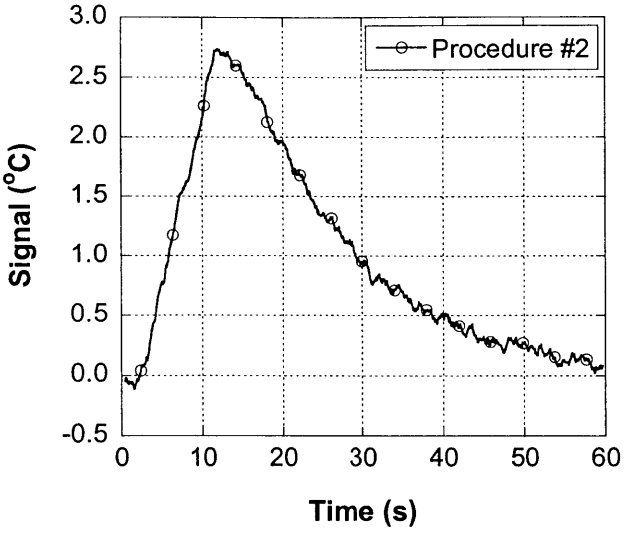

Fig. 5.22 Thermal signal for testing procedure #2

The two tests gave essentially the same results. This provides some assurance that the signals shown in Figs. 5.21 and 5.22 are valid.

5.5.4 Verification of FEM Simulations

5.5.4a Simulation Models

The numerical simulations were performed using ANSYS 5.6. To reduce computation time, two-dimensional models were used. The simulation object consisted of a 127 mm long by 20 mm thick concrete slab covered with one laminate of carbon FRP (CFRP). The CFRP laminate was 1.33 mm thick. A 0.9 mm thick by 25.4 mm long air void was introduced at the center of the specimen between the concrete substrate and the composite laminate. The bonding layer was modeled as a 0.9 mm thick layer of epoxy. The model is shown on the left side of Fig. 5.23. Since the air void was located at the centerline of the model, the simulation was simplified by using plane symmetry. Thus only one-half of the object was modeled, as shown on the right side of Fig. 5.23.

The material properties used in the model were those of concrete for the substrate, air for the defect, CFRP for the bonded composite, and epoxy for the bonding agent. The CFRP laminate had the fibers running in the longitudinal direction (x-direction). The material properties of air and concrete were gathered from the literature, and those of the FRP and epoxy were estimated from data provided by manufacturers. The thermal properties of carbon FRP varies significantly among products. The differences are due to the volumetric fraction of fibers used (which is usually greater than 68%), and due to the material properties of the composite (the fibers and the bonding agent). In addition, thermal properties of carbon fiber may vary widely. For example, a commercially available high strength fiber is reported to have a thermal conductivity of 9.38 W/m·K while its high-modulus counterpart is reported to have a thermal conductivity of 68.7 W/m·K. Since the material properties of the FRP composite used in this study were

unknown, their values were estimated from available information. The material properties used in the finite element simulations are listed in Table 5.6.

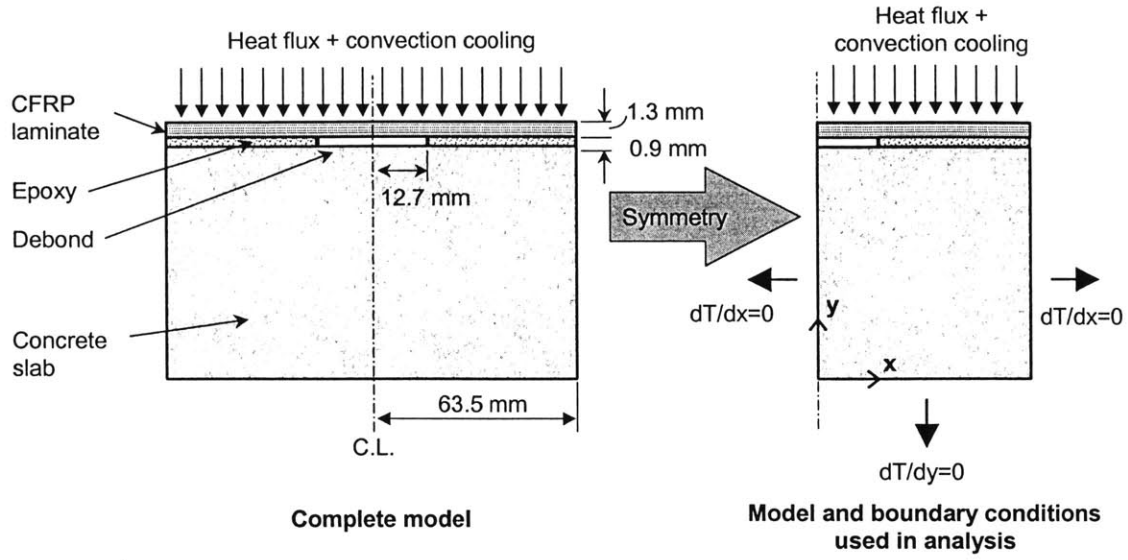

Fig. 5.23 Example of test object used in finite-element simulations

Table 5.6 Material properties used in numerical simulations

Material	Density, ρ (kg/m^3)	Thermal conductivity, k (W/m·K)			Specific heat, c (J/kg·K)
		k_x	k_y	k_z	
Concrete	2400	1.5	1.5	1.5	800
FRP	1760	8.9	2.9	2.9	800
Air	1.2	0.024	0.024	0.024	700
Epoxy	1960	0.19	0.19	0.19	1700

The model was meshed using 2-D solid elements and surface elements. Eight-noded quadrilateral elements were used for the solid model. The simulation of convective cooling required the use of surface effect elements. For this purpose, 2-D plane surface elements with two nodes were used. An extra node was added and linked to the surface elements to provide the input for ambient temperature. Each node in the model had one degree of freedom, temperature. Mapped meshing was used to allow direct control of the element size. The global element size was set to 0.1 mm. Mesh refinement was applied to the thin composite layers and at the FRP/concrete interface. The thickness of the composite laminate was subdivided into 4 elements while the thickness of the flaw was subdivided into 3 elements. The rest of the concrete substrate was meshed using a graded mesh with a finer mesh at the top and a coarser mesh at the bottom of the specimen. The average element size in the y-direction for the concrete was 0.00263 mm with a "spacing ratio" of 20. The spacing ratio is the ratio of the dimension of the largest element to the dimension of the smallest element.

The analysis was defined as a transient heat transfer problem. The applied heat pulse was based on the measured pulse shown in Fig. 5.20 as modified by Eq. (5.3). Uniform heating of the top surface was assumed. Convection cooling was applied to the top surface for the second and third simulations, and the heat transfer coefficients for the models were 10 W/m^2·K and 25 W/m^2·K, respectively. Adiabatic conditions ($dT/dx = 0$ and $dT/dy = 0$) were assumed for the additional surfaces. This assumption was realistic since the thermal pulse did not reach the bottom of the concrete during the duration of testing. The initial temperature for all the simulations was 22.8 °C, which represented the initial temperature of the specimen measured during testing. Perfect contact between the materials was assumed. Automatic time stepping with a minimum of 0.008 s and a maximum of 0.1 s was set for the analyses.

5.5.4b Results

Comparison of experimental measurements with analytical results was done by comparing three thermal response parameters: maximum surface temperature (T_{max}), maximum thermal signal (ΔT_{max}) and time for maximum signal (t_s).

The numerical simulations provided some interesting results. For example, the maximum surface temperature was affected slightly by convection cooling, and varied from 29.1 °C for no-convection to 28.7 °C for heat transfer coefficient of 25 W/m^2·K. The maximum surface temperatures measured in the two experiments were 28.7 °C and 28.4 °C.

The maximum thermal signal for the simulations ranged from 2.9 °C to 2.5 °C, while the experimental results indicated maximum thermal signals of 2.9 °C and 2.7 °C.

The time for maximum signal was 12 seconds for both experimental tests. The simulations provided similar values of t_s. The time for maximum signal was 12.5 s, 12 s and 11.7 s for simulations with convection coefficients of 0 W/m^2·K, 10 W/m^2·K and 25 W/m^2·K, respectively. Table 5.7 summarizes the experimental and analytical response parameters.

Table 5.7 Summary of response parameters for experiments and simulations

	IR measurements		**FEM results**		
	Test #1	**Test #2**	**h = 0 W/m^2·K**	**h = 10 W/m^2·K**	**h = 25 W/m^2·K**
T_{max} (°C)	28.7	28.4	29.1	28.9	28.7
ΔT_{max} (°C)	2.9	2.7	2.9	2.7	2.5
t_s (s)	12.0	12.1	12.5	12.0	11.7

Comparison of the thermal signal as a function of time, however, showed a systematic difference between the measured and computed results. As shown in Fig. 5.24, the experimental thermal

signal decayed at a faster rate than the analytical results. This mismatch may be the result of assumptions of the model. The model was assumed to be 2-dimensional and uniformly heated, which means no heat flow in the z-direction (normal to the cross-section shown in Fig. 5.23). In reality, this would not be the case and the rate of temperature drop would be expected to be higher. This will be verified through 3-D modeling.

For the purpose of quantitative nondestructive testing, however, the primary thermal response parameters are T_{max}, ΔT_{max}, and t_s. The analytical and experimental results were in good agreement, and provided reassurance that the analytical model is valid.

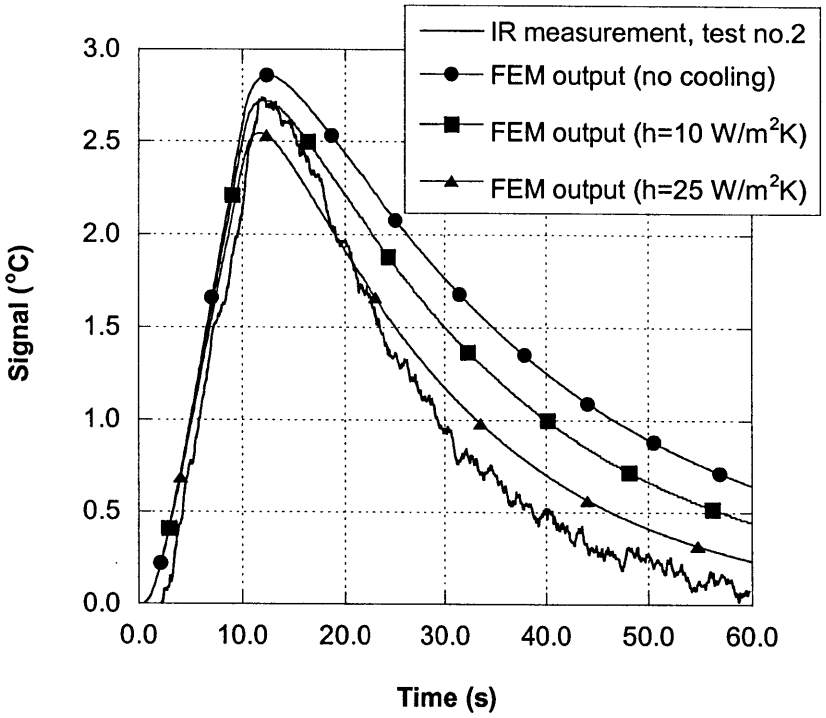

Fig. 5.24 Comparison of thermal signals for IR test #2 and FEM simulations

5.5.5 Conclusions of the Comparison of IR Thermography and FEM Simulation

Experiment #2 involved both experimental measurements and numerical simulations of infrared thermography testing of FRP laminates applied to concrete.

Infrared thermography testing was performed on an air void contained at the interface between a pultruded FRP laminate and the concrete substrate. In addition to thermography measurements, the experimental study involved the determination of surface emissivity using the contact and noncontact methods described in ASTM E 1933, and heat flux measurements. This was

necessary to allow comparison of measured thermal parameters with those computed using numerical models.

Numerical simulations were performed using 2-D models of the controlled-flaw specimen. Three cases were simulated to represent different levels of convective cooling of the surface. The measured thermal responses associated with the air void were compared with the analytical results. It was found that the amount of convective cooling had minor effects on the maximum signal and the time to maximum signal. The good agreement between the experimental and analytical results provided assurance that numerical simulations could be used to study the effects of different test parameters.

5.6 Experiment #3: Estimation of Flaw Width

During the qualitative test, it was observed that the air-filled flaw #6 was not square as intended. The bonding epoxy apparently flooded over the "wire dam" that was used to exclude epoxy and create the intended flaw. Thus flaw # 6 was chosen for verification of the procedure for width determination.

5.6.1 Test Procedure

The specimen was tested using the experimental configuration described in Fig. 5.2. The specimen was placed at 0.33 m from the camera lens. Moreover, the test object was placed so that the air-filled flaw was positioned at the centerline between the two heating lamps. The duration of the thermal pulse was set to 10 s, and the thermogram data were recorded at 15 Hz for a period of 60 s.

The surface temperatures above the flaw (T_{defect}) and above the bonded laminate near the flaw ($T_{background}$) were obtained as a function of time. The maximum signal was 2.7 °C, which occurred at 12 s after the beginning of the test. The maximum surface temperature registered was 28.4 °C.

5.6.2 Data Analysis

To estimate the width of the air-filled flaw, the thermogram corresponding to the time of maximum signal was analyzed. The surface temperatures of the region surrounding the flaw were retrieved using an *area*-measuring tool. The retrieved *area* had dimensions of 35 pixels × 28 pixels. Since the analysis software provides surface temperatures at each pixel, a conversion between pixel size and actual physical size was required. The conversion was done using the known dimension of a heat flux sensor and a piece of tape located on the surface of the specimen as reference. The heat flux sensor and the tape had actual widths of 25.4 mm and 18.7 mm, respectively, and in thermogram image the corresponding dimensions were 23 pixels and 17 pixels. Thus, each pixel corresponded to a 1.1 mm square, and the analyzed region surrounding the flaw was 38.5 mm × 30.8 mm. This area box is shown in Fig. 5.25.

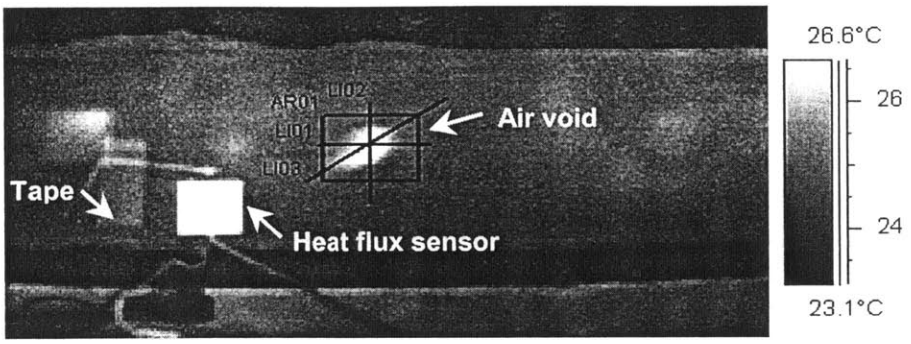

Fig. 5.25 Thermogram of air flaw at time of maximum signal

The plan dimensions of the flaw were estimated by analyzing the surface temperatures along three lines, as shown in Fig. 5.25. Unlike the FEM output, the surface temperature data along each line did not vary smoothly, and a 5-point moving average was computed to smooth the data. This smoothing was also applied to the second derivative of the temperature profile.

The smoothed surface temperature and the smoothed second derivative along the horizontal line (LI01) are presented in Fig. 5.26. The roots of the second derivative ($d^2T/dx^2=0$) were located at 8.8 mm and 25.6 mm from the origin. Thus, the estimated width of the flaw along the horizontal line is 16.8 mm.

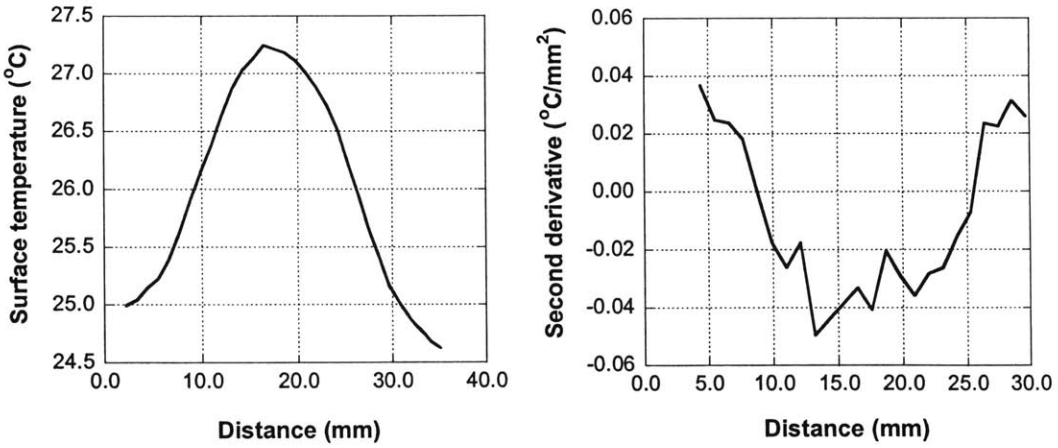

Fig. 5.26 Smoothed surface temperature profile and second derivative with respect to distance along horizontal line (LI01)

A similar procedure was used for the vertical line (LI02). In this case, the surface temperature profile and the second derivative curve were smoothed using the moving average of 5 points and 3 points, respectively. The resulting smoothed plots are shown in Fig. 5.27. The roots of the second derivative were located at 4.7 mm and 21.0 mm from the origin of the line. Thus the estimated width of the flaw along the vertical line is 16.3 mm.

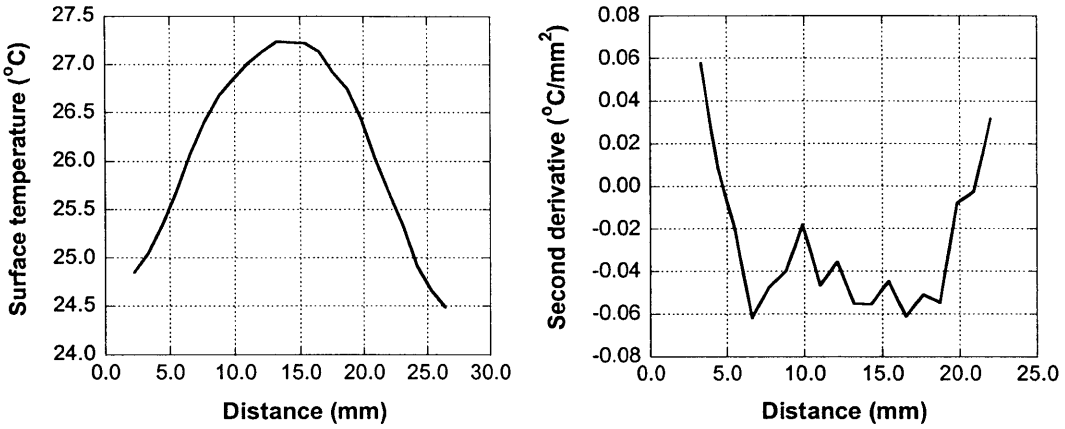

Fig. 5.27 Smoothed surface temperature profile and second derivative with respect to distance along vertical line (LI02)

Finally, the diagonal dimension was estimated. For this case, temperatures along the diagonal of the surface temperature matrix were used. The surface temperature was extracted every 3.97 mm along the diagonal. No smoothing of the temperature profiles and second derivative was required in this case. The temperature profile and its second derivative are presented in Fig. 5.28. The second derivative provided four roots. Based on observation of the surface temperature profile, the outer roots were used for estimation of the width. The outer roots of the second derivative were 1.4 mm and 29 mm, and the estimated diagonal width of the air void is 27.6 mm.

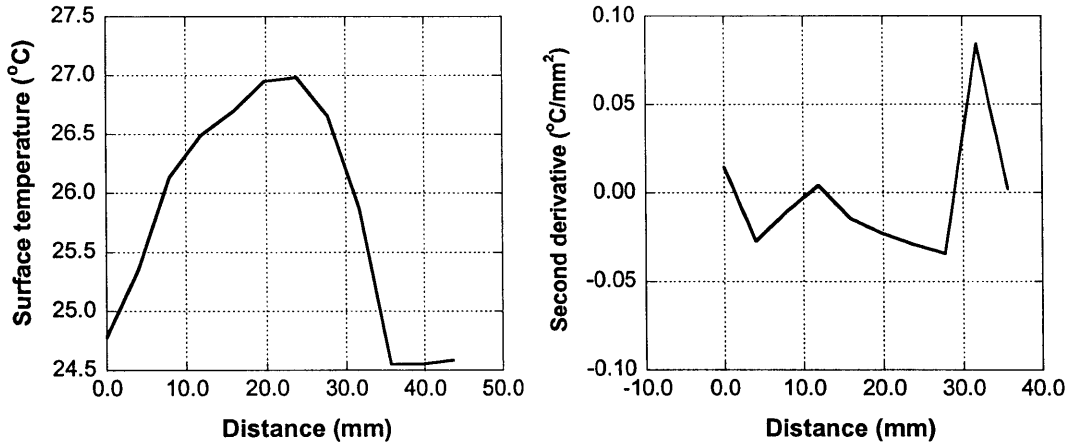

Fig. 5.28 Surface temperature profile and second derivative with respect to distance along diagonal line (LI03)

To verify the estimated dimensions, the portion of FRP laminate above the air flaw was removed carefully by using a miniature high-speed cut-off wheel. This procedure revealed the shape of the air void. A visual image of the exposed air void is presented in Fig. 5.29 and compared with its image during thermographic testing.

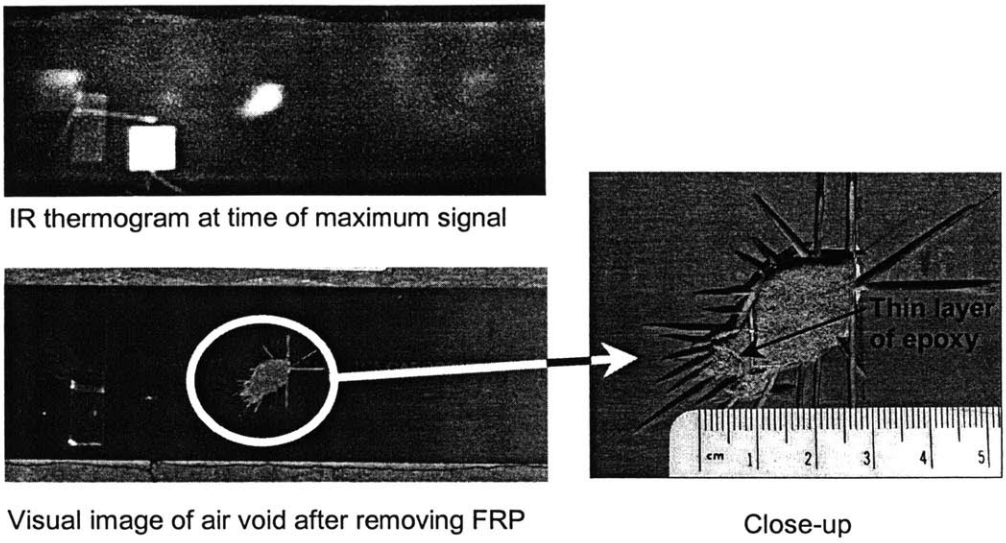

Fig. 5.29 Thermogram and visual images of air flaw

The measured horizontal, vertical, and diagonal dimensions of the actual air void were a horizontal width of 17 mm, a vertical width of 17 mm, and a diagonal width of 31 mm. Table 5.8 summarizes the estimated and actual widths of the air void.

Table 5.8 Estimated and actual widths of air void

	Estimated width (mm)	**Actual width (mm)**
Horizontal line	17	17
Vertical line	16	17
Diagonal line	28	31

The maximum estimation error was in the diagonal dimension, where the width was underestimated by 3 mm. Observation of the flawed region revealed that in the lower left corner of the flaw there was an unbonded area with a thin layer of epoxy on the concrete (see Fig. 5.29). Thus, the thickness of the air void was reduced in this region. The estimated diagonal width matched the distance between the upper right corner of the flaw and the edge of the thin layer of epoxy. The thinner air gap at the lower-left corner produced a lower signal than the rest of the flaw where there was no epoxy between the FRP and the concrete. It is possible that the error in width estimation could have been reduced by analyzing surface temperature measurements over a larger area.

The results show that curve smoothing using a moving average algorithm is an effective means for dealing with noisy signals. The number of points used in the smoothing may depend on the surface temperature profile. The goal is to easily identify the roots of the second derivative curve while minimizing the distortion of the original data. Thus, the number of points used to

smooth the curves should be kept as small as possible. Additional studies on estimating flaw size should lead to guidelines for proper smoothing of temperature profile data.

5.6.3 Conclusions of the Estimation of Flaw Width

The experiment involved the study of the estimation of the width of an air void located at the interface between the concrete and the pultruded FRP laminate. The width of the flaw was assessed by estimating the location of the second derivative of the surface temperature profile at the time of maximum signal. A smoothing procedure using a moving average algorithm proved to be an effective means for dealing with noisy signals and second derivatives.

5.7 Experiment #4: Screening Experiment

The next set of experiments involved a screening parametric investigation. The aim of this experiment was to verify the results found in the multi-factor parametric study

Development of a potential model requires the search for the important factors affecting a response. Three flaw parameters were investigated: flaw depth, flaw thickness, and flaw width. To investigate these three parameters, a full factorial design with 2 "center" points was planned.

5.7.1 Determination of Surface Emissivity of Wet Lay-Up FRP

The surface emissivity of the wet lay-up carbon FRP was determined using the procedures described in ASTM E 1993. Two different specimens were fabricated to measure the emissivity of the wet lay-up composite. The first specimen was built with the normal amount of epoxy. This test object was tested using the contact method, which involved the use of surface thermocouples and the noncontact method using tape. The remaining specimen was constructed with a smaller amount of epoxy than the recommended by the manufacturer and was used to determine the emissivity of the composite using only the noncontact method.

The procedures for measuring the surface emissivity were the same as those explained in section 5.5.1.

The ambient temperature of the room in the direction against the surface of the specimen was measured and its value was 24 °C. During testing the test object under testing was placed at a distance of 0.55 m from the infrared camera and placed perpendicular to the line of view of the camera.

The first method used to estimate the surface emissivity was the contact method using thermocouples. Surface temperatures of the FRP laminate were measured using a copper/constantan thermocouple (ANSI Type T, special limits, 0.010 mm in diameter). The thermocouple was bonded to the surface of the test object so half of the perimeter of the wire was embedded in the FRP material and half of the perimeter was in contact with the air. A notch of 0.02 m in length was cut into the composite and epoxy adhesive was used to hold the thermocouple in place.

The surface of the wet lay-up composite was heated in an oven 32 °C above room temperature. This procedure ensured that the test object was thoroughly heated to avoid rapid transient cooling. Once out of the oven, cooling of the specimen occurred slowly thus allowing emissivity measurement. Measurements were recorded for temperatures ranging from 32 °C to 10 °C above room temperature.

Temperature measurements of the surface were taken using a digital thermometer attached to the thermocouple and using the infrared camera. Surface temperatures next to the location of the thermocouple were taken with the infrared camera using the spot meter measuring tool. Surface temperatures were measured at 3 points next to a thermocouple using 3 spot meters. The emissivity at each spot meter was varied in order to match the temperature measured with the thermocouple and the temperature indicated by the camera. The measurements were repeated 231 times. The measured emissivity ranged from 0.94 to 1.0 (Fig. 5.30), the average emissivity of the FRP laminate was 0.98, with a standard deviation of 0.01. Thus the expanded uncertainty interval is 0.98 ± 0.02. It is important to note that a large number of measurements had to be disregarded because they had values of emissivity above 1.0. Emissivity values above 1.0 are theoretically impossible. This fact indicated a possible limitation of the contact method procedure for materials with high emissivity. This issue will have to be investigated further in the future.

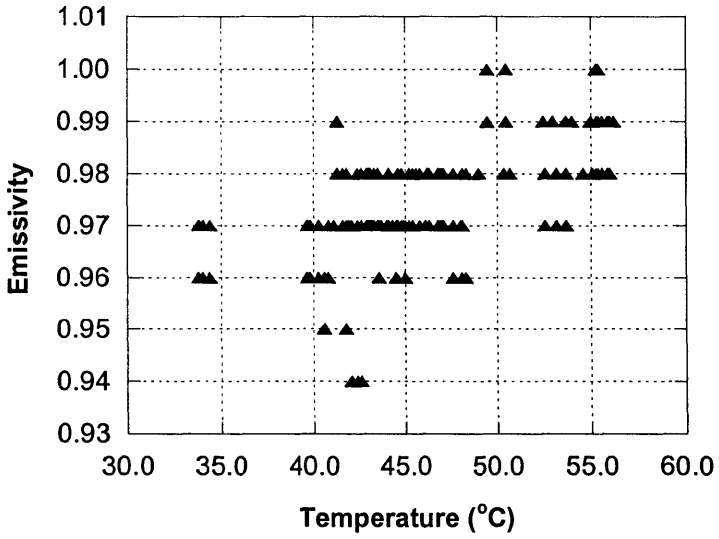

Fig. 5.30 Emissivity measurements using thermocouples for wet lay-up carbon FRP

The second method used to determine the emissivity of the wet lay-up composite was the noncontact thermometer method specified in ASTM E 1933. For this measurement, a small piece of electrical tape with an emissivity of 0.95 (Mikron, 2002 and Rineldi, 2002) was applied to the surface of the specimen. The specimen was heated in an oven to a temperature of 89 °C. The specimen was removed from the oven to take the emissivity measurements. An "area" measurement function was used to measure the average temperature of the tape. The temperature

of the FRP adjacent to the tape was measured using 3 spot meters. The temperature of the tape ($\varepsilon = 0.95$) was measured with the infrared camera. The emissivity of the "area" measuring the FRP's temperature was adjusted to match the temperature of the tape. The computation of the emissivity at the location of the spot meters was done automatically by the analysis software using an *Emissivity Calculation* tool. Emissivity measurements were recorded for surface temperatures ranging from 60 °C to 37 °C above room temperature.

A total of 81 measurements were recorded. The values of emissivity ranged from 0.95 to 0.97 (Fig. 5.31). The average emissivity of the wet lay-up FRP with normal amount of epoxy was 0.96, with a standard deviation of 0.005. Thus the expanded uncertainty interval is 0.96 ± 0.01.

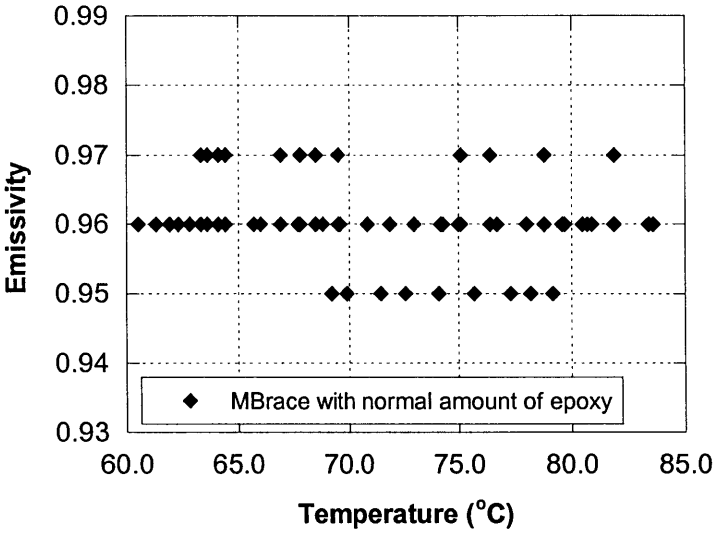

Fig. 5.31 Emissivity measurements using noncontact method for wet lay-up carbon FRP with normal amount of epoxy

The same noncontact procedure was used to measure the emissivity of the wet lay-up FRP composite fabricated with a small amount of epoxy. That is, the specimen was fabricated with less epoxy than the recommended by the manufacturer. As previously, the specimen was heated in an oven to a temperature of 89 °C. The specimen was removed from the oven to take the emissivity measurements. Emissivity measurements were recorded for surface temperatures ranging from 60 °C to 37 °C above room temperature. Room temperature was 23 °C while ambient temperature was 24 °C.

A total of 23 emissivity measurements were taken. The recorded values ranged from 0.88 to 0.92. The recorded data are presented in Fig. 5.32. The average emissivity of the wet lay-up FRP with small amount of epoxy was 0.90, with a standard deviation of 0.01. Thus the expanded uncertainty interval is 0.90 ± 0.02.

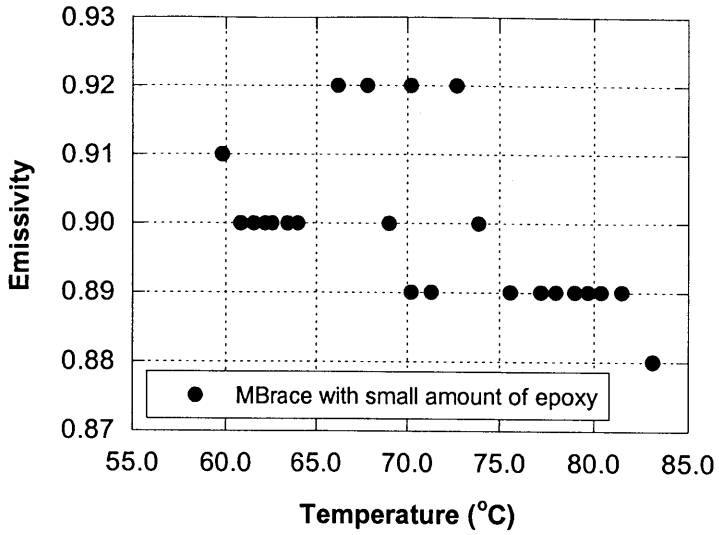

Fig. 5.32 Emissivity measurements using noncontact method for wet lay-up carbon FRP with small amount of epoxy

The results indicate a clear difference between the emissivity of wet lay-up carbon FRP containing different amounts of epoxy.

Also, it is important to remember that the emissivity values depend on temperature, angle of observation, and spectral wavelength at which they are measured. Temperature has to vary by several hundreds of degrees in order to have a significant effect in the emissivity of a material. The effect of angle of observation was not evaluated in this project. For this project, the angles of observation during thermography testing were smaller than 10° from the perpendicular to the surface of the test object. The emissivity values reported in this chapter apply to measurements taken in the 8-12 μm spectral wavelength, at angles near the 90° with respect to the surface of the FRP, and for temperatures near room temperature.

5.7.2 Determination of Heat Flux

Next, the incident heat flux as a function of time was measured. To measure the same heat pulse that the test object would see during thermography testing, the heating module was placed at 0.37 m from the surface of the test object and facing its surface and the pulse duration was set to 10 s using the pulse generator and the external trigger. The lamps were triggered to turn on at the beginning of the pulse. After 10 s, the pulse generator sent a signal to the trigger circuit board to turn off the lamps and to drop the shutter in front of the heating module.

The heat flux was measured using a heat flux transducer bonded to the surface of the FRP composite. The incident heat flux was measured using a data acquisition system that recorded the voltage through the transducer. The heat flux was computed using the measured voltage through the heat flux sensor and the transducer's calibration sensitivity provided by the manufacturer. As in previous heat flux measurements and in order to record the heat flux that the specimen would be subjected to during thermography testing, the heat flux sensor was placed

at the same position with respect to the heating lamps that the flawed specimen would be during thermography testing.

Ten heat flux measurements were performed. The first three tests showed some bonding difficulties of the heat flux sensor to the surface of the wet lay-up composite. Towards the end of each measurement, the transducer was barely attached to the surface, thus, those measurements were disregarded. The bonding problem arose because the uneven surface of the wet lay-up composite. Five additional tests were performed with the heat flux sensor bonded to the wet lay-up composite. The data of this set of test was kept since the transducer seemed to be in contact with the surface throughout the duration of the test. Since bonding of the heat flux sensor to the pultruded FRP was more reliable, two other measurements were performed by placing the pultruded FRP laminate with a bonded heat flux sensor at the location were the previous measurement were taken.

Table 5.9 summarizes the results of the heat flux measurements. The results are presented as the average heat flux for the experiments using the sensor bonded to hand lay-up FRP and the experiments involving the sensor bonded to the pultruded FRP. The results illustrate that the heat flux for both cases was similar. Finally, the overall average of all the measurements is presented in Table 5.9 and illustrated in Fig. 5.33. The maximum average heat flux was 1620 W/m^2 and the standard deviation was 97 W/m^2.

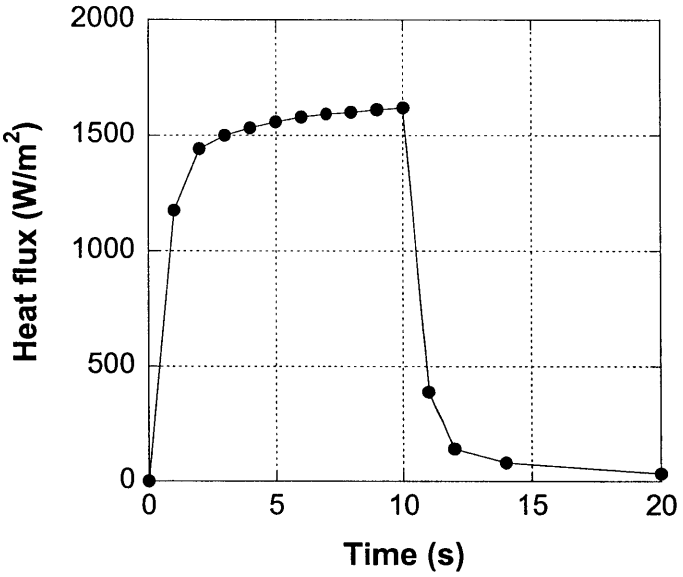

Fig. 5.33 Average heat flux for screening experiments

Table 5.9 Heat flux measurements

Time (s)	Incident heat flux, $q_{incident}$ (W/m^2)			
	Average with sensor bonded to hand lay-up FRP	Average with sensor bonded to pultruded FRP	Overall average	Standard deviation
0	0	0	0	0
1	1200	1100	1170	113
2	1430	1480	1440	94
3	1490	1540	1500	105
4	1520	1570	1530	105
5	1540	1600	1560	102
6	1560	1620	1580	100
7	1580	1640	1590	99
8	1590	1630	1600	95
9	1600	1640	1610	95
10	1610	1640	1620	97
11	360	460	390	68
12	150	110	140	23
14	100	40	80	35
20	50	0	33	23

5.7.3 Test Procedure

First, a qualitative test was performed to determine the potential detection of all the flaws in each of the two specimens fabricated for this experiment. The qualitative test followed the procedure explained in 5.3.1. The qualitative test showed that all the low-k fabric (Nomex®) flaws from one of the fabricated controlled-flaw were detectable. On the other hand, most of the thin film (Parafilm®) flaws from the remaining specimen were undetectable. Thus, the subsequent set of quantitative measurements was performed only on the specimen containing flaws made from Nomex®.

Before starting the test, the ambient temperature was measured following the procedure described in Sec. 5.5.1. The infrared camera was placed against the surface of the test object and facing away from its surface. The emissivity of the IR image was set to 1.0 and the average temperature of the image was measured. This average temperature corresponded to the ambient temperature and had a value of 24 °C.

Ten different tests were performed. Only one subsurface flaw was measured during each test. Testing of the controlled-flaw specimen was carried out following the running sequence indicated in Table 5.2. This running sequence was random to ensure unbiased of the results.

The test object was tested using the experimental configuration illustrated in Fig. 5.2. The specimen was placed at 0.37 m from the heating module and the IR camera. Additionally, the test object was placed so that the subsurface flaw under study was positioned at the centerline between the two heating lamps. The duration of the thermal pulse was set to 10 s, and the thermogram data were recorded at 15 Hz for a period of 60 s.

The surface temperatures above the flaw (T_{defect}) and above the bonded laminate near the flaw ($T_{background}$) were obtained as a function of time for each test.

5.7.4 Data Analysis

5.7.4a Analysis of Individual Tests

For each individual flaw, the surface temperature above the flaw and the surface temperature in the background were recorded. Both the signal and the contrast as functions of time computed. Similarly to previous tests, the results of the thermal response as a function of time were noisy and had to be filtered for proper interpretation of the results. Smoothing of the data was accomplished using a moving or running average algorithm. An example of the measured signal and the smoothed signal is presented in Fig. 5.34. The signal presented in Fig. 5.34 was smoothed using 25 points for the running average.

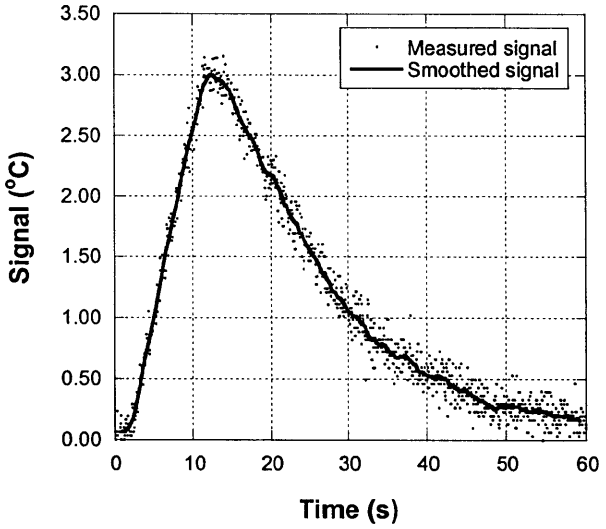

Fig. 5.34 Example of signal smoothing (run #3 corresponding to flaw #10)

The contrast was computed using Eq. 4.8. The value of contrast tended to have a small amount of noise at the beginning of the test until the heat source is turned off. The contrast, however, becomes increasingly noisier after the end of the heat pulse as illustrated in the example in Fig. 5.35.

In an attempt to gather values of maximum contrast and time to maximum contrast, a smoothing procedure similar to the one performed with the signal was used to smooth the computed contrast. First, the temperature in the background $T_{background}$ and the signal ΔT were smoothed. Typically, 9 data points were used for the running average of these two thermal responses. The contrast was computed using these two smoothed values and the initial temperature of the background at t = 0 s. After smoothing, the contrast still showed evidence of high noise thus preventing the determination of the maximum contrast and the time to maximum contrast. The contrast as a function of time was smoothed a second time using 75 points for the calculation of the moving average. The smoothed contrast curve is presented in Fig. 5.35 in addition to the measured (unsmoothed) contrast data.

The same analysis procedures were performed to analyze the data from each test. The results of the signal calculation for flaws #1 though #9 are presented in Fig. 5.36.

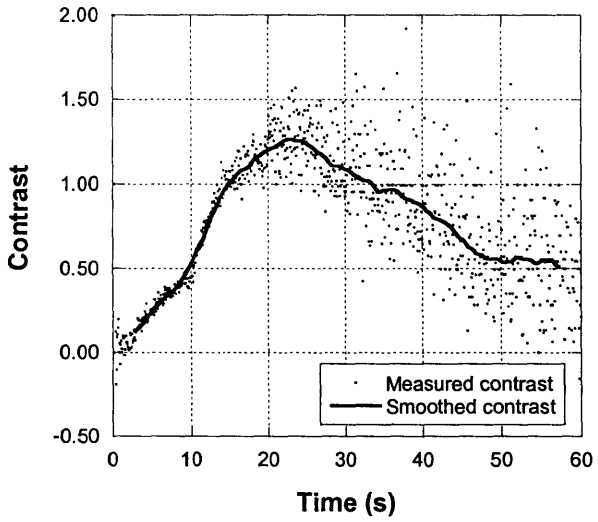

Fig. 5.35 Example of contrast smoothing (run #3 corresponding to flaw #10)

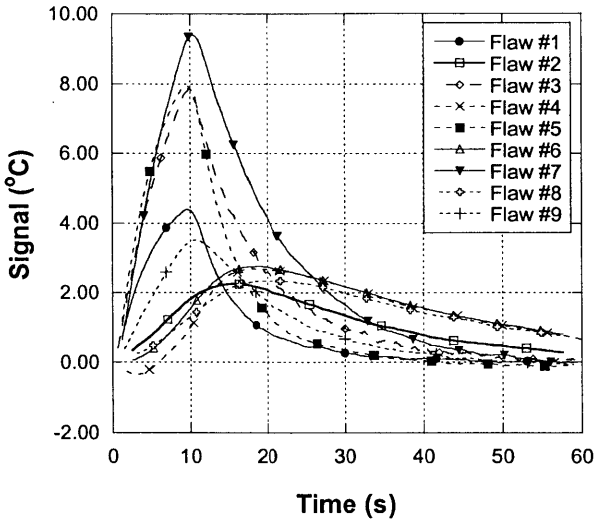

Fig. 5.36 Smoothed signals for flaws #1 through #9

The results of the smoothed contrast curves for flaws #1 through #9 are presented in Fig. 5.37.

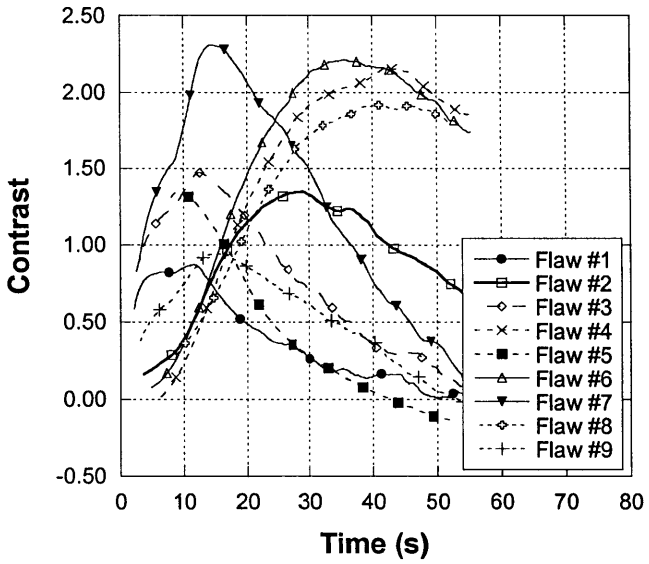

Fig. 5.37 Smoothed contrast for flaws #1 through #9

5.7.4b Analysis of Full Factorial Screening Experiment

Based on the results of the analysis of the individual tests, the results of the screening experiment were evaluated for five different thermal responses. The thermal responses recorded were t_s,

ΔT_{max}, *Contrast*, t_c, and T_{max}. A summary of the resulting thermal responses from the experiment is presented in Table 5.10.

The results of the parametric study described in Chapter 4 indicated that the only thermal response that has the potential to characterize the flaw is the time to maximum signal t_s. The magnitude of the maximum signal ΔT_{max} and the maximum temperature T_{max} provided data that was too spread to be used in an effective model to characterize the subsurface flaw. The same results were observed in the evaluation of the experimental data. Of all the responses summarized in Table 5.10, only the results of the study of the time to maximum signal and the time to maximum contrast will be summarized in the following sections.

Table 5.10 Experimental data for full factorial screening experiment

		Design of Study			**Results**				
Flaw #	**Run Sequence**	x_1	x_2	x_3	t_s (s)	ΔT_{max} (°C)	T_{max} (°C)	**Max.Contrast**	t_c (s)
1	6	−	−	−	10.2	4.6	33.5	0.87	11.5
2	4	+	−	−	15.5	2.3	30.6	1.35	28.9
3	2	−	+	−	10.0	8.1	37.9	1.47	12.4
4	1	+	+	−	17.9	2.9	32.0	2.16	42.7
5	9	−	−	+	10.0	8.1	38.2	1.51	10.6
6	10	+	−	+	19.0	2.8	31.8	2.21	34.4
7	5	−	+	+	10.4	9.4	40.3	2.31	14.4
8	7	+	+	+	19.9	2.4	31.8	1.92	40.9
9	8	0	+	0	10.8	3.5	33.1	0.94	15.2
10	3	0	−	0	12.3	3.0	32.6	1.26	23.0

5.7.4c Analysis of Results for t_s

The first thermal response investigated was the time to maximum signal. The effect from each factor on the thermal response was computed by subtracting the group averages as indicated in Eq. 4.113. The results of the calculation of the effect of each factor and their interactions on the time to maximum signal are presented in Table 5.11.

Table 5.11 Estimate of the effects of the factors and their interactions on the time to maximum signal

Factor or Interaction	$\bar{y}_+$ (s)	$\bar{y}_-$ (s)	$\hat{\beta}_i$ (s)
x_1	18.1	10.2	7.9
x_2	14.6	13.7	0.9
x_3	14.8	13.4	1.4
$x_1 \cdot x_2$	14.5	13.7	0.8
$x_1 \cdot x_3$	14.8	13.5	1.3
$x_2 \cdot x_3$	14.0	14.2	-0.2
$x_1 \cdot x_2 \cdot x_3$	13.8	14.4	-0.5

Figure 5.38 illustrates the results summarized in Table 5.11. As explained in section 4.9, each plot presents a factor or interaction versus the average of the thermal response at levels "+" and "−". The slope of each line is an indicator of the effect of the factor on the time for maximum signal. The plots that present greater slopes correspond to the factor or interaction with greater effect on the response. The results indicate that the depth of the flaw (factor x_1) is the parameter that affects the time to maximum signal the most.

Comparing the difference of the means ($\hat{\beta}_i$) to the minimum engineering significant response allows narrowing of the factors that have a significant effect on the thermal response. The minimum engineering significant response for t_s was selected a priori using engineering judgment. The selected minimum engineering significant response for t_s was greater than the sampling period of the data acquisition system but small enough to describe the thermal response. The value selected was 0.5 s. Based on the minimum engineering response, all the factors and interactions with the exception of the interaction between width and thickness should be considered to affect t_s. The ranking of these factors and interactions from the highest effect to the lowest effect are the following:

5. x_1 (depth of flaw) → $\hat{\beta}_1 = 7.9$ s
6. x_3 (width of flaw) → $\hat{\beta}_3 = 1.4$ s
7. x_{13} (interaction between depth and width of flaw) → $\hat{\beta}_{13} = 1.3$ s
8. x_2 (thickness of flaw) → $\hat{\beta}_2 = 0.9$ s
9. x_{12} (interaction between depth and thickness of flaw) → $\hat{\beta}_{12} = 0.8$ s
10. x_{123} (interaction between depth, thickness and width of flaw) → $\hat{\beta}_{123} = -0.5$ s

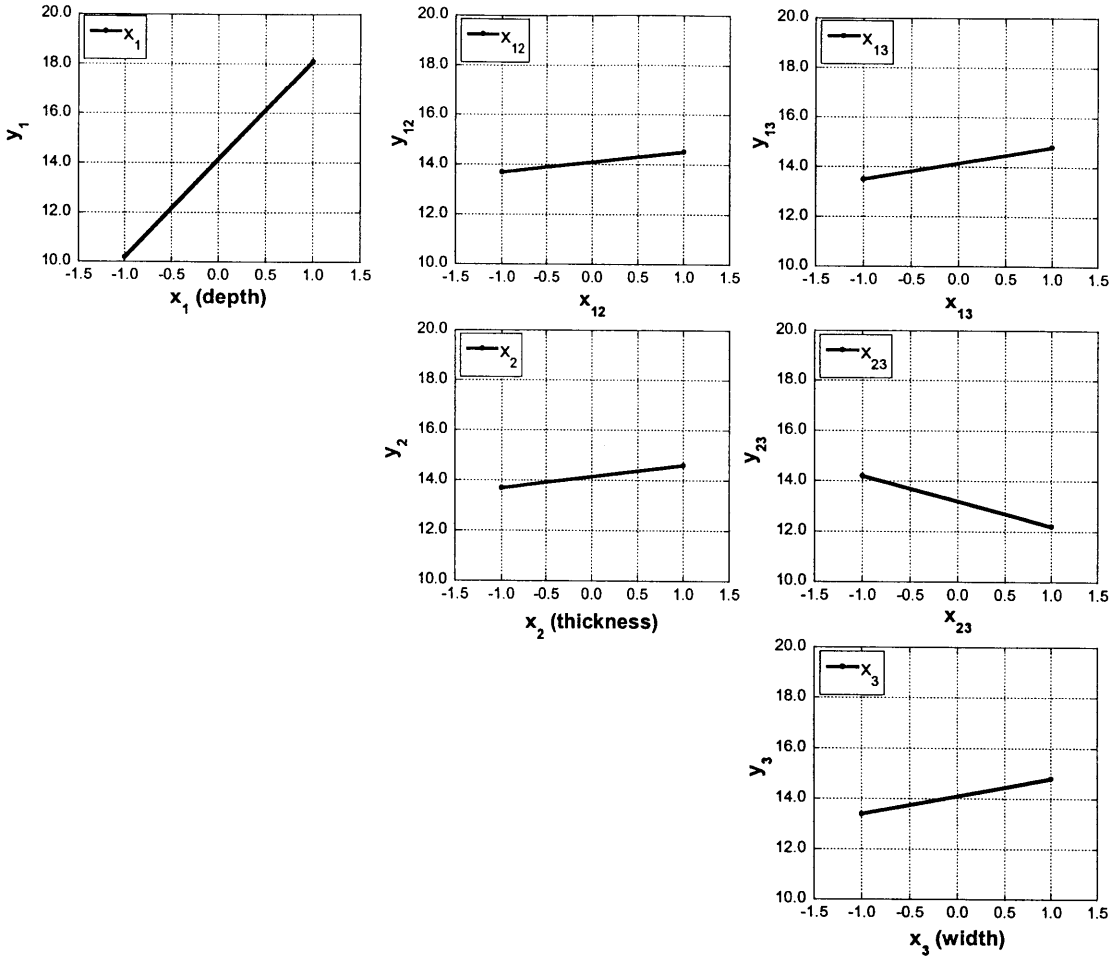

Fig. 5.38 Plots of means of factors and interactions for the time to maximum signal

The search for the important factors affecting t_s was refined using a plot of the halfnormal probability. The plot of the halfnormal probability is the most powerful tool to determine what factors and interactions are the ones that have an important effect on the response. To determine what factors and interaction had an important effect on the thermal response, the $\hat{\beta}_i$s were arranged in ascending order based on their magnitude. A straight line with a least square fit to the located near the origin was drawn. The criterion states that the factors and interactions that deviate from the straight line are the factors that have an important effect on the response. Figure 5.39 presents the halfnormal probability plot for this study. The plot confirms that only the depth of the flaw has an important effect on the time to maximum signal.

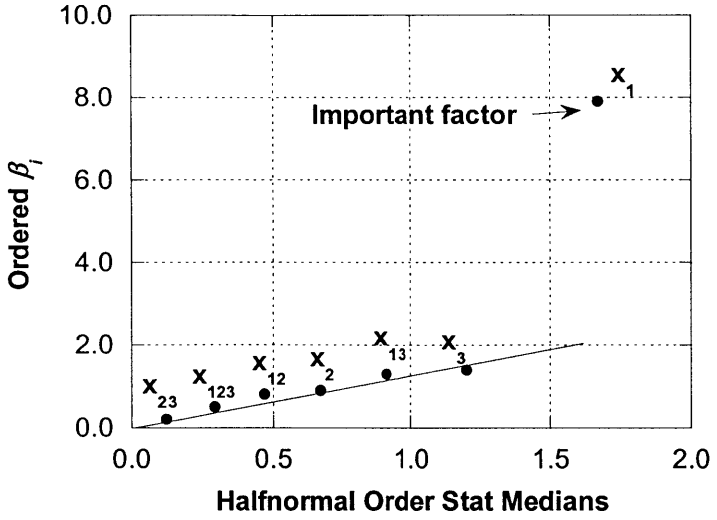

Fig. 5.39 Halfnormal probability plot for the time to maximum signal

Even though the previous criteria indicated that the width and the interaction between the depth and width have some effect on t_s, the halfnormal probability analysis shows that the depth of the flaw is the only main parameter affecting the time to maximum signal. This conclusion is illustrated in Fig. 5.39.

Development of any possible model for estimation of the depth of the flaw could be done using the time to maximum signal alone. Therefore, the results of this screening test are in agreement with the results presented for the simulations in Sec. 4.9.4.

To develop an estimation procedure, the time to maximum signal as a function of the depth was plotted from the results of the full factorial experiment and including the two center data points.

Figure 5.40 displays the time to maximum signal at each of the coded depths, -1, 0, and +1 (see data in Table 5.10). The graph illustrates that the time to maximum signal for flaws located near the surface is very similar regardless of the width and the thickness of the flaw. All the flaws at a coded depth of –1 generated times to maximum signal between 10.0 s and 10.4 s. The time to maximum signal starts spreading as the depth of the subsurface flaw increases. Thus at large depths, the remaining factors, width and thickness, have more effect on the response than at small depths. A potential approach to estimate the depth involves the development of an envelope function with an upper and a lower bound of the t_s as a function of the actual depth of the subsurface flaw, as illustrated in Fig. 5.41. A function using the averages at each depth is also plotted.

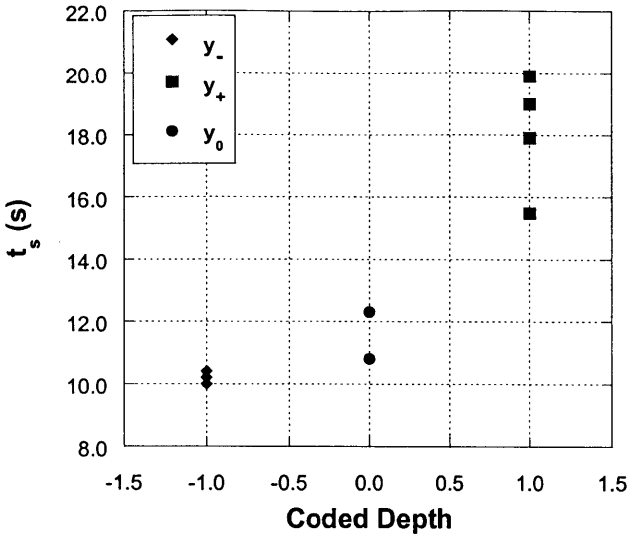

Fig. 5.40 Time to maximum signal data as a function of the coded depth (-1,0,+1)

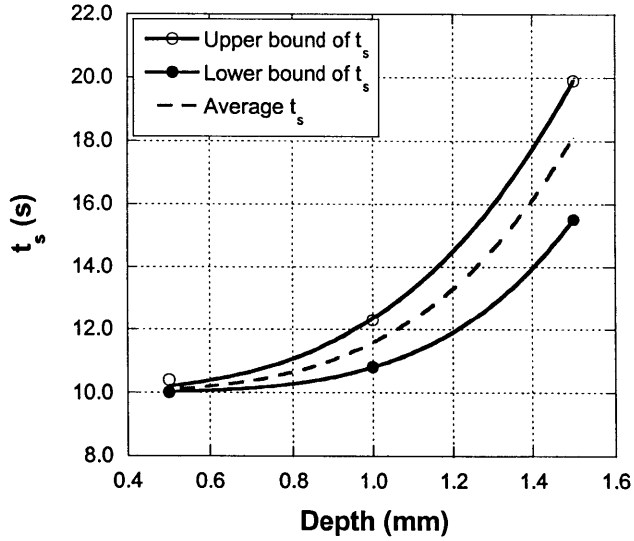

Fig. 5.41 Time to maximum signal data as a function of the actual depth

The functions that define the upper and lower bounds of the envelope are the following:

- for the upper bound,

$$t_s\big|_{upper} = 10 + 2.35 d_{flaw}^{3.55} \tag{5.4}$$

where $t_s|_{upper}$ is the time to maximum signal for the upper bound, and d_{flaw} is the depth of the flaw; and

- for the lower bound,

$$t_s|_{lower} = 10 + 0.80 d_{flaw}^{4.76} \tag{5.5}$$

where $t_s|_{lower}$ is the time to maximum signal for the upper bound, and d_{flaw} is the depth of the flaw.

The function defining the average time to maximum signal as a function of the depth is the following:

$$t_s|_{avg} = 10 + 1.57 d_{flaw}^{4.05} \tag{5.6}$$

where, $t_s|_{avg}$ is the average time to maximum signal and d_{flaw} is the depth of the flaw.

As stated, the depth of the flaw could be estimated using the average time to maximum signal. For example, as illustrated in Fig. 5.42, if the time to maximum signal is 13 s, the estimated depth of the flaw would be 1.2 mm, approximately. On the other hand, the estimation of the depth using the upper bound of the envelope assigns a depth of 1.1 mm to the 13 s time to maximum signal, while the estimation using the lower bound provides a value of 1.3 mm, approximately. The estimation of the depth using $t_s|_{avg}$ differs only by 0.1 mm from the values of the depth corresponding to the upper and lower bounds. Thus the potential error in the estimation of the flaw using the average t_s at a specific depth is smaller than the thickness of one layer of FRP, which is usually on the order of 0.5 mm. The estimation function results from inverting Eq. 5.7 as follows:

$$d_{estimate} = \left(\frac{t_s|_{measured} - 10}{1.57} \right)^{1/4.05} \tag{5.7}$$

where $d_{estimate}$ is the estimated depth of the flaw, and $t_s|_{measured}$ is the measured time to maximum signal.

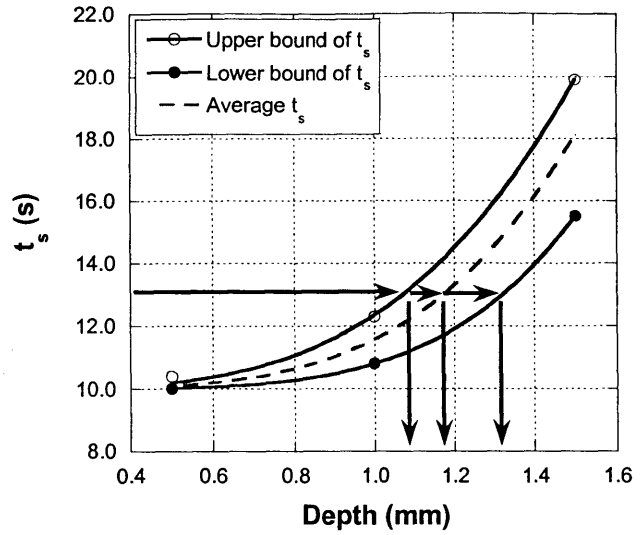

Fig. 5.42 Estimation of flaw depth as a function of the time to maximum signal

5.7.4d Analysis of Results for t_c

The next thermal response examined was the time to maximum contrast. Again, the effect from each factor on t_c was computed by subtracting the group averages as indicated in Eq. 4.113. The results of the calculation of the effect on the time to maximum contrast of each factor and the interactions are presented in Table 5.12.

Table 5.12 Estimate of the effects of the factors and their interactions on the maximum signal

Factor or Interaction	$\bar{y}_+$ (s)	$\bar{y}_-$ (s)	$\hat{\beta}_i$ (s)
x_1	36.7	12.2	24.5
x_2	27.6	21.4	6.2
x_3	25.1	26.4	-1.3
$x_1 \cdot x_2$	26.4	22.5	3.9
$x_1 \cdot x_3$	24.8	24.2	0.6
$x_2 \cdot x_3$	23.9	25.0	-1.1
$x_1 \cdot x_2 \cdot x_3$	23.2	25.8	-2.6

The minimum engineering significant response for t_c was selected a priori as 0.5 s. Comparing the difference of the means to the minimum engineering significant response is a means to narrow the field of factors that have a significant effect on the thermal response. Based on this criterion, however, all the factors and interactions had an effect in the thermal response. The ranking of these factors and interactions from the highest effect to the lowest effect (based on magnitude of the difference of the means $\hat{\beta}_i$) are the following:

1. x_1 (depth of flaw) → $\hat{\beta}_1 = 24.5$ s
2. x_2 (thickness of flaw) → $\hat{\beta}_2 = 6.2$ s
3. $x_1 \cdot x_2$ (interaction between depth and thickness) → $\hat{\beta}_{12} = 3.9$ s
4. $x_1 \cdot x_2 \cdot x_3$ (interaction between depth, thickness and width) → $\hat{\beta}_{13} = -2.6$ s
5. x_3 (width of flaw) → $\hat{\beta}_3 = -1.3$ s
6. $x_2 \cdot x_3$ (interaction between thickness and width) → $\hat{\beta}_{23} = -1.1$ s
7. $x_1 \cdot x_3$ (interaction between depth and width) → $\hat{\beta}_{13} = 0.6$s

In order to determine which of all the factors actually had an important effect on the time to maximum contrast, the half normal probability was plotted. The half normal probability is presented in Fig. 5.43. A close look to the plot of the half normal probability illustrates that the depth is the only important factor affecting the magnitude of the maximum signal.

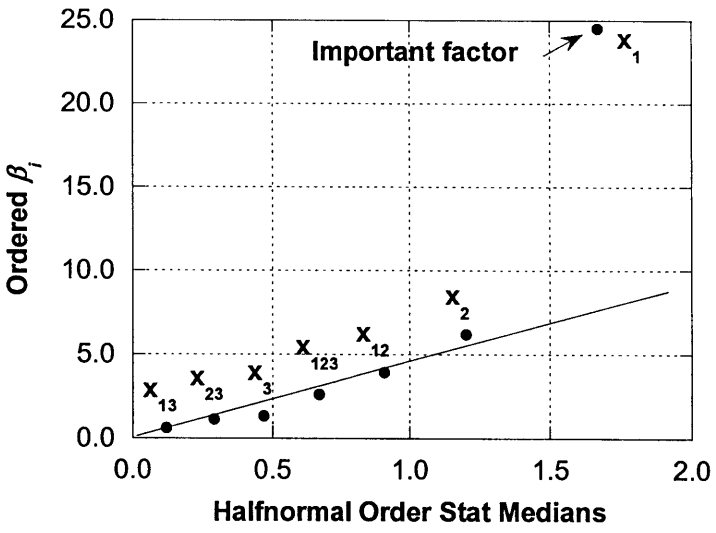

Fig. 5.43 Halfnormal probability plot for the time to maximum contrast

The results from the halfnormal probability plot established that the depth of the flaw is the only important factor affecting the time to maximum contrast. Thus, in order to solve the inverse problem, the time to maximum contrast could be used to estimate the depth of the flaw.

The time to maximum contrast as a function of the coded depth (-1, 0, +1) was plotted from the results of the full factorial experiment (including the center points) to develop an estimation procedure. Figure 5.44 displays the measured data at the coded depths, -1, 0, and +1.

The graph illustrates that the data for time to maximum contrast for flaws located near the surface spread less than the data for deeper flaws. The flaws at a coded depth –1, produced times to maximum signal between 10.6 s and 14.4 s. At the coded depth +1, the time to maximum contrast varied between 28.9 s and 42.7 s. This results show that the spread in the response data is larger for t_c than for t_s, thus making estimation of the depth more accurate using t_s than t_c.

Nevertheless, it could be possible to estimate the depth of the flaw based only on the time to maximum contrast. The estimation method is the same that the technique developed for the time to maximum signal. The approach also involves the development of an envelope function with an upper and a lower bound of the time to maximum contrast as a function of the actual depth of the subsurface flaw, as illustrated in Fig. 5.45. A function using the averages thermal response at each depth is also plotted in Fig. 5.45.

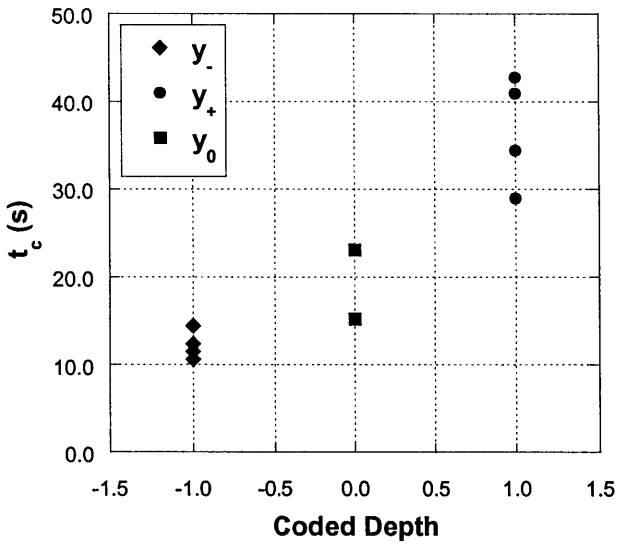

Fig. 5.44 Time to maximum contrast data as a function of the coded depth (-1,0,+1)

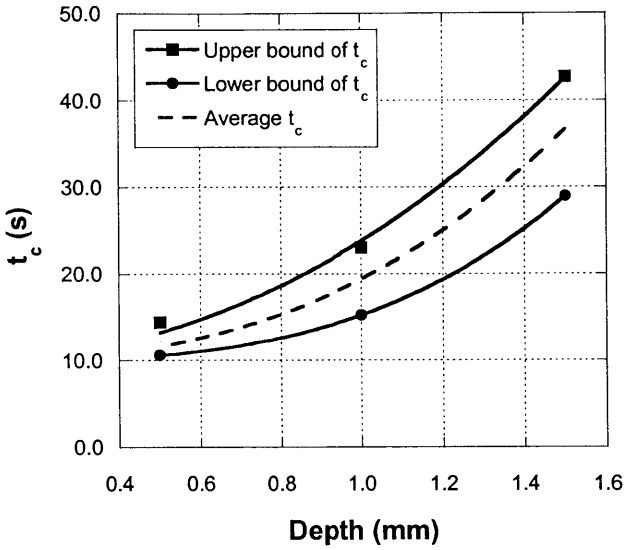

Fig. 5.45 Time to maximum contrast data as a function of the actual depth

Similarly to the case of the time to maximum signal, the time to maximum contrast is a power function of the depth of the flaw. The functions that define the upper and lower bound of the envelope are the following:

- for the upper bound,

$$t_c\big|_{upper} = 10 + 13.77 d_{flaw}^{2.11} \tag{5.8}$$

where $t_c\big|_{upper}$ is the time to maximum signal for the upper bound, and d_{flaw} is the depth of the flaw; and

- for the lower bound,

$$t_c\big|_{lower} = 10 + 5.21 d_{flaw}^{3.18} \tag{5.9}$$

where $t_c\big|_{lower}$ is the time to maximum signal for the upper bound, and d_{flaw} is the depth of the flaw.

The function defining the average time to maximum signal as a function of the depth is the following:

$$t_c\big|_{avg} = 10 + 9.38 d_{flaw}^{2.57} \tag{5.10}$$

where, $t_c\big|_{avg}$ is the average time to maximum signal and d_{flaw} is the depth of the flaw.

The estimation function using the measured time to maximum contrast results from inverting Eq. 5.10 as follows:

$$d_{estimate} = \left(\frac{t_c|_{measured} - 10}{9.38} \right)^{1/2.57} \tag{5.11}$$

where $d_{estimate}$ is the estimated depth of the flaw, and $t_c|_{measured}$ is the measured time to maximum signal. As illustrated in Fig. 5.46, if the time to maximum contrast is 20 s, the estimated depth of the flaw would be 1.0 mm. On the other hand, the estimated depth using the upper bound and lower bounds of the envelope is 0.85 mm and 1.23 mm, respectively.

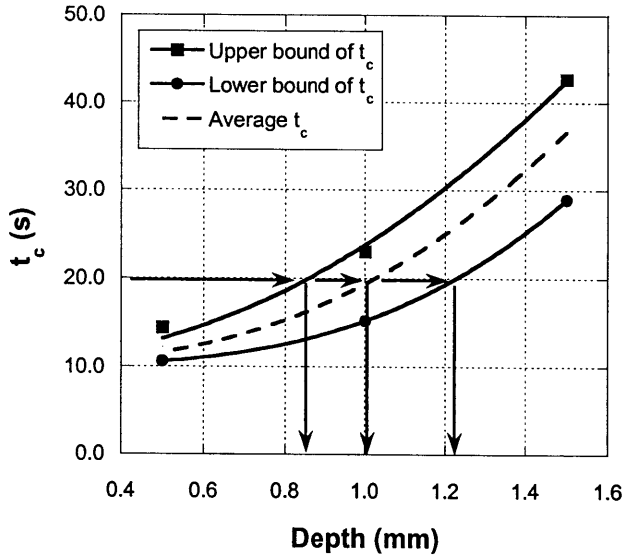

Fig. 5.46 Time to maximum contrast data as a function of the actual depth

Thus the estimation of the depth using $t_c|_{avg}$ differs by 0.15 mm and 0.23 mm from the values of the depth corresponding to the upper and lower bounds. This error in estimation is larger than the one observed in the estimation of flaw depth using the time to maximum signal t_s.

5.7.5 Conclusions for the Screening Experiment

The screening experiments provided several conclusions. The first phase of the experiment focused primarily on data gathering such as T_{max}, ΔT_{max}, t_s, Maximum Contrast and t_c. The analysis provided some insight to the procedures necessary to treat the data and interpret the results. The following are some of the conclusions from the data gathering:

- The thermal signal as a function of time may be smoothed using a moving average without compromising the results.

- The thermal contrast as a function of time may also be smoothed using a moving average. The contrast data, however, is very noisy. A large number of data points is required to smooth the contrast function to obtain the values of the maximum contrast and t_c .

The second component of the experiment was the analysis of the full factorial screening experiment. The evaluation of the result from the screening study highlighted the importance of the depth of the flaw as the principal factor affecting every thermal response. The evaluation of the results, however, indicated that the best thermal responses to estimate the depth of the flaw are the time to maximum signal t_s and the time to maximum contrast t_c. Thus, only the results of t_s and t_c were summarized in this section. The results showed that the depth of the flaw is the only factor that has a major effect on t_s and the data show a close-fitting behavior in spite of the thickness and the width of the flaw. That is, the width and the thickness of the flaw have little effect on the time to maximum signal and the time to maximum contrast.

The study of the results of the time to maximum signal and time to maximum contrast provides a method for estimating the depth of the flaw. Each estimation function is based on a power function fitted through the average $\hat{\beta}_i$ values as a function of flaw depth. The error in estimation is quite smaller when t_s is used rather than t_c. Thus evaluation of the results indicates the following:

- the depth of the flaw should be estimated using the time to maximum signal t_s;
- a power function fitted though the average t_s at each depth provides the tool to estimate the depth of the flaw; and,
- the full factorial experiment could be expanded to obtain a better model or function to estimate the depth of the flaw.

5.8 Experiment #5: Investigation of Test Repeatability and Effect of Sampling Rate

The final set of experiments involved the study of the repeatability of the infrared thermography measurements and the effect of sampling rate on the data analysis results. In order for any test method to have credibility it must be repeatable. That is, the results achieved on different sets of measurements under similar conditions should be the similar. For the investigation of the study of repeatability three sets of experiments were compared. The comparison was done for the following:

- Same test – different locations of spot meters for measuring T_{flaw} and $T_{background}$;
- Different tests – same location of spot meters for measuring T_{flaw} and $T_{background}$; and,
- Different tests – different location of spot meters for measuring T_{flaw} and $T_{background}$.

The second component of this experiment involved the study of the effect of the sampling rate on the test results. The purpose of this study was to evaluate what sampling rate was adequate for infrared thermography of FRP composites bonded to concrete using the test configuration investigated in this thesis.

The data acquisition system allows sampling rates either at the highest possible speed for the infrared camera or at hour-minute-second intervals (no fractions of seconds are allowed). For the uncooled infrared camera used in the experiments the highest possible sampling speed is 60 Hz. Thus, the fastest sampling rates allowed by the system is 60 Hz followed by 1 Hz. Sampling at a speed of 60 Hz permits the recording of the thermal response of the specimen at video speed, which a priori may seem desirable. It is, however, computationally intensive and it requires large data storage. Tests recorded at a speed of 60 Hz for a duration of 60 s require at least 500 Mbytes of data storage. On the other hand, tests recorded at a sampling speed of 1 Hz for a duration of 60 s require only 9 Mbytes for data storage.

This part of the investigation tried to answer if a 60 Hz sampling rate is necessary or if a 1 Hz sampling rate would be sufficient for the evaluation of FRP composites bonded to concrete. To answer this question, the results of eight tests performed using a 60 Hz sampling rate were compared to six tests performed using a 1 Hz sampling rate.

5.8.1 Determination of Heat Flux

First, the incident heat flux as a function of time was determined. The heating module was placed at 0.38 m from the surface of the specimen. The surface of the specimen being tested faced the heating module. The heating pulse was set to 10 s. This configuration was also used for the infrared thermography tests.

The incident heat flux was measured using an Episensor heat flux sensor. Three different sets of data were recorded. The measured data from the three tests and their average are presented in Table 5.13. The maximum average heat flux was 1730 W/m^2 with a standard deviation of 8 W/m^2.

Table 5.13 Measured incident heat flux for experiments involving the study of testing repeatability

	Heat Flux (W/m^2)				
Time (s)	**Test #1**	**Test #2**	**Test #3**	**Average**	**Standard Deviation**
0	0	0	0	0	0
1	680	1190	1350	1073	286
2	1480	1540	1570	1530	37
3	1570	1640	1610	1607	29
4	1660	1660	1670	1663	5
5	1690	1700	1690	1693	5
6	1710	1720	1700	1710	8
7	1720	1720	1710	1717	5
8	1730	1730	1720	1727	5
9	1730	1740	1700	1723	17
10	1730	1740	1720	1730	8
11	1040	320	230	530	362
12	290	210	160	220	53
14	105	75	59	81	19
20	28	22	0	17	12

The measured heat flux data is presented in Fig. 5.47.

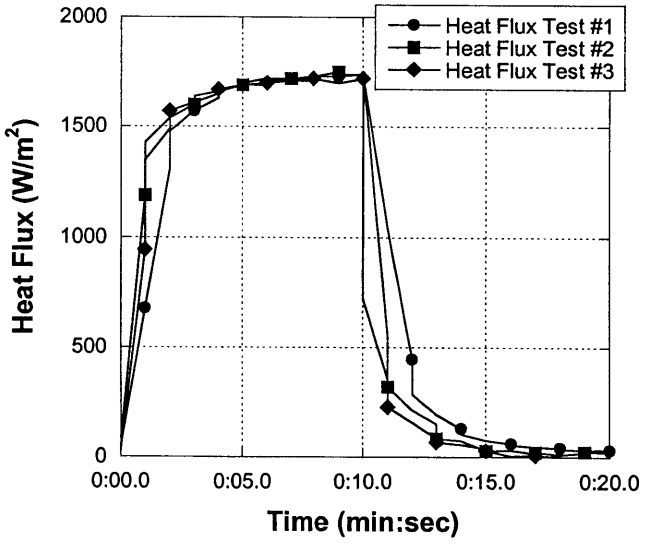

Fig. 5.47 Measured heat fluxes for experiments involving the study of test repeatability

5.8.2 Test Procedure

To investigate the repeatability of infrared thermography testing and effect of sampling rate, a series of measurements were performed on the same flaw. The tests were carried out on the specimen fabricated with wet lay-up CFRP and containing Nomex® flaws. The selected flaw for the study was flaw #3, which corresponded to the last run of the previous set of experiments (screening experiment). This flaw was chosen simply for convenience since the test configuration did not require any changes.

First, the ambient temperature was measured following the procedure described in Sec. 5.5.1. The measured ambient temperature was 24 °C.

Fifteen different infrared thermography tests were performed of the thermal response for flaw #3. The specimen was tested using the experimental configuration illustrated in Fig. 5.2. The specimen was placed at 0.37 m from the heating module and the IR camera. The test object was placed so that the subsurface flaw under study was positioned at the centerline between the two heating lamps. The duration of the thermal pulse was set to 10 s. Data was recorded for 60 s for each test. For nine of the measurement the sampling rate was 60 Hz. The remaining six tests were recorded at a sampling rate of 1 Hz.

The surface temperature above the flaw (T_{defect}) and above the bonded laminate near the flaw ($T_{background}$) were recorded as a function of time for each test.

5.8.3 Data Analysis

As mentioned in the previous section, fifteen infrared thermography measurements were performed. The set of tests were organized in three major categories as follows:

- Same test – different locations of analysis for T_{flaw} and $T_{background}$ (analysis set #1);
- Different tests – same location of analysis for T_{flaw} and $T_{background}$ (analysis set #2); and,
- Different tests – different location of analysis for T_{flaw} and $T_{background}$ (analysis set #3).

Two sets of analyses were performed for the case involving Set #1. For this case, the infrared thermography test was performed once. The temperature of the surface above the flaw T_{flaw} and the temperature in the background $T_{background}$ were measured three times using different spot meters at various locations. The locations, however, were positioned within the region above the flaw or background; that is the location of the spot meters was varied only by a couple of millimeters in different directions. Thus two sets of measurements were compared.

The second set of analyses (Set #2) involved five different infrared thermography tests. The locations of the spot meters to measure the surface temperature were fixed for the analysis of each test. Thus, the only variant in each analysis was the run of the actual infrared test, all the other factors such as test configuration, heat input, and location of analysis spot meters remained constant.

The third set of analyses (Set #3) involved three different infrared thermography test analyzed using different locations for T_{flaw} and $T_{background}$. For each analysis, the spot meters measuring T_{flaw} and $T_{background}$ were moved only by a couple of millimeters. An schematic of the design of this experiment is presented in Table 5.14.

Table 5.14 Summary of analysis configurations for the study of test repeatability (data recorded at 60 Hz)

		Tests or runs	
		Same	**Different**
Location of spot meters to measure T_{flaw} and $T_{background}$	**Same**	N/A	Set #2: 5 analyses
	Different	Set #1: 3 analyses	Set #3: 3 analyses

For each analysis, the magnitude of the maximum signal and the time to maximum signal were recorded for comparison.

The second component of the investigation focused on the comparison of the results for tests recorded at different sampling rates. For this comparison, six infrared thermography tests were performed at a sampling rate of 1 Hz. For Analysis Set #4, three infrared thermography measurements were done. The location of the spot meters was kept constant for the analysis of the three tests. The next set of analyses (Set #5) involved three new IR measurement. The analysis of set #5 required the use of different locations for the spot meters. For each analysis, the locations of the spot meter measuring T_{flaw} and $T_{background}$ were changed by 1 mm or 2 mm.

The recorded data was analyzed using different locations for the spot meter that measured T_{flaw} and $T_{background}$. These set of analyses are identified as Set # 4 throughout this section. To evaluate the effect of the sampling rate, Set #2 was compared with Set #4 and Set #3 was compared was compared with Set #5. A summary of the design of this component of the analysis is presented in Table 5.15.

Table 5.15 Summary of analysis configurations for the study of test repeatability (data recorded at 1 Hz)

		Tests or runs	
		Same	**Different**
Location of spot meters to measure T_{flaw} and $T_{background}$	**Same**		Set #4: 3 analyses
	Different		Set #5: 3 analyses

The thermal signal as a function of time was computed based on the recorded data for each test. Similarly to previous tests, the thermal signal as a function of time was smoothed to eliminate as much noise as possible. Smoothing of the data was required to be able to interpret the results and determine the maximum signal ΔT_{max} and the time to maximum signal t_s. Smoothing of the data was accomplished using a moving or running average algorithm. The thermal signal of the analyses from Set #1 was smoothed using 135 points. This high number of points was necessary since the data, recorded at 60 Hz, was very noisy. The resultant thermal signals for Analysis 1.1, 1.2 and 1.3, corresponding to Set #1 are presented in Fig. 5.48.

The measured signals for the set of analyses #2 were smoothed using 175 points for the moving average. The resulting smoothed signals are presented in Fig. 5.49.

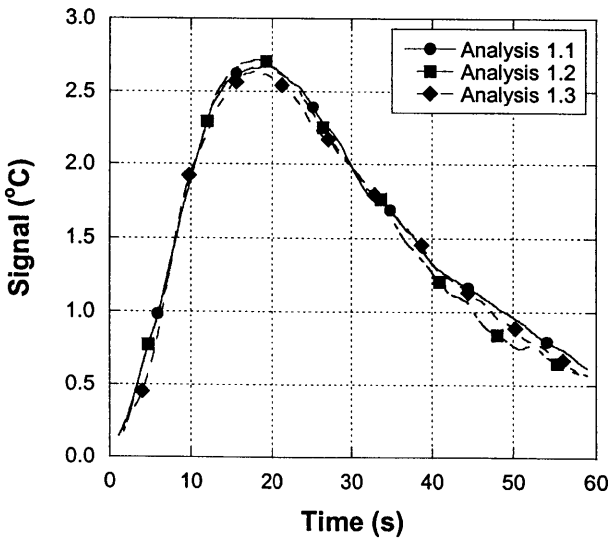

Fig. 5.48 Thermal signal as a function of time for analyses from Set #1

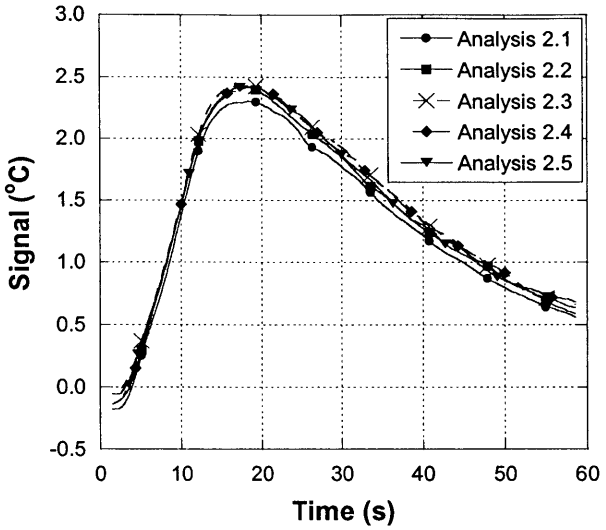

Fig. 5.49 Thermal signal as a function of time for analyses from Set #2

The measured signals for the set of analyses #3 were smoothed using 250 points for the running average. The resulting smoothed signals are presented in Fig. 5.50.

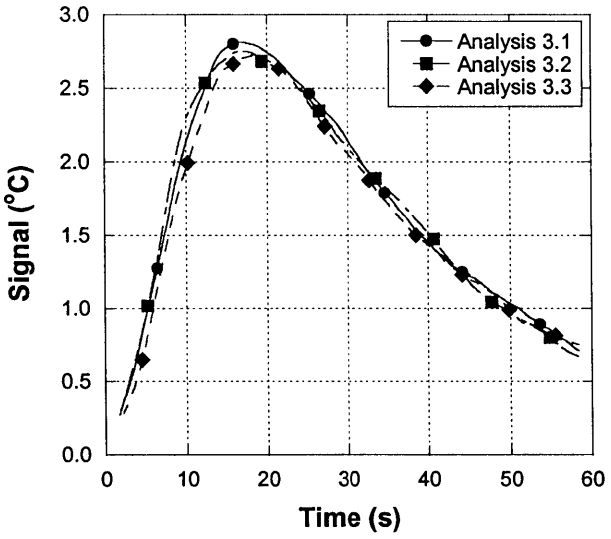

Fig. 5.50 Thermal signal as a function of time for analyses from Set #3

The data for Set #4 and Set #5 required fewer points for smoothing. For example, the data from Set #4 only required 5 points for adequate smoothing of the signal response. The thermal signal from Set #5 also required 5 points for smoothing. The results on the smoothed signals for Set #4 and Set #5 are presented in Fig. 5.51 and 5.2 respectively.

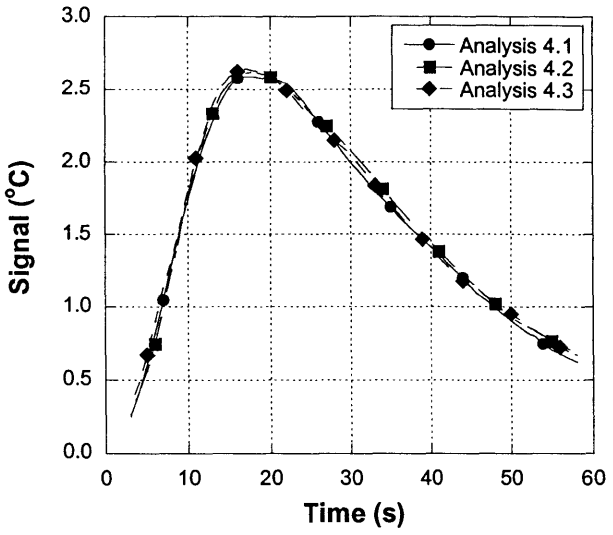

Fig. 5.51 Thermal signal as a function of time for analyses from Set #4

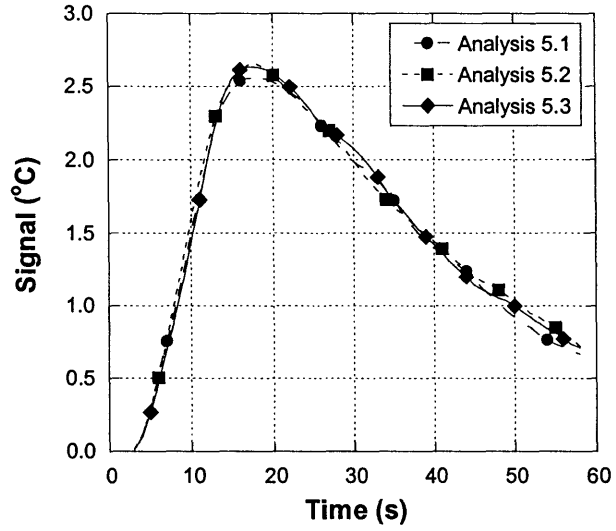

Fig. 5.52 Thermal signal as a function of time for analyses from Set #5

The results of ΔT_{max} and t_s for all the analyses involving sampling rates of 60 Hz are presented in Table 5.16. Similarly, the results of the analyses involving recording rates of 1 Hz are summarized in Table 5.17. Finally, Tables 5.18 and 5.19 summarize the averages and the

standard deviations of the thermal responses for the measurements involving sampling speeds of 60 Hz and 1 Hz, respectively.

Table 5.16 Results of individual analyses for the study of test repeatability (data recorded at 60 Hz)

		Tests or measurements	
		Same	**Different**
Location of spot meters to measure T_{flaw} and $T_{background}$	**Same**		Analysis 2.1: $\Delta T_{max} = 2.3$ °C, $t_s = 17.1$ s
			Analysis 2.2: $\Delta T_{max} = 2.4$ °C, $t_s = 18.1$ s
			Analysis 2.3: $\Delta T_{max} = 2.4$ °C, $t_s = 17.5$ s
			Analysis 2.4: $\Delta T_{max} = 2.4$ °C, $t_s = 18.6$ s
			Analysis 2.5: $\Delta T_{max} = 2.4$ °C, $t_s = 18.4$ s
	Different	Analysis 1.1: $\Delta T_{max} = 2.7$ °C, $t_s = 20.1$ s	Analysis 3.1: $\Delta T_{max} = 2.8$ °C, $t_s = 16.6$ s
		Analysis 1.2: $\Delta T_{max} = 2.7$ °C, $t_s = 19.2$ s	Analysis 3.2: $\Delta T_{max} = 2.7$ °C, $t_s = 17.4$ s
		Analysis 1.3: $\Delta T_{max} = 2.6$ °C, $t_s = 18.8$ s	Analysis 3.3: $\Delta T_{max} = 2.7$ °C, $t_s = 18.5$ s

Table 5.17 Summary of individual results of analyses for the study of test repeatability (data recorded at 1 Hz)

		Tests or measurements	
		Same	**Different**
Location of spot meters to measure T_{flaw} and $T_{background}$	**Same**		Analysis 4.1: $\Delta T_{max} = 2.6$ °C, $t_s = 18$ s
			Analysis 4.2: $\Delta T_{max} = 2.4$ °C, $t_s = 18$ s
			Analysis 4.3: $\Delta T_{max} = 2.7$ °C, $t_s = 18$ s
	Different		Analysis 5.1: $\Delta T_{max} = 2.6$ °C, $t_s = 17$ s & 18 s
			Analysis 5.2: $\Delta T_{max} = 2.6$ °C, $t_s = 18$ s
			Analysis 5.3: $\Delta T_{max} = 2.6$ °C, $t_s = 17$ s

Table 5.18 Summary of results of analyses for the study of test repeatability (data recorded at 60 Hz)

		Tests or measurements	
		Same	**Different**
Location of spot meters to measure T_{flaw} and $T_{background}$	**Same**		ΔT_{max} Average = 2.4 °C St.Dev = 0.05 °C t_s Average = 17.9 s St.Dev = 0.6 s
	Different	ΔT_{max} Average = 2.7 °C St.Dev = 0.06 °C t_s Average = 19.4 s St.Dev = 0.7 s	ΔT_{max} Average = 2.7 °C St.Dev = 0.06 °C t_s Average = 17.5 s St.Dev = 1.0 s

Table 5.19 Summary of results of analyses for the study of test repeatability (data recorded at 1 Hz)

		Tests or measurements	
		Same	**Different**
Location of spot meters to measure T_{flaw} and $T_{background}$	**Same**		ΔT_{max} Average = 2.6 °C St.Dev = 0.06 °C t_s Average = 18.0 s St.Dev = 0.0 s
	Different		ΔT_{max} Average = 2.6 °C St.Dev = 0.0 °C t_s Average = 17.5 s St.Dev = 0.5 s

First, the repeatability of infrared thermography testing was evaluated using the results from the analyses involving sampling rates of 60 Hz. The comparison of the results of the three different sets of analysis indicate that the magnitude of the thermal signal and the time to maximum signal vary depending on the measurement and the location of the measuring spot meters.

Data analysis of measurements taken at a sampling rate of 60 Hz is intensive and requires a large number of points to smooth the signal response as a function of time. Additionally, analysis of the data indicated that smoothing with a large number of points does not always guarantee that a single time to maximum signal would be found, thus requiring several iterations of smoothing until a single t_s is found. The time to maximum signal seemed to be very sensitive to the amount of smoothing of the signal as a function of time. An example of this behavior is illustrated in Fig. 5.54. Figure 5.54 shows a detail of the thermal signal at the location of ΔT_{max} for two different cases of smoothing.

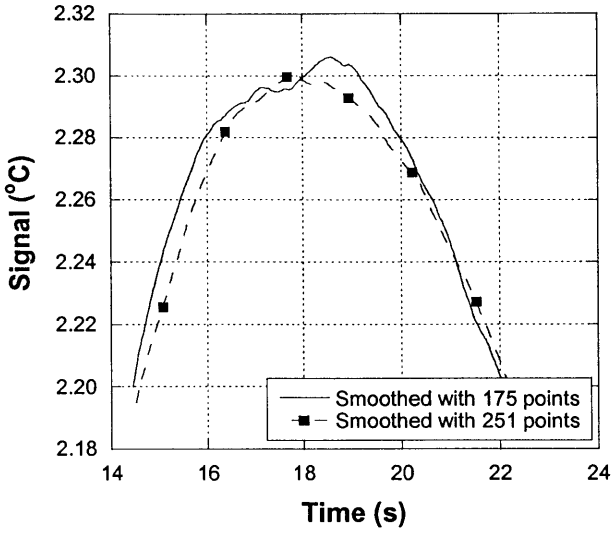

Fig. 5.54 Detail of thermal signal for two different cases of smoothing for Analysis 2.5

For sampling speeds of 60 Hz, the results of the experiment involving analyses of different runs or test using the same location for the spot meters (Analysis #2) yielded an average time to maximum signal of 17.9 s with a standard deviation of 0.5 s. The results of Analysis #3, involving different runs and locations of the spot meters, produced an average t_s equal 17.5 s and a standard deviation of 0.95 s.

The results of the tests recorded at sampling speeds of 1 Hz, the results yielded smaller standard deviations than those involving sampling rates of 60 Hz. For example, for the case of different tests analyzed using the same location for the spot meters, in Set #2 (sampling rate of 60 Hz) the average time to maximum signal was 17.9 s and the standard deviation was 0.5 s and in Set #4 (sampling rate of 1 Hz) the average time to maximum signal was 18.0 s with a standard deviation was 0.0 s. Next, Set #3 and Set #5 were compared. For Set #3, the average t_s was 17.5 s and the standard deviation was 1.0 s. Set #5 yielded an average value t_s equal to 17.7 s and a standard deviation equal to 0.6 s.

The comparison of these results suggest that recording speeds of 1 Hz could be adequate for quantitative infrared thermography testing of FRP composites bonded to concrete using the configuration presented in this project. Sampling speeds of 1 Hz provide results with smaller standard deviations. Additionally, tests data recorded at 1 Hz require less amount of computer storage and data processing than test data recorded at 60 Hz.

Similar to any other experimental technique, it is recommended to perform a series of measurements and compute the mean and standard deviation of the specific thermal response. For example, if the time to maximum signal is required to estimate the depth of the flaw, several infrared thermography measurements (at least 3) should be performed to obtain the mean and standard deviation of the time to maximum signal.

5.8.4 Conclusions of the Investigation of Test Repeatability and Effect of Sampling Rate

The closing set of experiments included the study of the repeatability of the infrared thermography measurements and the effect of sampling rate on the data analysis results. Five sets of analyses were performed for the investigation.

All the measurements were performed on flaw #3, which corresponded to the last run of the previous set of experiments (screening experiment). The results of the investigation indicated that tests recorded at a sampling rate of 60 Hz required large data storage space and computation. The resulting thermal signal as a function of time is quite noisy thus requiring several iterations of smoothing until the values for ΔT_{max} and t_s are revealed. Even after several iterations of smoothing, detection of ΔT_{max} and t_s may require comparison of signal data to 0.001 °C (this temperature is below the thermal resolution of the IR camera).

The results of the analyses involving sampling rates of 1 Hz indicated that tests recorded at this speed provide similar average values of the thermal responses than those recorded at 60 Hz. The standard deviations of the results were smaller than for the case of sampling rates of 60 Hz. Additionally, analysis of test recorded at 1 Hz required less computation and data storage than data recorded at 60 Hz.

Therefore, the comparison of these results suggest that recording speeds of 1 Hz could be adequate for quantitative infrared thermography testing of FRP composites bonded to concrete using the configuration presented in this project.

As in any other experimental measurement, a series of measurements should be taken to obtain the mean and standard deviation of the specific thermal response

5.9 Conclusions of Laboratory Studies

The experimental program was divided into 5 different studies. Following are the descriptions of the studies:

- The first part of the experimental study was qualitative in nature. The focus of the qualitative experiment was to evaluate the potential detection of simulated flaws embedded in the test object. A specimen having two bonded pultruded CFRP laminates and containing eight fabricated debonds was used for this experiment.

- The second experiment was quantitative and focused on the comparison of infrared thermography results and the output from FEM simulations. An air void contained in the specimen fabricated with pultruded CFRP bonded to concrete slab was evaluated.

- The third experiment involved the potential estimation of the width or area of the subsurface flaw.

- The forth experiment involved a screening parametric investigation. Three flaw parameters were investigated: flaw depth, flaw thickness, and flaw width. To investigate these three parameters, a full factorial design with 2 "center" points was planned. The purpose of the screening experiment was to determine the important parameters and interactions affecting thermal response, the ranking of the affecting parameters, and to develop a good model for the estimation of flaw depth.

- The final experiment focused on the investigation of infrared thermography testing repeatability and the effect of the sampling rate on the test results.

The series of laboratory studies provided some interesting conclusions regarding infrared thermography testing. The following is a summary of the conclusions:

- The qualitative test proved that detection of subsurface flaws might be achieved by sweeping an infrared heat lamp along the length of the FRP at a distance of 50 mm from the surface and at a speed of approximately 0.15 m/s. This quick technique could be used to easily detect and locate subsurface flaws.

- Characterization of the flaw requires precise measurement of thermal signals as a function of time.

- Knowledge of the surface emissivity is not required for flaw characterization using infrared thermography. Knowledge of the emissivity is required only for the estimation of absolute surface temperatures, for example for the determination of T_{max}. Measurement of the thermal signal, however, is independent of the value of the surface emissivity because ΔT is a differential between two temperatures measured using the same emissivity ($\Delta T = T_{defect} - T_{background}$). Thus, if the test object has uniform surface emissivity, the results for the maximum thermal signal and the time to maximum signal are the same regardless of the value of emissivity used to compute the surface temperatures.

  In this investigation knowledge of the emissivity was needed for comparison of experimental data with FEM simulations and for the estimation of maximum surface temperatures T_{max}. The emissivity of two varieties of FRP (pultruded laminates and wet lay-up sheets) was determined using the procedures stated in the ASTM E 1933.

  Using the contact method, the average measured emissivity of the FRP laminate was 0.80, with a standard deviation of 0.016. Thus the expanded uncertainty interval is 0.80 ± 0.03, for a coverage factor $k = 2$. Using the noncontact method, the average emissivity of the pultruded laminate was 0.80 with a standard deviation of 0.01.

  The emissivity of the wet lay-up FRP composite was also measured using both techniques described in the ASTM E 1933.

  Measurements using the contact method (involving thermocouples) proved unreliable. Emissivity values greater than 1.0, which is beyond the theoretical maximum value for emissivity, were monitored using this technique. This fact indicated the possibility of the limitation of the contact method procedure for materials with high emissivity. This issue will have to be investigated further in the future. The noncontact method, however, provided

more consistent results for the emissivity. Using the noncontact method the average surface emissivity of the wet lay-up composite was 0.98, with a standard deviation of 0.01. Thus the expanded uncertainty interval is 0.98 ± 0.02, for a coverage factor of $k = 2$.

- The heating module configuration designed for the experiments produced a relatively uniform heat flux at the surface of the test object and square pulses similar to those used in the FEM simulations.

- Agreement between the experimental data and the FEM simulations provided reassurance that the analytical model is valid.

- The width of the flaw may be estimated by determining the location of the roots of the second derivative of the surface temperature profile at the time of maximum signal.

- A smoothing procedure using a moving average algorithm proved to be an effective means for dealing with noisy signals, contrasts, and second derivatives.

- Thermal contrast is noisier and requires more smoothing than the thermal signal.

- The depth of the flaw is the only important factor affecting the time to maximum signal. Thus, the time to maximum signal is the ideal thermal response parameter to estimate the depth of the flaw. These results are in agreement with the screening parametric study described in Chapter 4, which involved FEM simulations. A procedure for estimating the depth of the flaw from the time to maximum signal was presented in this chapter. Expansion of the full factorial experiment should allow the definition of a better model in the future.

- The investigation indicated that test repeatability could be an issue depending on the location of the measuring spot meters and the run. A series of various measurements is recommended in order to attain the average thermal responses and their standard deviations.

- The study also indicated that sampling rates of 1 Hz are sufficient for quantitative testing of FRP bonded to concrete. For example, the thermal responses gathered at sampling rates of 1 Hz had similar average values and smaller standard deviations than those gathered at sampling rates of 60 Hz. Additionally, higher sampling rates (i.e. 60 Hz) are noisier, computationally intense and require large amounts of data storage.

Chapter 6

Discussion

6.1 Summary

6.1.1 Introduction

Fiber reinforced polymer (FRP) composites, in the form of pultruded laminates or wet lay-up woven fabrics, are being used to rehabilitate existing concrete and masonry structures. The success of these materials in performing their intended functions depends, to a large extent, on how well they are bonded to themselves and to the substrate. Thus, there is a need for an efficient and reliable method to detect and characterize defects at the substrate interface and within multi-ply systems.

Quality control of the final product is a requirement for the reliable performance of any new material in structural engineering systems. Presently, there are no standard quality control procedures to assess the integrity of bonded FRP composite systems used in civil engineering applications. The best NDE technique needed to detect and characterize subsurface defects in any material depends on the critical size of the defect, the size of the structure being tested, and the environment in which the inspection is carried out. Moreover, the ideal NDE method in civil engineering applications should be accurate, reproducible, reliable, robust, and economical; able to inspect large areas as well as localized areas; able to detect critical defect sizes; and non-obtrusive to the surrounding environment, and convenient to the users and evaluator of the structure.

Nondestructive testing of thin FRP laminates bonded to concrete or masonry presents a variety of difficulties in the use of the traditional methods developed for inspection of metals due to the anisotropy, variable and non-homogenous composition, non-magnetic properties, and high ultrasonic attenuation of FRP materials. Among the various available techniques, however, infrared thermography offers the greatest potential as a global NDE method.

Current inspection techniques using infrared thermography provide only qualitative assessments of the state of the structure, but give no quantitative information on existing defects. That is, they establish whether a subsurface flaw exists within the FRP-substrate system, but not the depth of the defect or its approximate volume. This qualitative nature of the results derives from the

complex relationships among the variables affecting the thermal response of the bonded laminates.

6.1.2 Research Objective

In order to allow widespread use of infrared thermography for quantitative assessment of FRP applied to concrete, a standard test method is needed. To develop such a standard, it is necessary to develop a greater understanding of the factors affecting the thermal response of FRP composites bonded to composites.

The purpose of this thesis was to develop the technical bases for quantitative infrared thermography testing of FRP bonded to concrete. Specifically, the dissertation focused on a preliminary assessment of testing and analytical procedures that will aid the development of a standard method for NDE of FRP bonded to concrete using infrared thermography.

6.1.3 Approach

The objective of the thesis was achieved by a series of numerical and laboratory studies that investigated the effect of testing parameters and different types of defects.

The dissertation was divided into three components: dimensional analysis, parametric studies, and laboratory studies

First, a dimensional analysis of a simplified one-dimensional heat transfer model was performed to determine the parameters that needed to be investigated in the parametric studies.

The second component involved parametric studies performed using finite element analysis. The parametric studies were subdivided into investigations involving single factors and investigations involving multiple factors. Two-dimensional planar models were used to simulate infrared thermography testing of a semi-infinite concrete slab strengthened with FRP laminates.

The single-factor parametric study aimed to determine the effect of the following individual factors on the thermal response:

- Thermal input;
- Material thermal properties;
- Flaw depth;
- Flaw thickness; and,
- Flaw width.

The second set of parametric studies involved a screening numerical experiment focused on the determination of the important factors and interactions affecting the response. The purpose of the screening experiment was to determine which factors have the most significant effect on the thermal responses, thus enabling the solution of the inverse problem.

The final phase focused on a series of laboratory studies aimed to confirm the potential of using infrared thermography for quantitative testing and to verify the results achieved in the numerical parametric studies. The experiments were conducted on controlled-flaw specimens fabricated

with pultruded FRP laminates and wet lay-up fabric. An infrared thermography test configuration was designed and constructed to perform quantitative measurements of the time dependent thermal behavior. The laboratory studies involved five experiments:

- Qualitative testing;
- Comparison of infrared thermography and finite-element simulations;
- Estimation of flaw width;
- Screening experiment; and,
- Investigation of test repeatability and effect of sampling rate.

The laboratory studies also involved measurements of the input heat flux and emissivitiy of both kinds of FRP composites used in the research.

6.2 Conclusions

6.2.1 Dimensional Analysis

A dimensional analysis of a semi-infinite half space solid was performed and is described in Chapter 3. The analysis demonstrated that for the case of a semi-infinite half space subjected to a heat flux, the physical quantities that influence the thermal evolution (the spatial and temporal variations of temperature) are the depth z, time t, thermal conductivity of the material k, thermal diffusivity of the material α, and the input heat flux q. In the case of a solid containing a subsurface flaw, additional physical quantities such as the thermal resistance of the flaw should be taken into consideration. The results from the dimensional analysis identified the parameters that had to be investigated in the numerical parametric study.

6.2.2 Parametric Studies

The investigation described in Chapter 4 focused on the effect that various parameters have on the thermal response. The key thermal response parameters are the maximum surface temperature, the maximum signal (surface temperature difference) and the time to maximum signal. The investigation was subdivided into a single-factor parametric study and a multi-factor parametric study.

The first single-factor study involved the effect of the thermal input. The magnitude and duration of the input heat flux were varied to evaluate the variation in the thermal response parameters. The results showed that selection of the thermal pulse is governed by the desired maximum signal and by the maximum surface temperature that can be tolerated by the material. The findings indicated that for a given flaw geometry, the maximum signal is a linear function of the input energy (product of pulse amplitude and pulse duration). Therefore, a maximum value of input energy can be selected for a desired minimum signal. The maximum surface temperature is also a linear function of the input energy, but it depends also on the pulse duration. The selection of the pulse duration to produce the minimum input energy is governed by the maximum surface temperature that the FRP composite can tolerate. These results led to a simple approach for selecting the thermal input for a specific test object so as to obtain a desired thermal signal while limiting the surface temperature. An additional important conclusion from

the study was that only the duration of the heat pulse affects the time to maximum signal; the magnitude of the input heat flux does not affect this thermal response parameter.

The second study involved the effect of thermal material properties on the thermal response of the test object. The thermal conductivity and specific heat of the FRP composite and the concrete substrate were varied. The investigation concluded that, while variations in the thermal properties of the FRP and concrete resulted in systematic variations in thermal response, none of the thermal response parameters were very sensitive to these variations. Thus it is concluded that the success of infrared thermography testing will not depend strongly on the specific values of the thermal properties of the FRP or concrete substrate.

The third parametric study involved the effect of the depth of the flaw on the thermal response. For this purpose, delaminations, debonds, and concrete spalls at various depths were modeled. Additionally, the number of laminates bonded to the concrete substrate was varied. The results indicated that the thermal responses are a function of both the depth of the flaw and the number of FRP. The time to maximum signal was, however, affected little by the number of FRP layers. A possible procedure for estimation of flaw depth was demonstrated using the time to maximum signal.

The fourth parametric study focused on the effect of the thickness of the subsurface flaw. Again, delaminations, debonds and concrete spalls were studied. This parametric study showed that the flaw thickness has a significant effect on the thermal responses in the case of delaminations near the surface, but the effect is minor for debonds and concrete spalls. Very thin delaminations are difficult to detect because their thermal resistance is negligible.

The last single-factor investigation involved the effect of the width of the flaw and it aimed to determine whether a suitable procedure could be developed to estimate the flaw width. The results indicated that the width of the flaw could be estimated from the second derivative of the surface temperature profile at the time of maximum signal. Additionally, the investigation demonstrated that the smallest detectable flaw is a function of the depth of the flaw and the maximum signal required to overcome noise in the measuring process. The width of the smallest detectable flaw varied as a power function of the depth of the flaw. Thus as flaw depth increases, the minimum flaw width that can be detected also increases.

Finally, a multi-factor parametric study was performed to determine which factors and interactions have statistically significant effects on the response parameters. Three parameters were investigated simultaneously: depth, thickness, and width of the flaw. A full-factorial experiment design was simulated using the three factors, each containing two levels. The screening study proved that flaw depth is the only factor that has a statistically significant effect on the time to maximum signal. Thus it should be possible to estimate using the time for maximum signal alone. On the other hand, the large scatter of the thermal responses T_{max}, ΔT_{max}, and t_s as a function of the thickness indicated that the thickness of the flaw would be difficult to characterize accurately.

6.2.3 Laboratory Studies

The laboratory studies demonstrated that quantitative testing of FRP bonded to concrete is possible.

The qualitative infrared thermography experiment confirmed that detection of subsurface flaws is achieved easily by sweeping an infrared heat lamp over the surface of the FRP at a distance of 50 mm and at a speed of approximately 0.15 m/s. This quick technique could be used to easily detect subsurface flaws. Characterization of the flaw requires, however, accurate measurement of surface temperatures as a function of time.

In the case of the simulations reported in Chapter 4, the calculated time dependent temperature data allow easy determination of the response parameters. In the case of experimental data, however, a smoothing procedure is required in order to determine the basic response parameters T_{max}, ΔT_{max} and, most importantly, t_s. Using a moving average filter proved to be an effective means for dealing with noisy data.

As part of the laboratory studies, the results of FEM simulations were compared to experimental data. Agreement between the experimental data and the FEM simulations provided assurance that the analytical model and thus the results from Chapter 4 are valid.

The experimental investigation confirmed that the width of the flaw may be estimated by determining the location of the roots of the second derivative of the surface temperature profile at the time of maximum signal. As was the case for the temperature profile, the second derivatives of the profile must be smoothed in order to determine where the second derivative equals zero. A moving average filter proved effective for this purpose.

Similar to the screening simulation study described in Chapter 4, the screening laboratory experiment involving the depth, thickness, and width of the flaw established that flaw depth is the most significant factor affecting the time to maximum signal. This conclusion confirmed that the time to maximum signal is the most appropriate thermal response parameter to estimate the depth of the flaw. It was shown that flaw depth can be estimated by using a pre-established relationship between the average time to maximum signal and the flaw depth The details of how this relationship should be established requires further research.

The investigation indicated that test repeatability could be an issue depending on the location of the measuring spot meters and the run. Replicate tests revealed that the response parameters are highly repeatable (low standard deviation) under laboratory conditions.

The study also indicated that sampling rates of 1 Hz are sufficient for quantitative testing of FRP bonded to concrete. Higher sampling rates (i.e., 60 Hz) are noisier, computationally intensive, and require large amounts of data storage.

The investigation also concluded that the use of thermal signal is a more reliable response parameter than the use of thermal contrast. In principle, contrast has the advantage of not requiring knowledge of the input heat flux. Thus, a priori, it may seem preferable to use the thermal contrast data instead of the thermal signal. The laboratory studies, however, indicated

that the thermal contrast is much noisier that the thermal signal making it difficult to determine the time to maximum contrast.

6.2.4 Summary

In summary, the objectives of the project were achieved through numerical and experimental studies. The investigation confirmed that qualitative testing, as already performed by some inspectors, is an efficient and simple way to detect the presence of subsurface air voids embedded in either FRP composites or in the concrete substrate. Characterization of the flaws, however, requires quantitative testing procedures.

The study concluded that both flaw depth and flaw width (or area) may be estimated easily. The flaw depth could be estimated by measuring the time to maximum signal. The flaw width could be estimated by locating the roots of the second derivative of the surface temperature profile at the time of maximum signal. Thus, for quantitative assessment of the depth and the width of the flaw only the thermal signal history of the test object is needed.

The magnitude of heat flux applied to the surface does not need to be measured. The first parametric study indicated that the time to maximum signal does not vary with the magnitude of the applied heat pulse, only with its duration. Additionally, knowledge of the surface emissivity of the test object is not required to determine the time to maximum signal and the roots of the second derivative of the surface temperature profile. These two findings will simplify the development of a standard test procedure.

It was also concluded that determination of the thickness of the flaw is not possible using the thermal response parameters considered in this study.

6.2.5 Research Limitations

The research conducted proved that quantitative nondestructive evaluation of FRP composites bonded to concrete is possible.

Some limitations, however, were identified in this research. For example, emissivity measurements using the contact method (involving thermocouples) proved unreliable. Emissivity values greater than 1.0, which are not possible, were measured using this technique. This fact indicated a possible limitation of the contact method procedure for materials with high emissivity. This issue will have to be investigated further.

A procedure for estimating the depth of the flaw from the time to maximum signal was demonstrated. The predictive model, however, was simple since it was developed using only a few flaw depths. Regression experiments with additional flaw depths and other relevant factors should allow the definition of a better model in the future. Development of graphs (or models) such as those illustrated in Fig. 5.46 and 5.47 is needed for typical air voids encountered in FRP composites bonded to concrete.

An additional limitation of this research is that testing was conducted under laboratory conditions. *In situ* testing would have been more realistic of actual testing for civil engineering

applications. Forced convection due to high wind speed and atmospheric attenuation may have an important effect on the thermal response of the test object and on the temperature measurement recorded by the infrared detector. Future research should focus on the implementation of the testing procedures for *in situ* evaluation. Experimental testing and numerical simulations similar to those carried out in this investigation should overcome this limitation.

6.3 Future Implications

The photonics industry is quickly developing more accurate and reliable infrared detectors at a lower price, and the use of infrared thermography for routine evaluation of civil engineering structures is growing. Additionally, widespread use of FRP composites in civil engineering infrastructure will depend on the development of a standard methodology to test the quality of the bond between the fiber composites and the substrate. There is a danger, however, of generalized used of infrared thermography testing without full understanding of the thermal response of these materials and components

The conclusions from this dissertation demonstrate that quantitative infrared thermography testing of FRP composites bonded to concrete has the potential to estimate the depth and width of subsurface voids. Further research, however, is needed to develop a standard test for quantitative infrared thermography testing. The research should focus on optimization of the testing configuration and on dealing with uncontrolled atmospheric variables (wind speed, air temperature, and solar radiation).. The ultimate goal is to use infrared thermography to test structures in the field. Thus a field demonstration project should be carried out to verify that test method can accurately evaluate the state of the FRP composite, the concrete substrate, and their bond.

A second field of study needed for the success of infrared thermography is the development of specialized software to allow automation of the data analysis process. Current data analysis software for infrared thermography testing provides only some of the tools needed for quantitative assessment. From the quantitative testing perspective, it would be beneficial to have data analysis software able to filter the raw data and compute and record thermal signals in real time. Then, based on the measured time to maximum signal, the flaw depth could be estimated. Algorithms using neural networks, for example, have the potential to answer this need. By automating the calculation of the second derivatives of surface temperature profiles, the size (area) of the subsurface flaw could be estimated quickly.

More research is needed on thermography of testing curved surfaces. Many civil structures retrofitted with FRP composites, such as columns, have curved surfaces. It is expected that the curved surface would produced a visually distorted image of the surface temperatures of the test object. Thus, quantitative infrared thermograph testing of these structural components would require different considerations because of their particular shape.

Bibliography

Allport, J.; McHugh, J. (1988) "Quantitative Evaluation of Transient Video Thermography." Review of Progress in Quantitative non Destructive Evaluation, Vol.7a, pp.253-262.

Almond, D.P.; Lau, S.K. (1994) "Defect Sizing by Transient Thermography I: An Analytical Treatment." Journal of Physics D: Applied Physics, Vol.27, pp.1063-1069.

ANSYS. (2000) ANSYS Heat Transfer Training Manual for Release 5.6.

Balageas, D.L.; Krapez, J.C.; Cielo, P. (1986) "Pulsed Photothermal Modeling of Layered Materials." Journal of Applied Physics, Vol.59, No.2, pp.348-357.

Ball, R.J.; Almond, D.P. (1998) "The Detection and Measurement of Impact Damage in Thick Carbon Fibre Reinforced Laminates by Transient Thermography." NDT & E International, Vol. 31, No. 3, p 165-173.

Bar-Cohen, Y. (1986) "NDE of Fiber-Reinforced Composite Materials-A Review." Materials Evaluation, pp. 446-453.

Bendada, A.; Maillet, D.; Degiovanni, A. (1992) "Nondestructive Transient Thermal Evaluation of Laminated Composites: Discrimination Between Delaminations, Thickness Variations, and Multidelaminations." Eurotherm Seminar 27, Quantitative Infrared Thermography QIRT'92, pp.218-223.

Bonacci, J.F.; Maalej, M. (2000) "Externally Bonded FRP for Service-Life Extension of RC Infrastructure." Journal of Infrastructure Systems, Vol.6, No.1, pp.41-51.

Büyüköztürk, Oral. (1998) "Imaging of Concrete Structures." NDT & E International, Vol. 31, No. 4, pp. 233-243.

Cielo, P.; Maldague, X.; Déom, A.A.; Lewak, R. (1987) "Thermographic Nondestructive Evaluation of Industrial Materials and Structures." Materials Evaluation, Vol.45, No.6, pp.452-460.

Connolly, M.P. (1992) "The Measurement of Porosity in Composite Materials Using Infrared Thermography." Journal of Reinforced Plastics and Composites, Vol.11, No.2, pp.1367-1375.

Connolly, M.P. (1991) "A Review of Factors Influencing Defect Detection in Infrared Thermography: Applications to Coated Materials." Journal of Nondestructive Evaluation, Vol. 10, No. 3, pp.89-96.

Connolly, M and Copley, D. (1990) " Thermographic Inspection of Composite Materials." Materials Evaluation, December, pp.1461-1463.

Cowell, S.D.; Burleigh, D.D. (1991) "Numerical Modeling of Thermographic Nondestructive Testing for Epoxy Laminates." Thermosense XII. Proceedings of SPIE, Vol.1313, pp.143-150.

Cramer, K.E.; Winfree, W.P. (1992) "Thermographic Imaging of Cracks in Thin Metal Sheets." Thermosense XIV. Proceedings of SPIE, Vol.1682, pp.162-170.

Dattoma, V.; Marcuccio, R.; Pappalettere, C.; and Smith, G.M. (2001) "Thermographic Investigation of Sandwich Structure Made of Composite Material." NDT &E International. Vol. 34, pp. 515-520

Delpech, Ph.M.; Boscher, D.M.; Lepoutre, F.; Déom, A.A.; Balagueas, D.L. (1993) "Quantitative Nondestructive Evaluation of Carbon-Carbon Composites by Pulsed Infrared Thermography." Review of Progress in Quantitative Nondestructive Evaluation, Vol.12, pp.1297-1304.

Ford, P. and Lovejoy, D. (2001) "Meeting the Challenge of Training for NDT of Advanced Composite Materials and Structures." Insight: Non-Destructive Testing and Condition, Vol. 43, No. 12, pp. 794-796.

Galmiche, F.; Maldague, X.P. (1999) " Active Infrared Thermography for Land Mine Detection." Proceedings of SPIE: Conference on Diagnostic Imaging Technologies and Industrial Applications, Vol. 3827, pp.146-154.

Ghiringhelli, G.L. (1997) "On the Thermal Problem for Composite Beams Using a Finite Element Semi-Discretisation." Composites, Part B: Engineering, Vol.28, No.5/6, pp.483-495.

Giorleo, G.; Meola, C. (1998) "Location and Geometry of Defects in Composite Laminates from Infrared Images." Journal of Materials Engineering and Performance, Vol. 7, No. 3, pp. 367-374.

Grinzato, E.; Bison, P.; Marinetti, S.; Vavilov, V. (1994) "Nondestructive Evaluation of Delaminations in Fresco Plaster Using Transient Infrared Thermography." Research in Nondestructive Evaluation, Vol.5, pp.257-274.

Grinzato, E.; Vavilov, V.; Kuppinen, T. (1998) " Quantitative Infrared Thermography in Buildings." Energy and Buildings, Vol.29, pp.1-9.

Hartikainen, J.; Jaarinen, J.; Luukkala, M. (1989) "Delamination and Crack Detection by the Synchronous Heating Method: Theoretical Aspects." Review of Progress in Quantitative Nondestructive Evaluation, Vol.8B, 1989, pp.1321-1328.

Hawkins, G.F.; Johnson, E; Nokes, J. (1999) "Typical Manufacturing Flaws in FRP Retrofit Applications." NISTIR 6288. Proceedings from NIST Workshop on Standards Development for the Use of Fiber Reinforced Polymers for the Rehabilitation of Concrete and Masonry Structures. January 7-8. Tucson, Arizona.

Hawkins, G.F.; Johnson, E.C.; Nokes, J.P. (1999) "Detecting Manufacturing Flaws in Composite Retrofits." SPIE, vol. 3587, pp.97-104.

der Hovanesian, J., Hung, Y.Y. (1995) "Shearography for Discontinuity Detection." Materials Evaluation, Vol.53, No.6, pp.725-729.

Hamzah, A.R.; Delpech, P.; Saintey, M.B.; Almond, D.P. (1996) "An Experimental Investigation of Defect by Transient Thermography." Insight, Vol.38, No.3, pp.167-173.

Howell, P.A.; Winfree, W.P.; Crews, B.S. (1991) "Numerical Simulations of Thermal Detection of Disbonds in Lap Joints." Review of Progress in Quantitative Nondestructive Evaluation, Vol.10B, pp.1367-1374.

Hung, Y.Y.; Luo, W.D.; Lin, L.; and Shang, H.M. (2000) "Evaluating the Soundness of Bonding Using Shearography." Composite Structures, Vol.50, No. 4, pp.353-362.

Kaminski, M.; Hien, T.D. (1999) "Stochastic Finite Element Analysis of Transient Heat Transfer in Composite Materials with Interface Defects." Archives of Mechanics, Vol.51, No.3/4, pp.399-418.

Jahnke, D.A.; Sandor, B.I. (1997) "Forced Diffusion Thermography for Nondestructive Evaluation of Microstructures." TMS Annual Meeting: Design Reliability of Solders and Solder Interconnections, 1997, pp.43-47.

Karbhari,V.M.; Seible, F. (1998) "Design Considerations for the Use of Fiber Reinforced Polymeric Composites in the Rehabilitation of Concrete Structures." NISTIR 6288. Proceedings from NIST Workshop on Standards Development for the Use of Fiber Reinforced Polymers for the Rehabilitation of Concrete and Masonry Structures. January 7-8, 1998. Tucson, Arizona.

Kleinfeld, Jack M. (1999) "Finite Element Analysis as a Tool for Thermography." Thermosense XXI. Proceeding of SPIE, Vol.3700, April 1999, pp.6 –13.

Lankford, Bill. (2000) "Infrared Imaging." Photonics Spectra. p. 115.

Lehtiniemi, R.; Rantala, J.; Hartikainen, J. (1995) "A Photothermal Line-Scanning System for NDT of Plasma-Sprayed Coatings of Nuclear Power Plant Component." Research in Nondestructive Evaluation, Vol.6, No.2, 1995, pp.99-123.

Lulay, K.E.; Safai, M. (1994) "Optimization of Thermographic NDT Using Finite Element Analysis." Thermosense XVI. Proceedings of SPIE, Vol.2245, 1994, pp.106-110.

Lüthi T.; Meier H.; Primas R.; Zogmal O. (1995) "Infrared Inspection of External Bonded CFRP-Sheets." International Symposium Non-Destructive Testing in Civil Engineering, Berlin, Germany. Lectures Volume 1, pp. 689-696.

Maji, A.K. and Satpathi, D. (1997) "Electronic Shearography for Detecting Disbonds in Lattice/Skin Structures." Research in Nondestructive Evaluation, Vol.9, No.1, pp. 1-11.

Maldague, Xavier. (1993) *Nondestructive Evaluation of Materials by Infrared Thermography.* New York: Springer-Verlag.

Malhotra, V.M.; Carino, N.J. (1991) *Handbook on Nondestructive Testing of Concrete.* Boca Raton, Florida: CRC Press.

Marinetti, Sergio; Muscio, Alberto; Bison Paolo G.; and Grinzato, Ermanno.(2000) " Modeling of Thermal Non-Destructive Evaluation Techniques for Composite Materials." Thermosense XXII. Proceedings of SPIE, Vol.4020, pp.164-173.

Maser, K.R.; Roddis, W.M.K. (1990) "Principles of Thermography and Radar for Bridge Deck Assessment." Journal of Transportation Engineering, Vol.116, No.5, Sept-Oct 1990, pp.583-601.

Mikron Instrument Company, "Table of Emissivity of Various Surfaces." Inc.http://www.transmetra.ch/pdf/publikatinen/emissivity.pdf

Morton, S. (2001) "Externally Bonded Composites for Strengthening Concrete Bridges." Proceedings of the 33rd International SAMPE Technical Conference. Vol. 33, pp. 808-820

Muscio, A.; Corticelli, M.A.; Tartarini, P.(2000) "Theoretical, Numerical, and Experimental Investigation of a One-Side Measurement Technique for Thermal Diffusivity." Thermosense XXII. Proceedings of SPIE, Vol.4020, pp.143-151.

Newnham, P. and Abrate, S. (1993) " Finite Element Analysis of Heat Transfer in Anisotropic Solids: Application to Manufacturing Problems." Journal of Reinforced Plastics and Composites, Vol. 12, August 1993, pp.854-864.

Özişik, M.N. (1985). *Heat Transfer: A Basic Approach.* New York: McGraw-Hill Book Company

Plattner, L. (1999) "In-Situ Measurement of Chip Temperature During Soft Solder Die Bonding Using Integrated Microsensors." International Symposium on Microelectronics. Proceedings of SPIE, Vol.3906, pp.213-220.

Rantala, J.; Hartikainen, J. (1991) "Numerical Estimation of the Spatial Resolution of Thermal NDT Techniques Based on Flash Heating." Research in Nondestructive Evaluation, Vol.3, 1991, pp.125-139.

Rantala, J.; Jaarinen, J.; Kuo, P.K. (1992) "The Effects of Experimental Parameters in the Thermal Diffusivity Measurements of Oriented Polymer Films Using Mirage Effect: Computer Simulation." Applied Physics A: Solids and Surfaces, Vol.55, 1992, pp.586-595.

Rinaldi, Roberto, (2002) "Emissivity: The Common Problem for All Thermographers." Inframation Newsletter, Volume 3, Issue 4.

Sainley, M.B.; Almond, D.P. (1995) "Defect Sizing by Transient Thermography II: A Numerical Treatment." Journal of Physics D: Applied Physics, Vol.28, 1995, pp.2539-2546.

Satonaka, Shinobu; Ohba, Hiroyasu; Shinozaki, Kenya. (1995) "Nondestructive Evaluation of Weld Defects by Infrared Thermography." Proceedings of the International Conference on Offshore Mechanics and Arctic Engineering, Vol.3, 1995, pp.305-312.

Sayers, C.M. (1984) "Detectability of Defects by Thermal Non-Destructive Testing." British Journal of Non-Destructive Testing, Vol.26, No.1, pp.28-33.

Shuler, S.F., Advani, S.G. Kaliakin, Victor N. (1999) " Transient Analysis and Measurement of Anisotropic Heat Conduction in Transversely Isotropic Composite Materials." Journal of Composite Materials, Vol.33, No.7, pp.594-613.

Sjökvist, S.; Georgson, M.; and Ringberg, S.; Uppsäll, M.; and Loyd, D. (1998) "Thermal Effects on Solar Radiated Sand Surfaces Containing Landmines-a Heat Transfer Analysis." Proceedings of the International Conference on Advanced Computational Methods in Heat Transfer, pp.177-187.

Snell, John R. Jr. (1995) "Problems Inherent to Quantitative Thermographic Electrical Inspections." Proceedings of SPIE Thermosense XVII An international Conference on Thermal Sensing and Diagnostic Applications, Vol. 2473, pages 75-81.

Valerand, S.; Maldague, X. (2000) "Defect Characterization in Pulsed Thermography: a Statistical Method Compared with Kohonen and Perceptron Neural Networks." NDT&E International, Vol.33, pp.307-315.

Varis, J; Rantala, J.; Hartikainen, J. (1996) "An Infrared Line Scanning Technique for Detecting Delaminations in Carbon Fiber Tubes." NDT & E International, Vol.29, No.6, pp.371-377.

Varis, J.; Rantala, J.; Hartikainen, J. (1995) "Numerical Study on the Effects of Line Heating in Layered Anisotropic Carbon Fiber Composites." Research in Nondestructive Evaluation, Vol.6, No.2, 1995, pp.69-83.

Varis, J.; Lehtiniemi, R.; Hartikainen, J.; Rantala, J. (1995) "Transportable Infrared Line Scanner Based Equipment for Thermal Nondestructive Testing." Research in Nondestructive Evaluation, Vol.6, 1995, pp.85-97.

Vavilov, V.; Maldague, X.; Dufort, B.; Robitaille, F.; and Picard, J. (1993) "Thermal Nondestructive Testing of Carbon Epoxy Composites: Detailed Analysis and Data Processing." NDT & E International, Vol. 26, No. 2, pp. 85-95.

Vavilov, V.; Kauppinen, T.; Grinzato, E. (1997) "Thermal Characterization of Defects in Building Envelopes Using Long Square Pulse and Slow Thermal Wave Techniques." Research on Nondestructive Evaluation, Vol.9, pp.181-200.

Vavilov, V. (2000) "Three-Dimensional Analysis of Transient Thermal NDT Problems by Data Simulation and Processing." Thermosense XXII. Proceedings of SPIE, Vol.4020, pp.152-163.

Wiecek B.; De Baetselier, E.; De Mey, G. (1998) "Active Thermography Application for Solder Thickness Measurement in Surface Mounted Device Technology." Microelectronics Journal, Vol.29, No.4-5, pp.223-228.

Wu, C.F; Hamada, M. (2000) *Experiments: Planning, Analysis, and Parameter Design Optimization.* New York: J. Wiley.

Zalameda, J.N. (1999) "Measured Through-the-Thickness Thermal Diffusivity of Carbon Fiber Reinforced Composite Materials." Journal of Composites Technology & Research, JCTRER, Vol.21, No.2, pp.98-102.